Travertine shrub structures: origin, diagenetic modifications and petrophysical characteristics – Tivoli case (Central Italy)

Marcelle Marques Erthal

Supervisors:

Prof. Rudy Swennen

Prof. Enrico Capezzuoli

Examination Committee:

Prof. Philippe Muchez

Prof. Patrick Degryse

Prof. Nöel Vandenberghe

Dr. Monique Mettraux

Dr. Eva De Boever

Dissertation presented in partial fulfillment of the requirements for the degree of Doctor of Science (geology)

February 2018

Arenberg Doctoraatsschool, W. De Croylann, 3001 Heverlee, België

ACKNOWLEDGEMENTS

I would like to acknowledge everyone who has assisted me throughout my doctoral studies over the years. Each one contributed in a different way, but my gratitude goes to all.

I would like to thank my supervisor Prof. Rudy Swennen for the opportunity to work with the travertine project, for his guidance and support throughout the course of this research. I also thank him for all the encouragement in trying different methodologies and joining many international conferences. Thank you for all continued support over the years and enthusiasm as I neared my goal.

A special thanks is due to Prof. Enrico Capezzuoli for all the field works that we went on together, for the very constructive discussions and to share his travertine knowledge with me during this period. Thanks for all the support and your effort with my thesis. I also wish to thank for all the learning about Italian culture and cuisine. Surely, his supervision made all the difference in the development and conclusion of the present thesis.

Additionally, I would like to thank the members of the examination committee, Prof. Philippe Muchez, Prof. Patrick Degryse, Prof. Noël Vandenberghe, Prof. Enrico Capezzuoli, Prof. Rudy Swennen, Dr. Eva De Boever and, Dr. Monique Mettraux. I am very honoured to be evaluated by this team of experts.

My gratitude goes to Petrobras for its financial and logistical support and laboratory analyses. Many thanks for giving me the opportunity to do a PhD in a renowned University. Special thanks for Petrobras technitians: Rose Maria de Lima Mencarelli, Ailton Luís da Silva de Souza, Alberto Carlos da Paz, Cláudia Figueiredo Silva, Gerson Felizardo de Souza Junior, Pablo Luigi Damasceno, Paulo Sérgio Rodrigues Campos, Bernardo Coutinho Camilo dos Santos and Julio César Ramos Justen. Further acknowledgement and thanks is due to my manager Vinícius de França Machado.

Special thank you to my Petrobras friends Jéssica Aguillar, Leonardo Gonçalves, Rodrigo Surmas, Yaro Parizek, Guilherme Vasquez, Thaís Fernandes de Matos, Gerson Felizardo de Souza Junior and Pablo Luigi Damasceno for all the support with my samples analysis. In particular to Leonardo Gonçalves, Rodrigo Surmas, Yaro Parizek and Guilherme Vasquez for all the technical discussions and advice.

I would like to thank my friends from the office 02.216: Helen Hamaekers, Hannes Claes and Jeroen Soete. Thanks Helen for your friendship, for all the companionship. Your laughter will always be in my memory. Thanks Hannes for the never ending discussions about shrubs and geochemistry and also for all your support. Thanks Jeroen, first, for putting up with talking about shrubs; second, for the nice music atmosphere in the office; and third, for all the technical discussions and support. Thanks you three for all the many daily moments. I could not be luckier for having shared an office with you three.

Additional gratitude is offered to many colleagues in the field of international education who were also my family in Belgium. This list of individuals includes the following: Asefeh Golreihan, Elisa Maupas, Cihan Aratman, Alexander Minor, Mahtab Mozafari, Tine

Derez, Dominique Jacques, David Debruyne, Ophélie Faÿ, Fábio Paixão, Fernanda Faot and Catarina Miragaia. Thanks for all the special moments that we had together and for always supporting me while I was abroad.

Thank you to all 200E-people for science insights and for the nice time together within and outside the department. Thanks to Alessandro Mancini for the partnership in travertine work, for all the discussions, nice talks and introduction to Italian culture. Herman Nijs is acknowledged for the preparation of thin-sections. Thanks to Eva De Boever for all the help with AVIZO® and discussions about microbes. Thanks to Julie Dewit for the initiative of using mini-permeameter study in the shrub samples from Tivoli. Without your motivation, the performed measurements in a travertine quarry at almost 50°C would not be possible. Julie, for you I have to say "give me a T".

My thanks goes to the quarry owners in the Tivoli-Guidonia area who opened their properties for our fieldwork and research.

I also thank you Prof. Mehmet Özkul, Cihan Aratman and the quarry workers for all the support provided during my short work period in Turkish quarries.

Finally, but most importantly, I wish to thank my lovely family and husband, without your support I would never have handled living far from home. Thank you for keeping me always focused on my purpose and for encouraging me every day. Guilherme, thank you for all the effort you made to come to visit me in Belgium, for handling all the situations and taking care of me and my family.

Thank you Belgium for welcoming me!

Thank you all!

Bedankt!

Obrigada!

Marcelle

ABSTRACT

The discovery of complex continental carbonate reservoirs in the South Atlantic (Brazil and Africa) rift-sag lacustrine basins has generated considerable industrial and scientific interest. One of the most common and promising reservoir lithotype described in the so-called "Pre-Salt" interval is characterized by shrub structures. Searching for analogues, the shrub morpho-types from Tivoli travertines (Central Italy) seems to be a candidate, since they display petrographic features and pore-morphologies remarkably similar to the Pre-Salt reservoir rocks. The shrubs from Tivoli also demand attention because of their laterally very flat and continuous layers, mapped over hundreds of meters, with local packages of more or less 40 m thick. They possess the dimensions of a small reservoir petroleum field.

To better understand and characterize the shrubs from Tivoli and their pore network, a 2D and 3D multi-method and multi-scale workflow was worked out, in which the sedimentology and geochemistry is first studied and subsequently the pore network is accessed. Understanding complex variations in pore geometry within different lithofacies is the key to improve reservoir description and exploitation. In fact, variations in pore geometrical attributes define distinct flow zones (hydraulic units) with similar fluid-flow characteristics.

The shrubs from Tivoli are mainly characterized by their branching texture, however, they are very variegated. By analyzing them petrographically and by using 3D micro computer tomography (µCT) images, it was possible to distinguish 6 shrub morpho-types, named: narrow dendriform shrubs, wide dendriform shrubs, fili dendriform shrubs, arborescent, arbustiform and pustular shrubs. Their textures (morphologies, size, size sorting and packing) greatly vary, however petrographic analysis showed that they are monotonous in relation to their mineralogy and basic fabrics. They are 100% calcite, and are constituted of peloidal micritic aggregates, always surrounded by a very thin coating of sparry calcite cement. Rarely, they possess a crystalline habit. The presence of these sparry calcite cements that surround the shrubs, influences the quality of the reservoir, because it shields micro-porosity, which is present in the center of the shrub, from meso- and macro-porosity surrounding the shrubs.

The travertine shrub structures from Tivoli are interpreted in the present study to have developed in very shallow extensive waterlogged, slightly inclined flat areas, changing laterally into a slope system with crusts as the main lithotype. Shrub morphologies likely reflect specific (micro-)environments that are controlled by water flow rates, evaporation and microbial activity. Under high flow conditions, CO_2 degassing is the main process leading to carbonate precipitation. Consequently, dense and tightly packed morphologies will precipitate, mainly consisting of the crust lithotype. In this setting, microbes are less dominant. Moreover, dendriform shrubs, with narrow, wide and fili morphologies are interpreted to occur in settings with moderate- to low-energy water flows. Narrow dendriform shrubs reflect faster flowing conditions, with decreasing impact of flow on the morphological characteristics toward wide dendriform shrubs to fili dendriform shrubs. Slow flowing waters to stagnant are more characteristic for the arborescent, arbustiform and pustular shrubs that are possibly highly influenced by evaporation. Besides, the shrubs in the study area make up three depositional sequences that are limited by erosive surfaces.

The stable C and O isotopes are also in agreement with the proposed sedimentological interpretation. The stable carbon isotope signature showed high values varying between +8.71 and +11.32‰VPDB, and stable oxygen

isotope values varied between -4.97 and -8.25‰VPDB, indicating that precipitation was mainly influenced by degassing and evaporation processes. The very high C stable isotope signatures and the shrub fabrics that are mainly composed of micritic peloidal aggregates suggest that microbes mediated also the carbonate precipitation. The $^{87}Sr/^{86}Sr$ ratio signatures pointed out that the Mesozoic limestones of Central Italy served as the main source rock. Besides, the presence of Sr, S, Na and Ba obtained by elemental analysis, suggest that the fluids also percolated the Triassic evaporites.

The main pore types observed in all the shrub samples consist of intershrub and interdigit growth framework pores. Plugs yield porosities from 0.8 to 20.9 % and permeabilities from 0.001 to 5255 mD. No relationship was observed between the shrub morphologies and porosity and permeability lab measurements. However, it was observed that the shrub packing, which corresponds to the ratio between shrub width and adjacent spacing, controls primarily the porosity and secondarily permeability. In addition, shrub size sorting, defined by the complexity of the shrub sizes within a sample, controls primarily permeability and secondarily porosity. Micro-Computer Tomography imaging was used to evaluate the 3D arrangement of shrub morphologies, pore connectivity and porous framework. The results pointed out that shrub morpho-types can be distinguished based on their pore shape volume and possess high pore network connectivity.

Therefore, an integrated methodology, including Nuclear Magnetic Resonance (NMR), Mercury Intrusion Porosity (MIP), Micro-Computer Tomography (μCT), porosity and permeability measurements, petrography and SEM analyses, was introduced to gain insight into the complex variations of the pore network within the Tivoli shrub facies. It was observed that micropores have a significant impact on the permeability by increasing the fluid pathways and tortuosity, and consequently negatively affecting the permeability. This workflow allowed observing that shrub size sorting not only controls permeability, but also pore entrances. Besides, they secondarily influence pore body sizes and porosity, while shrub packing influence primarily the pore body sizes and porosities. The study of the Reservoir Quality Index (RQI) and Flow Zone Indicator (FZI) displayed a relationship with pore parameters, and also evidenced that the amount of microporosity in the pore network negatively affects the quality of the Tivoli travertine shrub reservoir analogue. The relationship between RQI and FZI with MIP/NMR groups represents the heterogeneities of the complex travertine reservoir, and helped understanding the complexity of the pore network.

The application of the Lattice Boltzmann method for permeability simulation derived from μCT images pointed out that shrub morpho-types display a relationship with porosity (μCT results), permeability (K_{sim}) and tortuosity, which varies according to the different depositional shrub architectures (morphology, arrangement of the branches, packing and size sorting). Furthermore, by the use of a portable hand held air mini-permeameter it was possible to quantify the permeability distribution within a reservoir with different shrub morpho-types in detail. Vertical permeability variation was very high, as well as high lateral permeability variation is observed at cm-scale. High anisotropy occurs within laminae, with larger permeability continuity in the direction parallel to the laminae. Textural heterogeneities are responsible for the high permeability variation values within laminae.

The study of acoustic wave velocities showed a relationship between shrub morpho-types, pore-types and porosity. Samples with frame-forming pore-types as mouldic pores or encrusted bubbles show higher velocity values and lower porosities than samples with no frame-forming pores as vuggy pores, resulting in lower velocity values and higher porosities. Besides, the analyzed samples yield lower velocities with higher porosities. In addition, the comparison of Tivoli travertine samples with Turkish and Hungarian ones showed very similar acoustic wave velocity behavior. On the other hand, the comparison with marine carbonate indicates very different compressional-wave velocity relationships with porosity.

TABLE OF CONTENTS

ACKNOWLERDGEMENTS i

ABSTRACT iii

TABLE OF CONTENTS v

CHAPTER 1 General introduction and study aims 1

1.1 Introduction 1

1.2 Aims of the study 3

1.3 Structure of the thesis 4

CHAPTER 2 Shrub morpho-types as indicator for the water flow energy - Tivoli travertine case (Central Italy) 5

2.1 Introduction 5

2.1.1 Nomenclature 6

2.2 Geological setting 7

2.2.1Regional Geology 7

2.2.1.1The Acque Albule Basin 8

2.3 Methods 10

2.3.1 Field mapping and sampling 10

2.3.2 Petrography 10

2.3.3 Scanning Electron Microscopy (SEM) 11

2.3.4 Cold Cathodoluminescence (CL) 11

2.3.5 Total Organic Carbon (TOC) 11

2.3.6 Micro Computer Tomography (μCT) 11

2.4 Results 11

2.4.1 Shrub morpho-types 11

2.4.2 Associated lithotypes 16

2.4.3 Lithologs and sequence correlation 19
2.4.4 Diagenesis 24
2.5 Discussion 25
2.5.1 Interpretation of shrub fabrics and morphologies 25
2.5.2 Shrub growth history and diagenesis 27
2.5.3 Depositional system 28
2.5.4 Shrub morpho-types under different hydrological conditions 31
2.6 Conclusions 33
CHAPTER 3 Geochemistry of the (related-)shrub morpho-types from Tivoli travertines (Central Italy) 35
3.1 Introduction 35
3.2 Methods 35
3.2.1 Sr isotopes 35
3.2.2 Elemental analysis 35
3.2.3 Quantitative evaluation of mineral by scanning electron microscopy (QEMSCAN) 36
3.2.4 Stable carbon and oxygen isotopes 36
3.2.5 (Geo-)statistics 37
3.3 Results 37
3.3.1 $^{87}Sr/^{86}Sr$ isotope C and O Stable Isotopes 37
3.3.2 Elemental composition analysis 37
3.3.2.1 Geochemical (related-)shrub morpho-types dependency evaluation 41
3.3.3 Quantitative mineral evaluation by scanning electron microscopy (QEMSCAN) 42
3.3.4 C and O Stable Isotopes 45
3.3.4.1 Microdrill analysis 47
3.3.4.2 Statistical analysis of C and O stable isotopes 48
3.4 Discussion 50
3.4.1 Strontium isotopes 50
3.4.2 Elemental analysis 51
3.4.3 C and O stable isotopes 53
3.4.3.1 CO_2 origin 54
3.4.3.2 Isotope temperature calculations 59

3.5 Conclusions 59

CHAPTER 4 The influence of depositional textures and 3D shapes in the reservoir characterization of a shrub morpho-types – Tivoli case study (Central Italy) 61

4.1 Introduction 61

4.2 Methods 61

4.2.1 Porosity and Permeability Measurements 61

4.2.2 Micro Computed Tomography (μCT) and pore shape classification 62

4.2.3 (Geo-)statistics 63

4.3 Results 63

4.3.1 Shrub pore-types 64

4.3.2 Porosity and permeability measurements 66

4.3.3 Shrub Textures 69

4.3.4 Micro-Computer Tomography (μCT) 76

4.3.4.1 Pore shapes by using μCT analysis 77

4.3.4.2 Pore shapes and shrub textures 79

4.4 Discussion 81

4.4.1 Shrub textures and their poro-perm characteristics 81

4.4.2 μCT and pore shape types 82

4.5 Conclusions 83

CHAPTER 5 Study of pore network and hydraulic unit characterization based on NMR and MIP measurements of travertine shrub morpho-types - Tivoli case study(Central Italy) 85

5.1 Introduction 85

5.2 Methods 85

5.2.1 Mercury Intrusion Porosimetry (MIP) 85

5.2.2 Nuclear Magnetic Resonance 86

5.2.3 Reservoir Quality Index and Flow Zone Indicator 87

5.3 Results 88

5.3.1 NMR and MIP porosity 88

5.3.2 MIP and NMR pore-size distributions 89

5.3.3 Correlation between pore parameters and shrub textures 93

5.3.4 Reservoir characteristics – Reservoir Quality Index (RQI) and Flow Zone Indicator (FZI) 103

5.4 Discussion 106
5.4.1 Relation between pore body and pore throat size 106
5.4.2 Pore parameters and their relationship with shrub textures 108
5.4.3 Reservoir quality 108
5.5 Conclusions 109
CHAPTER 6 Shrub reservoir characterization - detailed permeability study based on Lattice Boltzmann Method (LBM) simulations and air mini-permeameter measurements
(Tivoli (Central Italy) case study) 111
6.1 Introduction 111
6.2 Methods 111
6.2.1 Petrophysical analysis 111
6.2.2 Micro Computer Tomography (μCT) 112
6.2.3 Representative Elementary Volume 112
6.2.4 Permeability simulations by using Lattice Boltzmann Method (LBM) 113
6.2.5 Tortuosity 114
6.2.6 Air mini-permeameter measurements 114
6.3 Results 117
6.3.1 Representative Elementary Volume (REV) 117
6.3.2 Permeability simulation (K_{sim}) 119
6.3.3 Tortuosity and K_{sim} in function of shrub textures 122
6.3.4 Mini-permeameter 130
6.3.5 Application of RQI and FZI methodology to the mini-permeameter results 135
6.4 Discussion 136
6.4.1 Permeability simulation and Tortuosity 136
6.4.2 Mini-permeameter 137
6.5 Conclusions 138
CHAPTER 7 Acoustic properties in shrub morpho-types from Tivoli (central Italy): relation to porosity-pore-types and comparison with continental carbonate results from Turkey and Hungary 141
7.1 Introduction 141
7.2 Methods 141
7.2.1 Acoustic velocity measurements 141

7.3 Results and discussions 142
7.3.1 Acoustic velocity measurements and petrophysical properties 142
7.4 Comparison between Tivoli travertines with Turkey and Hungary travertines 148
7.5 Conclusions 151
CHAPTER 8 General conclusions 153
REFERENCES 159
APPENDIX 1 175
APPENDIX 2 205

CHAPTER 1 General introduction and study aims

1.1 Introduction

Travertine rocks are continental carbonate deposits formed where hot spring waters, rich in calcium and bicarbonate emerge from springs (e.g. Pentecost, 1990, 2005; Guo and Riding, 1992, 1994, 1998; Pentecost and Viles, 1994; Ford and Pedley, 1996). Travertines from Tivoli, situated near Rome (Italy), comprise one of the most famous and studied deposits from sedimentological point of view. They have been used as prime building and ornamental stone since the Roman Age, including, for instance, the famous Colosseum and Roman fountains as well as the colonnade around Piazza San Pietro (Vaticano). The name "travertine" is derived from the Latin expression "Lapis Tiburtinus" that means "the stone of Tibur". Lately, the city Tibur became the modern Tivoli (e.g. Chafetz and Folk, 1984; Folk et al., 1985).

The study of travertine has become a point of interest since huge hydrocarbon reservoirs were discovered in complex continental carbonate deposits offshore south of Brazil (Campos, Santos and Espírito Santo basins) (Fig. 1.1A) and Africa (Kwanza Basin, Angola). According to Carminatti et al. (2009), this depositional succession and its related, so-called "Pre-Salt", may represent one of the most significant hydrocarbon provinces to be explored in this millennium. Its reservoirs are so named because they occur below a huge Aptian evaporitic sequence often thicker than 2 km (Fig. 1.1B).
The Pre-Salt deposits (Fig. 1.1B) dated as Lower Cretaceous, developed in harsh hypersaline shallow-water continental environments during an arid period in a compartmentalized sag basin (Bueno 2004; Dias 2005; França et al., 2007; Campos Neto et al. 2007; Moreira et al. 2007; Araújo et al. 2009; Beglinger et al. 2012).

Despite the fact that most of the Pre-Salt data remains confidential, some authors (e.g. Dias, 1998; Terra et al., 2010; Wright 2012; Wright and Barnett, 2015; Rezende and Pope, 2015; Saller et al., 2016) have pointed out that lithologies made by shrub structures (Figs. 1.2A to C) display one of the best reservoir characteristics of the Pre-Salt section. Terra et al. (2009) characterized the different shrub external morphologies and textures from the Pre-Salt. The latter authors described this feature as "stromatolite", where they divided them into "arborescent", "arbustiform" and "dendriform".

Tivoli travertines are well known worldwide for the abundance of laterally very continuous layers dominated by shrub-like or fern-like arborescent growth structures that resemble a succession of miniature forests (Chafetz and Folk, 1984). These structures present petrographic features and pore-morphologies remarkably similar to the Brazilian Pre-Salt reservoir rocks (Figs. 1.2D to F), characterized by their poro-perm complexity attributed to variegated and highly heterogeneous textures. Moreover, the shrub geobody in Tivoli possesses the dimensions of a small oil field, spanning several kilometers in width as well as in length and up to a few tens of meters in thickness.

Although modern hot spring travertines have been studied for many years, only a relatively small number of fossil travertines have been studied (Guo and Riding, 1998, Capezzuoli et al., 2014). Besides, the study of their pore network even received less attention, since the concern of the scientific community has been mainly related with the travertine formation process, its relation to global climate variation, tectonics, geochemistry, microbial deposition, among others (e.g. Carucci et al., 2012; Capezzuoli et al., 2014). Therefore, the characterization of porosity and permeability of this peculiar carbonate rock represents one of the biggest challenges for hydrocarbon exploration. In addition, shrub structures show a variety of textures (e.g. morphologies, size, size

sorting and packing), pore sizes and shapes that generate complex pore networks, which a 2D study cannot fully cover. Thus, petrographic observations in 2D and 3D, the latter based on µCT imaging, together with their relationship to petrophysical properties will provide key elements allowing to better understand the complex pore network related to the different shrub textures. This should allow to predict the reservoir characteristics and behavior for oil/water/gas exploitation.

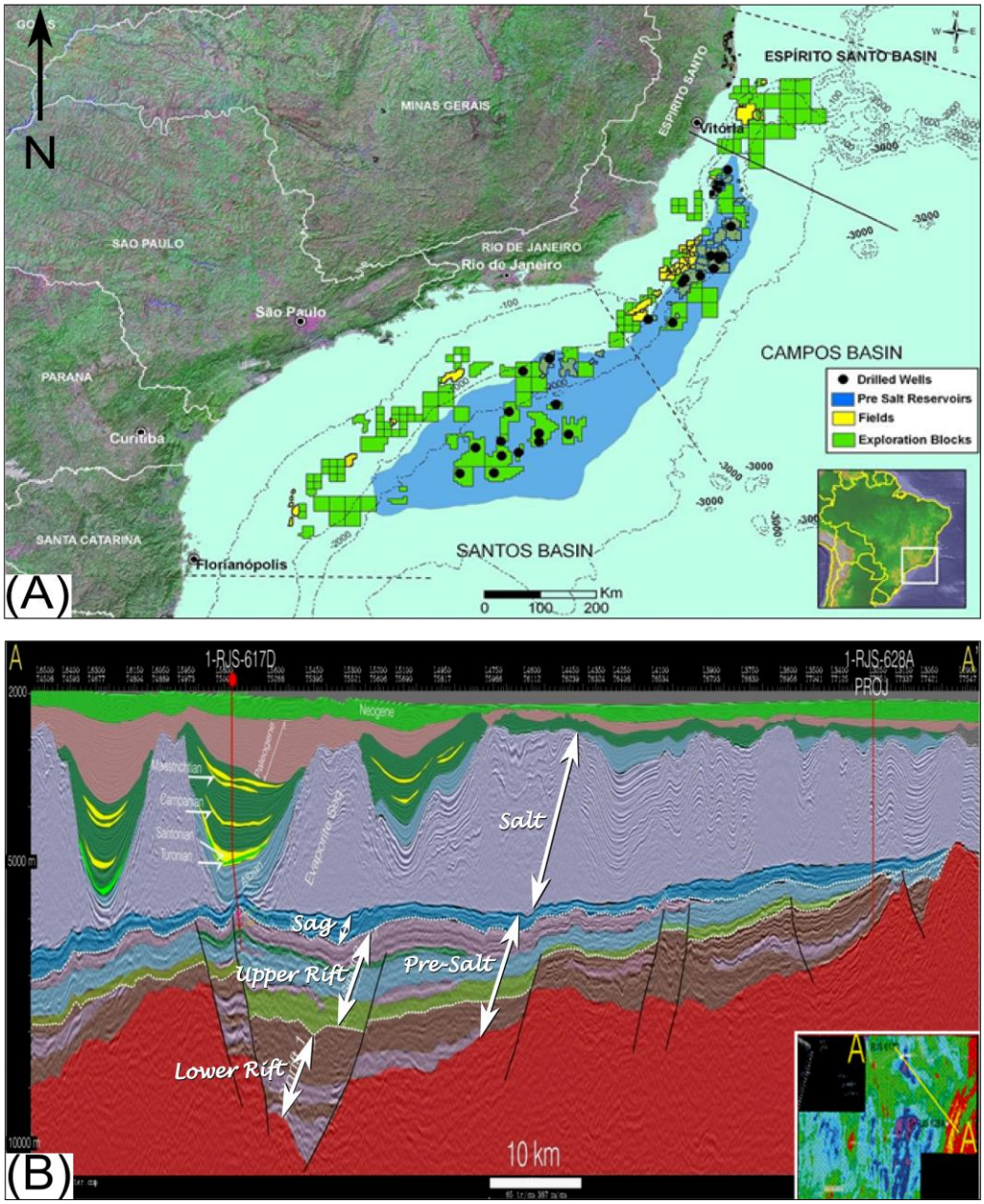

Fig. 1.1: (A) Pre-Salt location map of Santos, Campos and Espírito Santo basins, offshore Brazil. (B) Pre-Salt interpreted seismic section from Santos basin (Bueno et al., 2009).

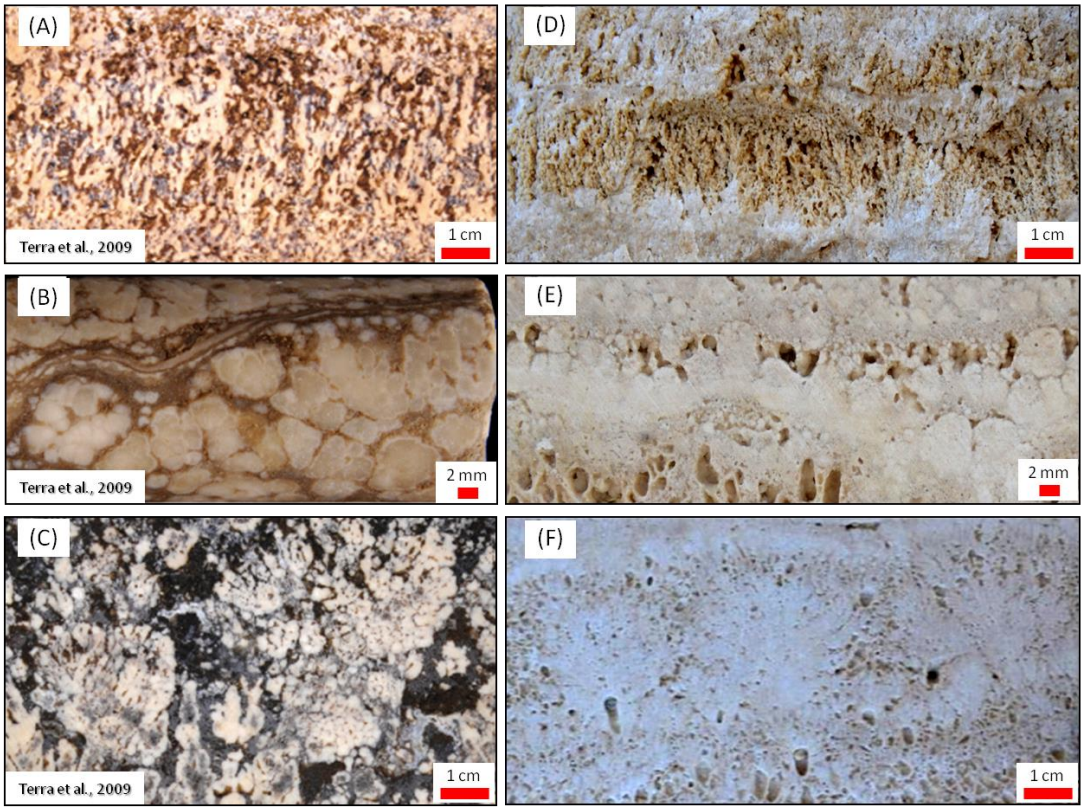

Fig. 1.2: Pictures from (A) to (C) represent shrub examples from the Pre-Salt (Terra et al., 2009). Pictures from (D) to (F) are from Tivoli travertine shrub structures. Notice how similar is the shrub morphologies from the Pre-Salt and Tivoli.

1.2 Aims of the study

One of the most important existing and emerging challenges is to improve reservoir characterization. In carbonate successions the complex relationship between the original properties associated to the depositional facies and the possible modifications inherited from diagenesis often causes large variations in the quality of reservoirs, which hamper the evaluation of flow predictability. It is well recognized that improvements in reservoir description will reduce the amount of hydrocarbon left in the reservoir rocks (Amaefule et al., 1993). A clear understanding of the factors controlling the vertical/lateral heterogeneity of porosity and permeability within carbonates is fundamental for building conceptual reservoir models (Brigaud et al., 2014). Accurate determination of pore-body and throat attributes and fluid distribution are essential to improved reservoir characterization.

The present thesis aims to characterize and understand the genesis of different travertine shrub structures of the Tivoli travertines and proposes a scenario, which explains their different textures and morphologies. The study also aims to understand the relationship between the shrub textures and heterogeneity with regard to pore network properties such as porosity and permeability. In addition, it aims to provide a methodological workflow for the characterization of travertine depositional setting as well as rock-typing to be used as a model for subsurface reservoirs. Since a 2D pore-type classification cannot fully incorporate and describe full 3D complexity, a multi-method approach has been used to address the distribution of petrophysical properties in the carbonates studied. The integrated approach combined; 3D micro-computed tomography; 2D studies at different scales; outcrop mapping to microfacies analysis; selected analytical tools such as isotopes (C, O, Sr), porosity and permeability measurements, Nuclear Magnetic Resonance (NMR), Mercury Intrusion Porosity (MIP), mini-permeameter and acoustic velocity measurements. Reservoir Quality Index (RQI) / Flow Zone Indicator (FZI), and permeability simulation was carried out to study the fluid characteristics of shrub facies reservoir. The

following sub-objectives of this study were defined:

1. Characterization and classification of different shrub morpho-types from Tivoli travertines by using 2D and 3D image analysis.

2. Inference of the palaeo-environmental setting in which the different shrub textures formed, addressing the dominant hydrodynamic / microbial and diagenetic processes which affect the shrub textures.

3. Geochemical characterization of the shrub structures by means of stable oxygen and carbon as well as strontium isotopes; major and trace elemental concentration in order to address the genesis and processes that promote carbonate precipitation, allowing to assess depositional water temperatures, CO_2-origin and fluids source rocks.

4. Evaluate the relationship between shrub textures and porosity and permeability measurements, in order to better understand factors controlling heterogeneities of the poro-perm characteristics.

5. Determination of the 3D pore shapes of shrub textures.

6. Perform rock-typing to better understand the pore network structure and its connectivity among the different shrub textures, involving NMR and MIP measurements.

7. Characterization of the Reservoir Quality Index and Flow Zone Indicator to access the possible hydraulic units within the shrub textures.

8. Application of flow modeling by using μCT analysis (reconstruction of the digital pore networks) and Computational Fluid Dynamics (CFD) in Palabos software (to simulate and calculate fluid dynamics) to better understand fluid behavior within each shrub morpho-type reservoir.

9. Evaluating the influence of shrub textures on porosity, tortuosity and, consequently, on permeability.

10. Defining acoustic wave velocity of Tivoli shrub morpho-types, and comparing this relationship to the results acquired from Turkish and Hungarian travertines according to Soete et al. (2015).

1.3 Structure of the thesis

Chapter 1 of the thesis consists of an introduction and presentation of the study goals. It is meant to familiarize the reader with the subject of the thesis. Chapter 2 describes the geological setting of the travertine from Tivoli, the description and classification of the different shrub morpho-types, the paleoenvironmental reconstruction and its specific water flow conditions. Chapter 3 deals with the geochemical characterization of the travertine shrubs from Tivoli, focusing on stable oxygen and carbon as well as strontium isotopes, major and trace elements, and the origin of the CO_2. Chapter 4 provides a petrophysical assessment of shrub textures (e.g. morphology, size, size sorting and packing) and its relationship with pore systems and petrophysical properties. In Chapter 5, the pore network and hydraulic unit characterization of the shrub textures are discussed based on NMR and MIP measurements. In Chapter 6, a detailed permeability study based on Lattice Boltzmann Method (LBM) simulations and air mini-permeameter measurements is discussed. Chapter 7 provides results from acoustic property measurements of shrub morpho-types from Tivoli and its relationship to porosity and pore typing. A comparison with continental carbonate results from Turkey and Hungary according to Soete et al. (2015) is also given in Chapter 7. Finally, Chapter 8 draws the general conclusions derived from the different topics studied.

In the appendix, an integral paper about shrubs and pore-type classification from Denizli Basin (SW Turkey), in which the author actively participated, is given.

CHAPTER 2 Shrub morpho-types as indicator for the water flow energy - Tivoli travertine case (Central Italy)

Based on Erthal, M.M., Capezzuoli, C., Mancini, A., Claes, H., Soete, J., Swennen, R., 2017. Shrub morpho-types as indicator for the water flow energy - Tivoli travertine case (Central Italy). Sedimentary Geology, 347, 79-99. http://dx.doi.org/10.1016/j.sedgeo.2016.11.008

2.1 Introduction

Continental carbonate research became of major interest in the last decade due to the discovery of giant hydrocarbon reservoirs in such carbonates in the South Atlantic, located offshore Brazil (Campos, Santos and Espírito Santo basins), but also offshore Angola (Carminatti et al., 2008). The carbonates in these oilfields are of Aptian age representing continental deposits formed in a rift-sag setting (Dias, 2005). The latter are known as 'Pre-Salt', because they occur just below a huge sealing salt succession, locally being 2 km thick (Dias, 2005). One of the most common features observed in the Pre-Salt succession are shrub-like fabrics (Dias, 1998, 2005; Rezende and Pope, 2015), forming very interesting reservoir lithologies in the South Atlantic prospects (Dias, 1998, 2004; Wright 2012; Wright and Barnett, 2015; Rezende and Pope, 2015). Little has been published on the Pre-Salt from Brazil and Africa (Terra et al., 2009; Wright, 2012; Rezende and Pope, 2015; Wright and Barnet, 2015; Saller et al., 2016) and few studies have been carried out looking for an analogue (Claes et al., 2015, 2016; De Boever et al., 2016; Soete et al., 2015; Schröder et al., 2016; Ronchi and Cruciani, 2015). Apparently, up to now no specific analogue was found that fully corresponds to such reservoir in all its aspects. This is partly because of confidentiality issues of the encountered systems in the discovered reservoirs, but also because detailed petrographical data are lacking. Of interest here is that the shrubs from the Acque Albule basin, near Tivoli (central Italy) (Folk and Chafetz, 1983; Chafetz and Folk, 1984) display remarkably similar fabrics and pore-morphologies as reported Pre-Salt cases (Dias, 1998, 2005; Carminatti et al., 2008; Wright, 2012; Rezende and Pope, 2015; Saller et al., 2016). Because of this, Tivoli shrubs can be used as potential analogue from a reservoir point of view.

The first shrub occurrence was described in travertine from Japan (Kitano, 1963) and subsequently in the extensive travertine outcrops from Tivoli, east of Rome, where it comprises the most abundant component found (Folk and Chafetz, 1983; Chafetz and Folk, 1984). Moreover, shrubs were described in many other travertine deposits as for example in Yellowstone National Park, Wyoming (Pursell, 1985; Fouke et al., 2000, 2011) and Rapolano, Central Italy (Folk and Chafetz, 1983; Chafetz and Folk, 1984; Guo and Riding, 1994, 1998). These structures have been attributed both to abiotic (Pentecost, 1990) and biogenic (Chafetz and Meredith, 1983; Chafetz and Folk, 1984; Chafetz and Guidry, 1999; Gandin and Capezzuoli, 2014) processes. According to many authors (Jones and Renaut, 1995; Chafetz and Guidry, 1999; Jones et al., 2000; Turner and Jones, 2005) shrubs are locally restricted to chemically harsh and hot-water travertine deposits (Capezzuoli et al., 2014), occurring as shallow lake-fill deposits (Chafetz and Folk, 1984) and in depressional depositional systems (Guo and Riding, 1998).

Despite the fact that shrub descriptions exists in literature (Kitano, 1963; Folk and Chafetz, 1983; Chafetz and Folk, 1984; Folk et al., 1985; Pentecost, 1990; Guo and Riding, 1992, 1994, 1998; Chafetz and Guidry, 1999; Chafetz, 2013) the data presented do not address the 3D geobody configuration neither the mutual vertical or lateral relationship between different complex shrub morphologies. The prime aim of

this study is to characterize shrub morpho-types from Tivoli, to infer the paleo-environments in which they precipitated, and to relate shrub types to specific water flow conditions based on observations made at different scale (from micron under the microscope till several hundreds of meters along quarry walls). Secondly, diagenetic overprinting, which can severely modify shrub primary fabrics, is studied in view of its impact on related pore network characteristics.

2.1.1 Nomenclature

The terms "tufa" and "travertine" are used to describe carbonate spring deposits (Rainey and Jones, 2009). The term “travertine” comes from the Latin name “lapis Tiburtinus” that means the stone of Tibur (the modern city of Tivoli, where our study is performed) (Chafetz and Folk, 1984) and it has been largely used for hydrothermal-derived precipitates, while “tufa” is reported to ambient temperature precipitates (Pedley, 1990; Brasier, 2011; Capezzuoli et al., 2014; Della Porta, 2015). The term “travertine” is used here to describe carbonate layered deposits, commonly with abundant shrub morpho-types (mainly dendritic macrofabric), precipitated from springs (Riding, 1991).

The term shrub was first described by Kitano (1963) and subsequently referred by Folk and Chafetz (1983,) and Chafetz and Folk (1984) as “shrub-like or fern-like arborescent growth forms that branch upward to form colonies 2 - 8 cm high, giving the appearance of a succession of miniature forests”. Later, Chafetz and Guidry (1999) separated shrubs in “bacterial shrubs”, showing very irregular forms, and “crystal shrubs” and “ray-crystal crusts” displaying regular geometric patterns.

The most common vertical shrubs are tree-like structures, showing upward expanding, irregular dendrite structures (Jones and Kahle, 1993; Guo and Riding, 1994; Jones and Renaut, 1995, 2010) as well as complex arrangements of non-crystallographic orientated structures (Keith and Padden, 1964; Jones and Renaut, 1995). In plain view shrubs resemble small, subspherical to mushroom-shaped clusters (Fouke et al., 2003) with low synoptic relief (Gandin and Capezzuoli, 2014).

The shrub morphologies are often described as “dendrite” possessing tree-like crystals and multiple branching levels (Keith and Padden, 1964; Lofgren, 1974; Jones and Kahle, 1986, 1993; Jones and Renaut, 1995). The latter is frequently used to define the branching characteristic of the structure. They can be divided as crystallographic and non-crystallographic dendrites according to the orientation of the crystals (Keith and Padden, 1964; Jones and Renaut, 1995). “Dendrolite with bacterial shrub fabric” (Gandin and Capezzuoli, 2014) is used to define “colonies of densely packed bacterial clumps with an evident vertical to radial pattern that forms dense clusters of dendrolitic arrays”.

Other terminologies in relation to shrubs found in literature are “arborescent” and “arbustiform” meaning “to grow like a tree” in Latin. These terms are used mainly to characterize structures with upward growing features. Terra et al. (2009) use the term “arborescent” for structures with their height larger than their width, while “arbustiform” possess a height/width ratio of about 1:1.

According to Chafetz and Guidry (1999), “shrubs and genetically related shrub-like features display considerably different morphologies. They range from those whose outline is typical of the common garden variety woody shrub or bush (bacterial shrubs) to those that have regular geometric patterns (crystal shrubs) to crystalline calcite fans (ray-crystal crusts)”. The same authors also mentioned that the morphologies vary according to the dominating process: i.e., biotic (bacterial shrubs) or abiotic dominated (crystal shrubs and ray-crystal crusts). Bacterial shrubs (Chafetz and Guidry, 1999) possess irregular morphologies and non-crystallographic characteristics. Crystal shrubs (Chafetz and Guidry 1999) have similar morphologies as the non-crystallographic and crystallographic dendrites described by Jones and Renaut (1995). However, Chafetz and Guidry (1999) use the term “crystal shrubs” to refer to features that are the product of both bacterially induced as well as abiotic precipitation. They also referred to the term “ray-crystal crusts” for structures that are made of coarse to extremely coarsely crystalline

calcite spar, being one order of magnitude larger than the bacterial and crystal shrubs.

The term "crystalline crust" (Chafetz and Folk, 1984; Folk et al., 1985; Chafetz et al., 1991; Jones and Renaut, 1995, 1996, 2010; Guo and Riding, 1998, 1999; Renaut et al., 2013; Gandin and Capezzuoli, 2014) and "ray-crystal crust" (Chafetz and Guidry, 1999) are reported to possess a spectrum of uncommon morphologies. The most typical crystalline lithotypes are the fan/ray (Folk et al., 1985; Guo and Riding, 1992, 1998; Fouke et al., 2000; Jones and Renaut, 2010) and feather-like forms (Chafetz and Folk, 1984; Folk et al., 1985; Guo and Riding, 1992; Koban and Schweigert, 1993). The latter is also known as "non-crystallographic dendrites" (Jones and Renaut, 1995), "crystal shrubs" (Chafetz and Guidry, 1999), "feather dendrites" (Rainey and Jones, 2009), "pseudodendrites with branching bundles of platy calcite" (Jones and Renaut, 1998) and "feather-like crystals" (Gandin and Capezzuoli, 2014). The feather-like crystals can be grouped in two main assemblages: formed by aggregates of rhombohedral crystals and by branching dendritic units (Jones and Renaut, 2010; Gandin and Capezzuoli, 2014).

The term shrub as used in this publication refers simply to the outer morphology of the upward growing structures as deduced by petrographic observations. Its use is independent from the fact whether they are crystalline or micritic in nature.

The term "crystalline" is used for the shrubs and crusts as an adjective. According also to previous works (Guo and Riding, 1998; Chafetz and Guidry, 1999), it is used to define the form of the crystal, i.e. the depositional fabric of the shrub is crystalline. Instead, the term "sparite" (see Flugel, 2004 for a review) is defined as the coarse crystalline calcite cement which fills pore spaces in many sediments after deposition, formed by the precipitation of calcite from carbonate-rich solutions passing through the pore spaces in the sediment.

2.2 Geological setting

2.2.1 Regional Geology

The Acqua Albule Basin (central Italy) is located in Italy, in the Central Apennines (Fig. 2.1). The fold-thrust chain architecture of the broader study area developed from the convergence and collision during late Cretaceous - Early Miocene between the Alpine orogen and the continental crust of the Adria promontory (Patacca et al., 1992; Molli, 2008; Barchi, 2010) and incorporating tectonic units from Meso-Cenozoic marine carbonate successions of the Thetys Ocean and from the adjacent continental passive margin. After nappe stacking, eastward migrating extension affected this Apennine sector (Jolivet et al., 1998; Brunet et al., 2000) resulting in reduced thickness of the lithosphere, volcanism and increased geothermal gradients (Funiciello et al., 1976; Chiodini et al., 2004). As a consequence of the extension, Late Miocene - Early Pleistocene hinterland basins formed where continental and/or shallow marine sedimentary successions were deposited (Martini and Sagri, 1993; Brogi and Liotta, 2008). Such basins are generally characterized by a system of NW-striking normal fault systems that are laterally bounded by a NE-striking transfer faults (Acocella and Funiciello, 2002, 2006). Interaction between the NW and NE fault systems locally increased crustal permeability and is considered to promote fluid flow circulation during hydrothermal stages (Dini et al., 2008; Liotta et al., 2015; Brogi et al., 2016).

In this tectonic setting, widespread volcanism took place during the Middle Pleistocene in the Tyrrhenian side of the Apennines (De Rita et al., 1988, 1995). The last episode of volcanism is marked by the eruptions of the Colli Albani volcano (Funiciello et al., 2003). The latter is Middle Pleistocene-Holocene in age and developed close to (~ 5 km) the SE margin of the Acque Albule Basin (Carucci et al., 2012).

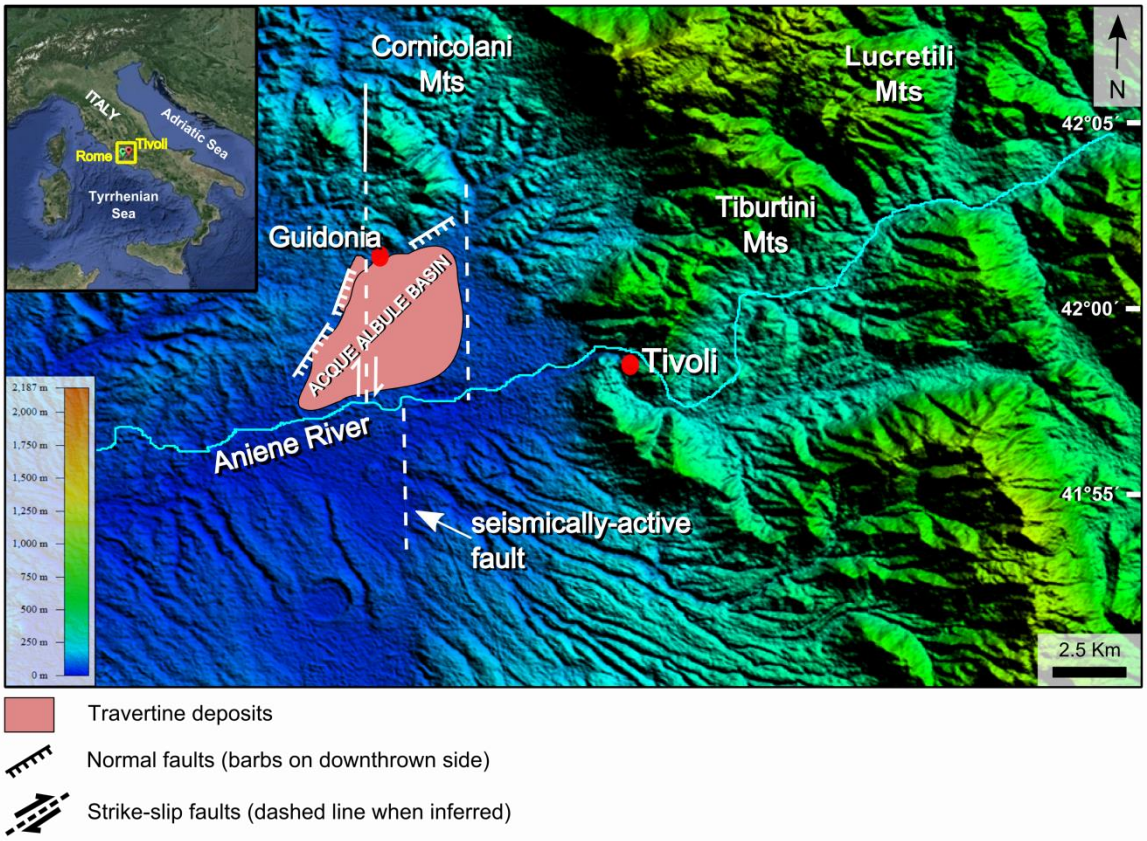

Fig. 2.1: Physiographic image of Acque Albule Basin (indicated in pink color) from Shuttle Radar Topography Mission (SRTM - NASA) data.

2.2.1.1 The Acque Albule Basin

The Acque Albule Basin corresponds to a morphological depression, gently dipping towards the south (Faccenna et al., 2008), where it is bordered by the Aniene River. Its northern and eastern boundaries consist of Meso-Cenozoic marine carbonates of the Lucretili, Tiburtini and Cornicolani mountains, while to the west and south Plio-Pleistocene marine-to-continental siliciclastics and Middle Pleistocene (from 500 to 350 ka; De Rita et al., 1995) epivolcanic deposits crop out.

The Lapis Tiburtinus travertines are located west of the Tivoli City (Fig. 2.1) covering an area of 7 km in length and 4 km in width, of which an area of 3.4 km by 1.3 km is quarried (Fig. 2.2), resulting in one of the largest and thickest exposed travertine plateau in the world (Faccenna et al., 1994b, 2008; De Filippis et al., 2013). This deposit, dated as Late Pleistocene (between 115 and 30 ka), fills up a pull-apart depression (Faccenna et al., 2008) controlled by N-striking right-lateral and NE-striking transtensional-to-normal faults (Alfonsi et al., 1991; Faccenna et al., 1994; De Filippis et al., 2013). The faults activity is also partially related to the latest stages of volcanism and hydrothermal discharge (e.g. Gasparini et al., 2002; Billi et al., 2007; De Filippis et al., 2013).

Travertine deposits reach an average thickness of 60 m in the central sector, with a reported maximal thickness of 90 m coincident with a N-striking active fault (Maxia, 1950). According to Chafetz and Folk (1984) the carbonate succession is particularly compact and characterized by a vertical succession of sub-horizontal, 8-10 m thick benches mainly formed by alternations of bacterial peloidal mud, tufa-like travertine and laminated bacterial stromatolites. The benches are separated by erosional surfaces, associated with pockets of clays and conglomerates (De Filippis et al., 2013) that gently dip towards the south (Faccenna et al., 2008). The upper 3 - 4 m of the travertine succession (named “testina”; Folk et al., 1985; Faccenna et al., 2008) which caps most part of the Tivoli plateau (Fig. 2.3A), is poorly compacted and therefore friable.

According to De Filippis et al. (2013) the travertines from the Tivoli plateau had an average depositional rate of 0.4 mm/a, which according to these authors also corresponds to the average vertical subsidence rate of the Acque Albule Basin.

The depositional environment has been interpreted as sub-horizontal pools and dammed-terraces (Faccenna et al., 2008) fed by vents (Chafetz and Folk, 1984; Guo and Riding, 1994; Wright, 2012; Chafetz, 2013) with high-energy travertine facies only locally present. The depositional system was controlled by fluctuations of the local water table and possibly influenced by paleoclimate cycles (De Filippis et al., 2013). The Lucretili-Tiburtini-Cornicolani mountains correspond to the recharge areas for the aquifers that feed the travertine system (Capelli et al., 2005; Carucci et al., 2012).

Chafetz and Folk (1984) and Minissale and Sturchio (2004) came up with a slightly different depositional setting emphasizing the existence of shallow lakes with minor contribution of clastic material.

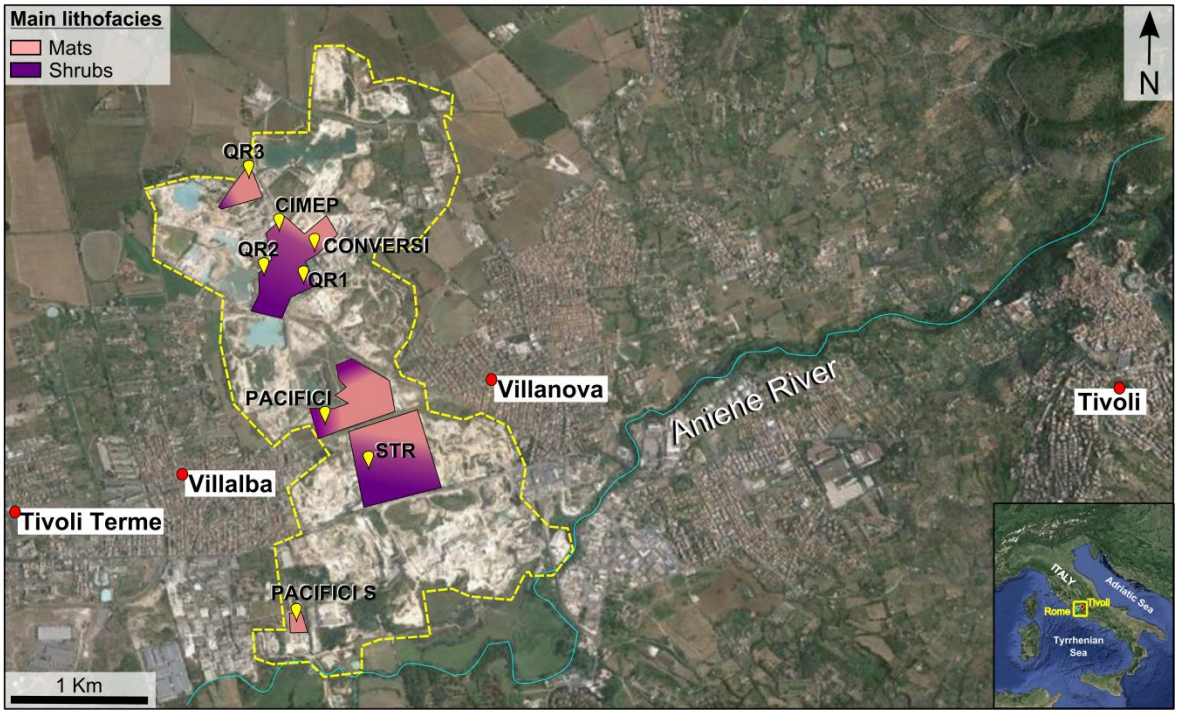

Fig. 2.2: Tivoli quarry area, delineated by yellow dashed line, localized almost 5 km from Tivoli city, Central Italy. The main lithofacies observed in the studied quarries are indicated: purple color is used for shrub lithofacies, and pink for mats lithofacies.

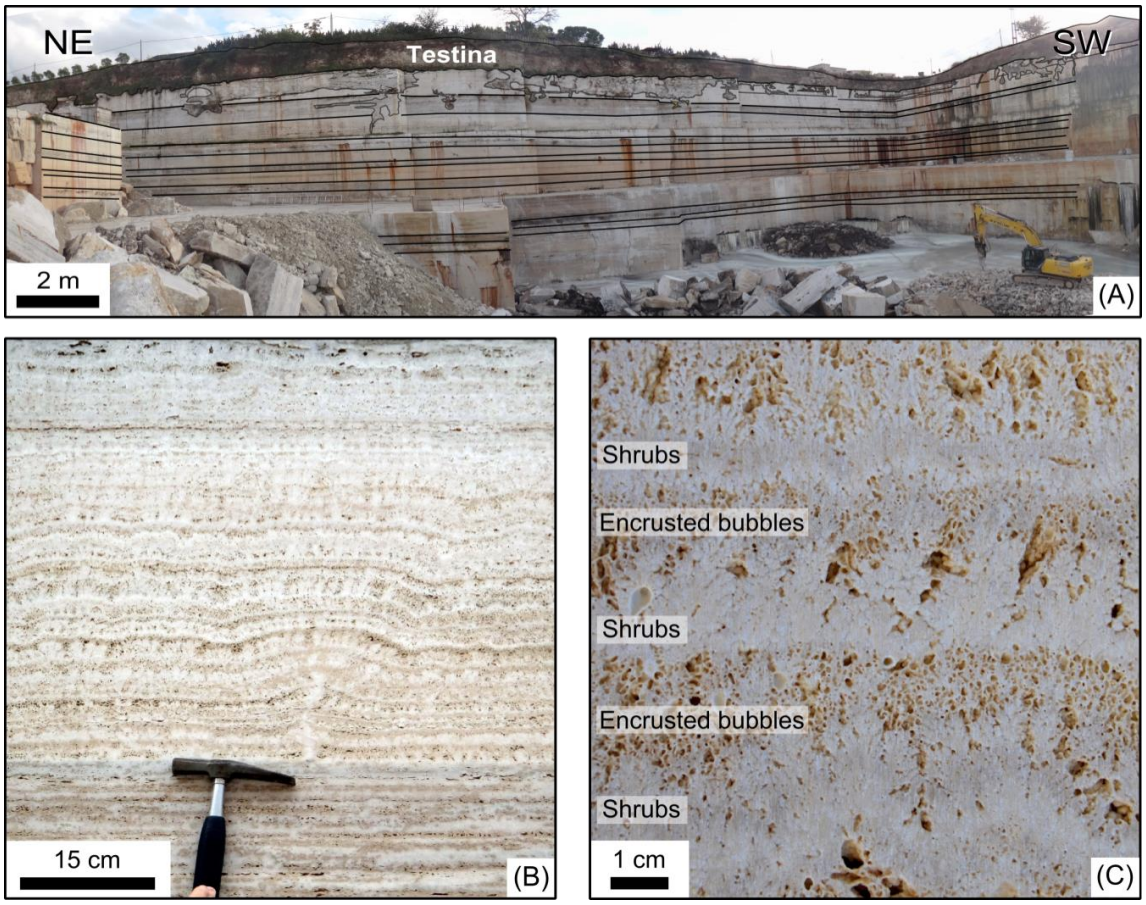

Fig. 2.3: (A) Overview of Querciolaie-Rinascente 1 quarry (QR1). Notice the lateral continuity of the travertine layers as accentuated by black lines. (B) Shrub stacking pattern. The shrub layers are intercalated with finely laminated micrite layers that can create morphologies displaying a pseudo-stromatolitic outline. (C) Detail showing dendritic shrubs finely intercalated with encrusted bubbles.

2.3 Methods

The detailed study of the travertines in the Tivoli quarries allowed working out a classification of the shrub morpho-types that were described and distinguished mainly macroscopically and by using micro Computer Tomography scans (µCT). Thin sections were studied for detailed characterization of the shrub nature. The different shrub morphologies were reconstructed in 3D by using µCT. Their branches, textures, and pore network distribution are in the end 3D features. Nevertheless, the high textural heterogeneity can create ambiguity when shrub types have to be distinguished. Micro-CT analysis show that shrubs possess a complex distribution of their branches in 3D, the differences in shrub morphologies are dependent of the organization of the latter.

2.3.1 Field mapping and sampling

Detailed fieldwork was undertaken in the Tivoli quarry area with approximately 50-60% of the travertine studied in the framework of this project (areas in purple and pink in Fig. 2.2). The examined quarries included in this specific study are: Querciolaie-Rinascente (QR) 1, 2 and 3, Conversi, Conversi S, Cimep, Pacifici, and STR. In the quarries, lithofacies were described and mapped. Lithologs were made that reveal details about the depositional setting and evolution of the system. Vertical and horizontal core plugs of 1 and 1.5 inch in diameter, representative of all the shrub types observed in the field, were collected and analyzed.

2.3.2 Petrography

All the samples were doubly impregnated with resin before thin section preparation. Blue as well as fluorescent dyes were used to highlight

the porosity when using classical and fluorescence microscopy, respectively. Petrographic characterization was conducted on an Olympus BX60 (Olympus Corporation, Tokyo, Japan) and Leica (Leica Microsystems, Wetzlar, Germany) DM LP microscope using parallel and crossed polars.

2.3.3 Scanning Electron Microscopy (SEM)

For Scanning Electron Microscopy (SEM) freshly broken samples with uneven surface were adhered to an aluminum conductive support and covered by a thin Palladium-Gold layer, with an Emitech K750X. The analysis was performed on a ZEISS EVO LS15 SEM, which creates images by secondary electrons, operating under high vacuum and 20kV.

2.3.4 Cold Cathodoluminescence (CL)

During cold cathodoluminescence microscopy, electrons are generated by an electric discharge between two electrodes under a low gas pressure (Marshall, 1988; Rémond et al., 1992). The CL stage consists of an electron gun, a vacuum chamber with windows and a stage allowing X-Y movement. The working conditions varied around 10 KeV and 250 mA. A Zeiss MK5-2 microscope was used for CL observations.

2.3.5 Total Organic Carbon (TOC)

The amount of organic matter in the sediments is expressed as the relative percentage of organic carbon on a dry weight basis (Mendonça Filho et al., 2010a, 2012). For the TOC analysis the sample has to be first weighted, then, digested by acid to remove the mineral phases. The most used acid is the hydrochloric (HCl) at 10% concentration, to remove the carbonate content. The sample was subsequently put into an oven at 80°C, and weighed again. After that, the sample was brought to an induction oven for burning. The signal of the cell is processed in an integrated circuit and recorded in a digital circuit for a direct reading of the amount of carbon in the sample, which is provided in terms of weigh percentage of organic carbon of the rock.

2.3.6 Micro Computer Tomography (µCT)

Nineteen representative samples were scanned with µCT to render the pore network in 3D and to describe its 3D shapes. A Phoenix Nanotom s CT system (GE Measurement and Control Solutions, Wunstorf, Germany), equipped with a 180 kV/15 W high-performance nanofocus X-ray tube and a 2304 x 2304 pixel Hamamatsu detector, was used to perform the scans. A 0.3 mm thick copper filter was installed during the scans. The plugs were scanned at 120 to 130 kV tube voltage and a current of 220 to 290 µA. Radiographs are reconstructed with the Phoenix datos|x 2.0 reconstruction software (GE Measurement and Control Solutions, Wunstorf, Germany) and images with an isotropic voxel size of respectively 13 and 17 µm for 1 and 1.5 inch diameter plugs were exported. The registered slices were segmented in Matlab by applying a dual thresholding technique (Claes et al., 2016). The resulting images were processed in Avizo Fire (v.7), where pores were labeled and rendered in 3D.

2.4 Results

2.4.1 Shrub morpho-types

Shrub morphologies present in the Tivoli travertines make up one of the most impressive lithofacies, reaching thickness of ~ 40 m, and are characterized by a remarkable lateral continuity over hundreds of square meters (Chafetz and Folk, 1984) (Figs. 2.2 and 2.3A). They mainly consist of arborescent structures that resemble small trees, usually show branches that split from a stem in a dendritic way (Figs. 2.3B, C, and 2.4A to C). In general, they are 1-3 cm in height, and grow in dense masses to more divergent irregular branches (Chafetz and Folk, 1984; Folk et al., 1985) (Figs. 2.3C and 2.4A to C). The branches can radiate from a rod-like structure being present in the central part of the shrubs or they can develop from a common point (Figs. 2.4A and B). The shrub morpho-types occur in alternation with 1-3 cm thin layers composed of laminated peloidal micrite, resembling sometimes stromatolite-like structures due to their macroscopic stratiform and domal morphologies (Fig. 2.3B), and laminae (~ 1 cm high) containing encrusted bubbles (Fig. 2.3C) (Chafetz et al., 1991). The

encrusted bubbles, also known as 'foam rock' (Chafetz and Folk, 1984) or 'coated bubble' (Rainey and Jones, 2009), are vertically elongated, with a hollow center surrounded by a dense micritic rim. The alternations occur on mm- to cm-scale. On macro-scale, the peloidal micrite layers, ~ 0.5 cm thick, show a smooth lamination that follow the shrub layering.

Tivoli shrubs on micro-scale are mainly composed of dark-grey tiny spherical to sub-spherical micritic aggregates of 0.5 – 0.1 mm, with knob-like shape (Figs. 2.4A to F). They rarely show millimeter scale alternation of micrite with sparite (Fig. 2.4G) that formed parallel to bedding and are perpendicular to the shrub growth, and rarely consist of pure sparite (Fig. 2.4H). They are almost all surrounded by euhedral to sub-euhedral rhombic spar calcite (Fig. 2.4). The cements often possess a halo of cloudy micrite around the internal peloidal micritic aggregates (Fig. 2.4I). Fluorescence microscopy showed that areas where peloidal micrite occurs, display a natural light to bright green fluorescence (Figs. 2.5A to C), while the surrounding sparite crystals do not fluoresce (Figs. 2.5A to C). Filamentous features trapped in sparite cements between the shrubs structures were observed under the microscope (Figs. 2.5D to F). Total Organic Carbon (TOC) shows very low values (< 0.2 %). Under SEM, the shrub nucleus show hollows surrounded and sometimes completely filled by peloidal micritic aggregates (Figs. 2.5G and H). The latter is composed of spherical to sub-spherical micrite, smaller than 1 µm in size (Figs. 2.5I to L) that resembles colonies of bacteria (cf. Guo and Riding, 1992, 1994; Vasconcelos and McKenzie, 1997; Dupraz et al., 2004, 2009). Ostracods and small plant moulds occur between shrubs or as a substrate of the latter.

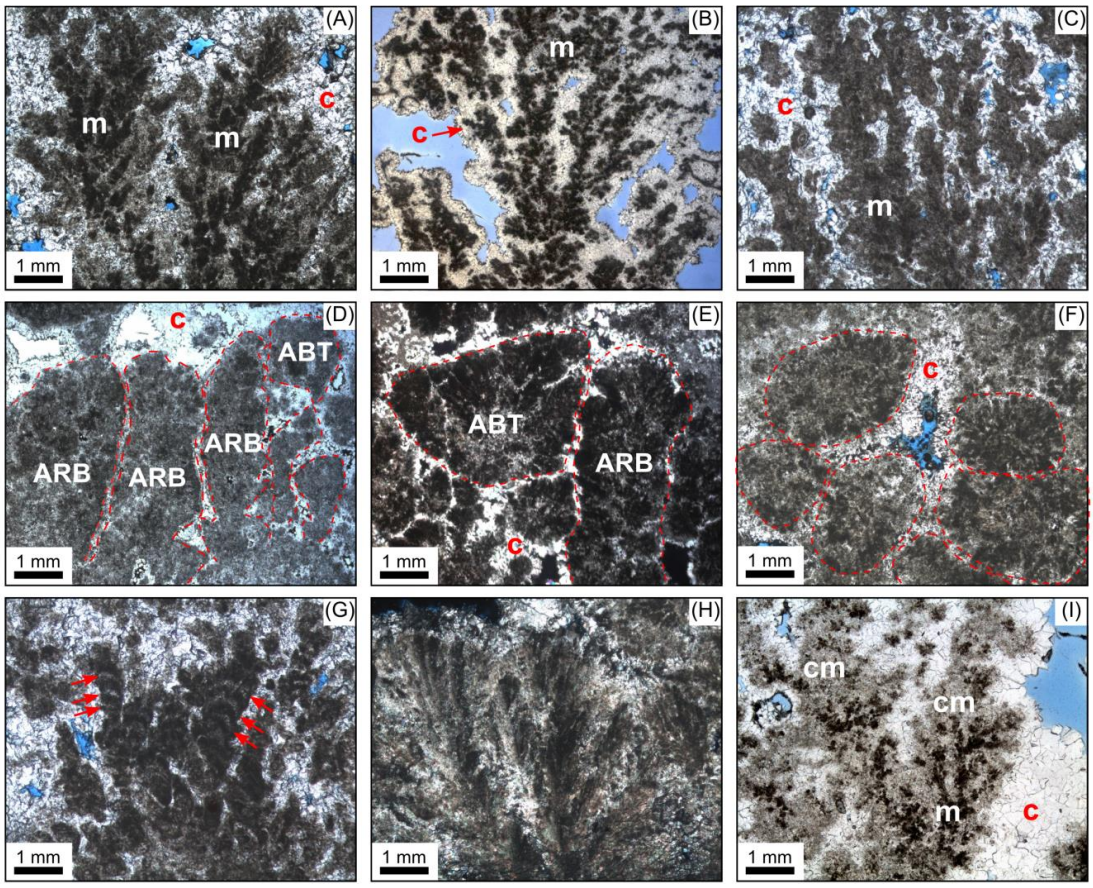

Fig. 2.4: Pleistocene shrubs from the Tivoli quarries. The pictures are taken perpendicular to bedding. (A) NDS with peloidal micritic aggregate nucleus (m), surrounded by calcite spar crystals (c). (B) Petrographic images of WDS composed of aggregates of dark-grey tiny spherical to sub-spherical micrite (m) covered by sparite crystals (c). (C) FDS characterized by very thin and elongated branches, composed of peloidal micritic aggregate (m) surrounded by sparry calcite (c). (D and E) ARB and ABT morpho-types. (F) PS showing sub-rounded morphology, with slightly preferential growth. (G) Micro-laminated shrubs of isopachous micrite and microsparite laminae (arrows). (H) Shrubs showing undulose extinction under crossed polarizers. (I) NDS surrounded by calcite spar crystals (c) and halo of cloudy micrite (cm) around internal micritic (m) aggregates.

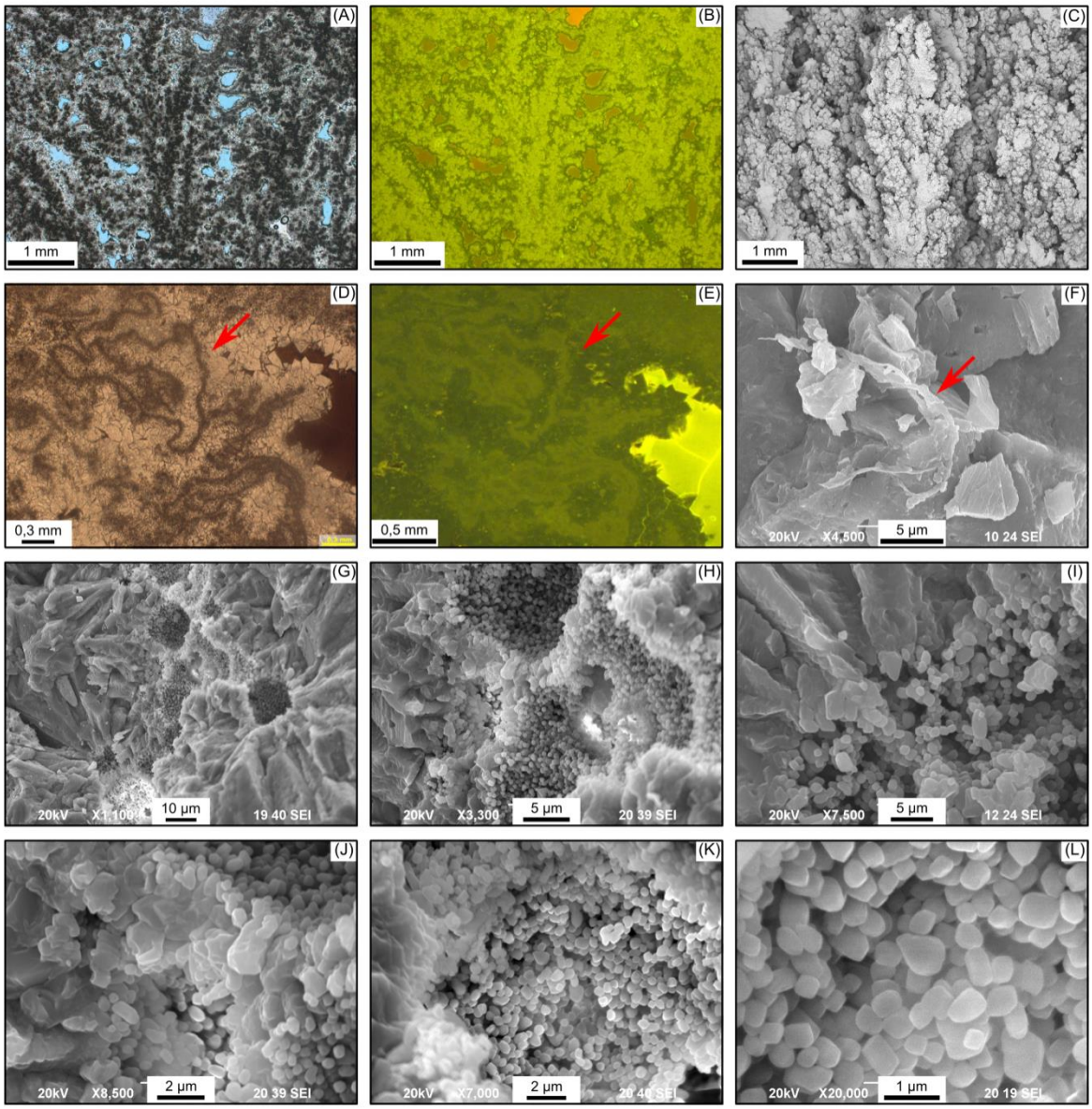

Fig. 2.5: (A) NDS under transmitted light, characterized by peloidal micritic aggregates. (B) Fluorescence microscopy from (A) displaying bright green fluorescence in the peloidal micritic areas, while the surrounding sparite crystals do not fluoresce. (C) SEM image from (A) showing a close up view of the dendritic growth morphology off the shrub where the peloidal micritic aggregate fabric is evidenced. (D) Photomicrography of filamentous (arrow) features under transmitted light trapped within sparite calcite cements. (E) Fluorescence microscopy from (D) shows filaments with light to bright green fluorescence, whereas the surrounding sparite crystals do not fluoresce. (F) SEM image showing possible fungal filaments (arrow) observed within the shrub. (G) SEM photomicrograph of a shrub displaying a hollow center (possibly organic origin) surrounded by calcite spar crystals. (H - L) SEM photomicrograph showing peloidal micrite aggregates (spherical to sub-spherical shape) in the shrub center possible consisting of bacterial bodies.

The shrub morpho-types are differentiated as: “dendriform”, “arborescent”, “arbustiform”, and “pustular”, with “dendriform” shrubs being the most abundant morpho-type in Tivoli quarries.

The shrub morpho-types (Figs. 2.6 and 2.7) identified in Tivoli quarries can be described as follows:

Dendriform shrubs (Figs. 2.6A to F) are mainly characterized by their branching structure, with their height much larger than their width. They are the largest shrub morpho-type encountered. Their size ranges from a few mm to a few cm, usually 1 to 3 cm reaching up to 5 cm. On a micro-scale they are formed mainly of micritic aggregates and peloids 0.1 to 1 mm in size, surrounded by sparry calcite (Figs. 2.4A to C).

The peloidal micritic aggregates are clearly oriented along the growth axis, perpendicular to the substrate (Fig. 2.5C), and give the shrubs a stubby and knobby form (Guo and Riding, 1994). The branches extend in all directions, being aligned parallel to water flow. According to the arrangement and distribution of the branches, it is possible to subdivide the dendriform shrubs in three sub-types: i.e. narrow, wide and fili dendriform shrubs.

- *Narrow dendriform shrubs* (NDS) are characterized by a pronounced vertical stem with small and narrow branches that expand upward in a narrow tightly packed fashion (Figs. 2.4A, 2.6A and B). Their margins show a crenulated or tooth-like outline and their overall appearance resembles a fern leaf or wheat (Fig. 2.4A). μCT analysis showed that the branches are distributed in a tight packing fashion, with elongated and straight growth framework pores (Fig. 2.6B). Due to their morphology, NDS can resemble the "feather dendrites" described by Rainey and Jones (2009) or the "feather-like crystals" reported by Guo and Riding (1992) and Gandin and Capezzuoli (2014). However, "feather-like crystals" are composed of tightly packed very thin and long crystals, while NDS possesses a peloidal micritic aggregate fabric with complex distribution of the branches.

- *Wide dendriform shrubs* (WDS) are formed by branches arranged in a broad and open packed fanning array, giving the aspect of an open hand (Figs. 2.4B, 2.6C and D). Their edges show a crenulated outline (Fig. 2.4B). Their pores follow the shrub growth framework, but they are patchier and less elongated than in the NDS as could be seen in μCT images (compare Fig. 2.6D with the NDS in Fig. 2.6B).Within the WDS, it is possible to observe larger pores between the main branches and smaller and thinner pores in the irregularities between the secondary branches (Fig. 2.6D).

Both NDS and WDS have a star-like shape in cross-section perpendicular to the growth direction as they display branches growing from a central stem. WDS and NDS also have a similar micro-fabric (Figs. 2.4A and B). Basically, the difference between WDS and NDS relates to the arrangement of their branches (Figs. 2.6B and D), with NDS possessing elongated and tight packed arrangement and WDS showing branches with fan-like open packing distribution.

- *Fili dendriform shrubs* (FDS) are identifiable by their very fragile, thin (~ 0.05 mm) and elongated branches (Figs. 2.4C, 2.6E and F) that resemble filamentous structures. These shrubs have rounded edges, sometimes showing an irregular curved outline (Figs. 2.4C and 2.6E). In μCT scans they show very thin and vertical elongated growth framework porosity (Fig. 2.6F). Microscopically, they are characterized by irregular elongated forms, composed of micrite and peloidal micrite that coalesces (Fig. 2.4C). Sparry calcite surrounds the peloids.

Arborescent shrubs (ARB) show an elongated vertical growth form, with their height larger than width (Figs. 2.4D, 2.7A and B). Branches are not present or are under developed (Fig. 2.4D). In μCT they display an elongated growth framework pore network, with their cross-sections displaying irregular rounded shapes (Fig. 2.7B). Microscopically, they are mainly composed of dense micrite and rarely sparite. They are locally covered by sparry calcite cements (Figs. 2.4D and E).

Arbustiform shrubs (ABT) have a preferential vertical growth, but their height is shorter than their width in a ratio of 1:2 (H/W) 1:2 (Figs. 2.4E, 2.7C and D). In μCT scans, the pore network is mainly characterized by very thin and short vertical elongated growth framework pores, with horizontal and some isolated pores (vugs) (Fig. 2.7D). On micro-scale they can have a fan-shape or a dendritic fabric (Figs. 2.4D and E). They commonly possess a clotted micritic fabric, often with undulose extinction under crossed polarized nichols. In short, arborescent, arbustiform and dendriform shrubs can be differentiated by their height/width (H/W) ratio and presence or absence of branches.

Pustular shrubs (PS) possess a sub-rounded morphology, with an irregular surface and slight preferential vertical growth, having a height to width ratio of approximately 1:1 (Figs. 2.4F, 2.7E and F). They are usually smaller than 2 cm. Sometimes, depending on their size and roundness, they are difficult to distinguish from spheroids. PS were described as 'pisoids' by Guo and Riding (1998) due to their radial shrub microstructure, and as 'radiating dendrite' by Rainey and Jones (2009). In μCT, PS possesses

a very irregular porosity pattern, because they do not have any preferential orientation (Fig. 2.7F). They are characterized mainly by rounded to small-elongated pore shapes that are randomly distributed (Fig. 2.4F).

On micro-scale their fabric is composed of clotted micrite (Fig. 2.4F), locally with clusters of peloids, and rarely of a mixture of micrite and sparite, often they possess an undulose extinction. The pustules can show a nucleus that often is micritic, but moulds of plants and ostracods shells were also observed. PS can show a clotted fabric that resembles thrombolites.

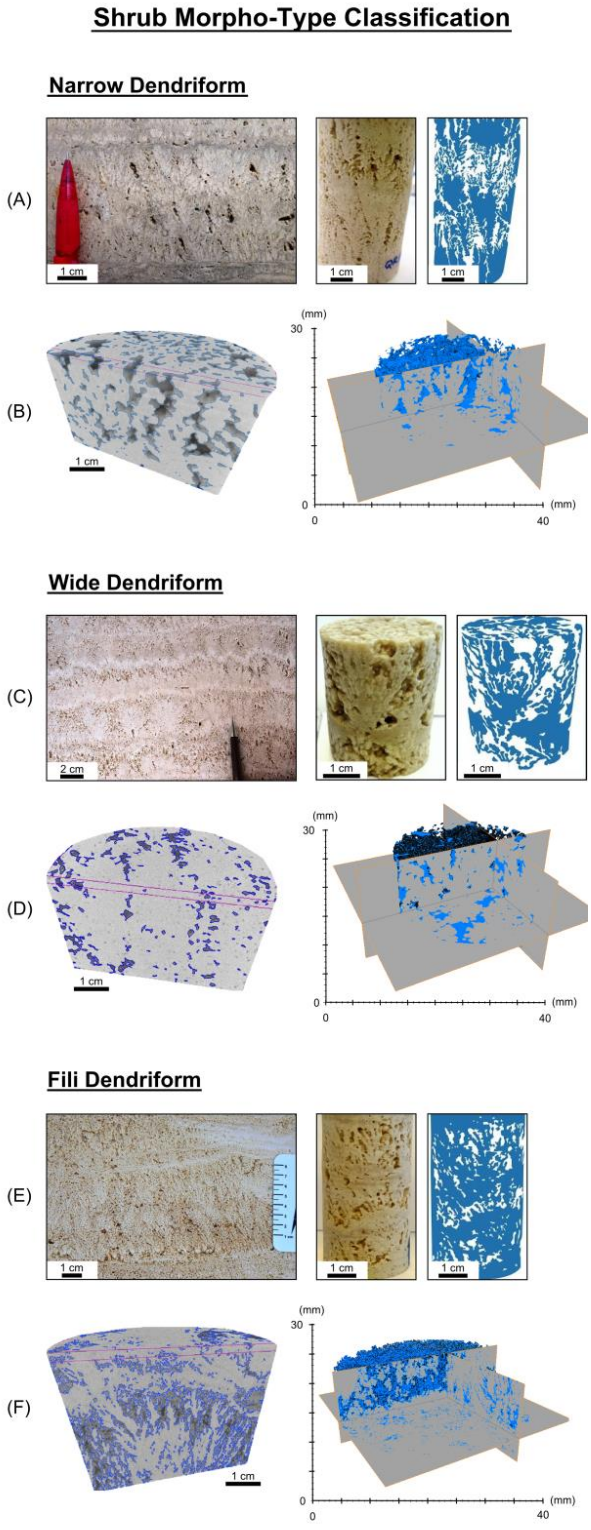

Fig. 2.6: Shrub morpho-types from Tivoli travertines. The classification is based on macro-scale description and µCT volume renderings. The µCT reconstructed pore networks (blue) of the different shrub (-related) morpho-types. (A) and (B) characterized by narrow branches distributed in a tightly packed fashion. (B) µCT analysis emphasizing the tightly packed distribution of the NDS, and the pore network occurring elongated and parallel to each shrub. (C) and (D) WDS with branches arranged in a broad and open packed fanning array. (D) The pore network occurs more localized and spread when compared with NDS. (E) and (F) FDS possess very fragile vertical growth forms. (F) µCT analysis highlight that the pore network from FDS also present very thin, elongated and dense characteristics.

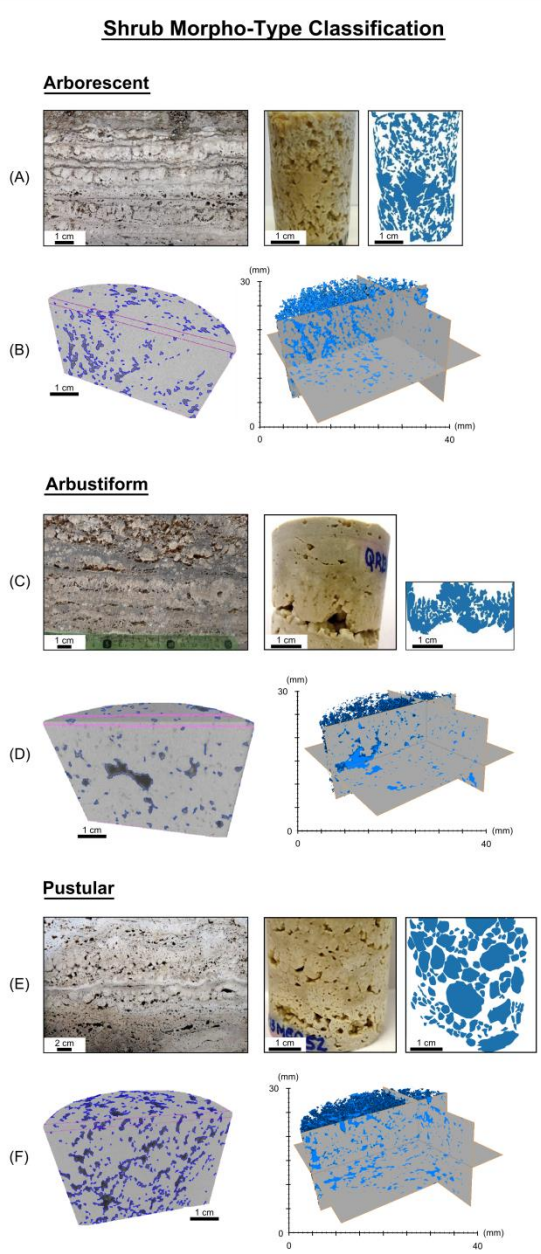

Fig. 2.7: (A) And (B) ARB with elongated and vertical growth from. (B) µCT show a dense population of elongated pores, related to the growth framework of the ARB. (C) and (D) ABT is characterized by their height shorter than their width (ratio H/W ~ 1:2). (D) µCT show very thin and short vertical elongated growth framework pores, with some isolated pores (vugs). (E) and (F) PS showing sub-rounded morphology, with slightly preferential growth (ratio H/W ~ 1:1). (F) µCT show a pore network more chaotic, comprise many different pore shapes.

2.4.2 Associated lithotypes

Associated with the shrub litho-type, other litho-types, such as fine laminated micrite (mats), crusts, crystalline crusts, rafts, encrusted bubbles, immature palaeosols, mouldic phytoclasts and reed deposits build up the travertine deposits in the Tivoli area.

One of the most common lithotypes observed are the macroscopically white *fine laminated micrite* or *micrite mats* (Fig. 2.8A) characterized by a stromatolitic-like outline (Folk et al., 1985). They are composed of multi-layered sheets, with flat to wavy morphologies with thicknesses of 0.1 to 1 mm, resembling microbial mats (Vasconcelos and McKenzie, 1997; Dupraz et al., 2009; Gandin and Capezzuoli, 2014). The mats aggregate into layers that can reach 3 cm in thickness. They possess elongated pores that resemble fenestral porosity. On micro-scale they display a peloidal to clotted brownish micritic fabric, resembling bacterial clumps (Chafetz and Folk, 1984, Figs. 22A and B) that sometimes grades up into shrubs, most of the time consisting of ABT shrub morpho-type. Commonly, rafts occur associated with this lithotype.

Crusts (Fig. 2.8B) are characterized mainly on macro-scale by laminated bands of densely packed shrub-like structure that developed perpendicular to the substratum. However, the shrubby texture is not always easily identifiable on macro-scale because of their very tightly packed nature, being more evident on micro-scale. Crust thickness can vary from few mm to few cm. They can be finely laminated, with laminas < 1 mm, or thick laminated (cm-scale). The thickness of the crust is reflected in the shrub morphologies on micro-scale. Microscopically, their fabrics mostly consist of dendriform shrubs with densely peloidal micritic aggregates, which rarely are fully sparitic resembling to “ray-crystal shrub” (Chafetz and Guidry, 1999) and morphologically similar to the feather-like crystals described by Guo and Riding (1992, 1998), however showing primary micritic fabrics. In µCT, crusts display mainly elongated horizontal pores that occur isolated because of the shrubby nature of these crusts. Vertical elongated pores are rare.

The described crusts can be misinterpreted with micrite mats due to their common laminated aspect when amalgamate into layers with a

thickness of a few cm. One of the characteristic, to distinguish them is the presence of shrubby morphologies present in the crusts, and mats possess a more irregular surface (crenulated).

Crystalline crusts lithotype (Fig. 2.8C) consists of vertically elongated, dendritic calcite crystals organized in centimeter to decimeter thick, white in color and dense layers. Generally these crusts pinch out into other lithotypes (mainly micrite mats, shrubs and paper-thin rafts). Dendrites are usually composed of rhombohedral turbid crystals departing from a central elongate crystal ("feather crystals" of Chafetz and Folk, 1984 and Guo and Riding, 1998) and exhibiting uniform extinction under crossed polarizers. The vertical crystal growth is locally interrupted by horizontal laminae of mm-thick clotted peloidal micrite. Dendrites are surrounded by cloudy microsparite and limpid equant microsparite to sparite.

The crystalline crusts from the studied area differ from the crust types because the thickness of each crust bundle is thinner than the crystalline crusts, and crusts rarely possess crystalline habits.

Paper-thin rafts (Fig. 2.8D) (Kitano, 1963; Folk et al., 1985; Chafetz et al., 1991b; Guo and Riding, 1998; Özkul et al., 2002) consist of very thin (0.1 to 2 mm thick) and flat-sheeted layers of white to cream colored calcite. They precipitated at the water-air interface, leaving the subaerial upper surface flat (Folk et al., 1985; Chafetz et al., 1991; Guo and Riding, 1994). When rafts sink, shrubs can grow on top of them. Rafts overgrown with WDS were regularly observed. Encrusted bubbles between the rafts are often present. Microscopically the raft center is made of very thin micritic laminae surrounded by shrub morphologies, mainly composed of sparitic crystals with fan-like or botryoidal shapes. They occur as structures deposited parallel to the substrate and/or in broken pieces due the agitation of the water surface by wind or by rain splash.

Encrusted bubbles (Fig. 2.8E) are formed by rapid calcite precipitation around a gas bubble (Kitano, 1963; Chafetz and Folk, 1984; Chafetz et al., 1991; Guo and Riding, 1998; Fouke et al., 2000; Özkul et al., 2002). They consist of white calcite rims, 1 to 3 mm in diameter, appearing as two morpho-types: 1) vertically elongated structures, and 2) spherical structures. Under the microscope both possess a dense micritic rim fabric. The vertical elongated bubbles often occur entrapped between shrub structures or are intercalated between them at cm-scale. The intercalation of shrubs and elongated encrusted bubbles is more common than the intercalation with peloidal micrite in the studied sections. The spherical encrusted bubbles mainly occur entrapped between mats and rafts, being locally broken. Sometimes, shrub morphologies grew upon encrusted spherical bubbles.

Reeds and *Phytoclasts* lithotype (Fig. 2.8F) corresponds to moulds of plants like reeds and coarse grasses. They are characterized mainly by cylindrical moulds of plant stems and roots, coated by grey to brown-orange micrite. The size of these plant accumulations can reach more than 10 cm in diameter and their arrangement reflects both reworking and preservation of the growth position.

Pisoids (Fig. 2.8G) were very locally observed, always occurring in small depressions. They possess white to yellowish colours. They display rounded to sub-rounded morphologies, with irregular edges, and sizes larger than 2 mm. Internally, they show concentrically irregular laminations. Pisoids with a radial shrub microstructure were reported by Guo and Riding (1998). They occur associated with exposure features, showing extensive early cementation, being formed in large cavities or within depressions and precipitated from emerging saturated spring-fed continental waters (Tucker and Wright, 1990).

Ooids lithotype (Fig. 2.8H) can be differentiated from *Pisoids* based on their rounded shapes with concentrical laminations and based on its size (pisoids possess sizes larger than 2 mm). Cross stratified bedding structures sometimes occur associated with the ooids.

Dark micrite with intraclasts lithotype (Fig. 2.8I) is characterized by reworked intraclasts and rarely extraclasts, displaying sizes varying from pebble to silt. Exposure features, such as cracks, tepees and locally pseudo-microkarst features are abundantly associated with this lithotype. They are evidence of temporary exposure of the strata. The lower part of such intervals is often composed of flat pebble conglomerate deposits that sometimes marks the lower part of a fining upward succession. Roots, plant moulds (including reeds, grass, charophyte

and sometimes bryophytes), ostracods and gastropods are present. The dark micrite with intraclasts evolve vertically into immature palaeosols. Petrographycally, the micrite possesses a peloidal fabric. No volcanic ash was observed within these layers.

Grey to brown-orange very immature palaeosols (Fig. 2.8J) is characterized by dense masses of micrite with bioturbation, presence of roots, intraclasts, ostracodes, gastropods, coated grains, and nodules, besides multiple phase of brecciation. Presence of detrital grains is also observed. Microfractures and granification of the rock it is also observed. The top of the uppermost horizon of the palaeosol is usually truncated sharply by an erosion surface. These deposits vary from few centimeters to few meters in thickness. These deposits are considered immature because they do not present the complete soil profile degrees of development (Tucker and Wright, 1991; Alonso-Zara and Wright, 2010).

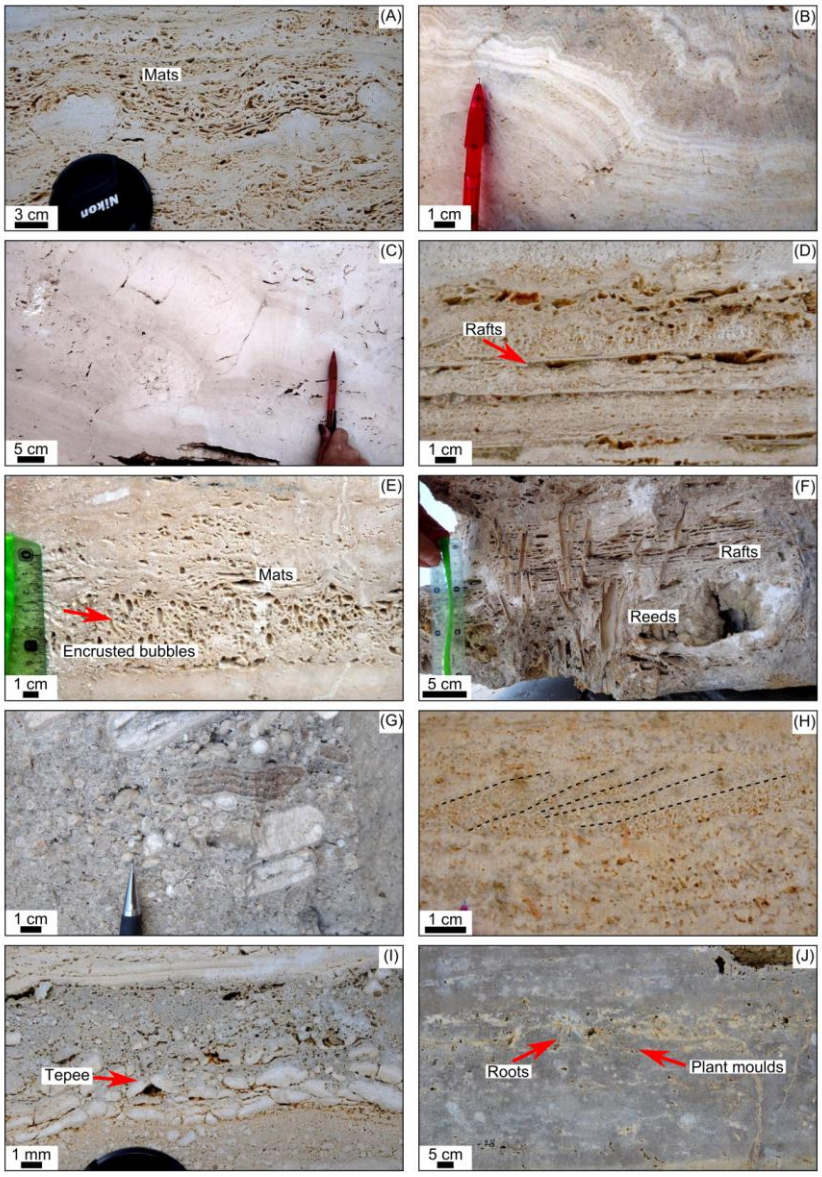

Fig. 2.8: (A) Fine laminated micrite (mats) with horizontal elongated pores resembling fenestral porosity. (B) Crust lithotype characterized by dense laminated bands. (C) Crystalline crust displaying dense, layered and coarsely fibrous. (D) Rafts associated with NDS growing upon them. (E) Vertically aligned encrusted bubbles, with overlying mats with horizontally elongated pores. (F) Reeds lithotype, with moulds of reeds and coarse grasses. (G) Pisoids in immature paleosols. (H) Ooids with cross stratification beddings. (I) Immature paleosols composed of carbonate intraclasts in an organic-rich (responsible for the dark color of the layer) micritic matrix. Tepee and desiccation crack structures indicating exposure surface. (J) Immature palaeosols with bioturbation (mainly roots and gastropod traces) and plant moulds.

2.4.3 Lithologs and sequence correlation

Shrub deposits are characterised mainly by their flat and sub-horizontal layering, lateral continuity over several square decameters, showing a gentle dip (< 3°) towards the south (Faccenna et al., 2008). Laterally, these flat deposits locally evolved into smooth slope (~ 10°) crust lithotype deposits, covering an area of few square decameters. The lateral thickness variation of each layer is almost not noticeable. The stacking patterns of these layers are aggradational and slightly progradational from the northeast to southwest.

Lithological loggings were performed in areas where shrub morphologies were present. Based on the logs, lateral and vertical lithofacies variations were worked out. The interpretation of the lithofacies and their correlation allows to reconstruct the paleoenvironment, and to address the different processes that prevailed within the different depositional settings. The shrub layers are abundant in some quarries, where they locally reach around 40 m in thickness but are almost absent in others.

The shrub deposits were subdivided into three main sequences, bounded by erosional surfaces that are locally highlighted by immature palaeosols (Figs. 2.9, 2.11 and 2.13). Faccenna et al. (2008) distinguished five main erosional surfaces (S1 - S5) that affect the Acque Albule travertine body. The three shrub sequences are limited between the erosive surfaces S1 and S4. The "testina" occurring above S1 is not of interest in the present study. The sequence between S4 and S5 was not reachable in the studied quarries, because most of the time this interval was almost completely flooded.

Sequence 1

The first sequence (Figs. 2.9 and 2.10), which is limited by the erosive surfaces S4 (bottom) and S3 (top) of Faccenna et al. (2008), displaying a flat to very low inferred paleo-topography. The sequence 1 can be subdivided into two sub-sequences. Sub-sequence 1.1 (Figs. 2.9 and 2.10A, B) consists mainly of light-coloured mats and shrub morpho-types. Mats, rafts, encrusted bubbles, micrite and WDS occur in small depressions behind rimstone dams (sensu Chafetz et al., 1991) and grade into NDS and crust at the dam positions. The rimstone dams in the quarry walls range in height from few cm to 1 m and are composed of several layers each maximum 5 cm thick. The inter-dam distance (IDD – Pentecost, 2005) can range over more than 100 m. Based on slope and arrangement of the rimstone dams, the palaeo-flow direction was from N to SE. Toward the top, the layers become more flat and horizontal, being composed mainly of WDS, ARB, ABT, PS and mats. The shrub layers occur interlayered with very thin grey phytoclast deposits displaying exposure features at the contact between them. Locally ooids are present, sometimes displaying cross stratified bedding.

Sub-sequence 1.2 (Figs. 2.9 and 2.10 C, D), is characterised by its abundance of shrub morpho-types. The shrub-bearing units are intercalated by thin (0.5 - 5 cm) dark micrite and encrusted bubble strata. The shrub morphologies and sizes vary vertically and horizontally. Locally, they present small bumps possessing some smooth wavy outline. The bumpy substrate morphologies are conditioned by the local presence of phytoclast accumulations, or by small paleochannels (Guo and Riding, 1998). The bumps are represented by NDS morpho-type, with WDS and FDS morpho-types occurring in the flat areas. Laterally, few small flat palaeochannels occur with low relief levees marked by mats, which gradually change inward to PS and to WDS morpho-types in most of the studied channels. The shrub layers are also interlayered with grey phytoclast deposits displaying fining upward trends.

The sub-sequence 1.1 and 1.2 are covered by dark grey to dark brown-orange deposits mainly containing phytoclasts moulds and lithoclasts which occur above an erosional surface. They occur in layers of ~ 2.5 m thick displaying a low dip (< 3°) that pinches out toward the S-SW. Towards the northeast these layers are full of root tubes and root traces, phytoclasts, including charophytes and bryophytes, and locally gastropods and ostracods. ABT and PS morpho-types and rarely ARB morpho-type shrubs are present in the lower part of some of these layers. Exposure features such as desiccation cracks and tepees are common features associated with the erosive surface. The top of sub-sequence 1.2, specifically showed palaeokarst features with widespread collapse breccias. Large vugs follow

the contact between sequence 1 and 2. They mark the end of the first sequence, and correspond to the S3 erosional surfaced of Faccenna et al. (2008).

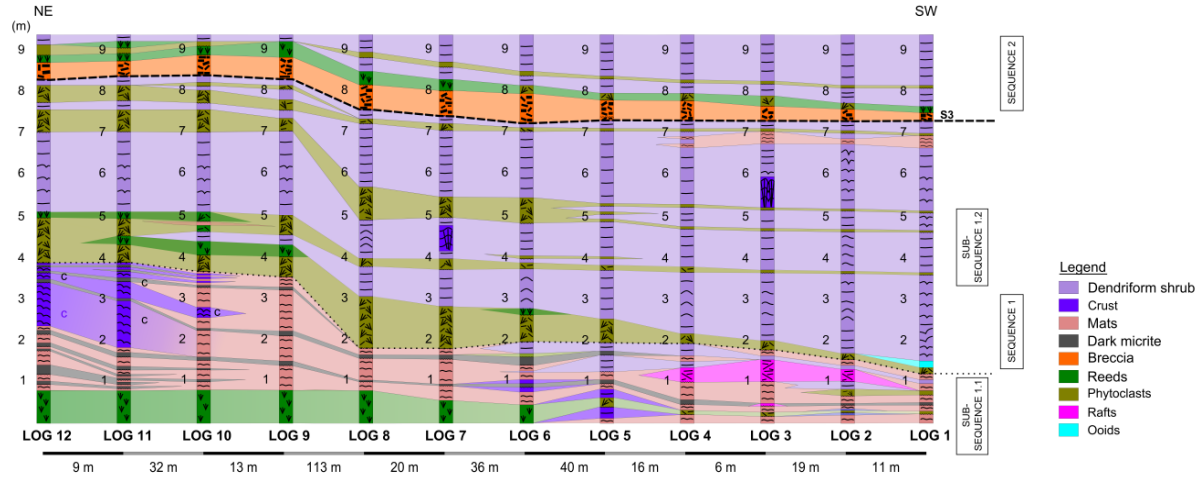

Fig. 2.9: Log correlation of shrub occurrences in the Querciolaie-Rinascente (QR1) quarry. The logged interval was subdivided in sequence 1 and 2 limited by erosive surface S3 of Faccenna et al. (2008). Erosive surface S4, that comprises the bottom of this sequence is not represented in the logs, because it occurs bellow the logged interval (flooded area). Based on the logs, the sequence 1 was subdivided in sub-sequences 1.1 and 1.2. Shrub layers are especially abundant in sub-sequence 1.2, which thickens toward the SW. Marsh-pool deposits are more common in the N, pinching out to the S.

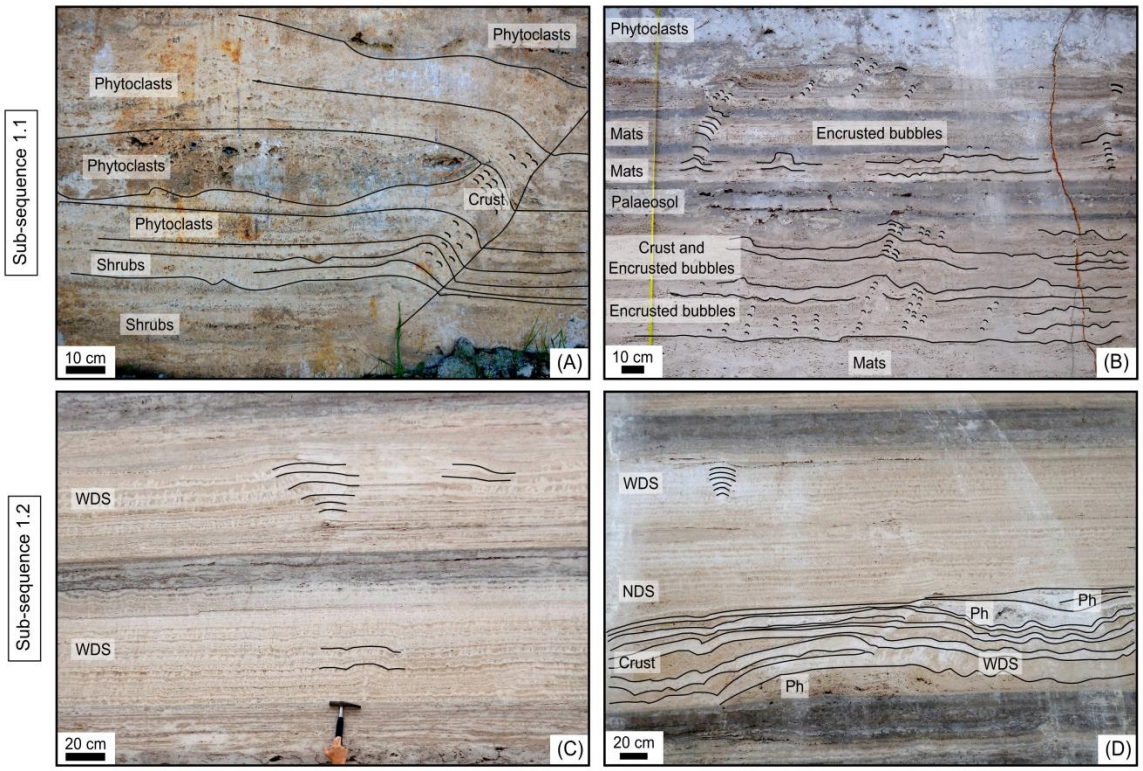

Fig. 2.10: Representative pictures for sequence 1, with emphasis of the main structures by line drawings. (A) And (B) corresponds to sub-sequence 1.1, while (C) and (D) represent sub-sequence 1.2. Shrub crusts occur in the rims. Between the rims, encrusted bubbles and mats are present. (A) Flat to wavy shrub morpho-types (WDS, NDS and FDS) precede terrace setting. Locally, phytoclast accumulations created morphologies. (B) Small terracetes with very low angle (< 3°) horizons. (C) Flat to wave shrub morpho-types. (D) Locally, some shrub crusts developed in small (few cm) depressions.

Sequence 2

Sequence 2 (Figs. 2.11 and 2.12) is limited by erosive surfaces S3 (bottom) and S2 (top) (Faccenna et al., 2008). It consists of horizontal aggradational flat shrub deposits that evolve vertically and horizontally into prograding smooth slope deposits with dips below 10°, toward to the Aniene River in the south. The horizontal interval that dominates in the northern and central area of the quarries shows lateral facies variation from very wavy mats (stromatolitic-like aspect) to flat shrub surface. WDS, NDS and FDS are the dominant morpho-types in the flat areas. Small bumps with tightly packed dendriform shrubs are slightly inclined in agreement with the possible water flow direction. Laterally, in the central and south sector of the quarry area, the flat horizons grade into deposits reflecting a slope setting, with crusts being the main lithotype. Grey fine-grained lithoclast deposits commonly occur as intercalations between the light coloured shrub deposits. Sequence 2 ends with an erosive surface, with well-developed karstic features, such as sink holes and collapse breccias, and dark immature palaeosols. The immature palaeosol and sinkholes are thicker (up to 2 m) and better displayed in the northern part of the study area (Fig. 2.12B).

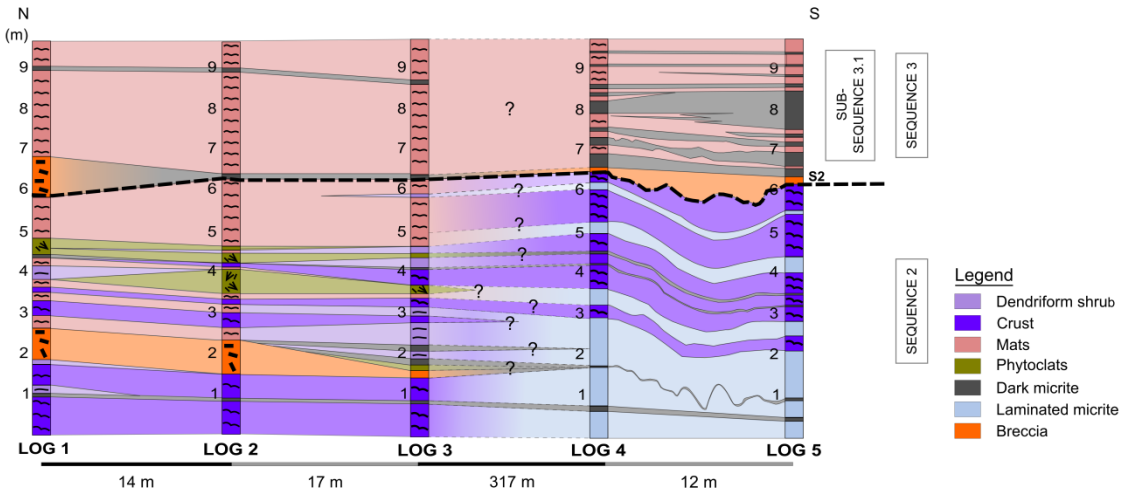

Fig. 2.11: Representative correlation logs of the Sequence 2, and part of the lower part of the sub-sequence 3.1 of Sequence 3. Notice that the layers vary laterally towards to the south from horizontal to sloping.

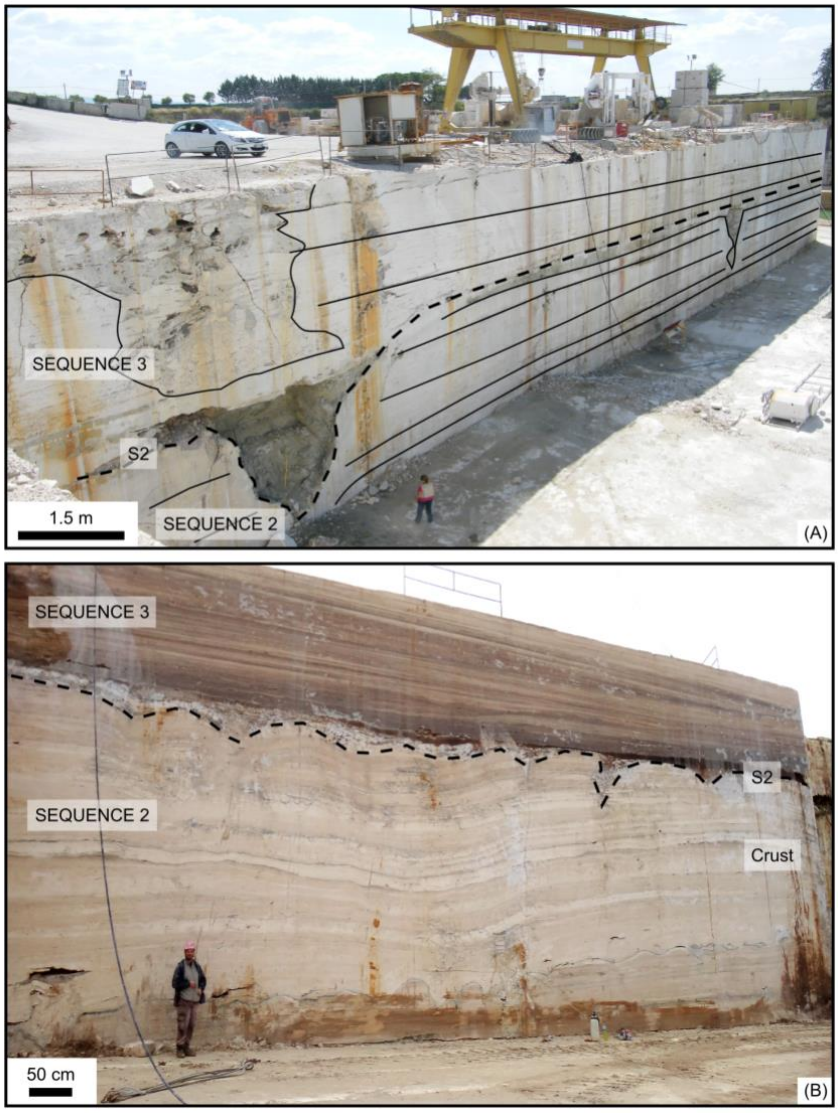

Fig. 2.12: (A) Illustration of flat and horizontal deposits observed in Sequence 2, as observed in the northern area of Tivoli quarries. S2 is marked by erosive surface and sinkholes. (B) Sequence 2 represented by slope layers that are mainly composed of shrub crusts, located in the southern part of the study area.

Sequence 3

Sequence 3 (Figs. 2.13 and 2.14) is limited by erosive surfaces S2 (bottom) and S1 (top) (Faccenna et al., 2008) and it is better developed in the central and southern part of the study area. This sequence can be subdivided in 2 sub-sequences (Figs. 2.13 and 2.14). Sub-sequence 3.1 (Figs. 2.13 and 2.14), consists of very flat and horizontal deposits of PS, ABT and ARB, frequently intercalated at cm-scale by dark micrite layers containing very small phytoclast mouldic pores (< 0.05 mm). This is the interval where the PS, ARB, ABT are most abundant. This sub-sequence is limited at its top by a discrete erosive surface.

Sub-sequence 3.2 (Figs. 2.13 and 2.14) consists of dendriform shrubs with rimstone dams. NDS is present in the rimstone dams, while WDS and FDS are the main morpho-types in the inter-dam pools with an IDD of around 0.5 m. This sub-sequence culminates in the erosive surface S1 of Faccenna et al. (2008). This interval reflects the development of smooth terrace system (Chafetz and Folk, 1984; Guo and Riding, 1998) (Figs. 2.13 and 2.14).

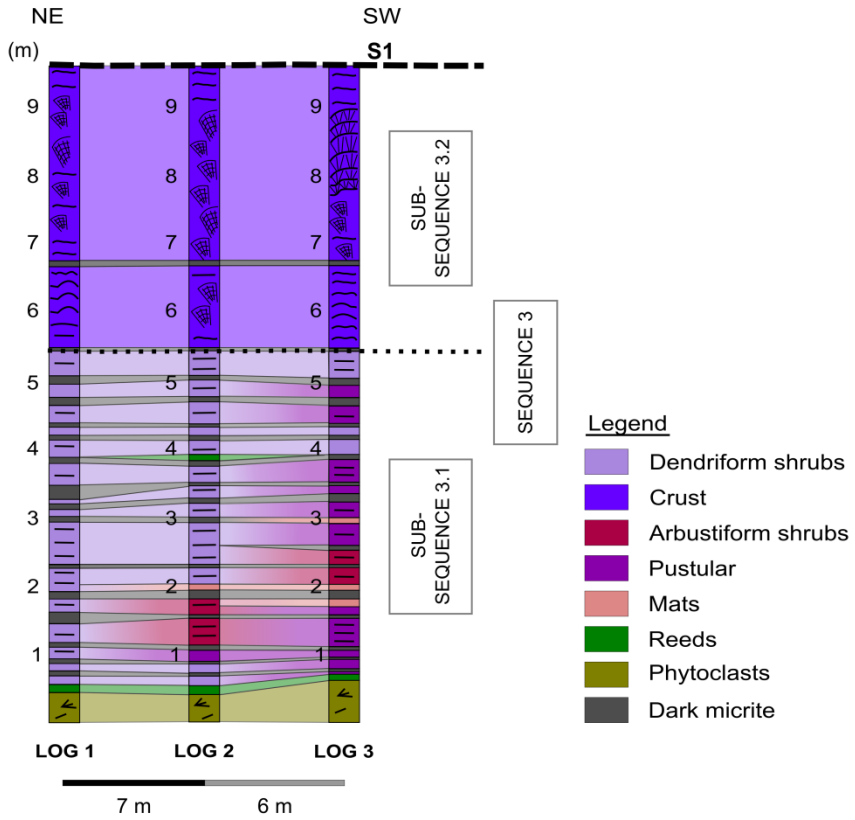

Fig. 2.13: Representative correlation logs within Sequence 3. Subsequence 3.1 is characterized by high frequency interlayering of shrubs and marsh-pool deposits, while sub-sequence 3.2 corresponds to terrace system association facies.

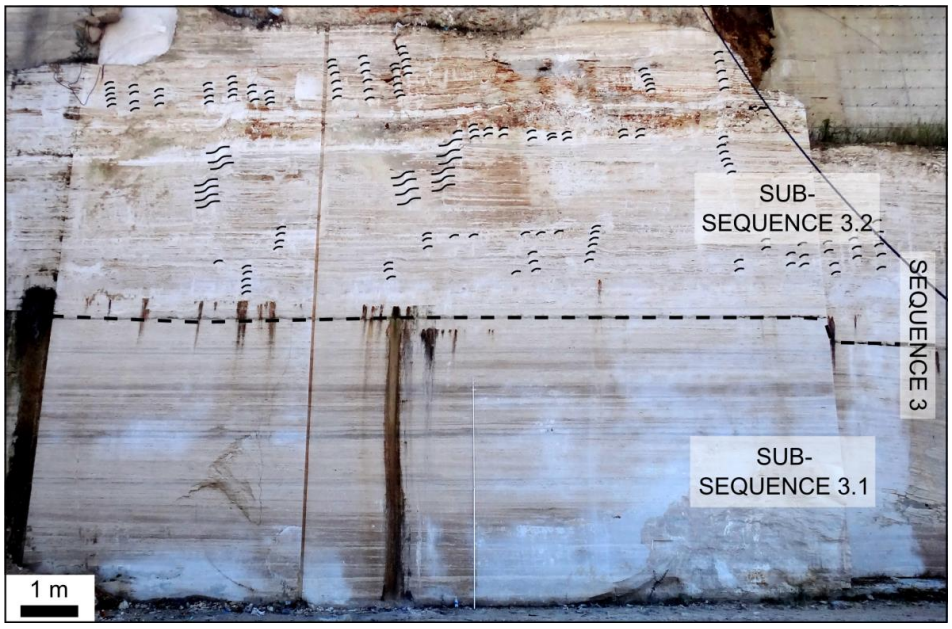

Fig. 2.14: Sequence 3.1 represented by flat and horizontal layers, while in sequence 3.2 rims are observed characterizing terrace system. Erosive surface S2, that comprises the bottom of this sequence is not represented in the logs, because it occurs bellow the logged interval (flooded area).

2.4.4 Diagenesis

One hundred and twenty four travertine shrub samples were analyzed with XRD indicating that they consist exclusively of calcite with exception of 4 samples that contain < 1 % of detrital quartz.

Almost all shrubs possess ~ 10 vol % of thin isopachous sparitic calcite crystal rims (Figs. 2.15A to C). Fine blocky calcite cement, making up less than 5 vol %, occurs dispersed between shrub structures (Figs. 2.15D and E). CL analysis showed multiple alternating bright red-orange and dull compositional zones in these isopachous and fine blocky calcite cements, whereas micritic shrubs systematically possess dull luminescence (Figs. 2.15B and E). Micritization of sparite is observed, giving a cloudy aspect to the latter (Figs. 2.15A and F). Recrystallization affects all samples, and is most evident where the micrite displays undulose extinction or where the calcite cement coatings show optical continuity with the micrite phases (Figs. 2.15F and G).

Geopetal crystal silt and micro-stalactitic cements are observed locally in shrubs with a dark brown surface of microcrystalline crust and lighter-colored crystal silt (Figs. 2.15H and I). On top, sparry calcite cements, coarse crystalline, radially-oriented, showing conical forms resembling micro-stalagmites grew from the shrub surface towards the pore-space, (Figs. 2.15H and I). Microstructures related with exposure like roots, micro-cracks, crystallaria (Wright, 1991, Fig. 4; Brasier, 2011, Table 2), floated sediment grains (Fig. 2.15J) and micritic coatings were locally observed (Fig. 2.15K).

Dissolution is also manifested by corrosion of cement edges (Fig. 2.15L), as observed in cores of shrubs, but rarely results in important intracrystalline porosity development. Under SEM, the core of the shrub rod/stem show rounded to sub-rounded micritic spherical cavities (Fig. 2.15M), smaller than 1µm, and high density of micropores (Fig. 2.15N). The spar-rhomb crystals that cover the micritic nucleus phases, present locally intracrystalline pores, 1 to 2 µm in size (Figs. 2.15O and P). Small mouldic pores were also locally observed.

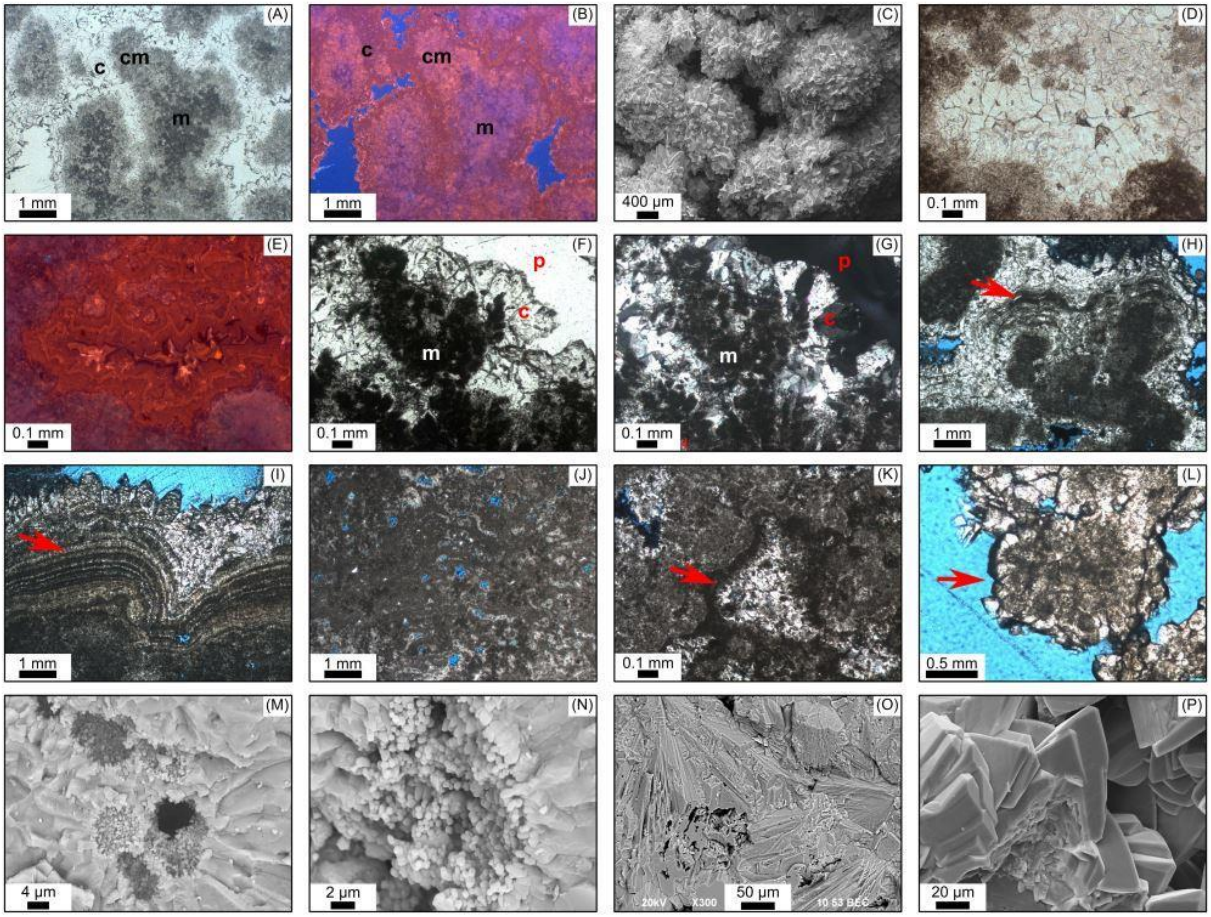

Fig. 2.15: Illustration of diagenetic features associated with shrubs. (A) Shrub structures showing dark grey micrite nucleus (m) surrounded by cloudy micrite (cm) and isopachous equant calcite cement (c). (B) CL of figure (A) with the cloudy micrite (cm) area showing brighter orange-yellow alternating zones than the sparry calcite cement (c) with red luminescence. The micrite (m) shows dull luminescence. (C) SEM photomicrography of the sparry calcite cement that surrounds the shrub morphologies. (D) Detail of fine blocky calcite cement. (E) CL of figure (D). Notice that the sparite calcite cement displays orange-yellow luminescent calcite zones, while the central part possesses a uniform bright orange luminescence. (F) Detailed observation of a shrub structure surrounded by sparite cement. (G) Cross polarized view of (F) showing optical continuity between micrite and cement. (H) Arrow indicating dark brown surface of microcrystalline crust. (I) Micro-stalagmite cement. (J) Calcrete with roots and floating sediment grains. (K) Micritic coating (see arrow) interpreted as calcrete microstructure. (L) Dissolution evidenced by corroded and rounded crystal (arrow). (M) SEM photomicrography displaying hollow center, suggesting organic nucleus that decayed. (N) SEM photomicrography showing microporosity related to rounded to sub-rounded micritic spheres (arrow) in the stem of a shrub. (O - P) SEM photomicrography showing intracrystalline porosity related to dissolution processes.

2.5 Discussion

2.5.1 Interpretation of shrub fabrics and morphologies

Shrubs display considerable different morphologies, but with similar internal peloidal micritic aggregate fabrics. They rarely show crystalline characteristics. The term “shrub” was chosen to represent simply the morphology of the arborescent structures observed in the Tivoli travertine. The shrubby structures are very well known in literature (Kitano, 1963; Folk and Chafetz, 1983; Chafetz and Folk, 1984; Folk et al., 1985; Guo and Riding, 1992, 1994, 1998; Chafetz and Guidry, 1999; Chafetz, 2013). The arrangement of the Tivoli shrub morphologies and their branches were important in their classification.

The majority of the peloidal micritic aggregate fabrics observed in Tivoli shrubs ascribe them to a bacterial influence during growth periods (i.e. crystal growth) (Folk and Chafetz, 1983; Chafetz and Folk, 1984; Folk et al., 1985; Guo and Riding, 1992, 1994, 1998; Chafetz and

Guidry, 1999; Chafetz, 2013). Some characteristics observed in Tivoli Shrubs are reported in literature as supporting evidences for a microbial origin of the shrub morpho-types (Chafetz and Folk, 1984; Guo and Riding, 1992, 1994, 1996; Chafetz and Guidry, 1999; Chafetz, 2013) as: 1) the non-coarse crystalline nature of the Tivoli shrubs, the abundance of regular morphologic forms; 2) the predominance of the peloidal micritic aggregate fabric; 3) the presence of tiny spheres and sub-spheres that resemble bacteria colonies in the peloidal micrite that only were found in the inner part of the shrubs; 4) the absence of regular repetition of crystalline habit; 5) presence of fluorescence in the peloidal micritic aggregate and absence in the surrounded sparry calcite; 6) microporosity in the central part of the shrub (in the peloidal micrite) and absence of it in the sparry calcite; 7) presence of filamentous and filamentous fabrics. It is well known that microbes may induce carbonate precipitation, as well as acting as catalyst in the shrub formation (Kellerman and Smith, 1914; Gerundo and Schwartz, 1949; Lalou, 1957; Boquet et al., 1973; Krumbein and Cohen, 1977; Krumbein, 1979a; Chafetz and Folk, 1984; Chafetz, 1986; Buczynski and Chafetz, 1991; Ehrlich, 1996; Guo and Riding, 1992a, b, 1994; Vasconcelos and McKenzie, 1997; Dupraz et al., 2004, 2009; Vasconcelos et al., 2013; Chafetz, 2013). Microbes produce microenvironments, in the surroundings of their colonies, in which mineral precipitation is facilitated (Guo and Riding, 1994; Chafetz and Guidry, 1999; Dupraz et al., 2004, 2009). According to Chafetz and Guidry (1999) the differences in morphology are the result of the relative influence of bacteria as compared to abiotic mineral precipitation. Varieties in growth shape of shrubs are thought to be more abundant and complex when they are biologically mediated (Chafetz and Folk, 1984; Guo and Riding, 1994; Chafetz and Guidry, 1999; Dupraz et al., 2009).

Abiogenically induced carbonate shrub development relates to precipitation caused by CO_2 degassing and existence of supersaturated waters (Pentecost, 1990; Jones and Renaut, 1995, 2008; Jones et al., 2000, 2005). The crystal shrubs and ray-crystal crusts (Chafetz and Guidry, 1999) that are thought to be controlled by abiotic precipitation of calcite, still may preserve remains of bacteria within the crystals, and they are interpreted to have influenced the calcite precipitation, but not the overall morphology (Chafetz and Guidry, 1999).

Shrub dendrites can be observed in plagioclase and pyroxene crystals associated to the rapid cooling of basalts and also in ice crystal structures (Jones and Kahle, 1993; Jones and Renaut, 1995), with supercooling being the most important factor in controlling crystal growth in these cases (Lofgren, 1974, 1980; Jones and Renaut, 1995). The sub-elements of the structures are in crystallographic alignment. Shrubs are also described in Mn- and Fe-rich travertine and they are interpreted to be bacterially (nano-bacterially) induced precipitates (Chafetz et al., 1998). According to the authors, the deposits display an abundance of rod- and sphere-shaped bacterial bodies.

Although it is still a speculation how the shrubs are formed, the observations made with regard to the Tivoli shrubs are in accordance with a microbial mediation, as described in the literature. According to Rainey and Jones (2009), the high amount of H_2S at Tivoli travertines (see Chafetz and Folk, 1984; Folk et al., 1985; Minissale et al., 2002) favored bacterial over cyanobacterial growth, influencing the shrub formation. The latter authors also mention that the formation of bacterial shrubs is a result of the competition between microbial growth and calcite precipitation. Our interpretation that Tivoli shrubs had a microbial / EPS precursor is based on previous peer reviewed international literature and microscopic evidences. The EPS was not directly observed, however, it is based on the presence of filamentous and microscopic spherical shapes resembling previous bacterial forms (cf. Guo and Riding, 1992, 1994; Vasconcelos and McKenzie, 1997; Dupraz et al., 2004, 2009). In literature (Vasconcelos and McKenzie, 1997; Dupraz et a., 2004, 2009; Turner and Jones, 2005; Vasconcelos et al., 2006, 2013) it is pointed out that micrite nucleation is initiated within a polymer biofilm (EPS) that embeds microbial communities. They are responsible to produce the micritic micropeloidal structures. According to Dupraz et al. (2004), partial degradation of EPS by sulphate-reducing bacteria, increases alkalinity in microdomains, inducing $CaCO_3$ precipitation. The EPS is also responsible to stabilize the microenvironment (Dupraz et al., 2004) and paste the peloids together. Microbes associated

with EPS promoted carbonate precipitation inside and outside their cells, but also remained active after their decay by creating a micro-diagenetic environment, which accelerated precipitation (Guo and Riding, 1994; Dupraz et al., 2004; Turner and Jones, 2005). It is very likely that the peloidal micritic aggregates that form the Tivoli shrub morpho-types reflect a microbial precursor, which facilitated the nucleation and also acted as substance adhering the small aggregates together. If the microbes would not have existed then the aggregates likely were became disaggregated.

The microbes are reported to decay rapidly after been enveloped within the carbonate precipitate (Krumbein et al., 1977; Chafetz and Meredith, 1983; Chafetz and Guidry, 1999). Consequently, little remains of the bacterial bodies or calcified bacteria, which is likely the reason why direct evidence of microbial activity is relatively scarce in the studied travertines.

Turner and Jones (1995) studied dendrite shrubs from cold-water tufa in Big Hill Springs, (Alberta, Canada). They observed tiny coatings covering dendrite substrates and concluded that EPS facilitated the nucleation of calcite, but subsequent dendrite growth is independent of the EPS. This observation indicates that EPS is essential for the initiation of the dendrites. EPS likely passively controlled biogenic and also abiogenic precipitation, especially as it is commonly negatively charged and attracts cations (Turner and Jones, 2005). The latter authors concluded that if the microenvironment is properly supersaturated, calcite can nucleate spontaneous within or upon EPS (Turner and Jones, 2005). The consumption of EPS during calcification leads to the formation of micropeloids (Guo and Riding, 1994; Dupraz et al., 2004, 2009). The different shrub morphologies reflects the balance between microbial growth rates and calcite precipitation rates, which is affected by flow conditions that are consequence of the environmental gradient (Guo and Riding, 1994; Rainey and Jones, 2009) and discharge (Rainey and Jones, 2009).

2.5.2 Shrub growth history and diagenesis

Based on the range of shrubs and shrub fabrics, it was possible to work out a paragenesis of the shrubs. Initially the shrubs formed very delicate and friable structures. They became denser and more robust due to early cementation (Figs. 2.16A and B). The shrub structures became finally covered by isopachous calcite cement (Figs. 2.16C and D), which builds a rigid framework, preserving most of the primary porosity. In localized areas, further reduction of primary porosity is observed, when cementation continued filling the space between the primary structures mostly with blocky calcite cement. The internal CL-zonation of the isopachous and blocky calcite cements provides evidence of multiple alternating orange to red bright CL colors reflects the crystallization in a phreatic meteoric setting. The color alternations likely reflect changes in redox conditions that might relate to alternating cementation episodes due to repeated subaerial exposure and/or due to water table fluctuations. Subsequently, most spar calcite cement was transformed into micrite, evidenced by the cloudy micrite within the cements (Figs. 2.16D and E). This process is called sparmicritization (Kahle, 1977; Guo and Riding, 1994), and it refers to the transformation of sparry calcite into micrite. Kahle (1977) reported that two mechanisms may cause the sparmicritization: dissolution-precipitation and activity of endolithic microbes. It can be a product of the decay of the EPS / microbes that generated acids that will dissolve the carbonate (Kahle, 1977; Chafetz and Folk, 1984), and by movement and chemical changes of the groundwater (Kahle, 1977). As a result of sparmicritization, sparry calcite is transformed into micrite and cloudy micrite as observed in thin section. Under SEM, the creation of microporosity related to dissolution and/or organic matter decay can be observed. It is a challenge to distinguish the primary depositional peloidal fabric from the diagenetic one, as was already pointed out by Guo and Riding (1994). Subsequently locally, micro-stalagmite and vadose silt phases formed, which reflect precipitation in a vadose meteoric setting. In the successions studied, various micro-structures testify of near-surface exposure, including roots, cracks, crystallaria, floating sediment grains and micritic coatings. Furthermore, calcite crystal overgrowth is observed. They are the result of

vadose and shallow phreatic diagenesis where waters may become saturated with respect to calcium carbonate (Wright and Tucker, 1991).

One of the last diagenetic processes observed is late-stage dissolution, evidenced by rounded and corroded cement crystals and vugs (Fig. 2.16E). Fluctuation of the phreatic water table, variations in dissolved CO_2 present in soil water, as well as exposure may cause dissolution (Guo and Riding, 1994).

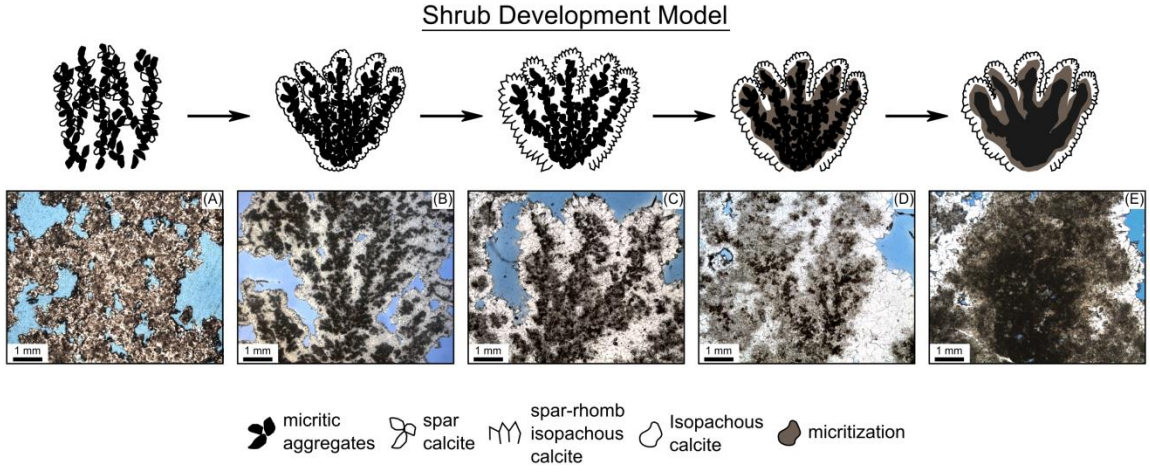

Fig. 2.16: Schematic diagram suggesting how the shrub morphologies develop through time in Tivoli area. (A) It is likely that the shrubs first have a microbial precursor that influence (directly) the precipitation of peloidal micrite aggregates and (indirectly) spar rhomb crystals. (B – C) The continuous precipitation of the sparry calcite builds a rigid framework to the shrubs that stabilized the morphologies. (D – E) Sparmicritization take place in the location areas close to the peloidal micritic aggregates area, possibly due to the fast decay of the microbial precursor. The later generate acids that will dissolve the carbonate.

2.5.3 Depositional system

The shrubs from Tivoli are interpreted by many authors to be deposited either in shallow lakes (Chafetz and Folk, 1984; Minissale and Sturchio, 2004), pool environments fed by vents (Chafetz and Folk, 1984; Guo and Riding, 1994; Wright, 2012; Chafetz, 2013) or terrace systems on distal slopes (Faccenna et al., 2008). Despite the fact that shrub deposits from Tivoli are mainly located in flat layers, they are slightly inclined indicating water flow direction. Because they present sharp and high heterogeneity with other lithotypes, it is very likely that the spring water flow rates varied gently and fluctuated often (Rainey and Jones, 2009). The development of specific shrub morpho-types can be observed locally in active settings worldwide, but they are never as extensive and abundant as the ones observed in the Tivoli area. Unfortunately, the absence of similar recent analogues hampers the interpretation of the depositional system. Pleistocene deposits from Rapolano Terme in Tuscany (central Italy) present a comparable setting where shrub morpho-types developed. They were interpreted to have formed in 'extensive waterlogged flats' (Guo and Riding 1992, 1994, 1998). Pentecost (2005) associated the sheet-like layers of travertine with a dip of a few degrees from Bagni di Tivoli as mounds with low relief. The latter author also supported that the mound outline became irregular due to minor differences in the ground level that surrounded the springs. It is difficult to find evidence that supports this interpretation because up to now, not any spring or feeding system deposit was observed in the area. Besides, a mound is expected to have deposits dipping in all direction, and the travertines from Tivoli are mainly prograding to the south. The three vertical sequences observed in the shrub occurrences in Tivoli point towards variations in the depositional setting.

For sequence 1 the intense alternation of shrub morpho-types with peloidal micrite and elongated encrusted bubbles, as well as mats and paper-thin rafts support deposition in an extensive waterlogged slightly inclined flat setting (Fig. 2.17). In this scenario, a sheet of water flowed southward towards the main river (i.e. the Aniene River). It is likely that water discharge may have varied as well as flow energy (Guo and Riding, 1994; Rainey and Jones, 2009) in areas where the water escaped

not along vents, but rather by diffusive flow from several places at the same time. Notice that, no real vents or fractures were observed in the area, neither the substrate made of non-lithified volcanic tuff. Another important factor relates to water depth, which in extensive waterlogged slightly inclined flat areas is expected to be very shallow (< 5 mm is the average thickness, slightly deeper than the largest shrub), and consequently possessing high facies heterogeneity, due the variations in the water flow rates (Rainey and Jones, 2009). These factors will influence the microbial growth rate and calcite precipitation rates, and consequently the differences in shrub morpho-types, fabrics and areal distributions.

Mats, observed in the Tivoli quarries, often occur associated with rafts, which are interpreted to reflect slow flowing water rates that finally reach stagnant conditions as indicated by the presence of the rafts. The latter also indicate evaporative water, as being reported in cavities and stagnant pool deposits (Folk et al., 1985; Guo and Riding, 1998; Gandin and Capezzuoli, 2014). Encrusted bubbles are reported to occur in terrace and pool systems reflecting nearly stagnant water conditions (Chafetz and Folk, 1984; Chafetz et al., 1991; Jones and Renaut, 2010; Gandin and Capezzuoli, 2014). Shrubs, however, are reported to happen in moderate water flow rates. So, the high frequency intercalation between these lithotypes, show how the system was dynamic and shallow.

The mud layers that occur between the shrubs, were reported by Chafetz and Folk (1984) as layers of compacted peloidal which show presence of bacterial bodies (Chafetz, 2013, Figs. 3C and D) in SEM and fluorescence characteristics under fluorescent microscope. The latter authors interpreted those layers as seasonal, that is periods of none shrub growth.

Adjacent to the main flow water discharge, small and very shallow (< 5 mm deep) pools characterized by flat-lying surfaces, may have developed, with pustular and dendriform shrubs morpho-types as observed on the quarry walls. The rimstone dams represent fast flowing setting and also very shallow water depth (Guo and Riding, 1998) (Fig. 2.17). They are characterized by finely laminated dense shrubs, represented by NDS and very thin crusts, each lamina < 1 mm in thickness.

Ooids are reported to be formed in more turbulent water (Tucker and Wright, 1990) mainly in an abiotic way (Folk and Chafetz, 1983), but biotic mediated oolite formation has also been reported (Brehm et al., 2004, 2006; Andres et al., 2006).

In Sequence 2, the very flat horizons are also interpreted as related to waterlogged settings. They varied laterally in southern direction into smooth slope setting (Fig. 2.17). This explains the progradational stacking pattern for the interval. The smooth slope facies (Fig. 2.17), represented by crusts, but also (rarely) crystalline crusts, characterizes faster water flow and reflects more energetic conditions with more rapid CO_2 degassing. In flat areas, mats, WDS and FDS are the main morpho-types (Fig. 2.17). The lateral variation from mats with stromatolitic-like outline to WDS and NDS likely reflects the increase of the water flow rates, from very slow to moderate flow conditions. The variation from flat to smooth slope system also reflects an increase in water flow rate. The crusts from smooth slope and terrace rimstone dam facies in the present publication are not comparable to the "crystalline crust" from Cava la Chiusa, central Italy (Guo and Riding, 1992, 1998), neither they are "ray-crystal crusts" from Rapolano Serre, or from central Italy (Chafetz and Folk, 1984; Folk et al., 1985), neither are they "ray-crystal shrubs" described by Chafetz and Guidry (1999). The crusts from the studied area in the Tivoli quarries differ from these crust types because they do not possess crystalline habits and the thickness of each crust bundle is not higher than 5 cm, which is in contrast with the referred cases that can exceed 1 m in height.

The crystalline fabric of crystalline crusts is typically formed in sheets of water running under laminar flow conditions in variably steep sub-environments (smooth slopes, terraced slopes, pool rims and cascades - Rainey and Jones, 2009; Gandin and Capezzuoli, 2014; Croci et al., 2016). The thickness of crystalline layers is proportional to precipitation rates and thermal water flow velocity (Guo and Riding, 1998), whereas the growth lamination is attributed to periodic changes in water flow (Pentecost, 2005).

With regards to sequence 3, a slightly different interpretation needs to be formulated with regards to the two sub-sequences (Fig. 2.17). The environmental changed from a more stagnant and evaporative (sub-sequence 3.1) into a more dynamic scenario related to the development of a terrace system (sub-sequence 3.2) (Fig. 2.17). Shrubs in sub-sequence 3.1 are interpreted to have been developed under more evaporitic conditions, because there are no sedimentary structures or morphological evidences for flowing water. Sub-sequence 3.2, however, is interpreted to reflect more dynamic conditions due to the presence of the rimstone dams with NDS being the main morpho-type, while WDS and FDS prevailing in the pools behind the rimstone dams.

Marsh-pool deposits (Guo and Riding, 1998) according to many authors (Wright, 1991; Guo and Riding, 1998; Alonso-Zarza and Wright, 2010; Brasier, 2011) are formed in sub-aerial settings in more arid conditions. Such deposits were already reported to form distally from the hot spring water source, being more influenced by rain-water (Guo and Riding, 1998; Alonso-Zarza and Wright, 2010). The immature palaeosols indicate ephemeral fluctuations of the water table, with stages of reduced accommodation space. The marsh-pool and the dark micrite correspond to the shallowest parts of the described cycles. Notice that they pinch out towards to the Aniene River. The plants grew in locations where thermal water slightly cooled down (Capezzuoli et al., 2008; Pedley, 2009), which may reflect a morphological or a climatic influence (rainy periods as referred by Guo and Riding, 1998). The high frequency variation between the marsh-pool deposits with other lithotypes reflects changes in water hydrodynamics and discharge.

The shrub deposits developed aggradational and progradational stacking patterns. Aggradational patterns are the most common and originate from very shallow and flat areas where travertine lithotypes developed. Progradation patterns are particularly pronounced where relatively steep angle slope deposits accumulated and where each travertine bench downlaps laterally on sloping surfaces. As was already reported, the slope systems are well developed in the central and southern part of the basin, where accommodation space was higher. Probably, the accumulation of the travertine followed the subsidence of the Acqua Albule Basin. The relative slope morphology towards the Aniene River corroborates the interpretations of the direction of flowing water, which induced faster carbonate precipitation. This indicates that the system prograded according to the flow direction.

Mats likely developed in shallower settings than the shrubs. The mats occur intercalated (on cm-scale) with marsh-pool deposits. Because the shrub size varies mainly between 3 and 5 cm, and the mats possess a thickness of ~ 0.1 cm, it is very likely that the water column was higher during the development of the shrubs than for the mats. The water fluctuation is expected to be high for high frequency intercalations. The shrub lithotype shows much less intercalation with marsh-pool deposits, being thus less affected by water fluctuations. Exposure features as tepees and cracks are often observed at the interface between mats and marsh-pool deposits. Another evidence of the very shallow conditions where the mats developed is the very irregular wavy surface morphology. The latter is induced by encrusted bubbles entrapped within the mats and derived by gas leakage from biological activity or degradation of organic matter.

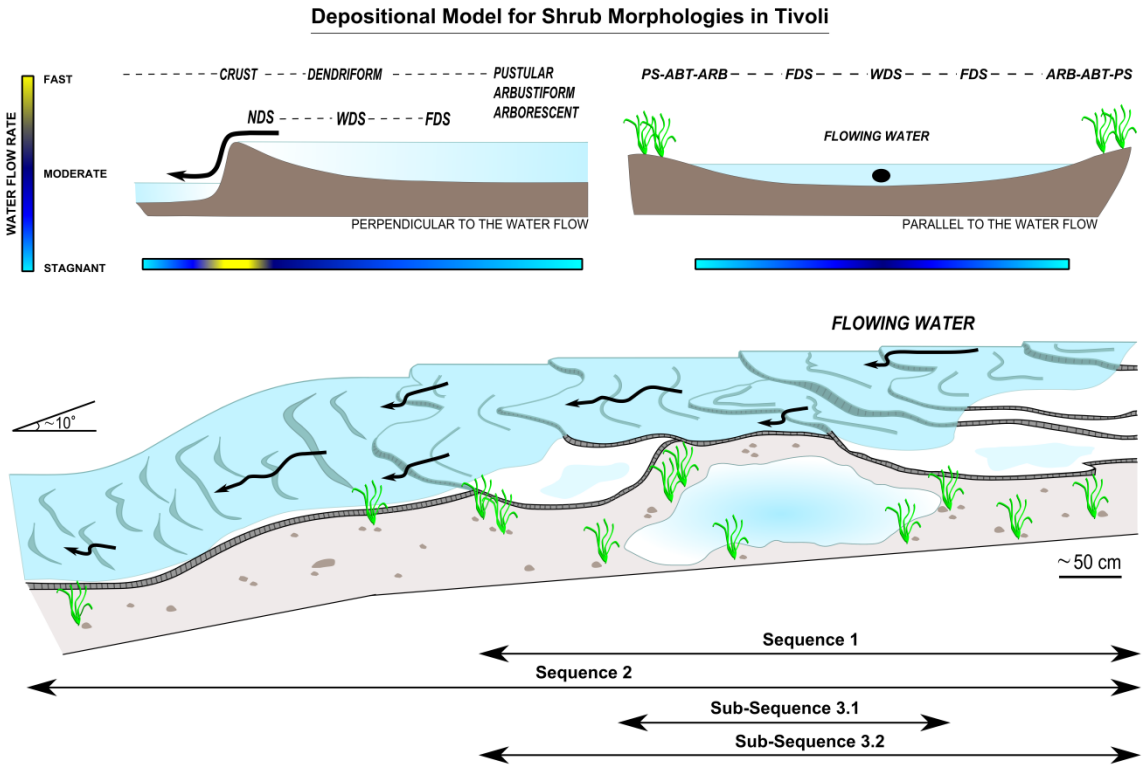

Fig. 2.17: Schematic depositional model for an extensive waterlogged flat setting varying laterally into slope system for the different shrub morpho-type in function of water flow rate. Dendriform shrubs in this model occur in moderate to low hydrological settings, being NDS occurring in the most energetic hydrological conditions, WDS in moderate and FDS in lower conditions. ARB, ABT and PS occur in very low hydrological conditions, possibly highly influenced by evaporitic conditions. In the hydraulic jumps the dendriform shrubs (NDS) will have a crustiform characteristic. This model can be applied for the three described sequences in Tivoli quarries. The sequences comprise the superposition of the different parts of the schematic depositional model.

2.5.4 Shrub morpho-types under different hydrological conditions

According to Okumura et al. (2012) hydrodynamic conditions, i.e. the flow and energy of the precipitating waters will impact the shrub morphologies. The latter authors noted that highly lithified dense travertine is formed under high-flow hydraulic conditions with water layers of less than 5 cm in thickness, whereas the more porous and loosely consolidated travertine deposits are more common within low-flow sites. Under high-flow conditions, microbes are more inhibited by high water energy. Water turbulence enhances CO_2 degassing responsible for mineral precipitation (Pedley and Rogerson, 2010; Okamura et al., 2012). This can be observed in the slope setting, for example, where water flows faster and where crusts are the most common lithotype. Guo and Riding (1998) also pointed out that crystalline crusts reflect rapid precipitation under high flow rates, while thinner crust development reflects slower precipitation in slower flowing water. According to Dupraz et al. (2009), in moderate to slow flowing settings, other processes such as evaporation and microbial mediation, have a higher influence on CO_2 degassing and carbonate precipitation. Here, the diversity and abundance of different shrub morpho-types will increase (Dupraz et al., 2009; Okamura et al., 2012).

The differences in the shrub morpho-types that are the result of interaction between biotic and abiotic processes are also controlled by local changes in the microenvironment. According to Pentecost and Viles (1994, see also Rainey and Jones, 2009) the balance between microbial formation rates and calcite precipitation rates is affected by flow conditions (Fig. 2.18) that changed in response to topography and discharge. Under high-flow conditions, thin EPS biofilms, that are the product of microbial activity (Dupraz et al., 2004, 2009), will develop due the relatively higher water energy, while under slower flow conditions thick EPS biofilms are more likely to develop. Okamura et al.

(2012) noticed that the recent shrubs from the Nagaya hot spring in Japan, is characterized by dense shrubs associated to high flow conditions and a relatively low presence of biofilms, while fragile shrubs formed under low flow conditions where the biofilms were more abundant.

Consequently, in function of the water energy and microbial setting, it is very likely that dendriform shrubs from Tivoli are associated to moderate-to-low energy hydrological settings, with NDS reflecting the most energetic conditions due to their more dense characteristics (Kano et al., 2006; Okumura et al., 2012), with decreasing importance of flow from WDS to FDS (Figs. 2.17 and 2.18), with the latter being more loosely packed. This is in line with their observed occurrence along palaeotopographical surfaces on the quarry walls. These shrub types occur in flat areas or are associated with small bumps and rimstone dams, with NDS preferentially developing in the rims and WDS and FDS being more common in flat areas (Fig. 2.17). The influence of microbes on carbonate precipitation hypothetically increased from the more dense NDS, to WDS until the more fragile FDS (Fig. 2.18) (Guo and Riding, 1994; Okamura et al., 2012). However, in palaeo-settings like our study area this is not straight-forward to proof. Crusts developed under relatively faster flowing water conditions marked by lower microbial activity (Fig. 2.18), with predominant CO_2 degassing processes (Folk et al., 1985; Guo and Riding, 1992, 1998; Gandin and Capezzuoli, 2008; Rainey and Jones, 2009; Jones and Renaut, 2010; Okamura et al., 2012). Finely (< 1 mm) laminated crusts are associated with slower flow rates when compared with thicker layers (cm-scale) (Fig. 2.17). Faster flow rates result in denser and more tightly packed shrub morphologies (Figs. 2.17 and 2.18).

Finally, ARB, ABT and PS morpho-types (Figs. 2.17 and 2.18) observed in flat-lying surfaces, could not have formed as a result of turbulence-induced CO_2 degassing (Rainey and Jones, 2009). It is likely that they were generated in very slow flowing water settings reaching almost stagnancy, being the main process influencing the calcite precipitation, rapid evaporation and/or CO_2 degassing driven by solar heating (Fig. 2.18) (Rainey and Jones, 2009). These morpho-types likely were more influenced by microbes. This interpretation is based on the lack of primary depositional structures, such as bumps or rims. The abundance of elongated encrusted bubbles and paper-thin rafts both intercalated within and between the shrubs corroborates with the interpretation that the energy of the system was very low reaching stagnancy (Chafetz et al., 1991). Because ARB is taller than ABT and PS, and also because exposure features are commonly observed associated with ABT and PS layers, it is very likely that an increasing influence of evaporation is expected from ARB to PS morpho-types. PS, despite being more rounded, was not transported, such as lithoclasts. PS resemble spherical aggregations found in supersaturated microbial mats (Dupraz et al., 1994; Jahnert and Collins, 2013).

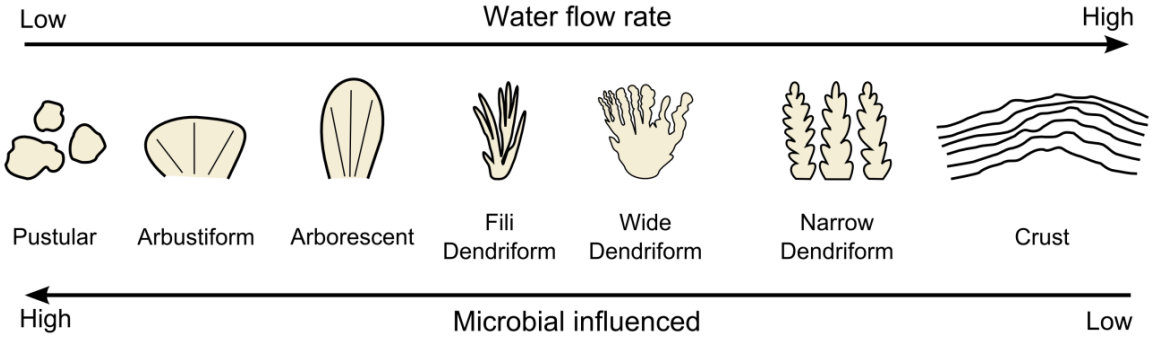

Fig. 2.18: General model proposed for Tivoli shrub morphologies showing the relationship between hydraulic conditions, microbial influenced and development of shrub morphologies. It is very likely that the microbial influence increase from crust lithotype (mainly abiotic), to NDS, WDS, FDS, ARB, ABT and PS (mainly biotic).

2.6 Conclusions

Six shrub morpho-types were identified in the Tivoli travertines. µCT analysis was an important tool to observe and distinguish the 3D arrangement of the different morphologies. The shrubs were interpreted to have formed in very shallow "waterlogged slightly inclined flat areas", varying laterally and vertically into low angle slope systems, with a sheet of water flowing in southern direction towards the Aniene River. Locally, shrubs were also observed in terraces and small pool systems.

It is very likely that hydrodynamic conditions influenced the precipitation rate of the calcite, as well as controlled the abundance of microbes (i.e., bacteria), which both affected the morphology of the shrub structures. The hydrodynamic conditions associated with the shrub morpho-types can be summarized as follows: 1) in fast flowing water more dense and tight packed shrub structures will develop, and crusts are the most abundant lithotype; 2) moderate flowing waters will promote NDS and WDS morphologies. NDS reflect faster flowing conditions compared to WDS, in line with the denser fabric of the former; 3) slow to very slow flowing waters allow the development of PS, ABT, ARB and FDS morpho-types, with the first three likely being more influenced by evaporative processes based on their petrographic fabrics, associated rafts and encrusted bubbles, and because of the lack of stratification that all reflects low energy flowing to standing water conditions. The microbial influence is interpreted to increase from NDS, over WDS, FDS, ARB, ABT to PS, according to the decrease in flow velocity.

CHAPTER 3 Geochemistry of the (related-)shrub morpho-types from Tivoli travertines (Central Italy)

3.1 Introduction

Travertines form by precipitation from supersaturated waters caused, primarily, by CO_2 degassing. Waters giving rise to travertine deposits undergo rapid chemical changes (Pentecost, 2005). Travertine deposits possess crystal fabrics and mineral compositions that are a sensitive environmental record of water chemistry, hydrologic transport, climate and microbial populations (Fouke et al., 2000). Travertine can be precipitated almost instantaneously when groundwaters contact the epigean atmosphere (Pentecost, 2005). In this way, travertine-related carbonates are therefore important repositories for paleoenvironmental reconstructions

Travertine shrub structures from Tivoli area possess peloidal micritic aggregate fabrics indicative of bacterially influenced crystal growth (Folk and Chafetz, 1983; Chafetz and Folk, 1984; Folk et al., 1985; Guo and Riding, 1992, 1994, 1998; Chafetz and Guidry, 1999; Chafetz, 2013). Moreover, shrubs have very distinct and various morphologies that were attributed to the influence of hydrodynamic water conditions and microbial influence (Erthal et al., 2017).

The aim of the present chapter is to better constrain the sedimentologically-based interpretation, to characterize geochemically the shrub morpho-types and crusts by means of stable oxygen and carbon as well as strontium isotopes, and major and minor/trace elements concentration, in order to comprehend their genesis and processes that promote carbonate precipitation, depositional water temperatures, CO_2-origin and source rocks of the fluids.

3.2 Methods

3.2.1 Sr isotopes

The $^{87}Sr/^{86}Sr$ ratios were determined for 10 samples representing different shrub morpho-types from Tivoli travertines. The samples were initially leached with ammonium acetate. Carbonates were dissolved in diluted acetic acid / HCl before going through Triskem Sr spec resin columns (method adopted from Pin et al., 1992) where the Sr fraction was collected. The samples were loaded onto Re filaments employing Ta emitter solution and analyses were carried out on a modified VG-54-30R thermal ionization mass spectrometer (TIMS) at SUERC (UK), where the ratio is measured with respect to the Standard Reference Material number 987 from the National Institute of Standards and Technology USA (NIST SRM 987 $CaCO_3$).

3.2.2 Elemental analysis

Major and minor/trace element concentration of 36 bulk shrub samples from Tivoli travertines have been analyzed using inductively coupled plasma optical emission spectroscopy (ICP-OES). The method consists in dissolving the sample by using three different acidification protocols (Claes, 2015).

First acidification digestion protocol (HCl)

0.50 g powdered sample was dissolved in 10 ml of 1 M HCl prior to measuring the element concentrations. Then, the container with the sample and HCl was swirled and heated to 100°C for 2 hours. After that, about 10 ml of 1 M HCl was added to the “almost dry” residues, and this mixture was warmed up for 15 minutes. At last, the solution was filtered and diluted up to 50 ml of 1 M HCl.

Second acidification digestion protocol (HCl and HNO_3)

For this protocol, 2 acids were used: HCl and HNO_3. 10 ml of 1 M HCl was added to 0.50 g of a powered sample which was swirled and heated to 140°C, till it was "almost dry". Then, 1 ml of 1 M HNO_3 and 5 ml ultrapure water (MilliQ or MQ) was added. The solutions were again swirled to be homogenized and were warmed up at 140°C for 15 minutes. Subsequently, the solutions were filtered and diluted by adding 50 ml of MQ, before element concentrations were measured.

Third acidification digestion protocol (HNO_3, $HClO_4$, HF, HCl)

The last acidification protocol comprises the use of 4 acids: HNO_3, $HClO_4$, HF and HCl, with the aim of dissolving the samples completely. 3 ml of HNO_3 were added to the sample and heated to 200°C for 15 minutes. Then, 2 ml $HClO_4$ was added. Subsequently, the beakers were covered with watch glasses and heated to 230 °C for 1 hour. Then, the watch glasses were taken off and the liquid has evaporated to a "drop" at 230°C. After cooling, 3 ml HF was added and the beakers were placed back on the hot plate at 250°C. When the residue was almost dry, 1 ml $HClO_4$ was added and it was also topped with 7 ml HCl 2.5 M. Lastly, the resulting solution was removed to a volumetric flask and diluted to 25 ml with ultra pure water (> 18 MΩ/cm^3).

For analysis, a Varian 720-ES instrument provided with a double-pass glass cyclonic spray chamber, a concentric glass nebulizer SeaSpray and an "extend high solids" torch was used to determine 21 element concentrations (Ca, Al, As, Ba, Co, Cr, Cu, Fe, K, Li, Mg, Mn, Na, Ni, P, Rb, S, Sr, Ti, V and Zn).

3.2.3 Quantitative evaluation of mineral by scanning electron microscopy (QEMSCAN)

Two thin-sections have been analyzed at Petrobras Research Center (CENPES), Brazil. The operating principle of the QEMSCAN is the same as a conventional scanning electron microscope (SEM) coupled to EDS detectors. However, the latter operates in an automated way and has a robust database of chemical EDS in mineralogy. Thus, results generated digital mineralogical maps distribution present in the thin-section and a semi-quantitative data can be treated statistically. To make the mineralogical map, the equipment performs microanalysis points (10 by 10 µm each pixels) and compares the x-ray spectrum obtained with a database with mineral composition information. The distance between the analysis points is predefined by the operator and will result in the size of the map pixels and consequently the resolution. By identifying the mineral with the composition closest to the analyzed point, a default color is assigned. Mineralogy determination is expressed as a quantification area of each mineral (pixels-based) divided by the total area (including porosity), which gives an area percentage. The resolution limits of the analyses are 10 by 10 µm (pixel size). The software iDiscover was used for the mineralogical interpretation of the data. The porosity estimation is done by using the resin response or in areas with no EDS signals, indicating empty space. In this estimation, the pores in connection with the external area of the sample are disregarded.

3.2.4 Stable carbon and oxygen isotopes

Seventy six samples from shrub morpho-types, 7 samples from immature palaeosoils, 6 samples representative of mat lithotype and 1 sample of phytoclast lithotype, all taken from Tivoli travertines, were micro-drilled and analyzed at the Research Center of Petrobras (CENPES), Brazil. The carbonate powder was first 100% acidified with H_3PO_4 (phosphoric acid) at 70°C in a Gasbench II (automatic unit of CO_2 extraction). This process produces CO_2 which is injected in a ThermoFinnigan Five Plus mass spectrometer (Thermo Scientific Inc.). The isotopic values are converted to the equivalent carbonate ratio and are expressed in the conventional δ-notation (equation 3.1):

$$\delta(‰) = \left(\frac{R_{sm}-R_{std}}{R_{std}}\right) \mathcal{X} 1000 \qquad (3.1)$$

R_{sm} represents the isotopic ratio determined in the sample, and R_{std} represents the standard. In turn, R corresponds to the ratio $^{13}C/^{12}C$ for the case of the carbon isotopes and $^{18}O/^{16}O$ for the oxygen isotopes. The delta therefore expresses

the isotopic composition of the sample relative to an established standard, which has a fixed ratio. In this case, the $\delta^{13}C$ and $\delta^{18}O$ values of the carbonates are expressed in per mil (‰), relative to Vienna Pee Dee Belemnite (V-PDB) by assigning a $\delta^{13}C$ value of +1.95‰ and a $\delta^{18}O$ value of +2.20‰ to the standard NBS19. The analytical standard deviations for $\delta^{13}C$ and $\delta^{18}O$ are 0.04‰ and 0.05‰, respectively.

3.2.5 (Geo-) statistics

Unbalanced one-way ANOVA statistical analyses (variance analysis) was applied separately on the $\delta^{13}C$ and $\delta^{18}O$ data from the shrub morpho-types to perform a hypothesis test for the control of shrub morpho-types on the analyzed carbon and oxygen stable isotope signatures. ANOVA is a statistical model used to analyze the differences among group means and their associated procedures (such as "variation" among and between groups).

The formula for F used in ANOVA is F = MSB/MSW, where (MSB) is the group variance estimate and (MSW) is the within group variance estimate. Every variance estimate has two parts, the sum of squares and the rim (SSB and SSW), both between and within groups, and degrees of freedom (df). ANOVA tests the non-specific null hypothesis (H_0) that all group means are equal. The null hypothesis involves computing a particular ratio of variability in the group means to variability among replicates within each group. The resulting F statistic values can differ widely from 1) if the null hypothesis is true, larger values indicate that H_0 is false. Standard tables of the F distribution yield a significance level (p) for the observed F statistics. Roughly speaking, (p) is interpreted as the probability that the group means that have been observed (or a set of means which appear to differ from each other to an even greater extent) could have occurred if the null hypothesis is actually true.

For the elemental components, they were statistically analyzed using R software (R core Team, 2012). Multivariate analysis was carried out by using element values that were transformed by using centered log ratio (CLR) transformation. A correlation matrix and an elemental Ward hierarchical cluster, based on Euclidean distances, were performed in order to establish which elements are linked by similar geochemically processes or origins (Claes, 2015).

3.3 Results

3.3.1 $^{87}Sr/^{86}Sr$ isotope

The results of the $^{87}Sr/^{86}Sr$ isotope analysis determined for 10 representative samples are given in Table 3.1. The results display $^{87}Sr/^{86}Sr$ ratios varying between 0.70795 ± 0.0014 and 0.70816 ± 0.0022 with an average of 0.70801 ± 0.0015. The Tivoli shrub samples are characterized by generally high strontium concentrations, varying between 363 and 1946 µg/g with and average of 642 µg/g.

Sample	87Sr/86Sr	% Std Err
ST 03	0.70816	0.0022
ST 06	0.70795	0.0014
ST 70	0.70799	0.0013
ST 98	0.70802	0.0012
QR 32V	0.70797	0.0015
QR 33H	0.70799	0.0014
QR 32V	0.70798	0.0016
CL 03	0.70800	0.0011
CL 21	0.70798	0.0014
CL 31	0.70803	0.0015

Table 3.1: $^{87}Sr/^{86}Sr$ results of 10 shrub samples from Tivoli quarries. The darker red color represents the highest ratios while the lighter red color, the lowest ratios.

3.3.2 Elemental composition analysis

The results of elemental composition analysis for shrub morpho-types can be found in Table 3.2. Several elements (As, Co, Cr, Cu, Li, Ni, Rb, V, Ti and Zn) do not reach the detection limit (dl) and therefore were excluded from the statistical analysis (Table 3.2). Some elements were not measured, e.g. Si.

Mg, Na, S and Sr possess significantly higher concentrations than the other measured elements (Table 3.2). Mg varies between 1408 µg/g and 2369 µg/g, with an average of 1803 µg/g. Sulphur and strontium range between 1100 µg/g

and 3207 µg/g for S, and 363 µg/g and 962 µg/g for Sr. These elements present averages, respectively, of 1618 µg/g and 582 µg/g. Na possesses concentrations between 144 and 391 µg/g, with an average of 220 µg/g.

Sample	Ca (%)	Al (ppm)	Ba (ppm)	Fe (ppm)	K (ppm)	Mg(ppm)	Mn (ppm)	Na (ppm)	P (ppm)	S (ppm)	Sr (ppm)	Shrub morpho-types
QR15B	38.8	89	10	42	41	1765	20	211	51	1457	615	NDS
QR22	37.9	69	16	43	33	1408	17	195	55	1308	576	NDS
QR34V	38.2	70	11	36	42	1878	23	219	73	1602	560	NDS
QR35H	38.4	128	12	46	60	1880	18	256	60	1684	717	NDS
QR65	38.9	73	9	56	35	1970	25	229	73	1655	558	NDS
QR116H1	38.4	67	9	131	34	1812	22	148	57	1386	600	NDS
QR134V	38.0	37	8	38	25	1241	19	162	62	1075	408	NDS
QR135H	39.8	66	7	29	27	1601	21	180	60	1246	433	NDS
CR12	38.7	101	10	33	41	2017	27	243	88	1780	621	NDS
QR31H	38.4	60	8	29	44	1867	18	237	66	1701	600	WDS
QR36H	38.2	87	9	42	44	2032	24	233	75	1769	610	WDS
QR38H	35.9	73	9	39	32	1607	21	192	53	1286	553	WDS
QR21	38.4	87	7	73	43	1756	26	216	79	1515	552	FDS
QR24V1	38.4	103	6	46	29	1897	30	216	85	1555	502	FDS
QR24V2	38.6	125	9	47	47	1913	23	241	75	1724	690	FDS
QR28	38.3	152	10	61	51	1752	19	223	63	1428	612	FDS
QR29	38.9	124	7	81	40	1444	20	174	61	1066	552	FDS
QR33H	38.1	48	9	31	39	1937	21	223	69	1803	619	FDS
QE40	38.0	59	15	34	44	1634	15	217	46	1602	713	FDS
QR47	38.5	105	9	55	36	1662	23	198	63	1331	505	FDS
QR136V1B	38.2	85	8	27	33	1588	22	184	65	1240	431	FDS
QR139V	37.9	84	10	41	38	1925	28	195	83	1894	558	FDS
QR63	38.3	55	5	54	26	1545	24	170	72	1052	363	ARB
QR133H2	37.5	164	10	83	43	2336	36	294	110	2302	663	ARB
QR140H1	37.9	88	17	26	71	2369	20	391	64	3207	962	ARB
CR03	37.8	194	14	73	76	2422	22	301	34	2349	839	ARB
QR138H	38.1	80	9	30	31	1788	22	213	86	1586	523	ABT
QR117H	38.6	52	7	88	30	1771	24	206	63	1344	504	ABT
QR118H	38.4	103	7	185	31	1985	32	229	91	1698	476	ABT
QR52	38.4	84	11	48	56	1955	25	323	71	2760	801	PS
QR55	38.2	113	6	319	27	1500	46	176	77	959	390	PS
QR103H1	37.6	110	8	75	47	2029	22	249	83	1826	688	PS
QS11T	38.6	70	7	99	23	1420	35	169	72	1100	388	PS
CR002	37.3	263	28	213	86	2884	31	437	49	3864	1270	PS
QR68	38.3	243	14	89	61	1871	38	302	102	2086	722	CRUST
CR05	36.4	189	23	84	99	2840	29	502	34	5720	1946	CRUST

Table 3.2: Thirty-six travertine shrub elemental composition results from Tivoli quarries. NDS corresponds to narrow dendriform shrub, WDS to wide dendriform shrub, FDS to fili dendriform shrub, ARB to arborescent shrub, ABT to arbustiform shrub and, PS to pustular shrub.

To evaluate a common incorporation or origin for elements, correlation matrices from the CLR transformed data were constructed (Fig. 3.1) and Ward hierarchical cluster dendrograms were calculated (Fig. 3.2) to show the relationship between the analyzed elements.

The non-linear dendrogram combination of how compact a group is, and how well-separated it is from the other groups, was assessed based on the calculation of the silhouette statistics (internal measurements) (Table 3.3) (Rousseeuw, 1987). The dendrogram of the elements can have their results grouped into 12 groups according to the silhouette statistical analysis, being 4 (yellow in Table 3.3) the optimal number of clusters (closest to 1). They can be distinguished as: Group I consisting of Ba, K, Sr, Mg, Na and S; Group II containing Ca, Mn, P; Group III with Al; and Group IV with Fe.

Silhouette		
(2) 0.5042	(3) 0.5743	(4) 0.6078
(5) 0.5703	(6) 0.5666	(7) 0.5269
(8) 0.5133	(9) 0.3981	(10) 0.2950
(11) 0.2378	(12) 0.1078	

Table 3.3: Silhouette of internal measurements of the dendrogram of the elements. The silhouette is calculated for all the possible number of groups. The optimal number of clusters for the elements in the dendrogram graphic is 4 (yellow, closest to 1).

However, if other stability measurements are taken into account as average proportion of non-overlap (APN) and average distance between means (ADM), then 6 groups (closest to zero) form the most optimal solution (Table 3.4).

APN	ADM
0.0304	0.0970
0.0473	0.1638
0.0394	0.1000
0.0552	0.1921
0.0000	0.0000
0.0079	0.0188
0.0000	0.0000
0.0000	0.0000
0.0059	0.0067
0.0059	0.0075
0.0296	0.0329

Table 3.4: Stability measurements of average proportion of non-overlap (APN) and average distance between means (ADM). 6 groups (yellow color – closest to zero) are optimal results.

The "stability measures" compares results from clustering based on the full data and clustering based on removing each column (sample), one at a time (Datta and Datta 2003; Yeung et al., 2001). The APN measures the average proportion of observations not placed in the same cluster (Brock et al., 2008). The ADM computes the average distance between cluster centers for observations placed in the same cluster (Brock et al., 2008).

From the R2 data (Fig. 3.1), the significance results for 36 samples vary from 0.32 (0.05 level) and 0.41 (0.01 level). Positive correlation occur between Ba with S, Sr, Na and K which are negatively correlated with Fe, Mn and P. Fe shows only weak positive correlations (not significant) with Al and Mn. The strongest negative correlation occurs between Ca and Al (-0.60).

So, based on the statistics (mainly silhouette and correlation coefficients), 6 groups were established (Fig. 3.2): Group I: Ba, K, and Sr; Group II: Mg, Na, and S; Group III: Ca; Group IV: Mn and P; Group V: Al; and Group VI: Fe.

Fig. 3.1: Pearson element correlation matrices of the CLR transformed results in Table 3.6. Correlation coefficient of > 0.65 is indicated in red. Correlation coefficient of < -0.65 are indicated in blue. The correlation is significant on a 0.01 level from 0.413 and from 0.32 on a 0.05 significance level.

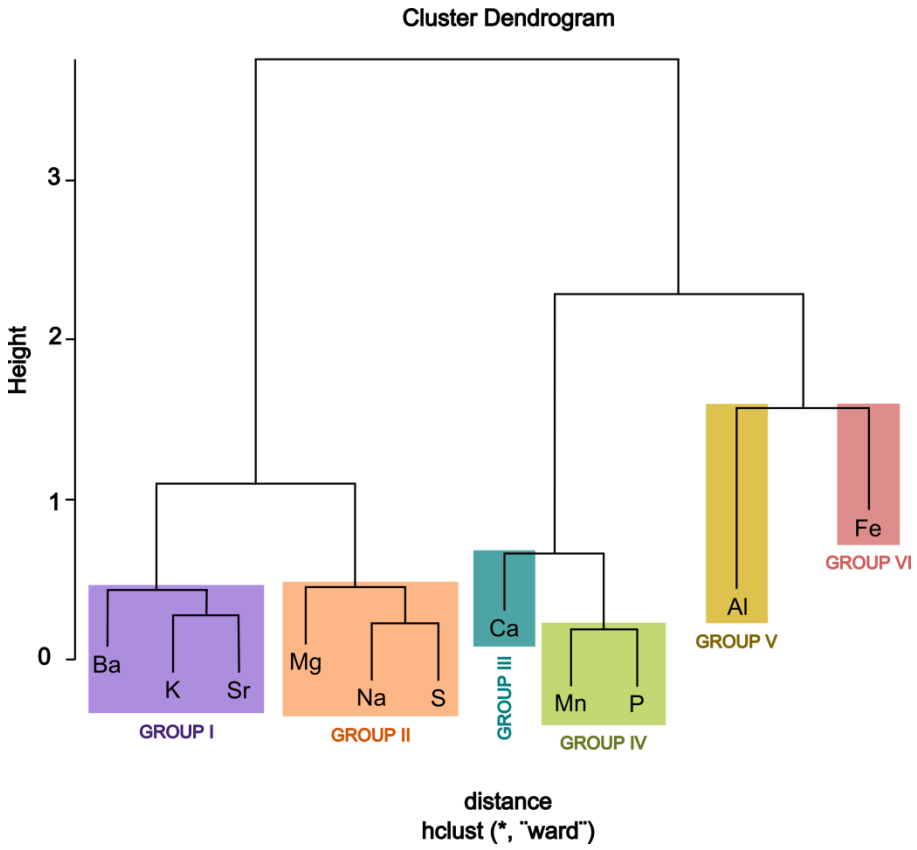

Fig. 3.2: Hierarchical cluster dendrograms based on Pearson correlation between the elemental concentrations results in Table 3.6. The six elements groups are indicated with different colors.

3.3.2.1 Geochemical (related-) shrub morpho-types dependency evaluation

The elemental variation of the shrub (related-) morpho-types (Fig. 3.3) shows a rather clear contrast mainly between crust and the shrub morpho-types. Elements of Groups I and II (Ba, K, Sr, Mg, Na and S) possess much higher concentrations for the crust in comparison to the shrub morpho-types. Groups I and II, among the shrub morpho-types, ARB possesses higher concentrations of Ba, K, Mg, Na, S and Sr than the other shrubs morpho-types. Group III possesses the lowest values of the Ca element for the Crust in comparison with the shrub morpho-types. Group IV (Mn and P), crust and PS possess the highest Mn concentrations, but any shrub (related-) morpho-types can be differentiated in function of P. In Groups V crusts possess higher concentration of Al elements. Group VI (Fe) the PS possesses higher concentrations of Fe among the other (related-) shrub morpho-types.

The interpretation of these data should however be done with care, since the results are not necessarily statistically representative as less than 10 samples per shrub morpho-types and only 2 crust samples were analyzed.

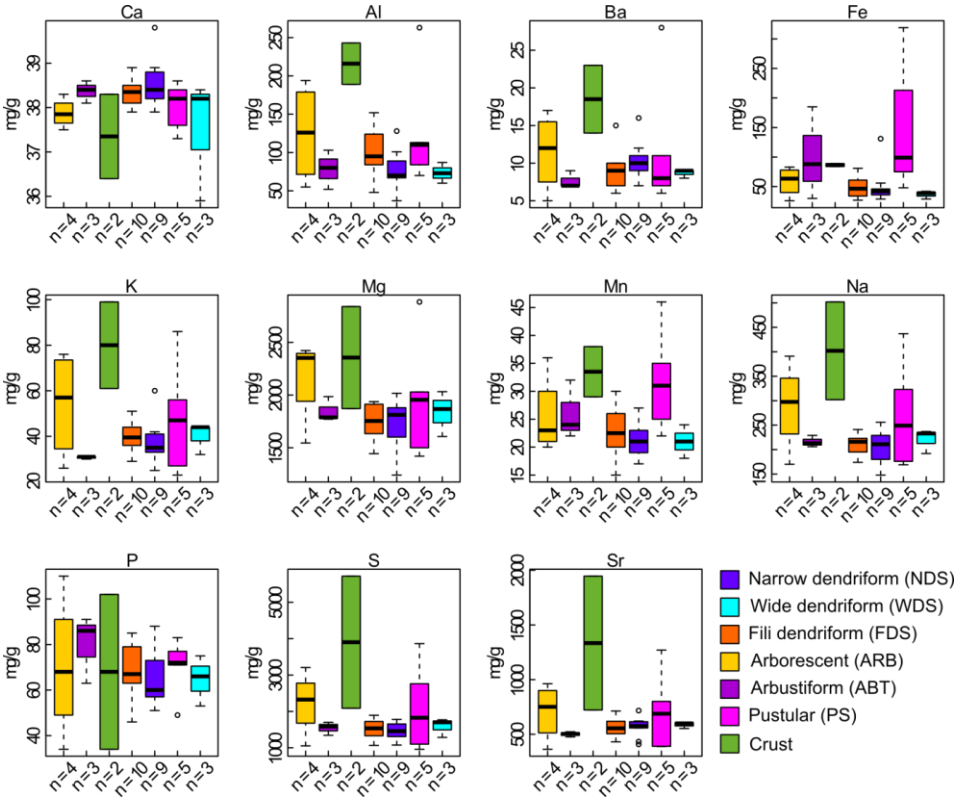

Fig. 3.3: Box plots of the different shrub morpho-type samples for the different elements.

3.3.3 Quantitative mineral evaluation by scanning electron microscopy (QEMSCAN)

Two samples were analyzed by QEMSCAN with the aim to identify trace minerals, organic matter, pores and their distribution in the sample (Figs. 3.4 and 3.5), and consequently support the interpretation of the element analysis. The most abundant mineral encountered in the samples is calcite, as indicated by XRD's analyses. The latter corresponds more than 98-99% of the rock (Figs. 3.4 and 3.5). However, the other 2-1% relates to a mineral assemblage not measured by XRD analysis (Figs. 3.4 and 3.5). Indeed, XRD results from Tivoli shrubs pointed out that the samples consist of 100% calcite. This happen because the trace minerals are under the detection limit of the XRD technique. QEMSCAN analysis, however, could not differentiate between polymorphs of calcium carbonate, due to the dependency of the system on chemical composition of minerals rather than their crystallography. The error of the analysis is not reported in literature, neither in the thesis because of the nature of the technique. There are many evolved parameters which makes the error calculation to become very complex, such as: acquisition of the EDS, elementary quantification, mineralogical interpretation from the chemistry by the software, pixel size, etc. For statistical analysis of systematic data error, it will be necessary to introduce a reference standard with known detailed mineralogical composition. Unfortunately, such a standard was not available for more precise error determination in the lab where the analyzes were carried out. However, there is no reasons to believe that the analyses could have given large errors, and therefore the analyses results were suitable for the present work. Besides, the present study aims to use these results only to support the identification of trace minerals and for the interpretation of major/minor element analyzes.

The minerals identified in both samples are almost the same and are located close to the pores and randomly distributed in the calcite matrix (Figs. 3.4 and 3.5). These are: quartz, pyrite, K-feldspar, mica, dolomite, gypsum/anhydrite, barite, titanium oxide, albite, anorthite, celestite, apatite and kaolinite. Mg-clay is detected in sample QR 68H only. Traces of organic matter were observed in both samples.

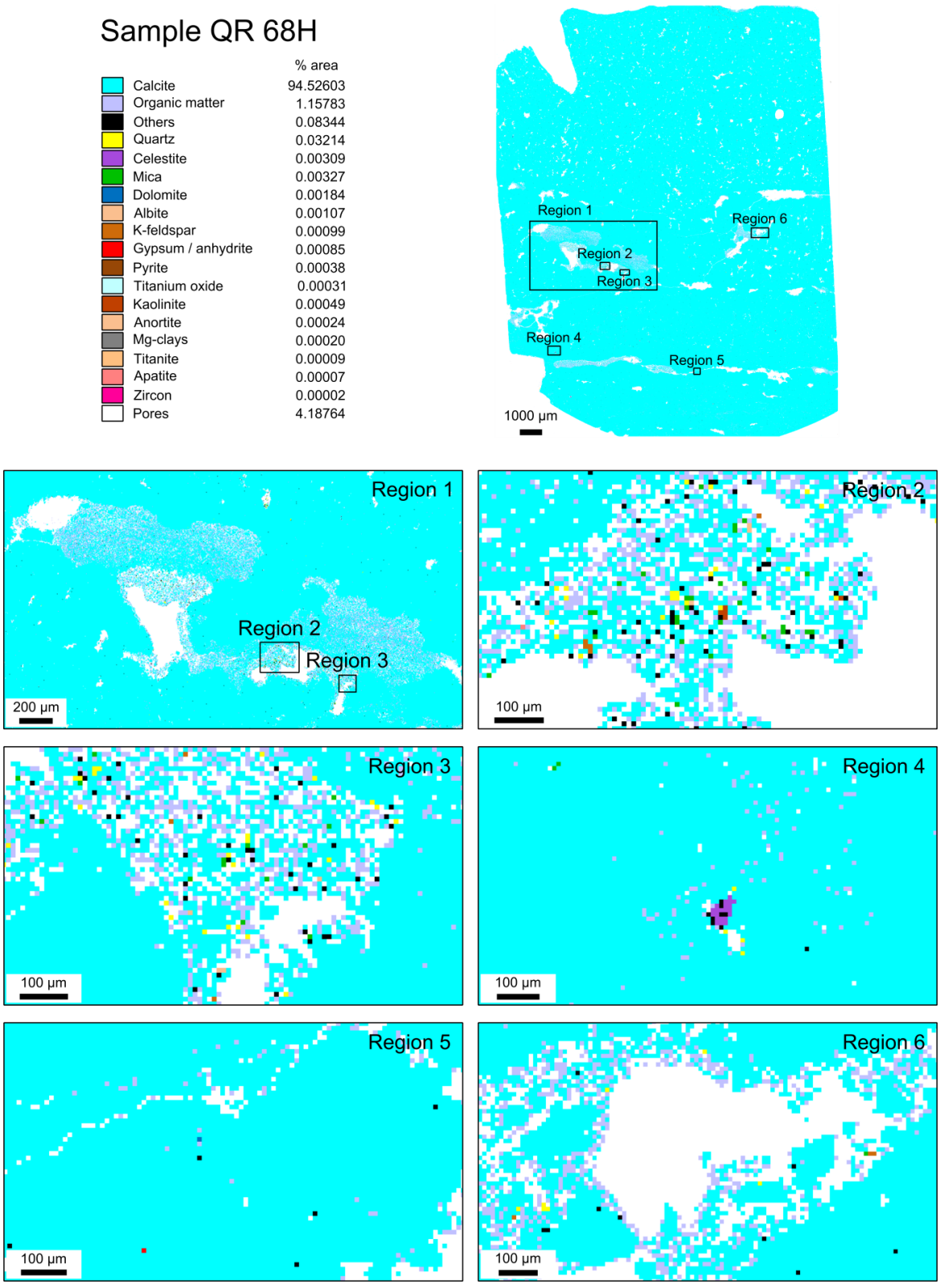

Fig. 3.4: QEMSCAN result of sample QR 68H. The analysis gives a digital representation of the rock where each pixel possesses a pre-defined color corresponding to a mineral or organic matter. "Others" are attributed to imperfections in the thin-section related to the thin-section preparation or "dust" in the thin-section that do not allow a precise mineralogical characterization. Mineralogy determination is expressed as a quantification area of each mineral (pixels) divided by the total area (including porosity), which gives an area percentage. The resolution limits of the analyses are 10 by 10 µm (pixel size).

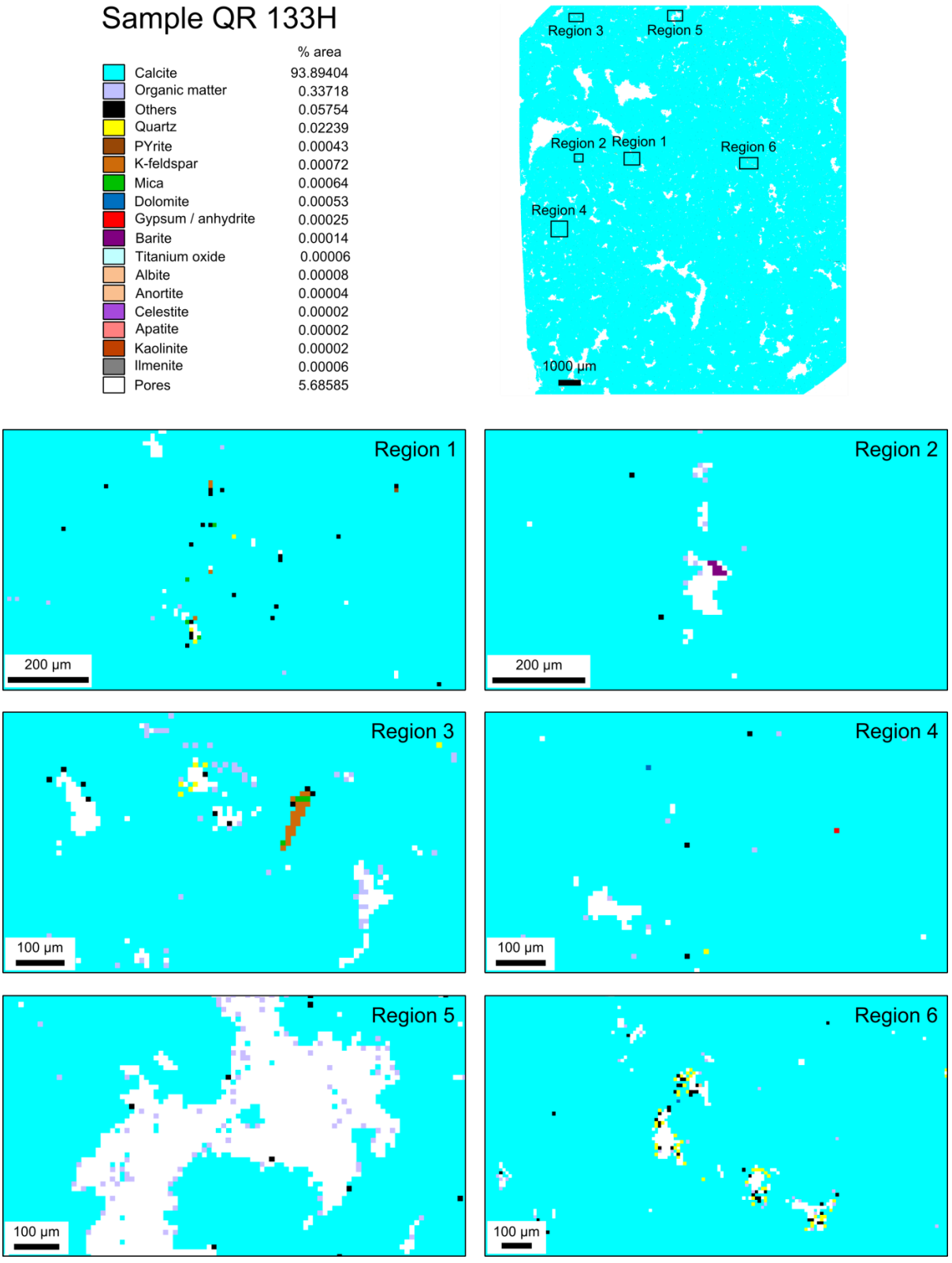

Fig. 3.5: QEMSCAN result of sample QR 133H. The analysis gives a digital representation of the rock where each pixel possesses a pre-defined color corresponding to a mineral or organic matter. "Others" are attributed to imperfections in the thin-section related to the thin-section preparation or "dust" in the thin-section that do not allow a precise mineralogical characterization. Mineralogy determination is expressed as a quantification area of each mineral (pixels) divided by the total area (including porosity), which gives an area percentage. The resolution limits of the analyses are 10 by 10 µm (pixel size).

3.3.4 C and O Stable Isotopes

The $\delta^{13}C$ and $\delta^{18}O$ results of the 76 shrub morpho-type bulk samples are present in Table 3.5 and plotted in Fig. 3.6. According to Erthal et al. (2017) the following shrub types can be differentiated: narrow dendriform shrub (NDS), wide dendriform shrub (WDS), fili dendriform shrub (FDS), arborescent (ARB), arbustiform (ABT) and pustular shrub (PS). The crust shrub represents a different lithotype (Claes et al., 2016; Erthal et al., 2017). The results show that $\delta^{13}C$ values plot between +8.71‰ and +11.32‰ V-PDB and $\delta^{18}O$ values between -4.97‰ and -8.25‰ V-PDB. The different shrub morpho-types plot in the same range for $\delta^{13}C$ (between +8.71 and +10.73‰) and $\delta^{18}O$ (between -5.72‰ and -8.25‰), while crust plots in a distinct area in the graph. The latter possesses heavier $\delta^{13}C$ (between +9.61‰ and +11.32‰) and $\delta^{18}O$ (between -4.97‰ and -7.64‰) results.

The variation of $\delta^{13}C$ and $\delta^{18}O$ signature was plotted along the stratigraphic sections of sequence 1 and 2 (see Chapter 2). In Fig. 3.7, an example is given for the Querciolaie-Rinascente 1 (QR1) quarry. No first order correlation between $\delta^{13}C$ and $\delta^{18}O$ was observed. While $\delta^{13}C$ stays relatively constant over the entire section (Fig. 3.7A), $\delta^{18}O$ varies somewhat (Fig. 3.7B). Shrub and mat samples below immature palaeosols have a mean $\delta^{18}O$ of -6.5‰ and $\delta^{13}C$ of +10.18‰, samples of the immature palaeosols have a mean $\delta^{18}O$ of -6.83‰ and $\delta^{13}C$ of +9.65‰, while shrub samples above immature palaeosols have a mean $\delta^{18}O$ of -7.52‰ and $\delta^{13}C$ of +9.83‰. The results indicate that $\delta^{18}O$ are slightly less depleted in sequence 1, than in sequence 2. This represents a shift of -1‰ for $\delta^{18}O$.

Samples	**$\delta^{13}C$ (VPDB)‰**	**$\delta^{18}O$ (VPDB)‰**	Shrub morpho-types
QR 15	+10.15	-6.62	NDS
QR 17	+10.00	-6.80	NDS
QR 19	+9.71	-7.05	NDS
QR 20	+9.88	-6.99	NDS
QR 27H	+9.99	-7.01	NDS
QR 31V	+9.78	-7.62	NDS
QR 32V	+9.97	-7.15	NDS
QR 35V	+9.88	-7.57	NDS
QR 65H	+9.78	-7.00	NDS
QR 116H1	+10.20	-6.53	NDS
QR 134V	+9.65	-7.88	NDS
QR 135H	+9.17	-7.91	NDS
QR 137H	+10.20	-7.17	NDS
QN 20	+9.99	-7.02	NDS
CI 08	+10.01	-7.68	NDS
QR 16	+10.17	-6.81	NDS
QR 18	+10.03	-6.65	NDS
QR 34H	+9.73	-7.55	NDS
QR 34V	+9.70	-7.39	NDS
QR 35H	+9.68	-7.39	NDS
QR 135V	+9.55	-8.18	NDS
QR 31H	+9.92	-6.91	WDS
QR 37H	+9.66	-7.02	WDS
QR 38H	+10.07	-6.81	WDS
QR 25	+10.09	-6.24	FDS
QR 28	+10.03	-6.90	FDS
QR 33V	+9.76	-7.11	FDS
QR 47	+9.75	-7.12	FDS
QR 116V1	+10.15	-6.72	FDS
QR 121H2	+10.36	-6.46	FDS
QR 121H3	+10.15	-6.77	FDS
QR 133V1	+9.92	-7.37	FDS
QR 136V1	+10.04	-7.32	FDS
QR 136V2	+10.45	-7.34	FDS
QR 24	+10.26	-6.80	FDS
QR 40	+10.09	-7.11	FDS
QR 139V	+9.74	-7.68	FDS
QR 24V2	+9.86	-7.33	FDS
QR 21	+9.10	-5.90	FDS
QR 29	+9.83	-5.70	FDS
QR 33H	+10.08	-6.95	FDS

QS 15	+10.73	-5.60	FDS
QR133H2	+9.77	-7.61	ARB
QR 140V	+10.18	-6.75	ARB
QR 63H	+8.92	-7.57	ARB
QR 73H	+9.96	-7.28	ARB
CI 01	+9.87	-7.39	ARB
QR 140H1	+9.85	-7.09	ARB
QR 118V	+10.26	-6.37	ABT
QR 138V	+9.72	-7.79	ABT
QR 138H	+10.03	-7.41	ABT
QR 140H3	+10.01	-7.24	ABT
QR 117H	+10.20	-6.50	ABT
QR 134H1	+9.84	-7.82	ABT
QR 140H2	+9.82	-6.90	ABT
QS 011Base	+9.72	-6.06	PS
QR 55	+10.13	-5.72	PS
QR 52	+9.92	-6.87	PS
QR 96H	+8.71	-8.25	PS
QS 4Base	+10.47	-6.07	PS
QS 4Top	+10.02	-6.16	PS
QR 103H1	+9.68	-7.12	PS
QR 74H	+9.35	-7.13	PS
QR 103H1	+9.68	-7.12	PS
ST 66	+9.66	-6.56	PS
ST 82	+9.93	-6.55	PS
QR 68H	+9.81	-7.64	SC
ST 2	+10.38	-6.04	SC
ST 10	+10.90	-5.49	SC
ST 24	+10.16	-5.82	SC
ST 29	+10.22	-6.00	SC
ST 51	+9.61	-6.16	SC
ST 54	+10.81	-4.97	SC
ST 55	+10.40	-5.48	SC
ST 94	+9.71	-6.57	SC
ST 96	+11.32	-5.81	SC

Table 3.5: Carbon and oxygen stable isotope results for the 76 shrub morpho-type samples from Tivoli travertines. NDS - narrow dendriform shrubs; WDS - wide dendriform shrubs; FDS - fili dendriform shrubs; ARB - arborescent shrubs; ABT - arbustiform shrubs, PS - pustular shrubs; SC - shrub crust.

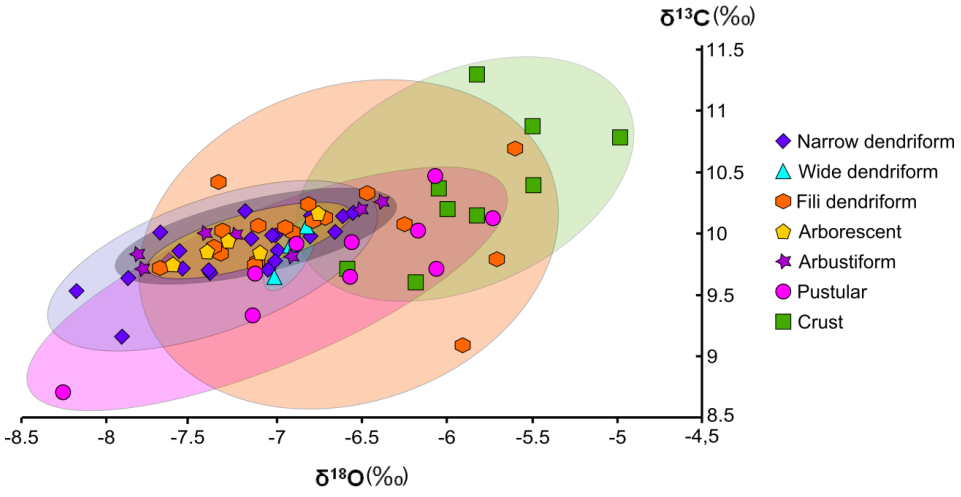

Fig. 3.6: Stable C and O isotopes plotted according to shrub morpho-types. The results illustrate that no clear isotopic differentiation exists; however, the data displays some covariance between $\delta^{13}C$ and $\delta^{18}O$.

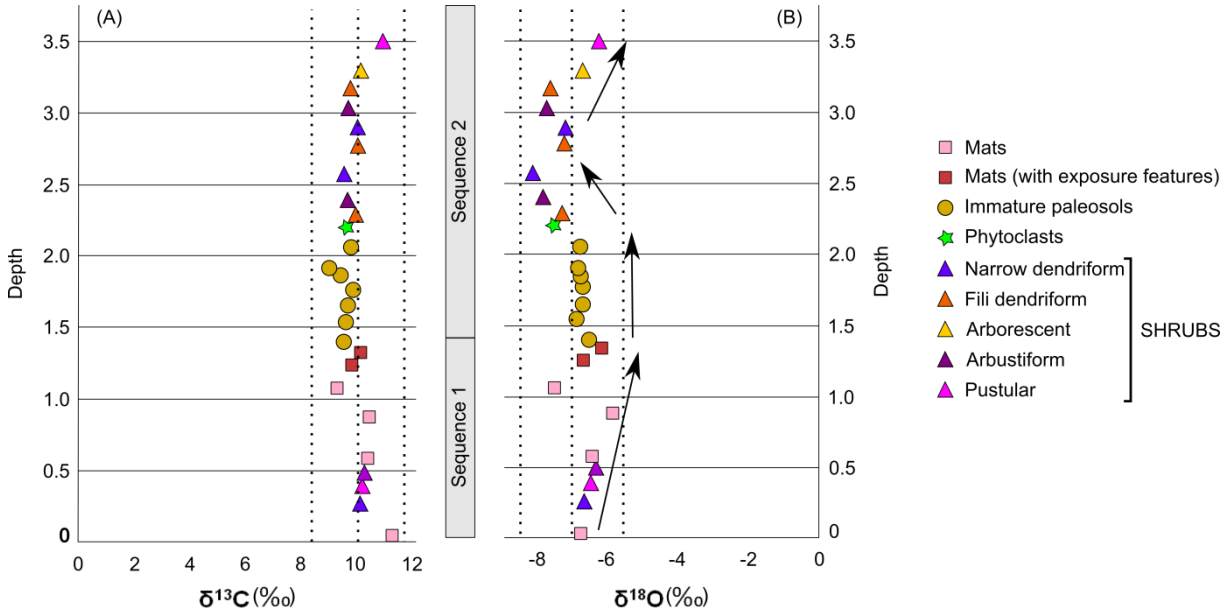

Fig. 3.7: $\delta^{13}C$ and $\delta^{18}O$ values plotted along the stratigraphic sections of sequence 1 and 2 of Querciolaie-Rinascente 1 quarry (QR1). Note that $\delta^{13}C$ stays relatively constant, while $\delta^{18}O$ are slightly less depleted in sequence 1, than in sequence 2, representing a shift of -1‰.

3.3.4.1 Microdrill analysis

From the 76 shrub samples, six representative shrub morpho-types were selected where the matrix framework of peloidal micritic aggregates and the surrounding cement phase were separately micro-drilled by using a binocular microscope and drilling micro-needle (15µm). Only Crust lithotypes were not sampled, because of the limited thickness of the cement layers. The results of the stable carbon and oxygen isotopic differences between micrite and cement can be seen in Table 3.6 and Fig. 3.8. Overall, the peloidal micritic aggregate framework possesses slightly heavier $\delta^{13}C$ and less depleted $\delta^{18}O$ signatures in comparison to the surrounding cements. The $\delta^{13}C$ values range between +8.89‰ and +10.22‰ for the peloidal micritic aggregate framework, and between +8.33‰ and +9.76‰ for the cement samples. The $\delta^{18}O$ values range between -5.51‰ and -7.52‰ for the peloidal micritic aggregate framework, and between -6.69‰ and -7.49‰ for the cement samples.

The values of $\delta^{13}C$ and $\delta^{18}O$ for the cement phases thus respectively exhibit a positive and negative shift relative to the peloidal micritic aggregate framework phases. A general depletion of the $\delta^{13}C$ values (+0.24‰ to +0.68‰) and enrichment of the $\delta^{18}O$ values (-0.05‰ to -1.27‰) is observed for the cement samples in comparison to the peloidal micritic aggregate framework samples. Only the WDS possesses the highest $\delta^{18}O$ difference values between the cement and the peloidal micritic framework. The cement sample (-6.78‰) from WDS possess more depleted $\delta^{18}O$ values than the peloidal micritic aggregate framework (-5.51‰) with isotopic difference between them of -1.27‰ (Fig. 3.8, Table 3.6). ABT samples is the only example where the micritic aggregate framework possess more depleted $\delta^{18}O$ (-7.52‰) values than the cement (-7.47‰) (Fig. 3.8, Table 3.6).

Sample number	Shrub morpho-types	Sample	$\delta^{13}C$ (‰)	$\delta^{18}O$ (‰)	$\delta^{13}C$ (‰) diferences between micrite and cement	$\delta^{18}O$ (‰) diferences between micrite and cement
QR 22	NDS	MICRITE	9.93	-6.66	0.38	-0.73
		CEMENT	9.55	-7.39		
CI 25	WDS	MICRITE	9.83	-5.51	0.59	-1.27
		CEMENT	9.24	-6.78		
QR 139V	FDS	MICRITE	10.22	-7.08	0.68	-0.41
		CEMENT	9.54	-7.4914		
QR 138H	ABT	MICRITE	10.08	-7.52	0.44	-0.05
		CEMENT	9.64	-7.47		
QR 140 H1	ARB	MICRITE	10.00	-6.79	0.24	-0.39
		CEMENT	9.76	-7.18		
ST 70	PS	MICRITE	8.89	-6.12	0.56	-0.57
		CEMENT	8.33	-6.69		

Table 3.6: Summary of the micro-drilled sample results for carbon and oxygen stable isotope analysis. In red color it is show the highest $\delta^{18}O$ difference values between the cement and the peloidal micritic framework. And in green color it is observe the only sample (ABT) where the micritic aggregate framework possess more depleted $\delta^{18}O$ values than the cement. FDS - dendriform shrub; ARB - arborescent shrub; NDS - narrow dendriform shrub; ABT - arbustiform shrub; WDS - wide dendriform shrub; PS - pustular shrub.

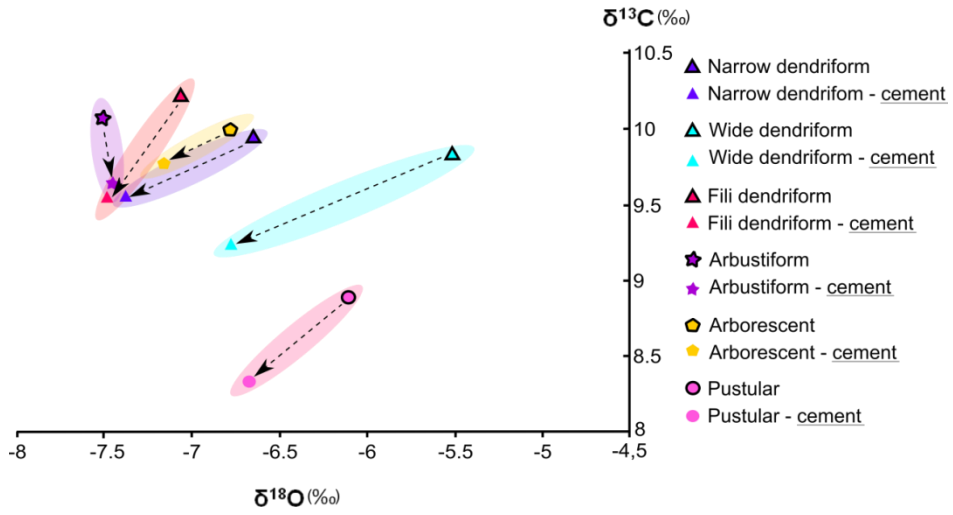

Fig. 3.8: Carbon and oxygen stable isotope values of peloidal micritic aggregates within the shrubs and sparry calcite cement covering the shrub structures.

3.3.4.2 Statistical analysis of C and O stable isotopes

Box plots of $\delta^{13}C$ and $\delta^{18}O$ in function of shrub morpho-types (Figs. 3.9A and B respectively) provide the possibility to graphically evaluate differences in the mean population for each shrub morpho-type. The first observation that calls attention is the $\delta^{13}C$ box plot of the shrub morpho-types possessing very similar results, while $\delta^{18}O$ of the shrub morpho-types possesses a more broad distribution, however, with similar mean values. Only crust samples can be differentiated from the different shrub morpho-types in both $\delta^{13}C$ and $\delta^{18}O$ box plots (Fig. 3.9). The crust $\delta^{13}C$ possesses the heaviest $\delta^{13}C$ in comparison to the shrub samples (Fig. 3.9A), and the box plot of the $\delta^{18}O$ shows that crusts possess less depleted mean values than the different shrub morpho-types (Fig. 3.9B).

ANOVA statistical analysis was applied in order to test whether shrub morpho-types can or cannot be differentiated based on their $\delta^{13}C$ and

$\delta^{18}O$ results (Tables 3.7 and 3.8). The variability calculations (Tables 3.7 and 3.8) are based on the differences among the column means (intergroup variability) and differences between the data in each column and the column mean (intragroup variability). The ANOVA table lists the source of variability, the Sum of Squares (SS), degree of freedom (df) and the Mean Squares (SS/df) for each source. The F-statistics is calculated as the ratio of the mean squares. For p-values below a pre-defined value of 0.05 (Sheskin, 2004), the null hypothesis (H_0) can be rejected. The null hypothesis involves computing a particular ratio of variability in the group means to variability among replicates within each group. ANOVA tests the non-specific null hypothesis (H_0) that the different shrub morpho-types means are equal, and only crusts are statistically different.

Given that the null hypothesis is rejected when at least one group mean is significantly different from the others, a multicomparison test had to prove whether all 7 (related-)shrub morpho-types have statistically different means. The results also indicate that $\delta^{13}C$ and $\delta^{18}O$ for the different shrub morpho-types are not significantly different, but crusts are (Fig. 3.10).

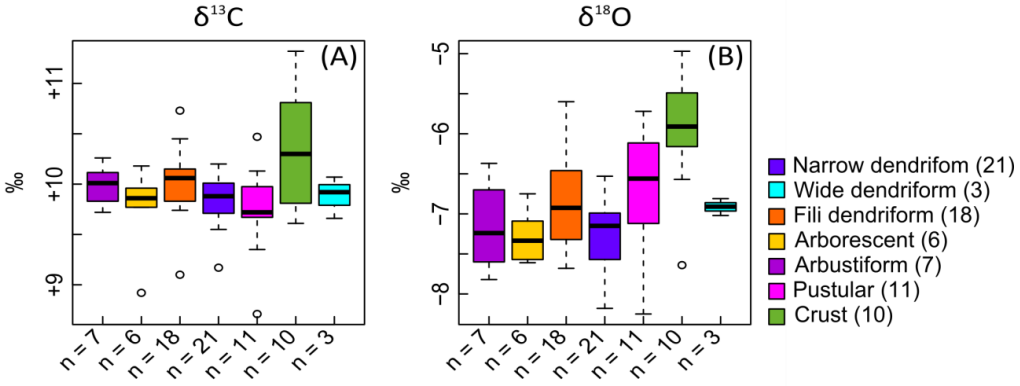

Fig. 3.9: (A) Box plots of carbon stable isotope signatures per shrub morpho-type. (B) Box plots of oxygen stable isotope signature per shrub morpho-types. N = number of samples.

	SS	df	SS/df	F	P
Groups	20.41	6	2.07	6.28	0.05
Error	22.75	69	0.33		
Total	43.15	75			

Table 3.7: ANOVA table for $\delta^{18}O$ and shrub morpho-types

	SS	df	SS/df	F	P
Groups	3.88	6	0.39	2.89	0.05
Error	9.38	69	0.14		
Total	13.25	75	0.53		

Table 3.8: ANOVA table for $\delta^{13}C$ and shrub morpho-types

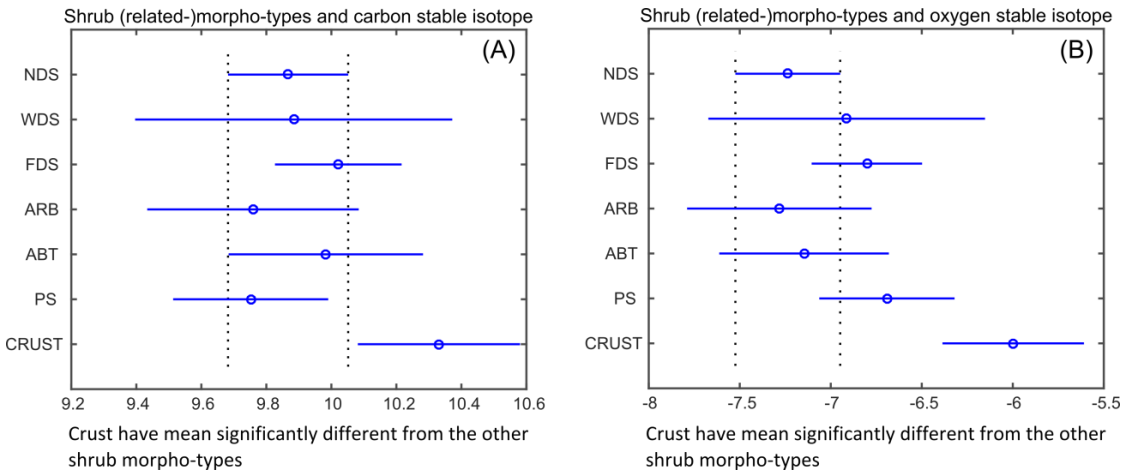

Fig. 3.10: Multicomparison test graphs for (A) shrub (related-) morpho-types for δ^{13}C-values and (B) shrub (related-) morpho-types for δ^{18}O-values of travertine samples from Tivoli. NDS - narrow dendriform shrub; WDS - wide dendriform shrub; FDS - fili dendriform shrub; ABT – arbustiform shrub; ARB – arborescent shrub; PS – pustular shrub.

3.4 Discussion

3.4.1 Strontium isotopes

The Sr isotopic signatures of the travertines reflect the isotopic composition of their precipitating fluids (El Desouky et al., 2015; Claes et al., 2015). In travertine, a uniform Sr isotopic signature reflects uniform characteristics of the precipitating fluids which often can be linked to the signature of the parental fluids. The latter may relate to dissolved parent carbonate sources (Minissale et al., 2002; El Desouky et al., 2015; Claes et al., 2015). Therefore, the strontium isotope results were compared with the Sr seawater curve of McArthur and Howard (2004) (Fig. 3.11) and other relevant literature. The $^{87}Sr/^{86}Sr$ ratio of ~ 0.708 found in the Tivoli shrubs are identical to the $^{87}Sr/^{86}Sr$ ratios of Mesozoic carbonate formations in Central Italy reported by several authors (e.g. Minissale and Duchi, 1988; Minissale et al., 2002; Minissale, 2004). According to Minissale and Duchi (1988) this Mesozoic carbonate sequence constitutes the main geothermal reservoir in north-central Italy.

Barbieri et al. (1979) pointed out that the basal Triassic anhydrite unit ("Burano" Formation) contains considerably more Sr than the Mesozoic limestone unit. This suggests, in addition that the concentration of Sr and S, which are soluble in water (at relatively low temperature), is related to the source groundwaters deeply circulating within the Triassic anhydrite and Mesozoic limestone.

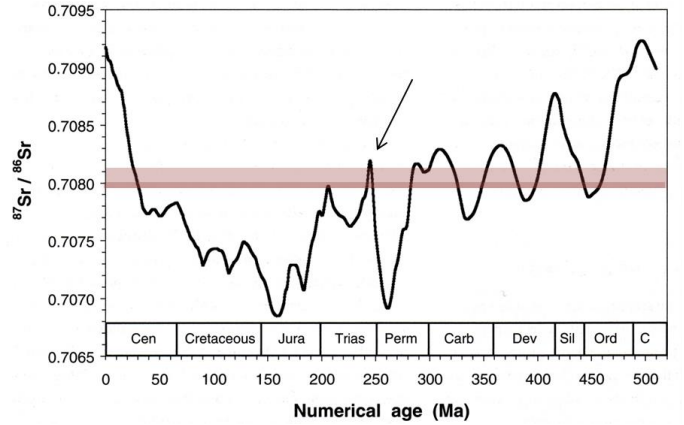

Fig. 3.11: Range of $^{87}Sr/^{86}Sr$ ratios of the shrub travertine samples plotted together with the marine Sr-isotopic sea water curve of McArthur and Howarth (2004). The red band indicates the samples. The darker colored red line represents the mode of the samples.

3.4.2 Element Analysis

Six main element groups can be distinguished within the Tivoli shrub samples, i.e. Group I with Ba, K, and Sr, Group II with Mg, Na and S, and Group III with Ca, are related to the carbonate fraction of the sample, while Group IV containing Mn and P, Group V with Al, and Group VI with Fe, can be related to the non-carbonate fraction (Salminen et al., 2006). Certain elements can be incorporated in different sites in the carbonates (Fairchild and Treble, 2009). Group I and II are ions that substitute for Ca^{2+} (Mg^{2+}, Sr^{2+} and Ba^{2+}) or CO_3^{2-} (SO_4^{2-}) in the $CaCO_3$ matrix. These elements can also be attributed to the presence of trace concentrations of dolomite ($CaMg(CO_3)_2$), gypsum ($CaSO_4.2(H_2O)$)/anhydrite ($CaSO_4$), celestite ($Sr,Ba(SO_4)$) and barite ($Ba,Sr(SO_4)$), as observed in QEMSCAN analysis. Besides, one of the sources of Mg is attributed to the low-Mg calcite that comprises the travertines from Tivoli. Mg-clays were also identified in QEMSCAN analysis, which thus are another source of Mg. This mineral may be of authigenic origin, likely microbial mediated since they occur in association with residue of organic matter. It is important to keep in mind that all the minerals described above and organic matter corresponds to less than 1% of the rock in the analyzed area.

The presence of the element Ca^{2+} relates to fluids percolating, through the Mesozoic carbonates. Minissale and Duchi (1988), Minissale et al. (2002) and Minissale (2004) pointed out that the fluids arise towards the basin and mix with meteoric-derived water infiltrated from the surrounding mountains (Lucretili, Tiburtini and Cornicolani). The mixed fluids dissolve the carbonate rocks and became enriched in HCO_3^-. Moreover, deep fluid circulation occurred along local faults and is driven by topography and due to convective circulation of hot fluids produced by the cooling magmatic intrusions (Minissale et al., 2002). Additionally, the high concentrations of Sr, S, Na, Mg, and traces of Ba and K (corresponding to Group I and II) indicate that the circulating fluids interacted also with Triassic evaporites (Teboul et al., 2016).

Potassium and sodium often occur in clays. In Figs. 3.4 and 3.5 it was demonstrated that Potassium occurs associated with micas and K-Feldspar. However, it may also relate to the carbonate phase, where Na^+ is usually located at the interstitial sites in the crystal lattice (Fairchild and Treblle, 2009). Its incorporation differs as a function of precipitation rate and associated crystal growth. It is likely that they are common in the fluid source rocks e.g. that it is derived from the evaporites.

The barium versus strontium (Fig. 3.12) cross-plot illustrates a positive trend. Similar concentration ranges was obtained by Teboul et al. (2016) for hypogean travertines associated with limestone, evaporite and dolomite as source rocks. The behavior of strontium during carbonate precipitation in travertine systems is relatively well constrained (Teboul et al., 2016). According to Turi (1986) the strontium content in calcitic or aragonitic travertine is directly linked to the availability of the element in the waters. Pentecost (2005) pointed to higher strontium content near the spring vents. Actually, syn- to post-precipitation partitioning of strontium is responsible for differences in the strontium content in the carbonates (Teboul et al., 2016).

The non-carbonate related elements occur in Group IV with Mn and P, Group V with Al, and Group VI with Fe (Salminen et al., 2006). The very low amounts of non-carbonate elements could be associated with a minor influx of detrital particles by surface run-off, taking into account that travertine formation occurs at the surface.

Both Mn and Fe may be mobile under phreatic anoxic conditions. The QEMSCAN analysis also indicate the presence of Fe as trace mineral as pyrite (FeS_2), however the latter mineral is really too low in percentage.

In order to assess the origin of the element Al that can be related with clays or other non-carbonate minerals, the latter have been cross-plotted with Sr, Ba and Fe (Fig. 3.13A to C). However, no positive correlation is observed. The elemental concentration of purely detrital origin should have a regression coefficient close to 1 and should intersect the y-axis close to its origin (Claes, 2015). Nevertheless, a purely carbonate related fraction, should remain a constant percentage of Calcium independent of

the Aluminium concentration, or show a negative correlation due to closure effect (Fig. 3.13D). The evidence of non-carbonate fraction is observed in the QEMSCAN analysis where trace minerals of anorthite ($CaAl_2Si_2O_8$), K-feldspar ($KAlSi_3O_8$), micas ($K_x,Al_2[Si_{4-x}Al_xO_{10}](OH)_2$), albite ($NaAlSi_3O_8$) indicate the presence of non-carbonate fraction rich in aluminium.

QEMSCAN analysis brings insights of the less than 1 % mineralogies present in the sample. This allows to understand how individual elements are related to each other. These mineralogical characterizations also help to interpret the detrital versus authigenic origin of these traces. For example, the presence of quartz (SiO_2), micas ($K_x,Al_2[Si_{4-x}Al_xO_{10}](OH)_2$), K-feldspar ($KAlSi_3O_8$) and albite ($NaAlSi_3O_8$) suggests a detrital origin of these minerals (e.g. Fig. 3.4, area 2), whereas the presence of Barite ($Ba,Sr(SO_4)$), Celestite ($Sr,Ba(SO_4)$), or Pyrite (FeS_2) is more likely authigenic in origin.

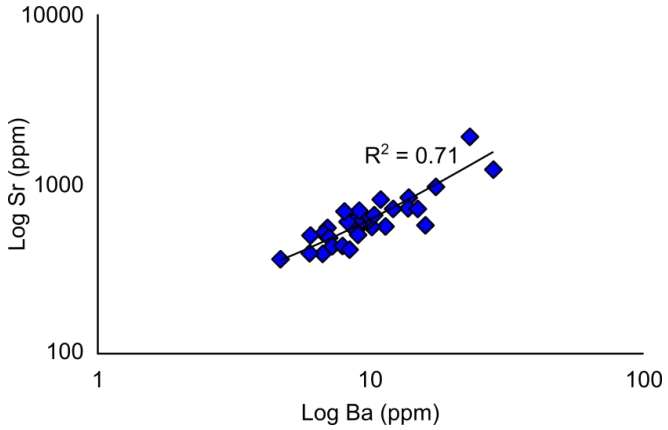

Fig. 3.12: Combined barium (ppm) and strontium (ppm) logarithmic plot for the 36 shrub samples from Tivoli.

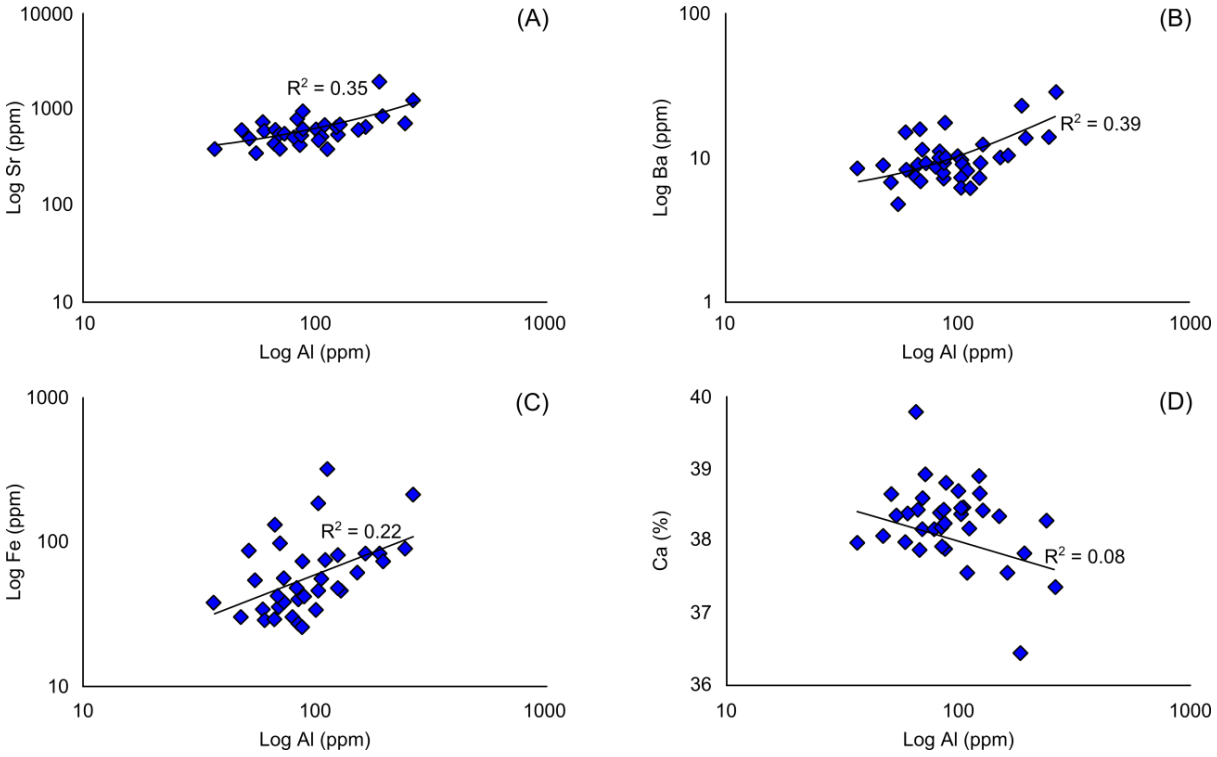

Fig. 3.13: Combined logarithmic plot of (A) strontium (ppm) versus aluminium (ppm), (B) barium (ppm) versus aluminium (ppm), (C) iron (ppm) versus aluminium (ppm), and Ca (%) versus aluminium (ppm).

3.4.3 C and O stable isotopes

$\delta^{13}C$ and $\delta^{18}O$ compositions of travertines provide insight into the origin (sources) of carbon and the precipitation conditions (Gonfiantini et al., 1968; Friedman, 1970; Panichi and Tongiorgi, 1976; Guo et al., 1996; Minissale et al., 2002). The $\delta^{13}C$ compositions reflect the source of the carbon species in groundwater, while $\delta^{18}O$ reflects the isotopic composition of local meteoric water that recharges groundwater, and the temperature of calcite precipitation. Isotopic equilibrium in the system is disrupted by rapid CO_2 degassing, being the system re-equilibrated under surface conditions as the rate of CO_2 loss decreases with distance from the spring. Evaporation processes also occur favored by the cooling of the water exposure to air. Chafetz et al. (1991) and Chafetz and Lawrence (1994) demonstrated that $\delta^{13}C$ composition of warm spring travertine-depositing waters can vary by > 2‰ over a period of days.

A covariant trend is observed in the graph $\delta^{13}C$ versus $\delta^{18}O$ (Fig. 3.6). Similar results were observed by Gonfiantini et al. (1968) and Guo et al. (1996) for the travertines from Rapolano Terme. A cursory glance at the Tivoli data, without considering the fabric of the samples, points towards an interpretation similar to that of the former authors. The $\delta^{13}C$ trend indicates a progressive influence of vigorous CO_2 degassing and evaporation. The progressive larger $\delta^{18}O$ values could be explained by the combined effects of calcite precipitation at cooler temperatures and greater influence of evaporation (Craig et al., 1963; Guo et al., 1996; Fouke et al., 2000; Kele et al., 2011).

If the bulk $\delta^{18}O$ data are plotted versus depth (Fig. 3.7) an increasingly negative $\delta^{18}O$-trend toward sequence 2 can be seen. This could be interpreted as a seasonal warming of the stream waters (Brasier et al., 2011) or due to interaction with groundwater/run-off water of different isotopic composition and/or temperature (Allan and Matthews, 1982). However, the $\delta^{13}C$ signature versus depth do not vary much, with sequence 1 being slightly heavier (mean +10.18‰) than sequence 2 (mean +9.83‰). In this case, it is more likely that a buffering effect occurred, where the C isotope signature stays relatively homogeneous due to a continuous re-equilibrium with new fluids (Brasier et al., 2011).

Shrub morpho-types (i.e. NDS, WDS, FDS, ARB, ABT and PS) cannot be isotopically differentiated, because they possess very similar $\delta^{13}C$ and $\delta^{18}O$ signatures. This indicates that shrub morpho-types were precipitated in very similar water conditions. Only the crust lithotype can be isotopically distinguished from the shrub morpho-types, because they possess the highest $\delta^{13}C$ and lowest $\delta^{18}O$ data. Indicating that the latter precipitated over more vigorous CO_2 degassing conditions in comparison with the shrub morpho-types.

A question to be addressed is whether the $\delta^{18}O$ and $\delta^{13}C$ signatures correspond to the original one, and thus, has not been reset as may occur during diagenesis (Guo et al., 1996; Fouke et al., 2000, Fouke, 2001; Minissale et al., 2002). The micro-analysis performed on the peloidal micritic aggregate framework and the surrounding sparry calcite cements show that the micritic framework possesses a slightly heavier $\delta^{13}C$ and a less depleted $\delta^{18}O$ signature than the cement, with differences smaller than 1‰ for both $\delta^{13}C$ and $\delta^{18}O$. Janssen et al. (1999) observed a similar magnitude of diagenetic shift in stable isotopic signature comparing recent and fossil tufa deposits. Under equilibrium condition, 1‰ fall in $\delta^{18}O$ corresponds to a difference of 4.5°C (Pentecost, 2005). Taking into account the latter value, the differences between the micritic framework and the cement from Tivoli samples varies between 0.2 and 5.7°C. These results indicate that the water which precipitated the cement was slightly warmer in temperature than the water that precipitated the micrite.

According to Brasier et al. (2011), dissolution and re-precipitation of calcite in relation to fluids with different composition and/or temperature, would also lead to an alteration of the $\delta^{18}O$ values. Allan and Matthews (1982) reported that $\delta^{18}O$ is more readily altered during meteoric diagenesis. Furthermore, $\delta^{18}O$ values tend to homogenize because meteoric water is a ubiquitous source of oxygen for the formation of new calcite during the recrystallization process (Allan and Matthews, 1982). The primary signal in $\delta^{13}C$ would have a better chance to be preserved due to buffering potential of carbon (Brasier et al., 2011). It means that the

preservation of the carbon stable isotope signature can be a result of a continuous re-equilibrium with new fluids reflecting syn-depositional conditions and diagenetic resetting can be relatively small (Brasier et al., 2011, 2013; Claes et al., 2016).

The cements observed under CL analysis show color variations in luminescence (yellowish-reddish zonations), while the peloidal micritic aggregates display a dull luminescence (see Fig. 2.15B, Chapter 2), indicating no or very minor recrystallization, but do represent changes in the redox conditions of the fluids precipitating the cements (Amieux et al., 1989). Dull luminescence is believed to be the intrinsic color of the carbonate (Giraud et al., 1968), but can also represent an oxidizing phreatic travertine environment. The alternation of yellowish-reddish zones suggest successive input of Mn^{2+} that could represent the mixing of continental fresh water and travertine water in a more reducing environment (Amieux et al., 1989; Mettraux et al., 2014).

The stable isotopes of these cements do show a very small shift to slightly lighter values (< 1‰) in comparison with the peloidal micrite, which supports the interpretation of the mixing influence with continental fresh water. However, this C and O isotope shift of < 1‰ between rock framework and cement, besides the CL petrography indicating no recrystallization, leads to the interpretation that the fluid precipitating the cement did not varied much from the fluid which precipitated the peloidal micritic aggregate framework. In this case, it is very likely that diagenetic resetting was indeed relatively small. The more depleted mean oxygen isotopic signatures of the cement phases is likely related to higher temperatures of the precipitating fluids or to a change in the original oxygen isotopic signature of the fluid.

Moreover, a purely surface meteoric water origin for the travertine fluids can be excluded based on the strontium isotope ratio data, which point to a fluid that interacted at depth with Mesozoic carbonates and evaporites. Therefore, a topographically-driven fluid flow, related to infiltration of rain water along the basin-surrounding mountains, and resurfacing along local normal faults, being further mixed with surface waters cannot be excluded.

3.4.3.1 CO_2 origin

According to Panichi and Tongiorgi (1976) the $\delta^{13}C$ composition of fossil travertine may reveal the source(s) of CO_2 (e.g. magmatic, geothermal, metamorphic or organic). However, isotopic fractionation during water transfer to the surface and travertine deposition must be taken into account (Minissale et al., 2002). So, depending on the main source of CO_2 and the processes that influence fractionation, the $\delta^{13}C$ signature of travertine may differ.

Fritz (1965) demonstrated that the $^{13}C/^{12}C$ ratio of some Italian travertines depends on the $^{13}C/^{12}C$ ratio of the dissolved CO_2, which in turn reflects the CO_2 source. Gonfiantini et al. (1968) concluded that the deposition of travertine from water springs emerging at temperatures much higher than ambient temperatures will result in isotopic disequilibrium, whereas equilibrium conditions tend to be approached as the distance from the spring vent increases and the water cools.

According to Kele et al. (2011), excluding fractionation processes during precipitation, the $\delta^{13}C$ in travertine deposits is mainly affected by 1) $\delta^{13}C$ of the primary carbonate (i.e. the parent rock of the travertine) dissolved in the parent water, and 2) $\delta^{13}C$ value of various CO_2 sources dissolved in the parent water of the travertine rock. Therefore, $\delta^{13}C$ can be used to determine the origin of CO_2.

The Tivoli shrub travertine carbon isotope data show high values (from +8.71‰ to +11.32‰, with an average of +9.89‰). Manfra et al. (1976) reported $\delta^{13}C$ values varying between +5.8‰ and +12.6‰. One of the frequently applied approaches used to determine the origin of CO_2 makes use of the Panichi and Tongiorgi (1976) empirical equation (3.2), which recalculates the original $\delta^{13}C_{CO2}$ values of the precipitating waters based on the measured $\delta^{13}C$ values in fossil travertine deposits (Table 3.9).

$$\delta^{13}C_{CO2} = 1.2 \times \delta^{13}C_{trav} - 10.5 \qquad (3.2)$$

For the studied travertines, the re-calculated $\delta^{13}C_{CO2}$ values varies from -0.04‰ and +2.06‰, with an average of + 1.37‰ (Table 3.9). These results were compared to the signature of the possible contributing sources (Fig. 3.14 modified from Claes et al., 2015). The Mesozoic carbonate rocks, indicated as the main source

rock by Sr isotope results, have water reservoir temperatures higher than 200°C in buried structural highs at 500-1500 m depths (Minissale and Duchi, 1988; Minissale et al., 2002). The carbon isotopic fractionation for temperatures above 200°C is between -1 and +2‰ (Rollinson, 1993). This is in accordance with Rollinson (1993) and Minissale (2004) who have reported that the main source of CO_2 in the Tivoli area relates to the metamorphism of Mesozoic limestones triggered by the presence of very shallow magmatic intrusions in the underlying crust. Even taking fractionation processes at the surface into account, only thermo-decarbonatation of carbonate rocks would lead to such high values.

However, it is not possible to affirm that all CO_2 exclusive came, from thermo-decarbonatation of the marine source carbonates. Other contributing sources with slightly lower $\delta^{13}C$-signatures have also been reported, such as mantle-derived CO_2 (Minissale et al., 2002). Furthermore, the empirical based equation of Panichi and Tongiorgi (1976) probably did not fully account for the strong fractionation processes during precipitation in Tivoli. Rarely, precipitation happens under isotopic equilibrium (Fouke et al., 2000; Kele et al., 2011, 2015). Furthermore, Friedman (1970) pointed out that the kinetic non-equilibrium factors are strongly dependent on spring temperatures, water cooling-rate, and morphology of flow paths, travertine precipitation rates, microbial activity, evaporation and CO_2 degassing rates. Besides, additional isotopic fractionation processes may occur during compaction and diagenesis (Manfra et al., 1974). Equilibrium conditions, especially for $\delta^{18}O$, tend to be reached as the distance from the spring vent increases and the water cools down (Gonfiantini et al., 1968; Kele et al., 2015), but $\delta^{13}C$-values tends to increase due to progressive escape of light CO_2, by i.e. degassing, evaporation, microbial activity and temperature effect (Panichi and Tongiorgi, 1976).

Sample	$\delta^{18}O$ (VPDB)‰	$\delta^{13}C$ (VPDB)‰	Original $\delta^{13}C_{CO2}$	Kele et al., 2015 (°C)	Kim and O'Neil, 1997 (°C)
NARROW DENDRIFORM SHRUB					
QR 15	-6.62	+10.15	+1.69	24.48	10.26
QR 16	-6.81	+10.17	+1.70	25.35	11.14
QR 17	-6.80	+10.00	+1.49	25.28	11.07
QR 18	-6.65	+10.03	+1.54	24.61	10.39
QR 19	-7.05	+9.71	+1.15	26.41	12.20
QR 20	-6.99	+9.88	+1.35	26.18	11.97
QR 27H	-7.01	+9.99	+1.49	26.23	12.02
QR 31V	-7.62	+9.78	+1.24	29.04	14.85
QR 32V	-7.15	+9.97	+1.46	26.87	12.67
QR 33V	-7.11	+9.76	+1.22	26.68	12.47
QR 34V	-7.39	+9.70	+1.14	27.99	13.79
QR 34H	-7.55	+9.73	+1.18	28.68	14.49
QR 35V	-7.57	+9.88	+1.35	28.80	14.61
QR 35H	-7.39	+9.68	+1.11	27.95	13.76
QR 65H	-7.00	+9.78	+1.24	26.19	11.99
QR 116H1	-6.53	+10.20	+1.74	24.10	9.88
QR 134V	-7.88	+9.65	+1.08	30.20	16.03
QR 135V	-8.18	+9.55	+0.96	31.63	17.46
QR 135H	-7.91	+9.17	+0.50	30.35	16.17
QN 20	-7.02	+9.99	+1.49	26.30	12.09
CI-08	-7.68	+10.01	+1.51	29.32	15.13

WIDE DENDRIFORM SHRUB					
QR 31H	-6.91	+9.92	+1.40	25.78	11.57
QR 37H	-7.02	+9.66	+1.09	26.28	12.07
QR 38H	-6.81	+10.07	+1.59	25.36	11.14
FILI DENDRIFORM SHRUB					
QR 21	-5.90	+9.10	+0.42	21.34	7.11
QR 24V1	-6.80	+10.26	+1.81	25.32	11.11
QR 24V2	-7.33	+9.86	+1.34	27.70	13.50
QR 25	-6.24	+10.09	+1.61	22.83	8.61
QR 28	-6.90	+10.03	+1.53	25.77	11.56
QR 29	-5.70	+9.83	+1.29	20.46	6.22
QR 33H	-6.95	+10.08	+1.59	25.97	11.76
QR 40	-7.11	+10.09	+1.61	26.69	12.48
QR 47	-7.12	+9.75	+1.20	26.75	12.55
QR 116V1	-6.72	+10.15	+1.67	24.94	10.73
QR 121H2	-6.46	+10.36	+1.93	23.79	9.56
QR 121H3	-6.77	+10.15	+1.68	25.17	10.95
QR 133V1	-7.37	+9.92	+1.40	27.86	13.66
QR 136V1	-7.32	+10.04	+1.55	27.65	13.45
QR 136V2	-7.34	+10.46	+2.03	27.74	13.55
QR 137H	-7.17	+10.20	+1.74	26.99	12.78
QR 139V	-7.68	+9.74	+1.19	29.30	15.11
QS 15	-5.60	+10.73	+1.37	20.02	5.78
ARBUSTIFORM SHRUB					
QR 117H	-6.50	+10.20	+1.74	23.95	9.73
QR 118V	-6.37	+10.26	+1.81	23.41	9.18
QR-134H1	-7.82	+9.84	+1.31	29.93	15.75
QR 138V	-7.79	+9.72	+1.16	29.79	15.61
QR 138H	-7.41	+10.03	+1.53	28.07	13.88
QR 140H2	-6.90	+9.82	+1.29	25.74	11.53
QR 140H3	-7.24	+10.01	+1.51	27.29	13.09
ARBORESCENT SHRUB					
QR 63H	-7.57	+8.92	+0.21	28.80	14.61
QR 68H	-7.64	+9.80	+1.36	29.13	14.94
QR 73H	-7.28	+9.96	+1.45	27.46	13.26
QR 133H2	-7.61	+9.77	+1.22	28.98	14.80
QR 140V	-6.75	+10.18	+1.72	25.08	10.87
QR 140H1	-7.09	+9.85	+1.32	26.62	12.42
CI 01	-7.39	+9.87	+1.39	27.97	13.77
PUSTULAR SHRUB					
QR 52	-6.87	+9.92	+1.40	25.64	11.42
QR 55	-5.72	+10.13	+1.66	20.53	6.29
QR 74H	-7.13	+9.35	+1.36	26.78	12.58
QR 96H	-8.25	+8.71	-0.05	31.96	17.79
QR 103H1	-7.12	+9.68	+1.37	26.74	12.53

QS 4B	-6.07	+10.47	+2.07	22.06	7.83
QS 4T	-6.16	+10.02	+1.12	22.46	8.23
QS 11B	-6.06	+9.72	+1.16	22.02	7.78
SHRUB CRUST					
ST 2	-6.04	+10.38	+1.36	21.93	7.70
ST 10	-5.49	+10.90	+1.36	19.55	5.31
ST 24	-5.82	+10.16	+1.36	20.96	6.72
ST 29	-6.00	+10.22	+1.36	21.74	7.51
ST 51	-6.16	+9.61	+1.36	22.48	8.25
ST 54	-4.97	+10.81	+1.36	17.34	3.09
ST 55	-5.48	+10.40	+1.37	19.49	5.25
ST 66	-6.56	+9.66	+1.37	24.25	10.03
ST 82	-6.55	+9.93	+1.36	24.17	9.95
ST 94	-6.57	+9.71	+1.36	24.27	10.05
ST 96	-5.81	+11.32	+1.35	20.94	6.70

Table 3.9: Stable carbon and oxygen isotopes values for different shrub morpho-types from the Tivoli area. Temperature calculations for $\delta^{18}O$ for equilibrium conditions, based on the equation of Kim and O'Neil (1997), and disequilibrium calcite fractionation calculated by the equation of Kele et al. (2015) are given in °C. Results of the original $\delta^{13}C_{CO2}$ are based on the equation of Panichi and Tongiorgi (1976). The abbreviations QR corresponds to Querciolaie-Rinascente quarry, QS to Querciolaie-Rinascente South quarry, QN to Querciolaie-Rinascente North quarry, CI to CIMEP quarry and ST to Straba quarry.

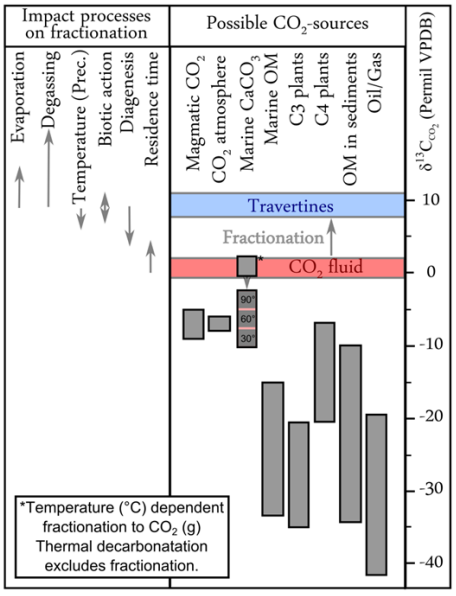

Fig. 3.14: Graph comprising main carbon dioxide sources and processes that influence the $\delta^{13}C$ signature of travertine (modified from Claes et al., 2015). The CO_2 fluid values obtained by the equation of Panichi and Tongiorgi (1976) are indicated by the red bar. The measured $\delta^{13}C$ range from the shrub travertine samples of Tivoli are indicated by the blue bar. The processes influencing the fractionation of the fluid are mentioned on the left side of the graph. Notice that the arrows indicating the impact of each of the processes on the fractionation are not to scale.

The very high $\delta^{13}C$ observed for Tivoli shrubs and crusts can be easily differentiated from other travertine $\delta^{13}C$ results (i.e. Turkish and Hungarian travertines) (Fig. 3.15). Fouke et al. (2000) studied the water and travertine deposits from Angel Terrace hot spring system (Yellowstone National Park, U.S.A.). They addressed the effect of photosynthesis, causing the preferential removal of $^{12}CO_2$ from the water, thus increasing $\delta^{13}C$ values. Guo et al. (1996) also demonstrated that shrub samples that display clear microbial involvement, causes $\delta^{13}C$ variations of at least 1‰ to 6‰. Therefore, microbial influenced calcites have anomalous $\delta^{13}C$ values that may have been caused by photosynthetic effects (Guo et al., 1996). The latter authors also concluded that with increasing distance from the spring, microbial activity has a progressively enhanced role on the isotopic composition of the precipitating travertines compared to degassing of ^{13}C-depleted CO_2.

The shrub morpho-types from Tivoli present reminiscence of filaments and bacterial bodies (see Figs. 2.5H to 2.5L in Chapter 2). Since these calcites formed under stagnant to moderate water flow, reaching even stagnancy (Erthal et al., 2017), it is likely that the effects of

photosynthetic microbes preferentially extracting $^{12}CO_2$ from the water, enriching the environment in $^{13}CO_2$ dominated. So, the very high $\delta^{13}C$ values encountered for the shrub morpho-types and also crusts can be attributed not only by abiotic (CO_2 degassing and evaporation), largely inducing disequilibrium effects, but also have been caused by photosynthetic interferences.

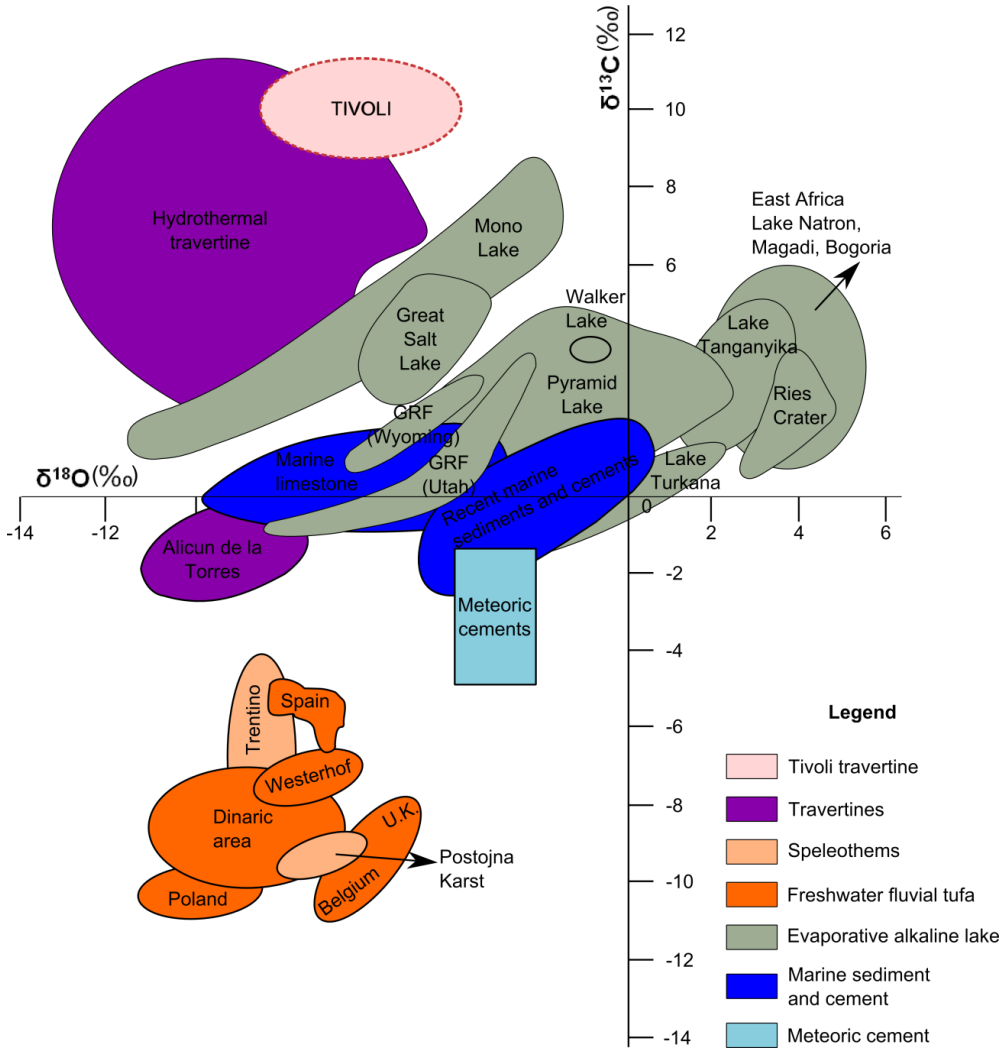

Fig. 3.15: Plots of $\delta^{18}O$ and $\delta^{13}C$ of non-marine carbonates (modified from Gandin and Capezzuoli, 2008; Kele et al., 2011; Della Porta, 2015) and Tivoli results. Notice that Tivoli carbonates present the heaviest $\delta^{13}C$ results in comparison with other travertines and non-marine carbonates.

3.4.3.2 Isotope temperature calculations

Table 3.9 summarizes the temperatures calculated from the $\delta^{18}O_{PBD}$-values of the shrubs. For equilibrium precipitation, the temperature of precipitation can be determined by means of the equation of Kim and O'Neil (1997) (Equation 3.3). For disequilibrium calcite fractionation, the formula from Kele et al. (2015) (Equation 3.4) can be used

$$1000\ln\alpha_{calcite\text{-}water} = 18.03(10^3/T) - 32.42 \quad (3.3)$$

$$1000\ln\alpha_{calcite\text{-}water} = (20 \pm 2) \times 1000/T - (36 \pm 7) \quad (3.4)$$

Where α is the fractionation factor and T is the temperature. The results for the equilibrium fractionation equation (3.3) show that the water temperatures varied from 3.1°C to 17.8°C with an average of 11.1°C. The disequilibrium fractionation equation (3.4) gives values between 17.3°C to 31.9°C with an average of 25.6°C. Water temperature below 30°C normally induces calcite precipitation, while temperatures above 30°C are referred for aragonitic crystallization (Friedman, 1970; Folk, 1994; Fouke et al., 2000).

Due to the fact that isotopic equilibrium rarely occurs during calcite precipitation in continental carbonate settings (Fouke et al., 2000; Kele et al., 2011, 2015; Claes et al., 2015), it is more likely that the equation of Kele et al. (2015) gives more realistic results.

The results suggest temperature fluctuations that can be caused by water cooling with distance from the vent, by evaporation, and by involvement of waters of different origins. However, no main feeder system was observed in the Tivoli quarry area. This leads to the idea that the main springs were located outside of the quarried area.

3.5 Conclusions

The geochemical analysis, stable and radiogenic isotopes (oxygen, carbon and strontium respectively) besides major and minor/trace element analysis was useful to comprehend the genesis and processes that promote carbonate precipitation, depositional water temperatures, CO_2—origin and source rocks of the fluids. Besides, QEMSCAN analyses bring insights of the less than 1% mineralogies present in the sample, allowing the understanding how individual elements are related each other and supporting the interpretation of the detrital versus authigenic origin of these traces.

Shrub morpho-types do not show a geochemical distinction between them. However, crust can be geochemically differentiated from the shrub morpho-types. The stable C and O isotope results of the shrub morpho-types indicate that precipitation was mainly influenced by degassing and evaporation processes. Besides, the range of $\delta^{13}C$ and $\delta^{18}O$ of the different shrub morpho-types are overlapping. These results indicate a similar physico-chemical setting for the precipitation of the shrubs. This is in agreement with a very flat waterlogged depositional setting that was formerly proposed (Chapter 2) for the Tivoli shrubs. The crusts possess different $\delta^{13}C$ and $\delta^{18}O$ values with heavier carbon and lighter oxygen signature, indicating the predominance of CO_2 degassing over other processes. The high C stable isotope signature and the micritic peloidal aggregate fabric observed for most of the shrub morpho-types suggest that microbes mediated also carbonate precipitation. Sr isotope signatures indicate that Mesozoic limestones of Central Italy served as the main source rock. However, element analysis, with high concentrations of Sr, S, Na and traces of Ba, support the interpretation that the fluids also percolated through Triassic evaporites. Besides, the re-calculated $\delta^{13}C_{CO2}$ values indicate that the main source of CO_2 in the Tivoli area is related to thermo-metamorphic decarbonatation of the Mesozoic carbonate rocks. Temperatures of the water that precipitated the shrubs and crusts were calculated from the $\delta^{18}O_{PDB}$-signatures, assuming disequilibrium fractionation. They plot in a range of 17.3°C to 31.9°C (with average of 25.6°C).

CHAPTER 4 The influence of depositional textures and 3D shapes in the reservoir characterization of a shrub morpho-types – Tivoli case study (Central Italy)

4.1 Introduction

Data on the petrophysical properties of travertine rocks are scarce in literature. However, some publications have been reported on this topic recently (e.g. Chafetz, 2013; Claes et al., 2015; Soete et al., 2015; Ronchi and Cruciani, 2015; Claes et al., 2017). Travertines dominated by shrub-like features, that constitute one of the most abundant lithotypes in Tivoli (central Italy), are also described from the rift-sag continental carbonates that are part of the intensively explored Pre-Salt succession (Dias, 1998; Terra et al., 2009; Wright, 2012; Rezende and Pope, 2015; Saller et al., 2016). Tivoli shrubs display petrographic features and pore-morphologies remarkably similar to the Brazilian Pre-Salt reservoir rocks. These shrub-dominated morpho-types are mainly characterized by dendritic or arborescent morphologies of grey-dark micrite aggregates, easily recognizable under transmitted light microscopy. The latter are often surrounded by sub-euhedral rhombic spar-calcite.

In this study, porosity has been categorized by using the classic scheme established by Choquette and Pray (1970). A special remark relates to the dominance of growth framework porosity that in marine carbonate is normally associated by elongated-vertical growth-framework reef structures. However, in the studied carbonates this porosity type, giving rise to a high pore network connectivity, relates to the shrub 3D arrangement. They display a variety of textures (e.g. morphologies, sizes, size sorting and packing) that generates complex pore networks. Six characteristic morpho-types (Erthal et al., 2017) were identified on macro-scale with regard to the Tivoli shrub structures (i.e. narrow dendriform, wide dendriform, fili dendriform, arborescent, arbustiform and pustular shrubs). Furthermore, these morphologies possess different macro-characteristics, covering a range from thin, dendritic and elongated to short, rounded and dense components. Besides, microporosity often occurs associated with the stem center of the shrub.

Since a 2D pore-type classification cannot fully cover the complexity of these carbonates, sometimes possessing cm-sized pores, Micro-Computed Tomography (µCT) imaging is used in this study to render and typify the 3D arrangement of shrub textures, pore distributions and pore shapes. The aim of the present study is to characterize the different shrub textures and unravel their relationship with reservoir characteristics by studying the 2D and 3D pore network and pore shapes and by integrating petrophysical (porosity and permeability) measurements. This study is of major relevance in predicting reservoir quality and behavior for oil, gas or water exploitation.

4.2 Methods

4.2.1 Porosity and Permeability Measurements

The petrophysical measurements were performed on 60 shrub-dominated plugs, 1 and 1.5 inch (respectively 2.5 and 3.8 cm) in diameter, including 24 plugs drilled parallel and 36 vertical to stratification. All the plugs were used for the petrophysical and textural study. The porosity and grain density were measured in a porosimeter *UltraPore* 400 from *Corelab*. The permeability was measured in an *UltraPerm* 400 from *Corelab* using nitrogen gas (N_2) during fluid flow.

4.2.2 Micro Computed Tomography (µCT) and pore shape classification

From the 60 shrub plug samples, 20 representative plugs with 1 and 1.5 inch diameter were scanned by µCT (see Chapter 2) to render the pore network in 3D and to describe 3D pore shapes. The percentage calculation of porosity in the porous system was performed by using AVIZO software, where the images were threshold and labelled with regard to pore connectivity. In order to improve the understanding of the petrophysical behavior of heterogeneous shrub textures, pore shapes were quantified. For this purpose the pore shape parameter (Fig. 4.1) was used to characterize the pores in the 3D pore network based on the classification presented by Soete et al. (2015) and Claes et al. (2016).

For the purpose to differentiate pores (gas phase) from matrix (solid phase), an image segmentation needs to be performed. The segmentation of the µCT slices is performed by using Matlab software. An in-house dual-thresholding algorithm, based on the principle first described by Canny (1986) for an edge detecting algorithm (Claes et al., 2016), was used. According to the latter authors, this method is an adaptation of the single threshold approach: selecting pixels/voxels on the basis of their unique histogram range. The dual or hysteresis thresholding uses two intervals of the histogram to determine the segmentation (Claes et al., 2016). The dual thresholding, first a strong threshold criteria to differentiate pores from matrix is used and then a soft threshold is added. Based on the first threshold only voxels that are certainly pores are selected and based on the softer threshold pore-voxels which are in contact with the pores already defined by the strong thresholding are added.

The segmented images were opened in AVIZO software. The calculation of pore shapes based on the generated binary images, requires first the segmentation of the image. The binarization of the images, identify voxels as foreground and background in a two-component system. The binarization is based on a dual thresholding algorithm with a strong and weak threshold, for higher accuracy than regular single threshold algorithms. By doing so, pores and rock are separated (Claes et al., 2016). From this dataset the total porosity as well as the volume of interconnected pores can be calculated. Porosity quantitative analysis requires a voxel by voxel determination of void and rock phases. The next step is labelling in AVIZO, after using a filter editor to remove the pores below 13 µm. The selection of connected pores is done manually by checking the color labelled orthoslices.

The AVIZO software gives an excel table with all the information about the connected pores. This table is then opened in MATLAB software and an in-house algorithm calculates pore shapes. According to Claes et al. (2016), to achieve a correct assessment of the pore shapes it is necessary to split complex pores into elementary pore bodies by determining the pore throats in the 3D dataset. The identification of these pore throats uses a so-called 'watershed transformation' approach. The latter has many applications in image processing by simulating the flooding from a set of labelled regions in the 3D images (Claes et al., 2016). These regions are expanded according to the distance map, until the watershed lines are reached. Therefore, the process can be seen as a progressive immersion of a landscape. The algorithm follows three steps: (i) calculating the distance map of the binary images, (ii) determining the local maxima in this new dataset, (iii) calculating the dividing lines (watershed lines) between different pore bodies (defined by the local maxima) based on a 26-connectivity in 3 dimensions (Meyer, 1994). The thresholding, segmentation and watershed method imply some user-defined criterion, and therefore the results will likely slightly differ between researchers that would work on the same images, but the overall result remains nearly the same, as experienced in the research carried out in our research group at KU Leuven.

Once the pore space is transferred into 3D images labelled for all individual pore bodies and disconnected from each other by rock or through the watershed procedure, the seed size was set to 2, since this visually resulted in the most natural splitting of the pores, then shape parameters of individual pores can be calculated. In the proposed classification individual pores are considered as discrete objects, making possible to calculate the mechanical moments of these objects.

This allowed to characterize the shape of these pores, based on the projection of a spheroid

positioned inside the pores. Pore shape distribution (Fig. 4.1) is plotted as the ratio of the longest, intermediate and shortest pore dimensions of a projected internal spheroid (Claes et al., 2015; Soete et al., 2016). Here rod- and cuboid-like pore shapes are elongated along one dimension (Fig. 4.1). Cubic pores are equidimensional, while blade- and plate-like pore shapes have a flattened appearance (Fig. 4.1). The data also provide information about the orientation of the pores, which allows assessing the anisotropy of the porosity parameter (Claes et al., 2016).

The Representative Elementary Volume (REV) is an important concept to evaluate petrophysical properties (Claes et al., 2016; Soete et al., 2016). To examine the effect of scale on the REV porosity of 17 µCT scanned plugs (2.5 and 3.8 cm diameter) at a resolution of 16 µm, semi-variograms were calculated (See table 6.1, Chapter 6), by applying the methodology of Claes (2015). The semi-variogram ranges differ along the axes x, y and z, indicating that meso- and macropores are heterogeneously distributed within the samples. For more detailed information about REV, the reader is referred to Chapter 6 and especially table 6.1.

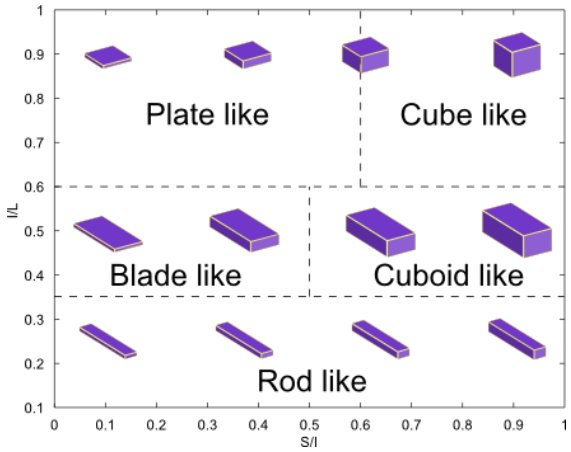

Fig. 4.1: Pore shape classification (Claes et al., 2015). The pore-types are differentiated according to the ratios of the longest (L), intermediate (I) and shortest (S) pore dimensions.

4.2.3 (Geo-) statistics

Unbalanced one-way ANOVA statistical analyses (variance analysis) were applied separately on the petrophysical data from the shrub morpho-types to perform a hypothesis test for the control of shrub morpho-types and shrub textures. With regards to the applied statistical analysis the reader is referred to Chapter 3.

4.3 Results

Shrub structures display variable growth textures that generate complex pore systems. Six different morpho-types were identified on macro-scale within the Tivoli shrub-dominated lithologies (Erthal et al., 2017), i.e. narrow dendriform (NDS), wide dendriform (WDS), fili dendriform (FDS), arborescent (ARB), arbustiform (ABT) and pustular shrubs (PS). In the Tivoli area, "**dendriform**" shrubs are the most abundant morpho-type. They are characterized by their branching organization, that according to the internal arrangement and distribution can be subdivided in **narrow**, **wide** and **fili** dendriform shrubs (Erthal et al., 2017). Moreover, **arborescent** (ARB), **arbustiform** (ABT) and **pustular** (PS) shrubs were described for features with under-developed or absence of branches. ARB is characterized by their height being larger than their width (H/W=2:1), while ABT display a height shorter than their width in a respective proportion of (H/W) 1:2 (Terra et al., 2009; Claes et al., 2017; Erthal et al., 2017). Besides, PS possesses a sub-rounded morphology, with an irregular surface and slight preferential vertical growth, with a H/W ratio of approximately 1:1 (Terra et al., 2009; Claes et al., 2017; Erthal et al., 2017). A more detailed description of the shrub morpho-types can be found in Chapter 2 (Erthal et al., 2017).

4.3.1 Shrub pore-types

The dominant pores observed within the shrub lithotype are **intershrub growth framework** and **interdigit or interbranching growth framework** pores (Figs. 4.2, 4.3A to J, 4.4A to G and I). These pore-types occur, respectively, between the individual shrubs and shrub branches within the shrub framework (Claes et al., 2017). Usually, the size of intershrub growth framework porosity is at least one order larger than the interdigit growth framework porosity. Sizes for both pore-types range between mm to cm scale, however, interdigit porosity is more often affected by cementation, which reduces the pore space. **Interlaminar** porosity (Figs. 4.2, 4.3C and D, 4.4A and B) is present between shrub layers but also along the interface between shrubs and other lithotypes (e.g. rafts, micritic layers and laminated mats). They can reach diameters of ~ 2 cm, and vary from mm to cm scale along the laminae. **Encrusted bubble porosity** often occurs trapped between intershrub growth framework porosity (Figs. 4.2, 4.3A and B, and E and F, 4.4C and D) and on top of the shrub layers, creating intercalations between them. They are formed by the encrustation of gas bubbles produced by photosynthetic processes of algae (Chafetz et al., 1991). Their outline sometimes can be misinterpreted as mouldic porosity, however, the latter presents more variable shapes. **Vuggy** porosity (Figs. 4.2, 4.3A to D, I and J, 4.4G) corresponds to non-fabric selective secondary pores (Choquette and Pray, 1970; Lucia, 1995; Lønøy, 2006). They often relate to solution-enlarged intershrub, mouldic and interlaminar pores. Their size varies from few μm to cm scale. Besides, **mouldic porosity** (Figs. 4.2, 4.3C and D, F and H) is rarely observed and is formed by calcite encrustation of organic compounds, a fabric that formed posterior after the decay of the latter. They are often observed as very small (10 to 50 μm) rounded pores and rarely display sizes up to ~ 100 μm. **Shelter** porosity (Figs. 4.2, 4.3 I and J) is regularly associated with broken rafts. **Intercrystalline** pores (Figs. 4.2, 4.4H) are located between sparry calcite cement. **Intracrystalline** porosity (Figs. 4.2, 4.4J and K) occurs within the sparry calcite crystals that cover shrub structures, being especially evidenced by fluorescence microscopy within fluorescent resin impregnated thin sections (Fig. 4.2J) and under SEM (Fig. 4.2 K) as micropores. **Intrashrub growth framework** (Fig. 4.2) porosity occurs mostly as **micropores**, being recognized in thin sections with fluorescent resin under fluorescent microscopy light (Figs. 4.4G and H), and in SEM analysis (Fig. 4.4L). These micropores occur associated with peloidal micritic aggregates, composed of spherical to sub-spherical micrite (Figs. 4.4I and J), smaller than 1 μm in size (Fig. 4.4L).

The pore-types become more complex as the rock becomes more heterogeneous. The presence of different shrub textures (i.e. morphologies, sizes, size sorting and packing) gives rise to complex pore networks.

The most common and widespread diagenetic feature modifying the shrub pore-types is a very thin fringe of sparry calcite cement covering all the shrub structures (see Chapter 2). Dissolution also occurs, as it is evidenced mainly by the rounded edges of the sparitic cement, however, with limited impact on the rock framework (see Chapter 2). These diagenetic features are mostly recognized in microanalysis. Despite the fact that porosity was slightly reduced by calcite cements, the importance of the latter seems crucial in the preservation of the primary growth framework porosity due to framework stabilization.

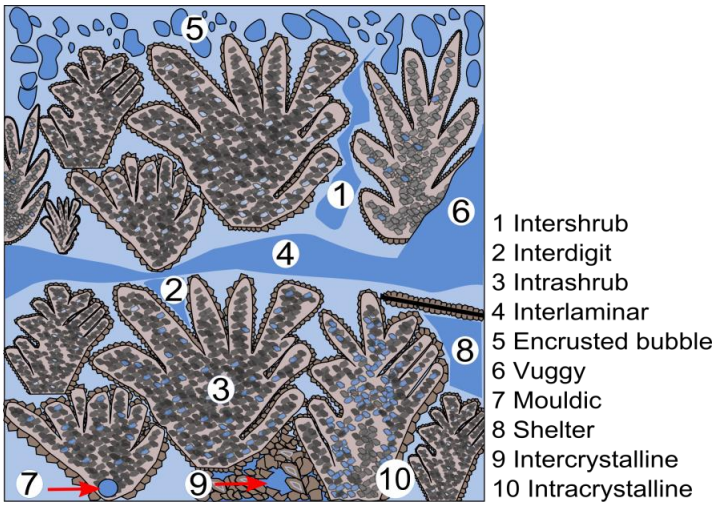

Fig. 4.2: Schematic drawing of the shrub pore-types for shrub-dominated Tivoli samples. Micropores are also observed but they are not shown in this figure. They occur in the peloidal micritic aggregates in the inner part of the shrubs and less commonly in the sparry calcite cement.

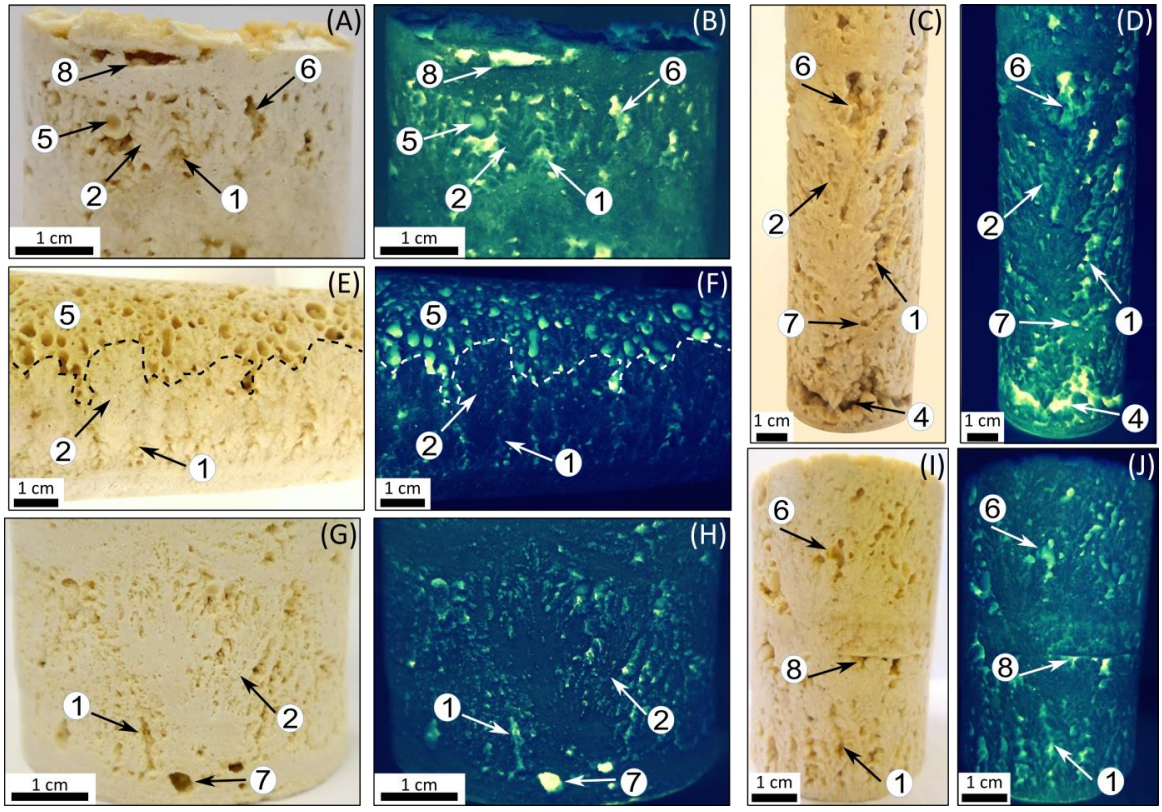

Fig. 4.3: Shrub pore-types on macro-scale with A, C, E, G and I scans from thin sections, and the other figures corresponding to images taken under fluorescent light of thin-sections impregnated with a fluorescent dye. (A) Intershrub growth framework porosity (1), interdigit growth framework porosity (2), encrusted bubble (5), vuggy (6), and shelter (8) porosities. The latter is associated to the raft structure. (B) The pores from figure "A" are highlighted by green color. (C) Intershrub (1) and interdigit (2) growth framework porosity (1), interlaminar (4), vuggy (6), and mouldic (7) porosities. (D) Green color highlighting the pores from figure "C". (E) In the bottom of the sample, associated with shrub lithotype occur intershrub (1) and interdigit (2) growth framework porosity. On top of the sample, encrusted bubbles are present (5). (F) Porosity from figure "E" highlighted by green color. (G) Intershrub (1) and interdigit (2) growth framework porosity, and mouldic pore (7). (H) Green color highlighting the pores from figure "G". (I) Intershrub (1) growth framework porosity, vuggy (6), and shelter (8) porosities. The latter porosity is associated with raft structure. (J) The pores from figure "I" are highlighted by green color.

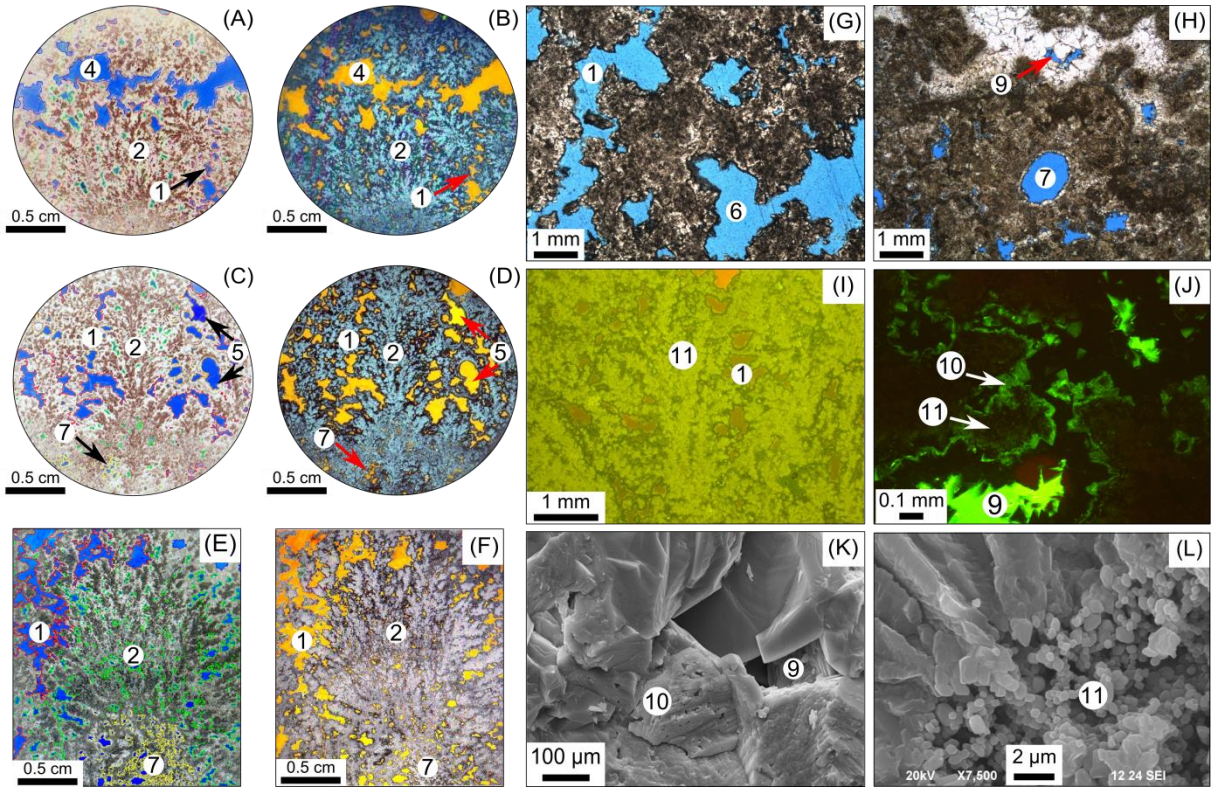

Fig. 4.4: (A) Intershrub (1) and interdigit (2) growth framework porosity outlined by red and green lines, respectively. Interlaminar porosity (4) occurs between shrub laminae. (B) Porosity from figure "A" is highlighted by yellow color. (C) Intershrub (1) and interdigit (2) growth framework porosity highlighted by red and green lines, respectively, besides encrusted bubble porosity (5) trapped between shrubs, and mouldic pores (7) occurring in the frame of the bottom shrubs. (D) Yellow color highlighting the pore-types from figure "C". (E) Intershrub (1) and interdigit (2) growth framework porosity outlined by red and green lines, respectively. In the shrub bottom tiny mouldic (7) pores, are highlighted by yellow lines. (F) Porosity from figure "E" is highlighted by yellow color. (G) Vuggy porosity (6) related to solution-enlarged intershrub growth framework porosity (1). (H) Mouldic porosity (7) with rounded shape, associated with the decay of a plant. Intercrystalline (9) porosity occurring between the calcitic sparitic cement. (I) Fluorescence microscopy picture highlighting the intrashrub microporosity (11) by light green fluorescence. Intershrub (1) growth framework porosity is marked by dark yellow color. (J) Fluorescence microscopy image with bright green fluorescence in correspondence to intercrystalline porosity (9). Light green fluorescence occurs within the sparry calcite cement (10, intracrystalline porosity) and dark green fluorescent is associated with intrashrub microporosity (11). (K) SEM image showing microporosity in the sparry calcite cement (10, intracrystalline porosity) and intercrystalline porosity (9). (L) SEM image showing an intrashrub microporosity (11) located within the peloidal micritic aggregate in the central part of the shrub.

4.3.2 Porosity and permeability measurements

Shrub structures developed perpendicular to their substrate and are often intercalated with other lithotypes in vertical cycles of ~ 3 cm in size (Erthal et al., 2017). The samples (1 and 1.5 inch, vertical as well as horizontal plugs), however, display no correlation in the porosity versus permeability plot (Fig. 4.5). Moreover, horizontal plugs possess in general higher permeabilities than vertical plugs. The permeability results for horizontal plugs range from 0.001 to 9654 mD versus 0.001 to 4691 mD for the vertical plugs (Fig. 4.5). Porosity values vary from 0.6 to 20.5 % and 0.7 to 22.5 % for the horizontal and vertical plugs, respectively (Fig. 4.5).

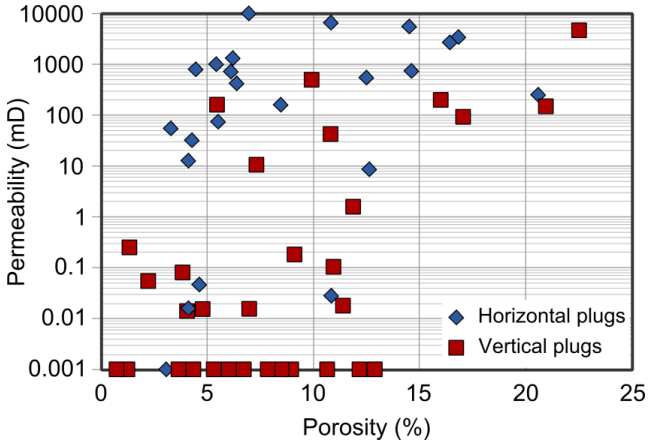

Fig. 4.5: Porosity versus permeability plot for vertical and horizontal plugs.

To investigate whether a relationship exists between shrub morpho-types and porosity or/and permeability, a differentiation in function of morpho-types was performed (Fig. 4.6A). As it can be observed, there is no clear relationship between the shrub morpho-types and poro-perm results.

In addition, to inspect whether shrub morpho-types display different poro-perm characteristics in function of plug orientation, 2 graphs were made: one displaying plugs drilled vertically, the other drilled horizontally (Figs. 4.6B and C, respectively). One of the main differences in function of shrub morpho-types between both dataset relates to samples with very low permeability (0.001 mD). They are very common in the vertical plug samples, while only one sample of the horizontal plug dataset displayed such a low permeability value. This result indicates that vertical plugs possess higher rock heterogeneities than horizontal plugs.

ANOVA statistical analysis was applied in order to test whether shrub morpho-types possess a relationship with porosity and permeability (Tables 4.1 and 4.2). The ANOVA table lists the source of variability, the Sum of Squares (SS), degree of freedom (df) and the Mean Squares (SS/df) for each source. The F-statistic is calculated as the ratio of the mean squares. For p-values below a pre-defined value of 0.05 (Sheskin, 2004), the null hypothesis, namely that porosity and permeability values were not performed on random samples of one and the same population, but originate from different shrub morpho-types, can be rejected. In the box plots for shrub morpho-types versus porosity (Fig. 4.7A) and permeability (Fig. 4.7B) it can be seen that for $p<0.05$, the null hypothesis of significant differences for the shrub morpho-types, porosity and permeability is rejected. A null hypothesis is rejected when at least one group mean is significantly different from the others. Based on the results of the multi-comparison test for porosity (Fig. 4.8A) and permeability (Fig. 4.8B) it can be concluded that the means for the shrub morpho-types are not significantly different.

	SS	df	SS/df	F	P
Groups	232.7	5	46.5	1.77	0.1
Error	1421.2	54	26.3		
Total	1653.9	59			

Table 4.1: ANOVA table for porosity and shrub morpho-types (abbreviations: see text).

	SS	df	SS/df	F	P
Groups	187.7	5	37.5	1.1	0.4
Error	1867.2	54	35.6		
Total	2054.9	59			

Table 4.2: ANOVA table for permeability and shrub morpho-types (abbreviations: see text).

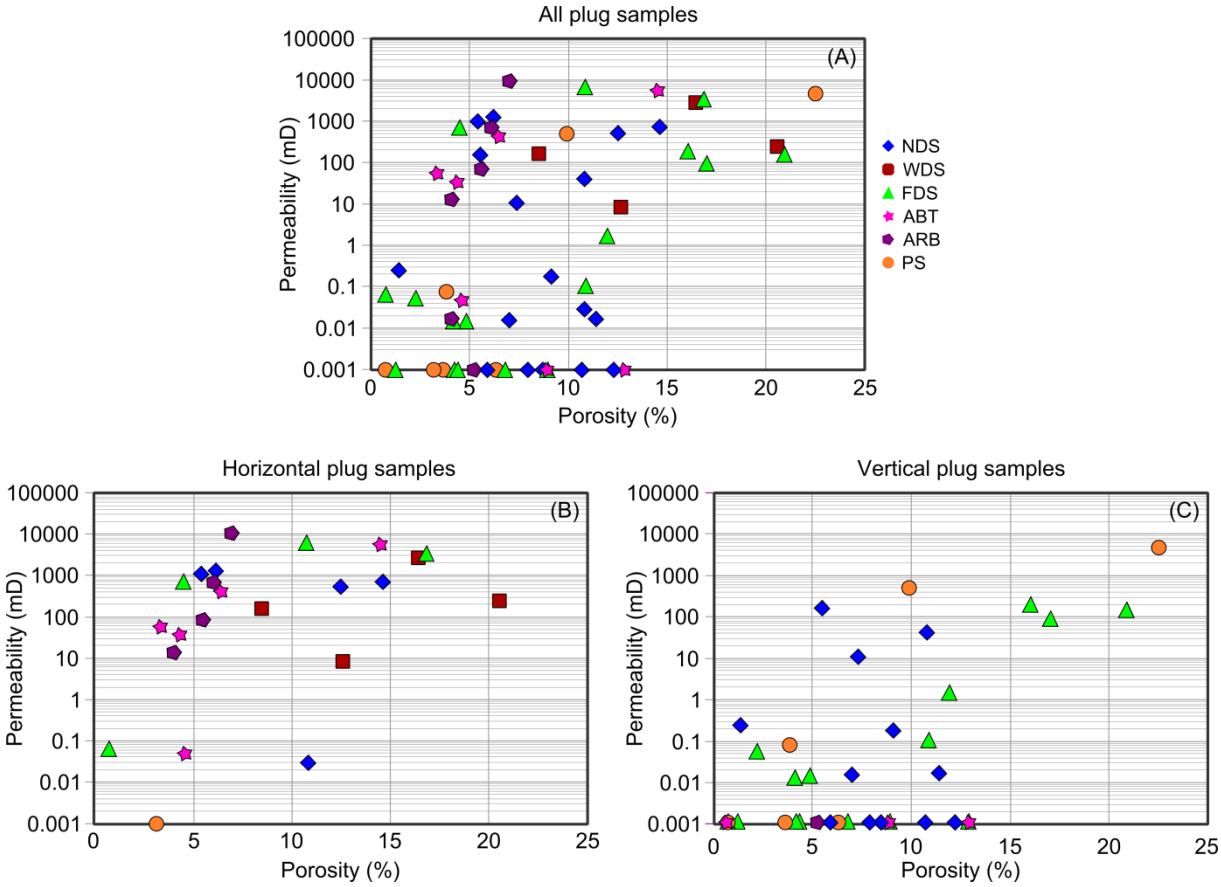

Fig. 4.6: (A) Shrub morpho-types plotted in porosity vs. permeability graph. (B) and (C) Shrub morpho-types of, respectively, horizontal and vertical plugs plotted in a porosity vs. permeability graph. NDS corresponds to narrow dendriform shrub, WDS to wide dendriform shrub, FDS to fili dendriform shrub, ARB to arborescent shrub shrub, ABT to arbustiform shrub and PS to pustular shrub.

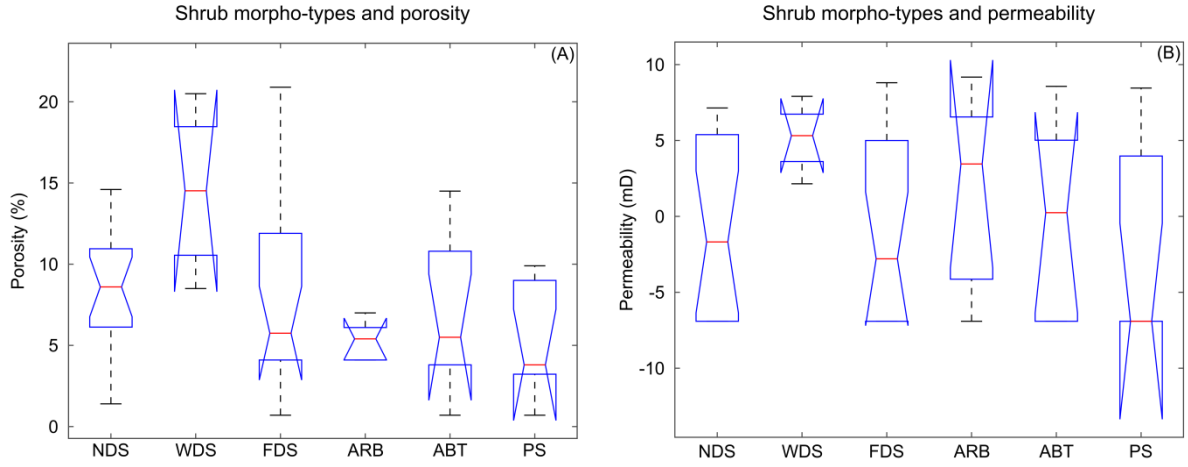

Fig. 4.7: (A) ANOVA box plots for shrub morpho-types vs. porosity and (B) versus permeability. Notice that the 95% confidence limits for the median values sometimes plot outside the 75 and 25% range. NDS corresponds to narrow dendriform shrubs, WDS to wide dendriform shrubs, FDS to fili dendriform shrubs, ARB to arborescent shrub, ABT to arbustiform shrub and PS to pustular shrubs.

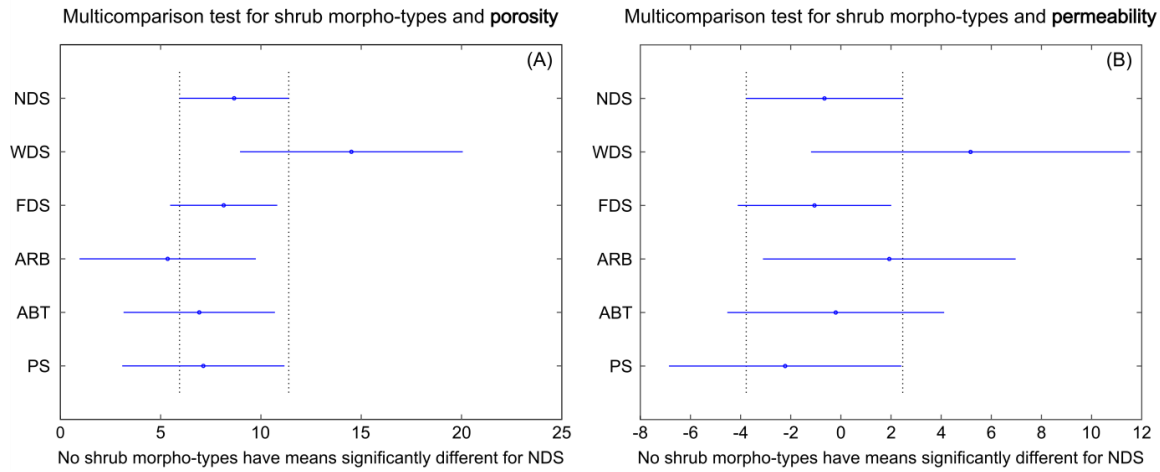

Fig. 4.8: "Multi-comparison" test graphs for shrub morpho-types in function of (A) porosity and (B) permeability. NDS corresponds to narrow dendriform shrubs, WDS to wide dendriform shrubs, FDS to fili dendriform shrubs, ARB to arborescent shrub, ABT to arbustiform shrub and PS to pustular shrubs.

4.3.3 Shrub textures

Shrubs from Tivoli possess complex morphologies. The term "texture" refers to the relationship between the shrubs, the physical appearance or characteristics of a rock, such as morphology, size, size sorting and packing, at both macro- and microscopic scale. Shrub morphology is a texture attribute that already was discussed above, while the other texture attributes are addressed below. Therefore, petrographic and micro-CT image analyses were used to characterize the shrub textures for getting more insight on the controlling parameters on petrophysical data. We also refer to Rezende and Pope (2015), who also addressed these attributes.

The shrub **size** was measured along the height axis of each shrub within a plug sample. They were categorized into 3 classes: 1) small, with length smaller than 1 cm; 2) medium, with lengths between 1 and 2 cm and 3) large, comprising lengths larger than 2 cm. The **size sorting** (Figs. 4.9A and B) considered the size variability within the samples (Rezende and Pope, 2015). "Well-sorted" (Fig. 4.9A) is attributed to samples with shrubs of similar average size, while "poorly-sorted" (Fig. 4.9B) refers to samples with high variability in shrub size. Shrub **packing** (Figs. 4.9C and D) is defined as the space of the mutual arrangement of the shrub constituents that corresponds to the ratio between shrub width and the adjacent spacing (Rezende and Pope, 2015).

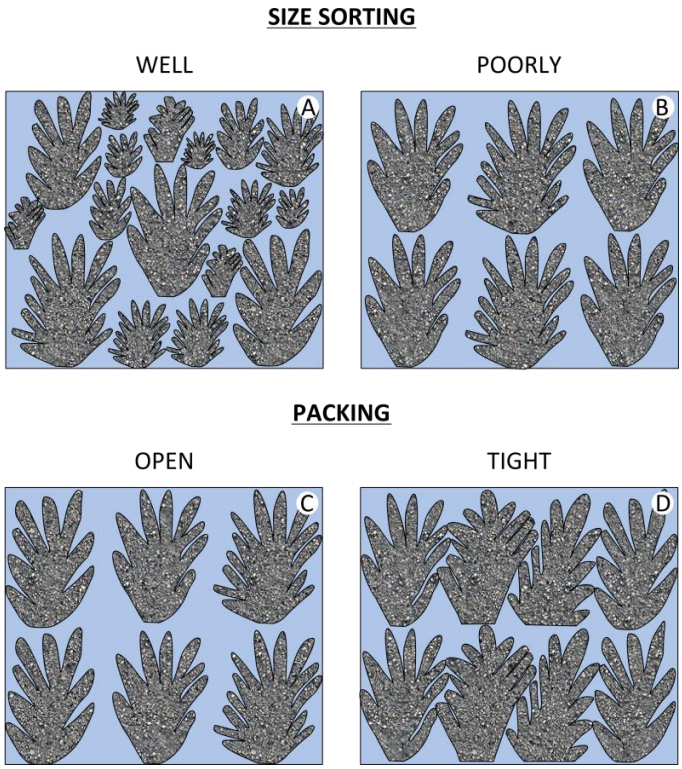

Fig. 4.9: Shrub textures based on (A and B) shrub size sorting and (C and D) shrub packing. The shrub size sorting (A and B) comprise the complexity of shrub sizes within one sample. Shrub packing (C and D) corresponds to the ratio between shrub width and adjacent spacing (modified from Rezende and Pope, 2015).

Shrub size

Shrub size plotted in a porosity versus permeability graph (Fig. 4.10) displays no clear relationship to the latter parameters. However, the ANOVA statistical analysis box plots for **shrub sizes** in function of porosity (Fig. 4.11A) shows that center lines of the small sized shrubs plot below the 25th percentile of the medium and large sized shrubs. Box plots of **shrub size** versus permeability (Fig. 4.11B) for $p<0.05$ indicates that the null hypothesis of significant differences for the **shrub size** and permeability, is rejected. Multi-comparison test for porosity in function of size also indicates that means of medium and small sized shrubs are significantly different (Fig. 4.12A). The results of the multi-comparison test for permeability in function of shrub size, however, show no significant differences (Fig. 4.12B).

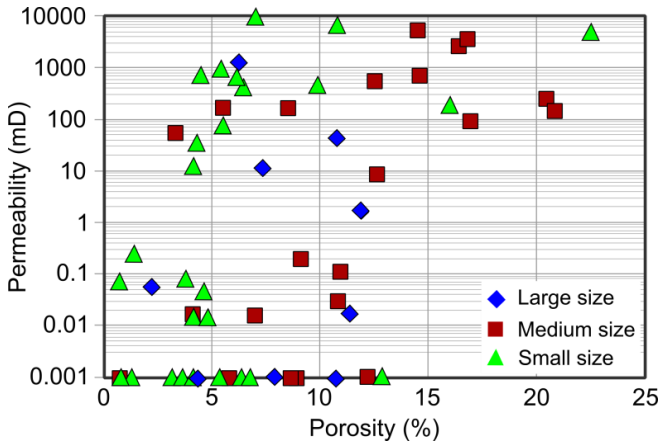

Fig. 4.10: **Shrub sizes** plotted in porosity vs. permeability graph. The data are scattered displaying only weak correlations.

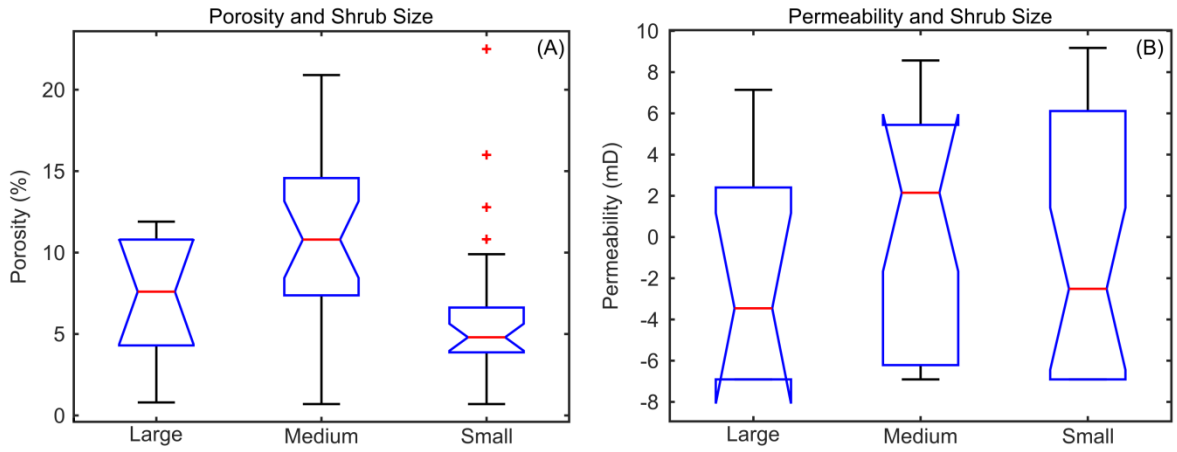

Fig. 4.11: ANOVA statistical box plots data for **shrub size** in function of (A) porosity and (B) permeability.

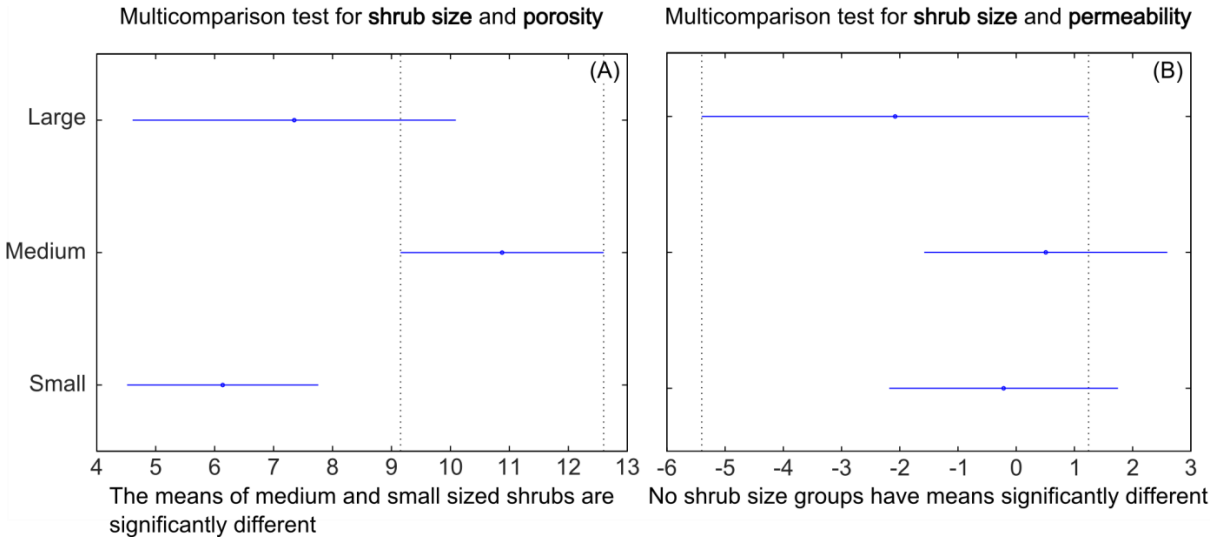

Fig. 4.12: "Multi-comparison" test graphs for **shrub sizes** in function of (A) porosity and (B) permeability.

Shrub size sorting

Shrub size sorting plotted in a porosity versus permeability graph (Fig. 4.13) displays a clear relationship with permeability, but no clear relationship with porosity. *Poorly size sorted* shrubs plot in the lower part of the graph which corresponds to the lowest permeabilities, while *well size sorted* shrubs display the highest permeability results (Fig. 4.13).

The ANOVA box plots statistical analysis for **shrub size sorting** in function of porosity (Fig. 4.14A) indicate that center lines of the *well sized sorted* shrubs plot just below the 25th percentile of the *poorly size sorted* shrubs, indicating that porosity is also slightly influenced by **shrub size sorting.** ANOVA box plots of **shrub size sorting** versus permeability (Fig. 4.14B) attested that for $p<0.05$, the *well sized sorted* shrubs can be distinguished from *poorly sized sorted* shrubs. Multi-comparison test for both porosity and permeability in function of **shrub size sorting** indeed indicates that means of *well-* and *poorly sized sorted* shrubs are significantly different (Fig. 4.15A and B). So, shrub size sorting exerts a primary control on permeability, and a secondary control on porosity.

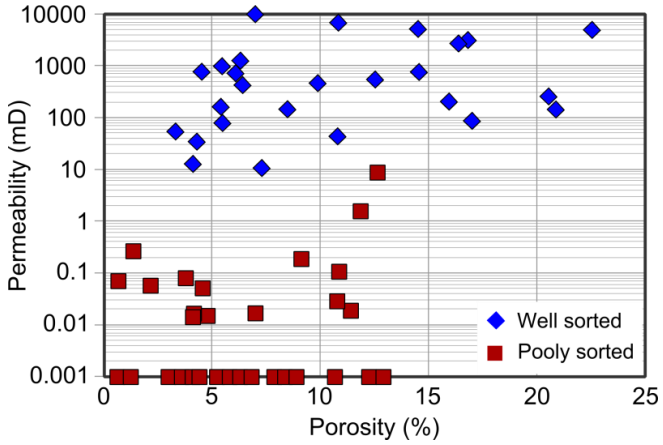

Fig. 4.13: **Shrub size sorting** plotted in a porosity vs. permeability graph. The results show strong relationship between shrub size sorting and permeability.

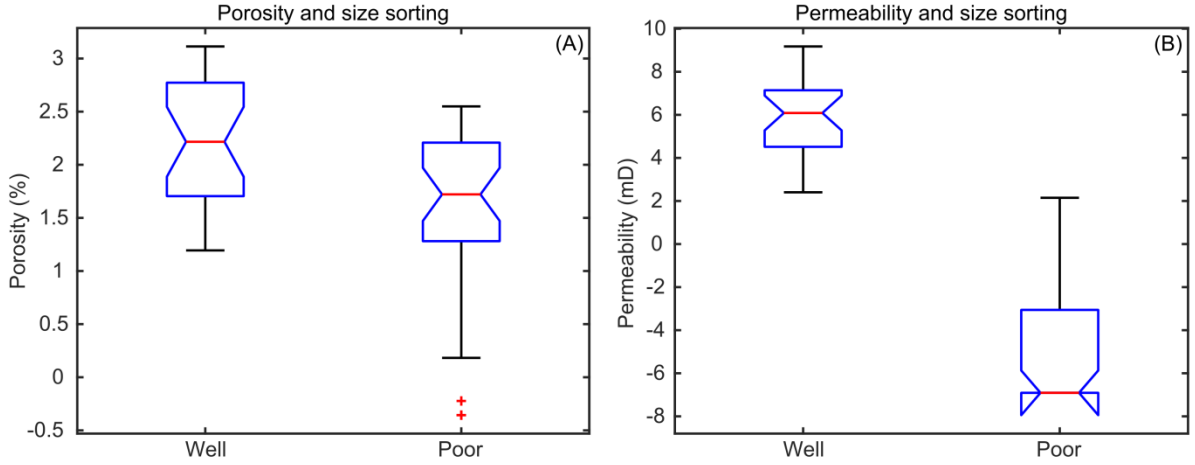

Fig. 4.14: ANOVA statistical box plots data for **shrub size sorting** in function of (A) porosity and (B) permeability.

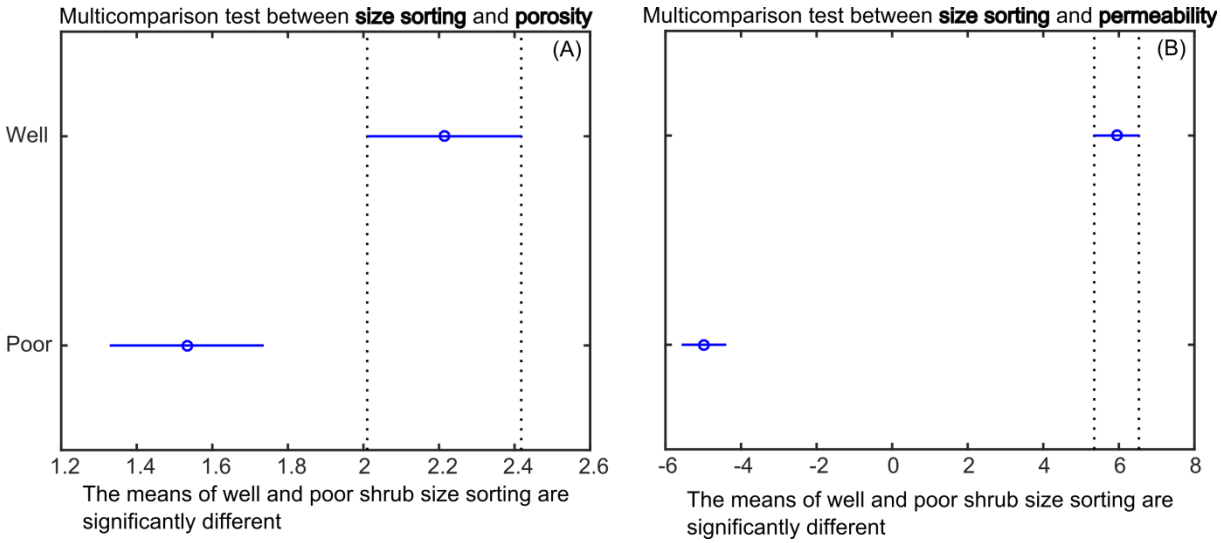

Fig. 4.15: "Multi-comparison" test graphs for **shrub size sorting** in function of (A) porosity and (B) permeability.

Shrub packing

The **shrub packing** plotted in a poro-perm graph (Fig. 4.16) shows a clear relationship with porosity data, but no clear relationship with permeability. The *open packed* shrub morpho-types possess the highest porosity values, while *tight packed* shrub samples, obviously, possess the lowest.

The ANOVA box plots statistical analysis for **shrub packing** in function of porosity (Fig. 4.17A) indicate that center lines of the *tight packed* shrubs plot just below the 25th percentile of the *open packed* shrubs. Similar observation is reflected in the ANOVA box plots of **shrub packing** versus permeability. The latter shows that the center line of the *tight packed* shrubs plot just below the 25th percentile of the *open packed* shrubs (Fig. 4.17B). This indicates that permeability is slightly influenced by **shrub packing.** Multi-comparison test testify that both porosity and permeability in function of **shrub packing** indeed possess means of *open-* and *tight packed* shrubs that significantly differ (Fig. 4.18A and B). Thus, shrub packing is a primary control on porosity and secondary control on permeability.

Table 4.3 summarizes the 60 shrub morpho-type samples in function of their macroscale, µCT image analyzes, their textures and poro-perm characteristics.

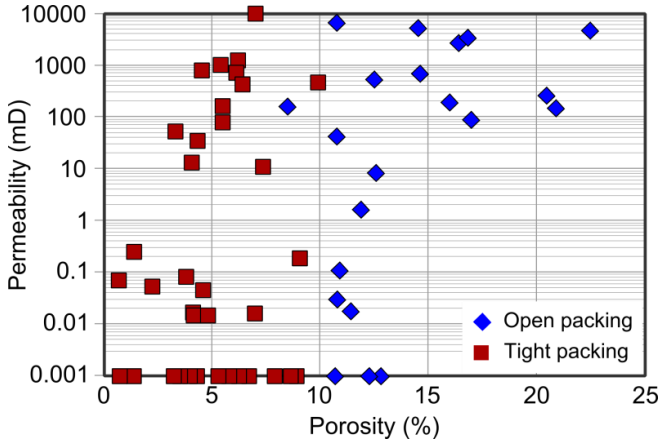

Fig. 4.16: **Shrub packing** plotted in a porosity vs. permeability graph showing a strong relationship to porosity data.

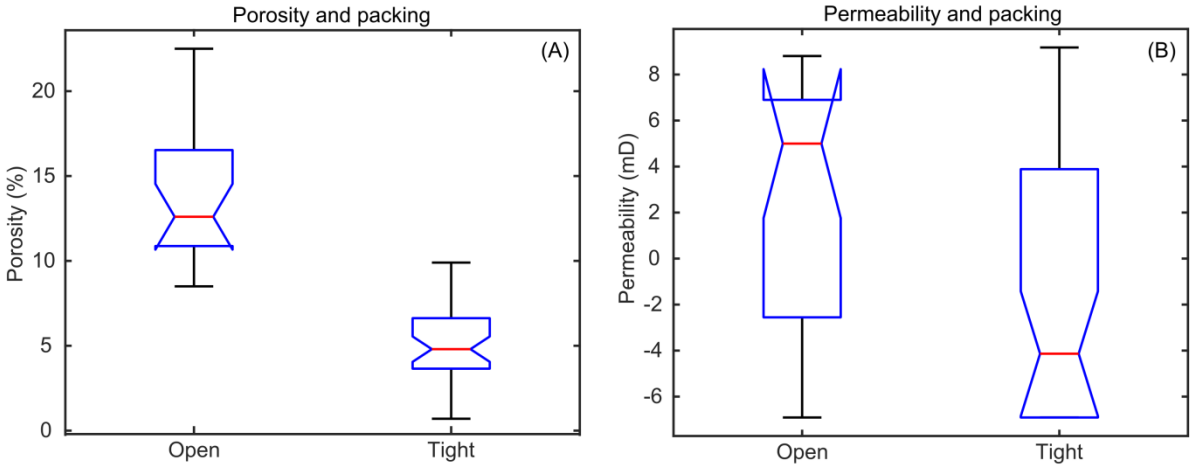

Fig. 4.17: ANOVA statistical box plots data for **shrub packing** in function of (A) porosity and (B) permeability.

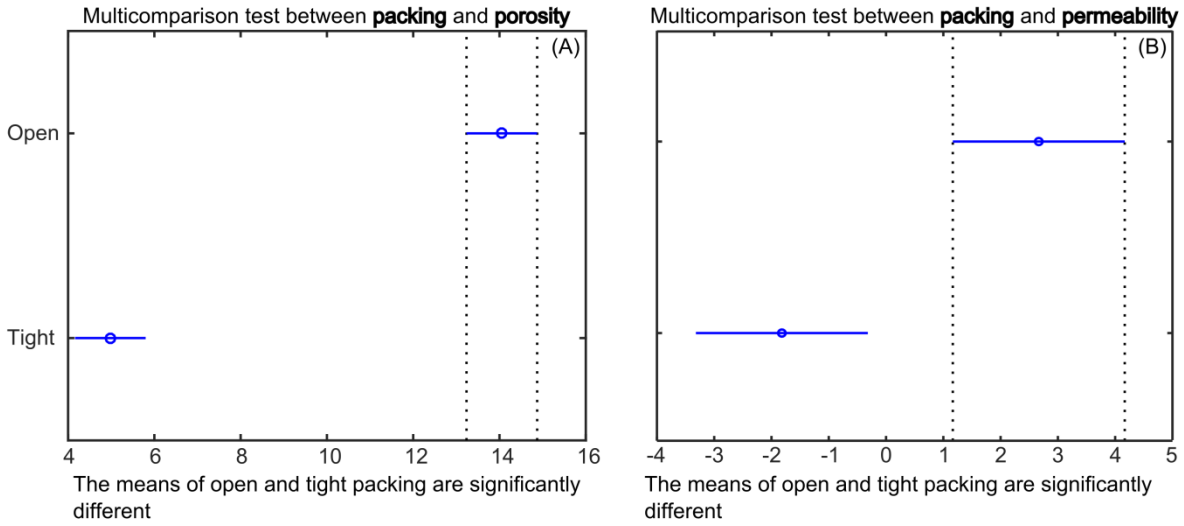

Fig. 4.18: “Multi-comparison” test graphs for **shrub packing** in function of (A) porosity and (B) permeability.

Shrub morpho-types	Images		Microscale fabric	Shrub size	Shrub size sorting	Shrub packing	Porosity (%)	Permeability (mD)	Pore-types
	Macro-scale	Micro-CT							
Narrow dendriform	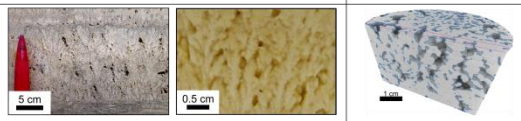		Mainly peloidal	Medium and large	Mainly poorly	Mainly tight	1.4 to 14.6	0.001 to 1263	Mainly intershrub, Interdigit; often interlaminar, encrusted bubbles, mouldic and vugular; rarely intrashrub
Wide dendriform	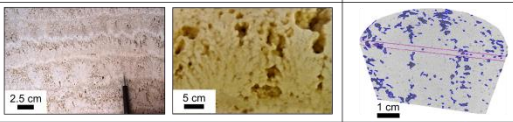		Mainly peloidal	Medium and large	Mainly well	Open	8.5 to 20.5	8.57 to 2716	
Fili dendriform	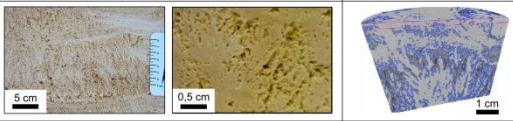		Mainly peloidal	Large, medium and small	Mainly poorly	Mainly tight	0.7 to 20.9	0.001 to 6661	
Arborescent	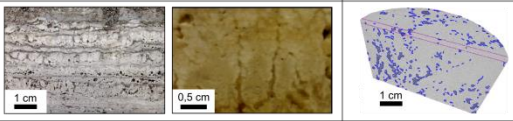		Mainly peloidal, rarely crystalline	Small and rarely medium	Mainly well	Tight	4.1 to 7.0	0.001 to 9654	Mainly intershrub; often mouldic and vugular; rarely intrashrub
Arbustiform			Mainly peloidal, rarely crystalline	Medium and small	Well and poorly	Mainly tight	0.7 to 14.5	0.001 to 5255	
Pustular	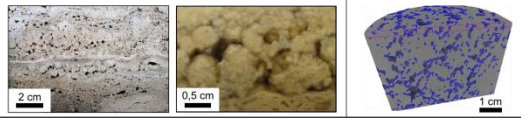		Mainly peloidal, rarely crystalline	Small	Poorly	Mainly tight	0.7 to 22.5	0.001 to 4691	

Table 4.3: Summary of the 60 shrub morpho-types, their textures, pore-types and petrophysical measurements.

4.3.4 Micro-Computer Tomography (µCT)

The complex pore networks that characterize the different shrub textures from Tivoli mainly relate to preserved depositional textures (e.g. morphology, size sorting and packing), marked by complex pore shapes and overall 3D morpho-types. µCT was used in order to evaluate the pore network and shrub textures in three dimensions. Based on this dataset, it is possible to visualize the porosity profile along a cross-section through the plugs (Fig. 4.19), whereby, for nearly all cases studied, a high heterogeneity in porosity distribution is a characteristic feature. So, with the purpose to calculate the percentage of open porosity in the porous system, the images were threshold and labeled (Fig. 4.20) with regard to pore connectivity. Here, the calculated open porosity closely relates to the calculated total porosity, with less than 3% difference (Table 4.4; Fig. 4.19). This indicates that Tivoli shrubs possess a high pore network connectivity (i.e. reflecting highly effective porosity).

Besides, the volume rendering and labelled of the pore network showed that the different shrub morpho-types indeed yield high pore network connectivity (Figs. 4.20A to L).

Samples	µCT total ø (%)	µCT open ø (%)	Difference between µCT total and open ø (%)
QS 11	6.0	3.4	2.6
QR 15	17.8	15.1	2.7
QR17	13.3	11.8	1.5
QR 18	10.1	9.3	0.8
QR 22	8.7	7.9	0.8
QR 24	7.3	4.5	2.8
QR 26	5.5	3.2	2.3
QR 28	17.7	16.6	1.1
QR 29	13.3	13.2	0.1
QR 30	12.0	10.7	1.3
QR 31H	10.9	8.1	2.8
QR 34H	16.2	15.5	0.7
QR 35H	14.3	13.6	0.7
QR 38	9.2	7.4	1.8
QR 52	16.0	15.3	0.7
QR 139V	3.3	3.3	0.0

Table 4.4: Results of µCT scan analysis. For each scanned sample, total and open porosities (ø) for each slice number were calculated using Matlab.

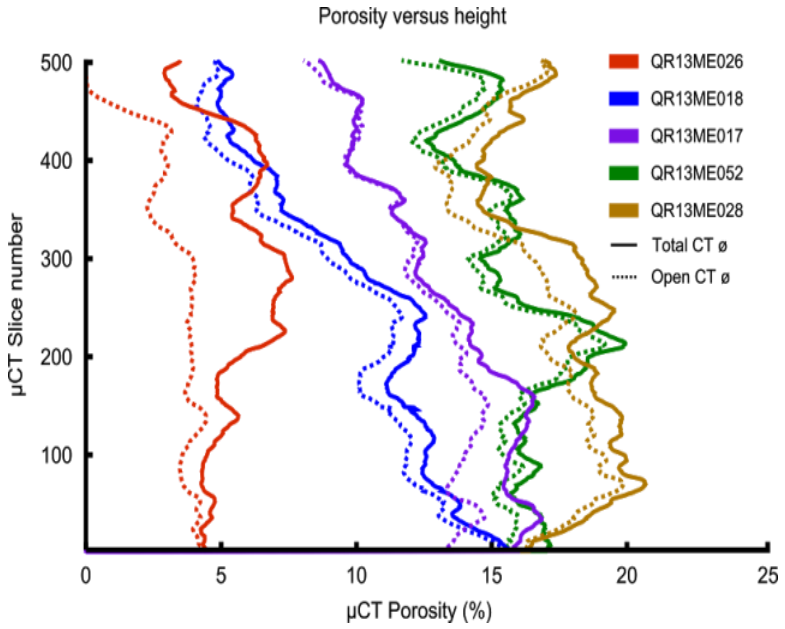

Fig. 4.19: Porosity profiles along 5 plug samples showing a strong heterogeneity of porosity. The dotted lines represent the open pores, while the full lines the total porosity. The difference between them, on average, is less than 3% in absolute porosity, indicating that most of the porosity is effective.

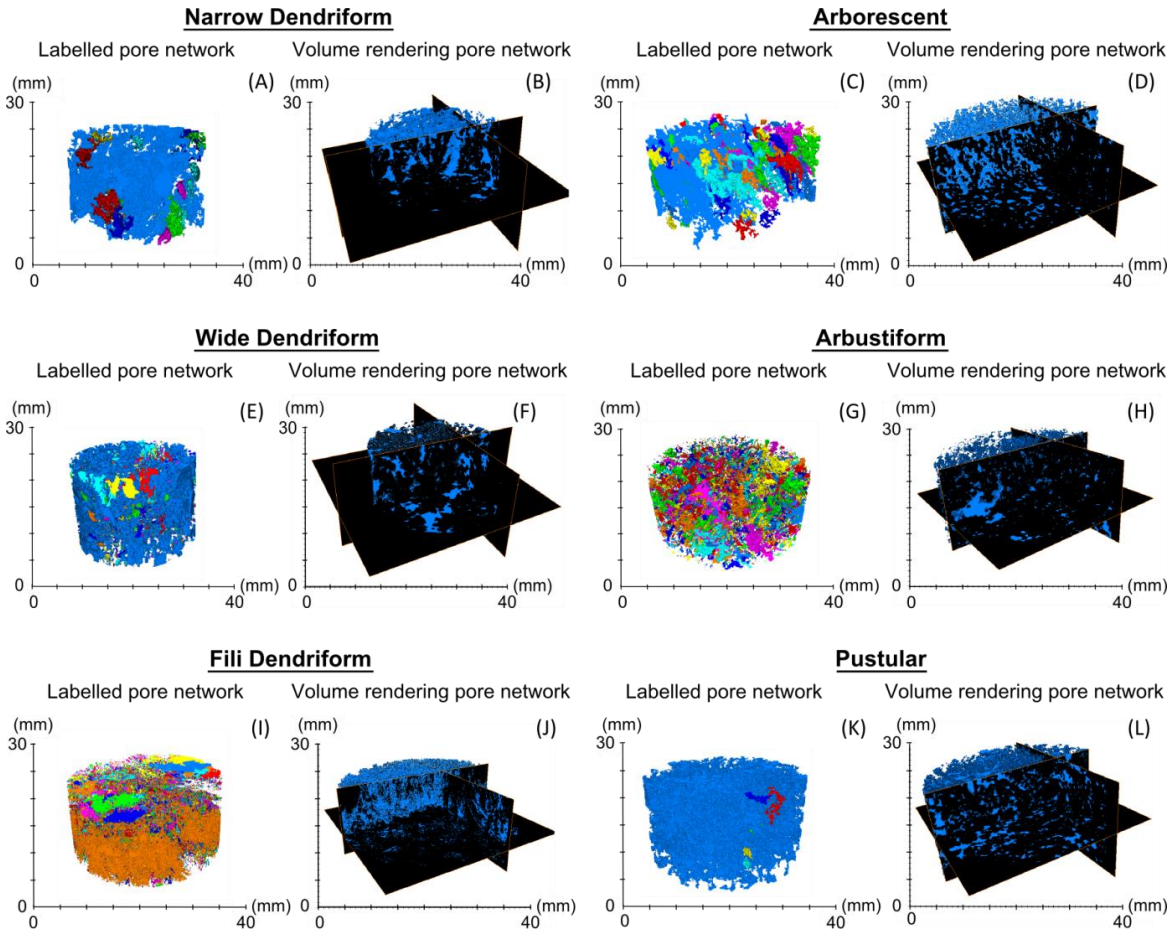

Fig. 4.20: (A, C, E, G, I, K) Labelled pore network and (B, D, F, H, J, L) volume rendering of the pore network of the 6 representative shrub morpho-types. The color variation illustrates the low pore-connectivity for the given resolution (16 µm). Pores below this resolution were not taken into account.

4.3.4.1 Pore shapes by using µCT analysis

Analyzing the pore shape of the pores, according to the classification of Claes et al. (2016), provided a better understanding of the petrophysical behavior of heterogeneous shrub morpho-types. Pore shapes are used as a tool to better typify the complexity of the lithofabrics and also, to unravel the contribution of each pore shape within the entire pore network.

Notice that for statistically correct interpretations/conclusions, the number of samples analyzed of the different shrub morpho-types is not sufficient. However, some observations can be made. It is possible to distinguish between the shrub morpho-types based on the pore volume (Vol). The cubeVol and plateVol seemed the parameters with the highest variation according to shrub morpho-types (Table 4.5; Fig. 4.21). FDS and ABT have high plateVol and low cubeVol; PS has high cubeVol and low plateVol; ARB has high and plateVol and low cubeVol; NDS has high cubeVol and low plateVol.

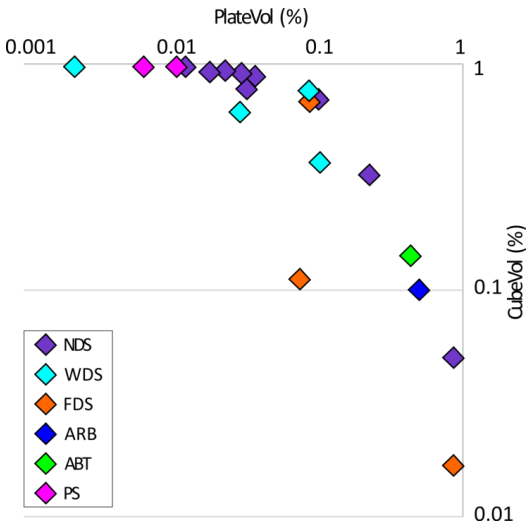

Fig. 4.21: PlateVol versus cubeVol in function of shrub morpho-types.NDS corresponds to narrow dendriform shrub, WDS to wide dendriform shrub, FDS to fili dendriform shrub, ARB to arborescent shrub, ABT to arbustiform shrub and, PS to pustular shrub.

Sample	Shrub morpho-types	Total (%)					Volume (%)				
		rod	blade	plate	cube	cuboid	rodVol	bladeVol	plateVol	cubeVol	cuboidVol
QR13ME015B	NDS	0.04	0.07	0.28	0.37	0.25	0.02	0.01	0.85	0.05	0.06
QR13ME017	NDS	0.02	0.08	0.46	0.29	0.15	0.01	0.01	0.02	0.91	0.05
QR13ME028	NDS	0.03	0.07	0.34	0.34	0.22	0.02	0.01	0.04	0.86	0.07
QR13ME030	NDS	0.03	0.06	0.37	0.34	0.20	0.03	0.01	0.10	0.69	0.16
QR13ME034H	NDS	0.04	0.05	0.28	0.38	0.26	0.05	0.03	0.22	0.32	0.38
QR13ME035H	NDS	0.05	0.06	0.26	0.35	0.28	0.01	0.00	0.02	0.92	0.04
QR13ME018	NDS	0.04	0.07	0.26	0.38	0.25	0.02	0.05	0.03	0.76	0.13
QR13ME031H	NDS	0.05	0.04	0.24	0.42	0.25	0.00	0.00	0.01	0.96	0.02
QR13ME037H	NDS	0.06	0.04	0.24	0.38	0.27	0.01	0.00	0.03	0.90	0.05
QR13ME038H	WDS	0.03	0.07	0.43	0.30	0.17	0.03	0.01	0.10	0.36	0.49
QR13ME024V1	WDS	0.05	0.04	0.24	0.41	0.26	0.01	0.01	0.03	0.60	0.35
QR13ME029	WDS	0.06	0.04	0.23	0.41	0.26	0.00	0.00	0.00	0.99	0.01
QR13ME139V	WDS	0.04	0.05	0.30	0.35	0.26	0.06	0.01	0.09	0.76	0.09
QR13ME019	FDS	0.04	0.06	0.31	0.33	0.26	0.07	0.02	0.09	0.68	0.15
QR13ME022	FDS	0.03	0.14	0.48	0.19	0.16	0.05	0.03	0.07	0.11	0.74
QS13ME011B	FDS	0.04	0.06	0.25	0.38	0.26	0.04	0.03	0.87	0.02	0.04
QR13ME026	ARB	0.04	0.09	0.31	0.36	0.21	0.12	0.04	0.50	0.10	0.25
QR13ME032V	ABT	0.04	0.05	0.28	0.37	0.26	0.05	0.06	0.43	0.14	0.31
QR13ME052	PS	0.04	0.03	0.25	0.44	0.23	0.00	0.00	0.01	0.98	0.01
CR05	PS	0.02	0.08	0.48	0.28	0.14	0.00	0.00	0.01	0.96	0.02

Table 4.5: Pore shapes quantification of 20 µCT-scanned shrub samples. NDS corresponds to narrow dendriform shrub, WDS to wide dendriform shrub, FDS to fili dendriform shrub, ARB to arborescent shrub, ABT to arbustiform shrub and, PS to pustular shrub.

There is no relationship between pore shapes, pore volumes and permeability. However, figure 4.22 displays some correlations between pore shape volumes and porosity. CuboidVol and cubeVol seem to show a negative and positive (respectively) logarithmic correlation with porosity (Fig. 4.22). However, this result is likely influenced by outliers. For higher porosities, it is observed that the volumetric contribution of the cuboid shaped pores decreases, and the one of the cubes increases. From figure 4.22, it is also clear that the highest volumetric contributions are nearly always cubes. However, 20 samples are still rather limited, so a higher number of samples could help to elucidate better these relationships. The R^2 are significant from 0.42 on 0.05 and 0.54 on a 0.01 level.

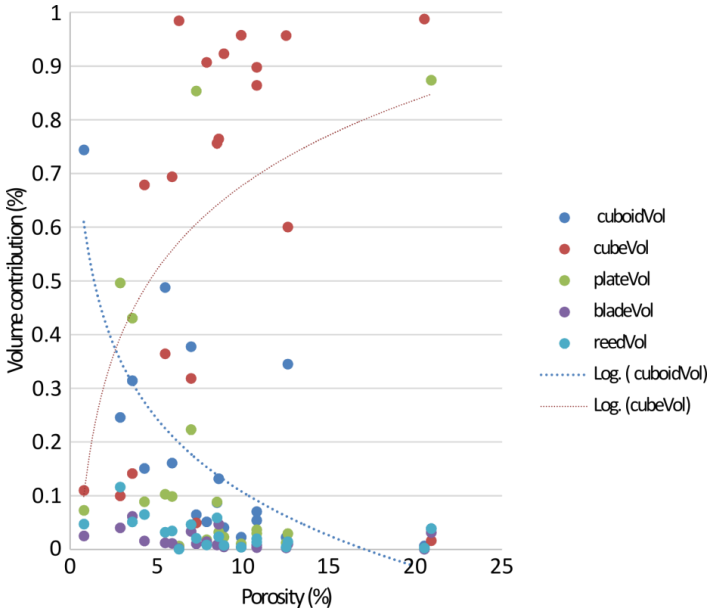

Fig. 4.22: Graph of porosity versus volumetric contribution of the pore shapes. CuboidVol and cubeVol possess a negative and positive correlation with porosity, respectively.

4.3.4.2 Pore shapes and shrub textures

The evaluation between shrub textures (e.g. size, size sorting and packing) and pore shape types were statistically analyzed by using R software (R core Team, 2012) based on a t-test. For a t-test it is only possible to compare two box plots with each other. The significance level (p) for the F (estimate variance between groups) statistics, indicate that the higher the significance that the data are distinct, the lower is the p-value. The confidence level used to compare the groups is 0.05 (5%).

Shrub size

For the size, only one sample characterizes small sized shrub (Figs. 4.23A to L). As this result has no statistical representativeness, the small shrub results is used only as indicative when compared to the other two groups (medium and large sized). It is remarkable that it has the highest amount of blade- (Fig. 4.23B) and plate-shape pores (Fig. 4.23C) but in volume they do not contribute too much (Figs. 4.23G to J, respectively to bladeVol and plateVol) because the volume contribution of blade- and plate-like shapes possess the lowest percentages. Only cube shape pores possess the lowest percentage for small sized shrubs (Fig. 4.23D), but in volume it is the one with a higher contribution (Fig. 4.23I). This indicates that for this sample, the pore shapes associated with small sized shrubs are mainly cube like.

Medium sized shrubs have a significantly higher amount of rod-, cube- and cuboid-shaped pores (Figs. 4.23A, D and E, respectively), while, large sized shrubs possess higher amounts of blade- and plate-shaped pores (Figs. 4.23B and C). However, the pore shape distribution can give a wrong impression about the dominating pore shape. Analysing the relative volume of the pore shapes, some of the box plot are overlapping (Fig. 4.23). The medium-sized shrubs have a lower volumetric contribution of rod- and plate-shaped pores (Figs. 4.23F and H respectively) and a significantly higher volumetric contribution of cube-shaped pores (Fig. 23I). The volumetric contribution of blade- and cuboid-like shapes (Figs. 4.23G and J respectively) is not significant. These results indicate that large sized shrubs have typically rod- and plate-like shapes, and medium sized shrubs have usually cube-like shapes.

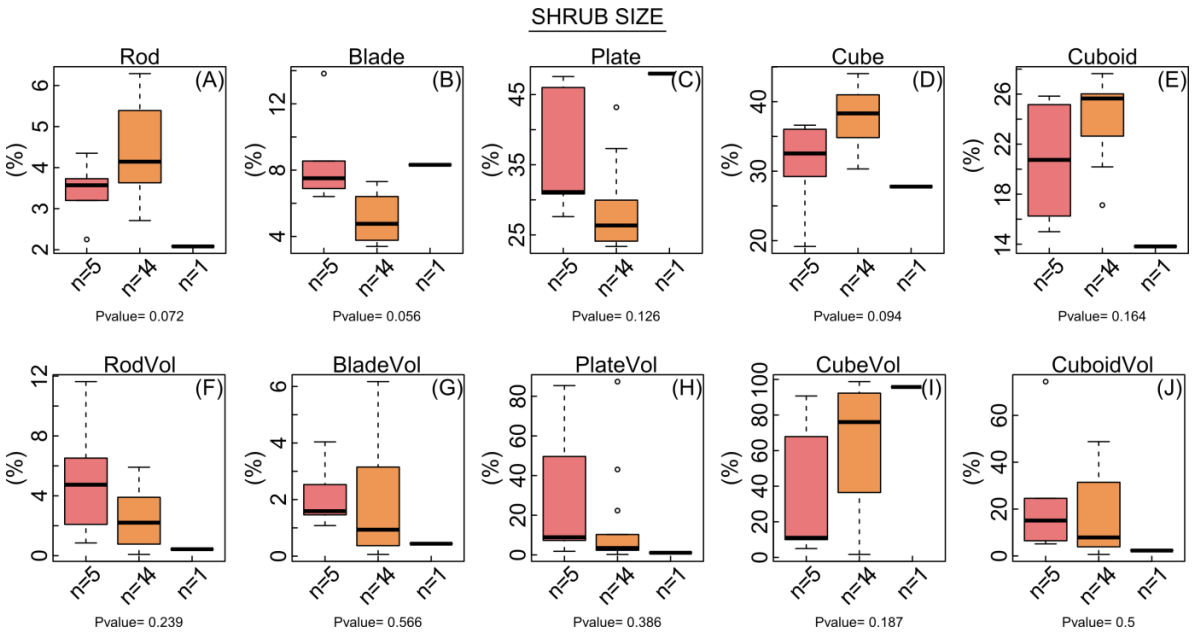

Fig. 4.23: Box plots with p-values of shrub size in function of (A to E) pore shapes, and (F to J) pore volume. Large sized shrubs (in red color) possess higher amounts of blade and plate shaped pores, however rod and plate like shapes is the volumetric dominant pore-type. Medium sized shrubs (in orange color) have a significantly higher amount of rod, cube and cuboid shaped pores, but the dominant pore shape is cube, because the latter is volumetric dominant. The small sized shrub sample (black line) possess mainly blade and plate-shape pores, however, cube like shape is the volumetric dominant pore-type.

Shrub Size Sorting

The box plot differences between the shrub size sorting and pore shape distribution (Figs. 4.24A to E) are not significant. However, the volume percentage of different pore shapes indicates that well size-sorted shrubs possess higher amounts of bladeVol (Fig. 4.24G) and cuboidVol (Fig. 4.24J). The center lines of the blade and cuboid volumetric contributions from the well size-sorted shrubs plot above the 75th percentile of the poorly size-sorted shrubs. This result indicates that well size-sorted shrubs have typically blade and cuboid like shapes.

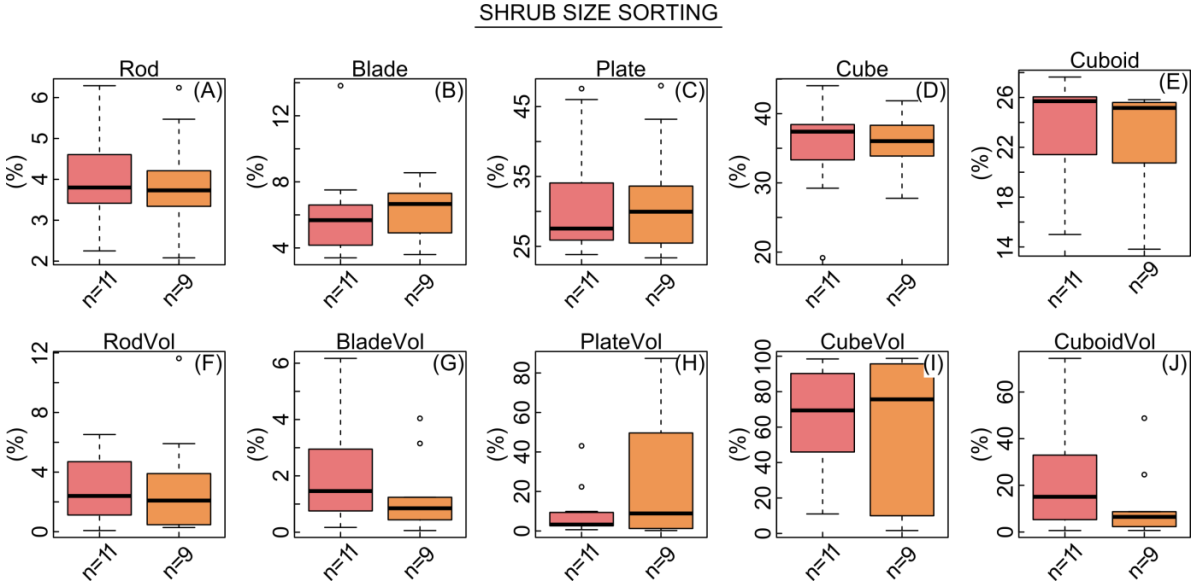

Fig. 4.24: Box plots with p-values of shrub size sorting in function of (A to E) pore shape distribution, and (F to J) pore volume. (A to E) Pore shape differences in function of shrub size sorting are not significant. (F to J) The pore volume in function of shrub size sorting indicates that the dominant pore shapes in well sorted (red color) shrubs are the blade (G) and cuboid (J) like shapes. Red color corresponds to well size-sorted shrubs and orange color to poorly sorted size shrubs.

Shrub Packing

Box plots of packing in function of pore shape distribution (Figs. 4.25A to E) indicate that open packing have a significantly higher amount of rod-, cube- and cuboid-shaped pores (Figs. 4.25A, D and E) and significantly lower amount of blade- and plate-shaped pores (Figs. 4.25B and C). The pore shape distribution for tightly packing shrubs is more heterogeneous than for open packing. Indicating that the main pore volume differences will be in the tight packing samples. As it was mentioned before, the dominant pore shape is given by the volume percentage of the different pore shapes.

The variation of the volumetric contribution of the pore shapes is higher for the tightly packed shrubs (Figs. 4.25F to J). The center lines of the volumetric contributions from the tight packing shrubs plot above the 75th percentile (Figs. 4.25F, G and J) and below 25th percentile (Fig. 4.25I) of the open packing shrubs. The box plots of plateVol in function of shrub packing possess p-values = 0.803 for a confidence level of 0.05 (Fig. 4.25I). So, the null hypothesis of significant differences for the shrub packing and plateVol is rejected. The volume percentage of different pore shapes in function of shrub packing indicates that tight packed shrubs possess higher amounts of blade (Fig. 4.25G) and cuboid shapes (Fig. 4.25J). This result indicates that tight packing shrubs have typically blade and cuboid like shapes.

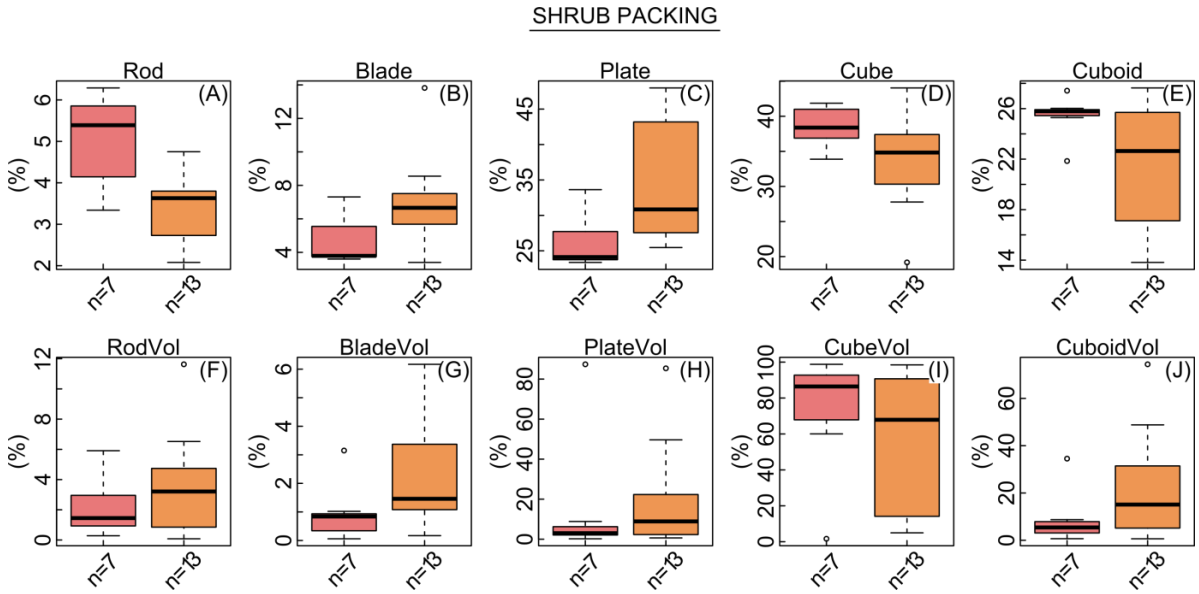

Fig. 4.25: Box plots with p-values of shrub packing in function of (A to E) pore shapes, and (F to J) pore volume. (A to E) Pore shape differences in function of shrub packing are not significant. (F to J) The pore volume in function of shrub packing indicate that the dominate pore shape in tight packing shrubs (orange color) are the blade (G) and cuboid (J) like shapes. Red color corresponds to shrubs with open packing.

4.4 Discussion

4.4.1 Shrub textures and their poro-perm characteristics

Rezende and Pope (2005) stressed the importance of the textures in the Pre-Salt reservoirs build by shrubs. Besides, the shrub geobodies in Tivoli have the dimensions of a small oil field, spanning several kilometers by several kilometers in width and length respectively and up to a few tens of meters in thickness. Very similar features and pore morphologies were described in huge oil fields from offshore Brazil and Africa (Dias, 1998, 2004; Terra et al., 2010; Wright, 2012; Rezende and Pope, 2015; Wright and Barnett, 2015; Saller et al., 2016), and the shrub-dominated lithologies generally form good reservoirs.

Shrub textures can vary considerably in morphology, size, size sorting and packing (Chafetz and Folk, 1984), and consequently, also in their petrophysical properties. The results indicate that the shrub morpho-type reservoirs are more complex than would be expected. As it was observed in Chapter 2 (Erthal et al., 2017), shrub morpho-types are strongly conditioned by the hydrodynamic conditions (fast flow to stagnant) of the precipitating water, which will

influence not only the morpho-types but also their sizes, size sorting and packing. So, the scattering of the petrophysical data is attributed to these textural heterogeneities. Actually, the size, size sorting and packing are the main textural controls on nuances in the variation of the petrophysical results for the different shrub morpho-types. These variations will consequently influence the shrub reservoir quality. Unless the depositional fabric is destroyed by diagenesis, petrophysical characteristics depend on the building blocks and their corresponding growth fabrics (Ahr et al., 2011; Claes et al., 2016).

Diagenesis can potentially impact porosity and permeability by modifying the original depositional textures, and consequently, the pore system. However, impact by diagenesis on the Tivoli shrub samples is considered to be of minor importance, based on textural evidences.

Besides the different shrub morphologies, the others textural (e.g. size, size sorting and packing) analysis of the shrub structures from Tivoli shows that shrub size sorting possesses a strong control on permeability and shrub packing on porosity. However, both textures also slightly influence, respectively porosity and permeability. Rezende and Pope (2015) already showed that shrub features from the Pre-Salt of Santos Basin (Brazil) have their petrophysical properties controlled by textural characteristics such as size, size sorting and packing. The latter authors obtained similar results as reported in this chapter.

It is likely that size sorting influences permeability by enhancing or reducing the tortuosity along which the fluids have to pass. More complex pore networks will result in lower permeabilities. From this point of view, it is also clear that the occurrence of multiple shrubs with different sizes in one sample will have a negative influence on permeability, but also on porosity. The presence of mm- to cm-scale laminae of encrusted bubbles, mats, plant moulds and rafts within shrub successions will also increase the tortuosity and consequently impact permeability. Moreover, the encrusted bubbles act as isolated mouldic pores, yielding increased porosities but low permeabilities.

Shrub size sorting possesses a "secondary" (minor) control on porosity, because it will also influence the adjacent space between each shrub, acting similarly to packing. In the studied shrubs from Tivoli, poorly sorted shrubs possess less space between the shrubs, resulting in lower permeabilities, but also in lower porosities. Generally, it is possible to affirm that well sorted and open packing shrubs result in higher porosity and permeability values in the shrub textures due to their textural control on the pore network (Rezende and Pope, 2015).

For size, medium sized shrubs possess higher porosities than large sized shrubs, which needs an explanation. More than one effect can influence this result, such as rock heterogeneities and different textures. Surely, the lithotype intercalations on mm- to cm-scale can create high porous and low porous shrub laminae, but this fact seems to influence more permeability than porosity. Applying a simple box plot of size sorting and packing in function of shrub size (Fig. 4.26), it is possible to notice that large sized shrubs possess more tight packing and poorly sorted textures than medium sized shrubs which possesses more open packing and well sorted textures (Fig. 4.26). This explains the better petrophysical results for medium sized shrub, also considering that tight packing and poorly sorted shrubs possesses the lowest porosity and permeability results.

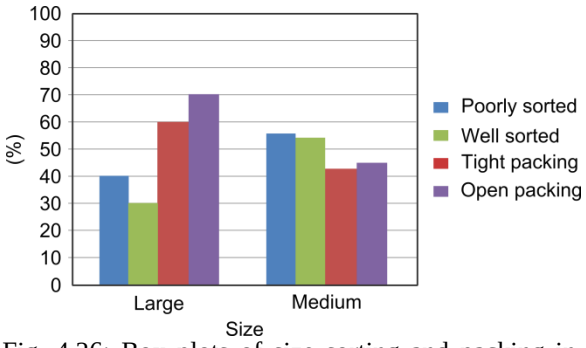

Fig. 4.26: Box plots of size sorting and packing in function of shrub size.

4.4.2 µCT and pore shape types

The µCT scan results show that shrub morpho-types have high pore connectivity marked by different pore shapes and types. This connectivity is mainly a reflection of the spatial distribution of the shrubs (shrub packing and size sorting) and their morphologies, which affect pore geometries and pore connectivity. The difference between total and open porosity

is less than 3%, meaning that the majority of pores are connected.

Shrub textures (e.g. morphology, size, size sorting and packing) generate complex pore networks. An example is given when the common intershrub growth framework porosity is observed in µCT images and they display a complex variation in shapes. The pore shape study allows comprehending the contribution of different pore shapes to the entire porosity network (Claes et al., 2016). According to the latter authors, more elongated shapes (i.e. rod and plate) have the potential to connect different pore clusters.

For statistically correct interpretations / conclusions, the number of analyzed samples of the different shrub morpho-types is insufficient. However, some observations could be made, as the shrub morpho-types can be distinguished based on the pore shape volume, even though morpho-types display overlapping results. The pore shape distribution can give a wrong impression about the dominant shape that has to be given by the volume percentage of the different pore shapes (Claes et al., 2016). It was observed that the volume of the plate-like shaped pores increases while the volume of cube-like shaped pores decreases (Fig. 4.22). It is also worth mentioning that the volumetric contribution of the cube-like shaped pores is associated with higher porosities, while the volume of the plate- and cuboid-like shaped pores display an opposite trend. According to Soete et al. (2015) rod- and cuboid-like pore shapes are strongly elongated in one-dimension, while cubic-like pore shapes are equidimensional, and blade- and plate-like pore shapes have a strongly flattened appearance. The samples dominated by cube-like pore shapes are mainly represented by vuggy porosity but also intershrub growth framework porosity. Furthermore, the cuboid shape is associated to intergrowth and interdigit growth framework porosity. Plate-like shapes are described associated to interlaminar, but also to interdigit porosities. Blade-like pore shapes are more usually observed associated with interlaminar pores, and rod-like shapes with reed lithotypes. The latter, however, was not observed associated with Tivoli shrub samples. So, the results indicate that the equidimensional cube-like shape transits towards more elongated cuboid- and plate-like shapes, meaning that the amount of vuggy pores decreases toward to plate-like shapes which predominates the intergrowth and interdigit framework porosity. This transition in the quantity of the dominated pore shape type occurring in all samples. So, this explains the overlap between the different shrub morpho-types in the graph of cubeVol and plateVol (Fig. 4.21), and also explains why different shrub morpho-types with intershrub growth framework porosity as the main pore type can have very similar as well as very different porosity and permeability results.

In addition, the influence of the shrub texture such as size, size sorting and packing on pore shape is also important. The medium sized shrubs possess a major volumetric contribution of cube like shaped pores, as well as highest porosities. The tight packing shrubs show the volumetric abundance of blade and cuboid pore-like shaped pores, as well as the lowest porosities. Moreover, well sized sorted shrubs comprise high volumetric contribution of blade and cuboid, and also represent the highest permeabilities. This brings us to the interpretation that blade- and cuboid-like pore shapes will mainly influence the pore connectivity (permeability results) because of their shapes. Blade and cuboid-shaped pores, with its flattened and elongated shapes (respectively), create long pathways, which can connect permeable zones in the sample. The distribution and shape of the pores play an important role in interpreting the relationship between poro-perm characteristics.

4.5 Conclusions

Petrophysical characteristics of the shrub lithotypes are controlled by their textures and pore shape types. Shrub morpho-types do not influence porosity and permeability results, but shrub size sorting, packing and shrub size do possess a relationship. The shrub size sorting comprises the complexity of the shrub sizes in the same sample. They strongly influence permeability and minor porosity. Shrub packing is the ratio between shrub width and adjacent spacing. They are the main control on porosity, but they also have a minor influence in the permeability. Shrub size sorting likely influences permeability by enhancing or reducing the tortuosity where the fluids have to

pass along, while packing influences porosity by modifying the space between the shrubs.

Shrub sizes, which are considered to correspond with longer linear length, show a relationship mainly with porosity, with the exception of small sized shrubs, likely due the fact that only one sample could be analyzed. Medium sized shrubs possess higher porosities than large sized shrubs, because the latter possess mostly tight packed and poorly sorted textures. In this way, the shrub sizes influence shrub size sorting and packing.

A 2D pore-type classification cannot fully incorporate and describe the complexity of these porous carbonate reservoirs. Micro-tomography imaging is used to render and evaluate the 3D arrangement of shrub morphologies, pore connectivity and porous framework. Differences in pore-types and shape, and their connectivity help to explain differences in porosity and permeability results, allowing to characterize the pore network accurately in 3D, which will, consequently, influence the hydraulic quality units that are controlled by pore geometry as a function of rock textures. Shrub morpho-types can be distinguished based on their pore shape volume. There exists a relationship between the volumetric contribution of the pore shape and porosity. The volumetric contribution of cube-like shaped pores is related with higher porosities and vuggy pores, while plate- and cuboid-like shapes present the lowest porosities and correspond to intergrowth and interdigit growth framework porosity. Besides, shrub size and packing also demonstrate a relationship between pore shapes and porosity. Cube-shaped pores possess a relationship with medium sized shrubs and higher porosities, while blade and cuboid pore-like shapes present mainly large shrubs with tight packing texture and low porosities. The same blade and cuboid pore shapes volume contribution were also observed to well size-sorted shrubs that possess a relationship with permeability. So, blade- and cuboid-like pore shapes will mainly influence the pore connectivity (permeability results) because they possess a flattened and elongated shapes (respectively), create long pathways, which can connect permeable zones in the sample.

The use of multi-method approach combining 3D µCT to classical 2D petrography and lab results must be applied to complex continental carbonate systems to achieve a better evaluation of reservoir characteristics. Besides, for a better understanding of complex shrub-dominated reservoirs, it is indispensable to characterize their textures and pore shapes in 2D and 3D. The scale at which the sample is analyzed is also important, since the shrubs are cm structures, micro-CT analysis was therefore the best approach. However, larger structures, with larger pore networks need an adapted scale study.

CHAPTER 5 Study of pore network and hydraulic unit characterization based on NMR and MIP measurements of travertine shrub morpho-types – Tivoli case study (Central Italy)

5.1 Introduction

Nuclear Magnetic Resonance (NMR) is an indirect method with enormous potential for characterizing petrophysical properties of saturated reservoir rocks (Kleinberg and Jackson, 2001). This method has been used extensively during the last decade in petroleum exploration (e.g. Vincent et al., 2011). Rock properties that can be derived from NMR measurements are porosity, pore size and estimated permeability but also parameters like the free fluid index (FFI), bound fluid (BVI), properties of reservoir fluids besides the typing of hydrocarbon content (Coates et al., 2001). The method is very simple, fast in its execution and it is not destructive. NMR parameters, in carbonate rocks, can sometimes vary in an unpredictable way being dependent on heterogeneity of the pore distributions, pore types, pore connectivity and grain size (Enos and Sawatsky, 1981; Lucia, 1983, 1995; Anselmetti and Eberli, 1993; Melim et al., 2001; Westphal et al., 2005). These complexities make permeability estimations on the basis of NMR-derived porosity particularly problematic for carbonates (Amabeoku et al., 2001).

Mercury Intrusion Porosimetry (MIP) is also a simple and fast method, however, after application of the technique the samples cannot be used anymore. The measurements determine the pore-throat size distribution, and measure directly the percentage of pore-space within a rock that is filled with mercury (non-wetting fluid) when a given amount of pressure is applied (Ausbrooks et al., 1999).

NMR and MIP are often comparable in terms of modal distribution (Vincent el al., 2011), thus both methods are complementary for rock-typing analysis, with NMR giving information on pore bodies and connectivity, while MIP providing information on the pore throat distribution.

Rock-typing, also termed in literature as types of flow units or Petrophysical Rock Types (PRT), is defined by Stalinski et al. (2009) as a type of rock characterized based on specific petrophysical properties. PRTs display distinct relevant relationships that characterize fluid flow. It is identifiable in well logs and it can be linked to geological attributes such as primary texture or diagenetic alterations. Thus, the concept of rock-typing considers not only lithological aspects (composition, texture, structure), but also petrophysical aspects (porosity and permeability), which directly influence the fluid flow capacity. In this way, distinct lithological aspects with similar porosity-permeability characteristics can be grouped in the same rock-type. Since the definition of rock-typing, it is recognized that often distinctive flow units exist inside a reservoir. Consequently specific flow properties should be associated to each flow unit.

To improve the understanding of the petrophysical characteristics studied in Chapter 4, and to have a better understanding of the pore network and connectivity among the different shrub morpho-types, the aim of this part of the study was to integrate NMR, MIP, petrophysical data (porosity and permeability), petrography and SEM analyses to perform a rock-typing of the different shrub morpho-types recognized in the Tivoli travertines. Furthermore, the Reservoir Quality Index (RQI) and Flow Zone Indicator (FZI) were calculated (Amaefule et al., 1993) with the aim to replicate the shrub morpho-types behavior as a reservoir.

5.2 Methods

5.2.1 Mercury Intrusion Porosimetry (MIP)

Twenty-three plug samples were cut in small pieces of ~ 2 cm for MIP measurements. The

aim was to compare the pore size data obtained by NMR and the pore throat distribution data acquired by MIP. The mercury injection measurements were performed at Petrobras Research Center (CENPES) and the equipment used was a Micromeritics Autopore IV that allowed determining the size distribution for pores with radii between 3.5 nm and 200 μm. The method measured the pore entrances (pore throats) and not the pores itself, meaning that some pores might only be accessible through smaller pore throats, a pitfall called "ink bottle effect" (Rigby and Gladden, 2000).

The MIP measurement is performed in two steps, first at low pressure and secondly at high pressure. In the low pressure regime the sample has the air and moisture initially removed from the pore system through a vacuum system. This is done to avoid possible air pockets and contamination issues (Giesche, 2006). The sample is then filled with mercury, while pressure is slowly increasing. This allows the mercury to infiltrate increasingly into bigger pores. In the high pressure regime the sample is surrounded by a hydraulic fluid and pressures up. When a threshold pressure of 2070 bar is reached, the intrusion is terminated and mercury is evacuated.

The volume of mercury intruding the pore space during the different pressure steps can therefore be related to a pore throat size. The measurements also allowed the estimation of porosity. The effective porosity of the sample is obtained by dividing the volume of mercury intruded at its highest pressure by the bulk volume of the sample.

The pore throat radii (r) can be calculated from the mercury capillary pressure curves (P) through the Young-Laplace formula (equation 5.1):

$$P = \left(\frac{2\sigma}{r}\right) cos\, \vartheta \qquad (5.1)$$

Where σ corresponds to the surface tension and ϑ to the contact angle, ranging within $90° \leq \vartheta \leq 180°$. The MIP curves are represented (equation 2) with pore throat radii as probability distribution of the pore throats (f(r)) versus mercury saturation (S) (Lenormand, 2003).

$$f(r) = \left(\frac{P^2}{(2\sigma * \cos\vartheta)}\right)\frac{dS}{dP} \qquad (5.2)$$

5.2.2 Nuclear Magnetic Resonance

Twenty-three samples were used for NMR analysis. The samples were measured at Petrobras Research Center (CENPES) and the equipment used was MARAN DRX2 (Oxford, England) with 2.2 MHz digital NMR spectrometer for ^{1}H isotope using the CPMG (Carr-Purcell-Meiboom-Gill) pulse sequence.

NMR refers to the response of atomic nuclei to the magnetic field (Coates et al., 2001). When subjected to an external static magnetic field (B_0), the nuclear magnetic moments of certain atomic molecule become aligned, in precession movement, around this field. Hydrogen (^{1}H), carbon (^{13}C), and sodium (^{23}Na), which are common molecular compounds found in the reservoir fluids (water or hydrocarbon), possess small magnetization aspects that can be detected by NMR tools (Fig. 5.1). This technique is applied on any nucleus that has an odd number of protons and neutrons or both (Coates et al., 2001), with hydrogen being one of the best nuclei to be measured. H^+ nuclei are abundant in reservoir fluids and have a strong magnetic moment, producing a strong signal in resonance mode (Coates et al., 2001). During NMR analysis, a magnetic field B_1 is generated to tilt the magnetization in a direction perpendicular to the static magnetic field B_0 (Fig. 5.1) (Vincent et al., 2011). The B_1 field must oscillate at a precise frequency depending on the B_0 value (Vincent et al., 2011), in the present study this corresponds to 2.2 MHz. The B_1 field is turned on for about 10 μs and then stopped. At the end of the pulse, the protons return to their original alignment, in a process called "nuclear magnetic relaxation". Magnetic relaxation is measured along the B_1 direction at regular time intervals.

During relaxation, an electric current is induced in a detection coil by the magnetization. The relaxation phenomena involves two distinct exponential processes affecting the magnetization decay rate: 1) the recovering of the initial alignment of the magnetization, governed by the constant time T_1 (longitudinal relaxation time), and 2) the magnetization governed by the relaxation time T_2 (transversal relaxation time), being the relaxation in a plane perpendicular to the static field B_0 (Fig. 5.1) (Coates et al., 2001; Rios et al., 2010; Vincent et al., 2011).

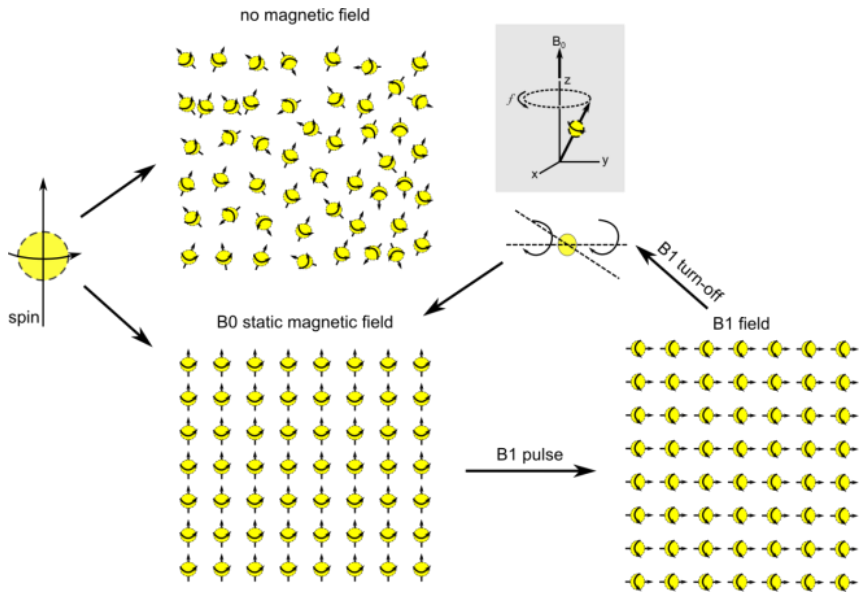

Fig. 5.1: Hydrogen nuclei magnetic properties. In the absence of an external magnetic field, the nuclear-magnetic axes are randomly aligned. The inherent nuclear magnetism makes the hydrogen nuclei behave as tine bar magnets aligned with the spin axes of the nuclei (B_0). A magnetic field B_1 is generated to tilt the magnetization in a direction perpendicular to the static magnetic field B_0. After the B_1 pulse is turned off, the protons begin a precessional motion around the magnetic field direction to return to their original alignment along B_0. The relaxation time (T_2) is measured along the B1 direction during this motion (Vincent et al., 2011).

The T_2 distribution is obtained by the Inverse Laplace Transform (ILT) using the software WinDXD 1.8.1.0 version. The result is shown in plots of amplitudes A_i as a function of T_2, called "distribution of relaxation times".

The NMR relaxation behavior can be used to derive pore sizes and permeability as it is related to the pore surface-to-volume ratio and physiochemical properties of the rock-fluid interface (Mohnke, 2014). Furthermore the NMR relaxation time (T_1 and T_2) can be linearly linked to the surface-to-volume ratio of a pore by a surface interaction parameter (mineral constituents), namely the surface relaxivity ρ_s (Torrey, 1956; Brownstein and Tarr, 1979; Kenyon et al., 1988; Kenyon and Kolleeny, 1995; Kleinberg, 1996; Fleury, 2007).

5.2.3 Reservoir Quality Index and Flow Zone Indicator

Flow units are obtained from the "Flow Zone Indicator" (FZI), defined by equation 5.3.

$$FZI = \frac{RQI}{\emptyset z} \tag{5.3}$$

The equation corresponds to the ratio between the "Rock Quality Index" (RQI) and normalized porosity (Øz).The Øz is the normalized porosity (equation 5.4).

$$\emptyset z = \left(\frac{\emptyset e}{1 - \emptyset e}\right) \tag{5.4}$$

The RQI contains the relationship between the permeability (mD) (absolute permeability) and effective porosity ($\emptyset_e$) with a value of 0.0314 as conversion constant between the units (equation 5.5).

$$RQI = 0.0314\sqrt{\frac{k}{\emptyset e}} \tag{5.5}$$

The equation indicates that for any hydraulic unit one should yield a straight line with a unit slope on a log-log plot of "Reservoir Quality Index" (RQI) versus "Normalized Porosity Index" ($\emptyset_z$) (Amaefule et al., 1993). The intercept of the unit slope line with Øz = 1, designated as the "Flow Zone Indicator" (FZI), is a unique parameter for each hydraulic unit. RQI, $\emptyset_z$ and FZI are based on He-porosity and permeability data measured on core samples (Amaefule et al., 1993).

5.3 Results

The study of reservoir rock-typing characterization requests information about pore types, pore sizes and pore throats, with the last two derived from NMR and MIP analysis, respectively. The shrub structures as it was already discussed in Chapter 4 present a complex pore network. For a better understanding of it, the study of NMR and MIP is important to assess the connectivity between the different pore compartments.

Petrographic observations showed that all shrub structures are covered by a thin sparry calcite cement surrounding a peloidal micritic aggregate nuclei (Chapter 2). This cementation provided a rigid framework to the shrubs, allowing preservation of primary porosity. Dissolution did not significantly affect either the porosity or pore connectivity within a sample. Dissolution mainly is related with the decay of the organic matter and the late telogenetic infiltration of meteoric fluids. The first is evidenced by mouldic pores and by microporosity observed under SEM in the core of the shrub stem (see Figs. 5G to L from Chapter 2). The latter dissolution is manifested by the existence of rounded sparitic crystals (see Fig. 5L, Chapter 2).

As mentioned in Chapter 4, the different shrub morpho-types (i.e. narrow dendriform shrub, wide dendriform shrub, fili dendriform shrub, arborescent, arbustiform and pustular shrub; see Chapter 2) are characterized by intergrowth framework porosity and secondary interdigit growth framework porosity. In addition vuggy, encrusted bubbles and rarely small (few mm) plant mouldic pores also occur.

5.3.1 NMR and MIP porosity

The initial NMR amplitude signal is a direct expression of the fluid volume present in the rock (Zhang et al., 2000). Applying an appropriate conversion factor, it is possible to estimate the porosity based on NMR initial amplitude of the decay curve, and MIP curve.

The NMR porosity varies between 6 and 19 %, with a mode of 8.8 %, while MIP possesses porosities between 0.5 % and 16.9 %. The good correlation between Archimedes and NMR porosity of travertines reported by Soete et al. (2015) demonstrates the reliability of the NMR measurements. Also in our case the Archimedes and NMR porosities display correlation between the two methods (correlation coefficient of 0.81) (Fig. 5.2).

In Fig. 5.2 it is observed that MIP porosities are much lower than NMR porosities, and there is no significant correlation between MIP and Archimedes porosities. MIP measures the mercury that is injected in the rock with a maximum pressure of 60000 psi. At this pressure the mercury can introduce pore throats as small as 3nm. Pores throat smaller than this measuring limit will not be reached, because mercury is a non-wetting element, and non-wetting fluids when invading a rock (drainage process) it is controlled by the size of the throat. The upper measuring limit of MIP method is 200 μm. Pore throats larger than 200 μm will be invaded without applying pressure and can thus not be quantified during the measurement. NMR measures the pore body size and not the pore throat size. The measuring limits of NMR instruments depend on the type and strength of the magnet, but usually vary between a few tens of a nanometer and centimeter scale. Given the fact that macropores with pore throats > 200 μm are largely missing from MIP pore size distribution (PSD) curves due to the measuring limit of the method, it is understandable that NMR yields higher porosities than MIP.

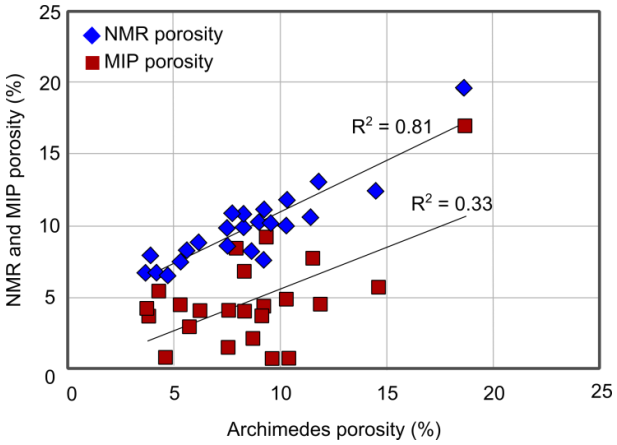

Fig. 5.2: Archimedes porosity versus NMR and MIP calculated porosity. It is observed a correlation between NMR porosity versus Archimedes porosity, and no correlation between MIP porosity and Archimedes porosity.

5.3.2 MIP and NMR pore-size distributions

The 23 shrub morpho-type samples selected for a detailed understanding of the pore network characteristics were plotted in porosity versus permeability cross plot (Fig. 5.3), and as it was observed in Chapter 4, there is no correlation between the results. Therefore NMR and MIP data were critically analyzed, where the connectivity between the different pore size compartments can be assessed. Results from both techniques are often combined since they yield complementary results and help the rock-typing analysis.

MIP is used to define micro-, meso- and macropores based on the pore throat radii (PTR) (Frank et al., 2005; Skalinski and Kenter, 2015; Faÿ-Gomord et al., 2016). They produce the pore volume behind pore throats of a given size, accessible at a given pressure. The MIP results showed 3 main pore-size classes, with micropores defined as pore-throat sizes of r < 1 µm (in line with Zinszner and Pellerin, 2007), mesopores for pore-throat sizes between r = 1 and 10 µm, and macropores between r = 10 and 200 µm (in line with Cantrell and Hagerty, 1999). The log mean of the pore throat radii is 59 µm. This mean value roughly corresponds to the point where most of the MIP curves deflect. Meso- and micropores are only observed in SEM analysis (Cantrell and Hagerty, 1999; Soete, 2016).

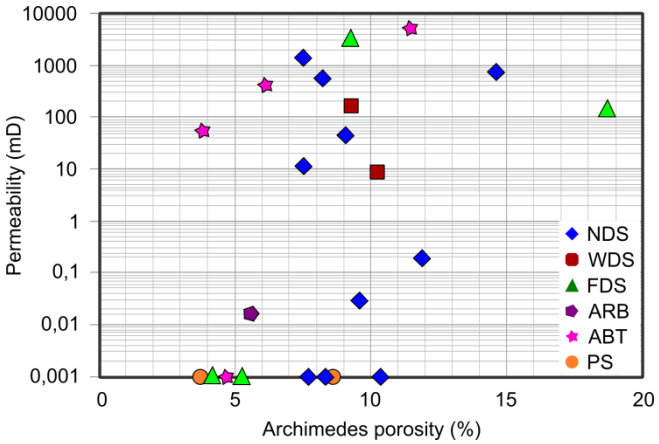

Fig. 5.3: Porosity – permeability cross plot of the shrub morpho-types samples that were analyzed by MIP and NMR methods. NDS corresponds to narrow dendriform shrub, WDS to wide dendriform shrub, FDS to fili dendriform shrub, ARB to arborescent, ABT to arbustiform and PS to pustular shrub morpho-types.

The NMR T_2 distribution obtained for fully saturated samples reflects the distribution of volume/pore surface (V/S) ratios which includes a shape factor as well as rugosity (Vincent et al., 2011). They are often called "Pore size distributions" (PSDs). The analyzed NMR T_2 distributions plot between 0.1 and 10000 ms. T_2 distributions show a remarkable correlation with PTR distributions. The NMR and MIP curves show unimodal and bimodal distributions. Based on this distribution, the samples could be subdivided into 3 groups, namely:

Group 1: with unimodal response in both NMR and MIP (Fig. 5.4);

Group 2: with bimodal NMR distribution curves and unimodal MIP curves (Fig. 5.5), displaying limited correspondence;

Group 3: with bimodal NMR and MIP distributions (Fig. 5.6), with well-developed peaks for both macro- and microporosity.

The separation of the groups in the distributions is in correspondence with the point where NMR and MIP curves deflect. The different groups are distinguished mainly by the presence of microporosity in NMR and MIP curves, as will be explained below.

Group 1: Unimodal NMR and MIP curves

In Group 1, NMR and MIP curve patterns are unimodal (Fig. 5.4A and B). The primary peak in the NMR T_2 distribution curve occurs between 200 to 10000 ms (Fig. 5.4A). This interval corresponds to the meso- and macropores. Below 200 ms, NMR curves from Group 1 are not completely flat. In this interval, the curves present a rough pattern suggesting the presence of very low amount of micropores. The amount of micropores is so insignificant that a secondary peak in NMR curve is not established.

MIP curves possess a primary peak occurring between 8 and the limit of technique 200 μm (Fig. 5.4B) which again reflects meso- and macropores. As for the NMR curves, MIP displays a faint pattern of pore throats below 8 μm, which corresponds to micro- and mesopores. The similarity between the distributions confirms the strong dominance of macropores and limited presence of meso- and micropores for group 1 samples (Fig. 5.4C).

The main pore-type is intergrowth / interdigit growth framework porosity (Figs. 5.4C and D). The shrubs are characterized by aggregated nuclei of peloidal micrite that are surrounded by a dense sparry calcite cement (Fig. 5.4D). Under SEM, meso- and micropores occur isolated and they are rarely observed. When they occur, it is mainly in the central part of the shrubs, but also in the sparite calcite crystals that cover the shrubs (Figs. 5.4E and F).

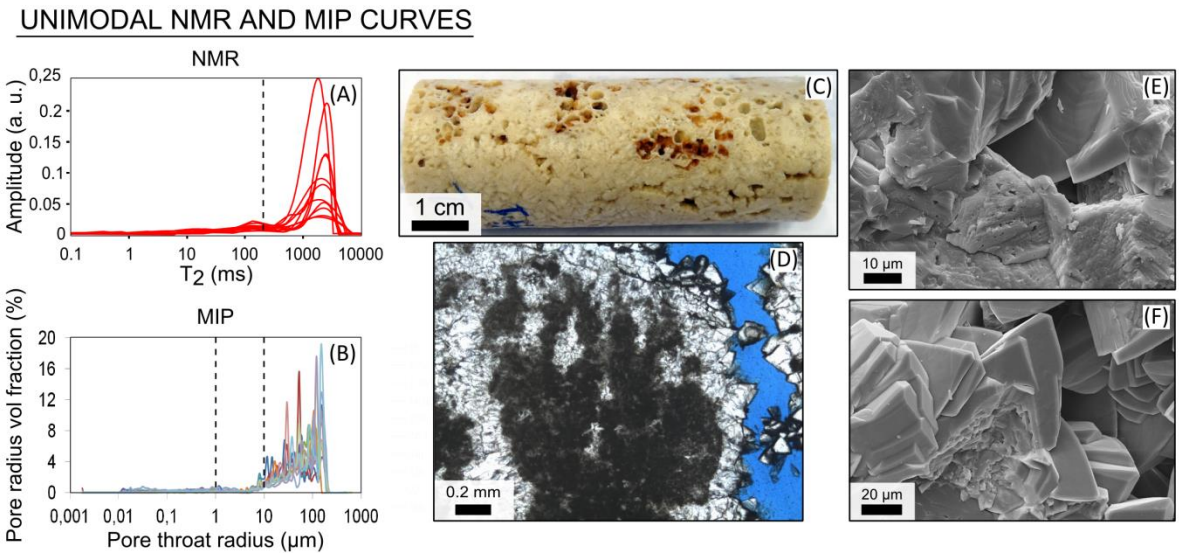

Fig. 5.4: Group 1 samples displaying (A) unimodal NMR curves with very short amplitude of the secondary peak (present at the left side of the dotted line) and (B) unimodal MIP curves with very short amplitude below 8 µm, related to micro- and mesopores. (C) Representative shrub sample of Group 1. (D) Microscopy image of a shrub sample from Group 1. Notice the growth framework porosity and the shrub with a peloidal micritic aggregate making up the inner part of the structure. The latter is surrounded by a clear sparry calcite cement. (E and F) SEM images illustrating micropores in the sparry calcite cements.

Group 2: Bimodal NMR and Unimodal MIP curves

In this group, NMR curves are bimodal (Fig. 5.5A), while MIP curves possess an unimodal distribution (Fig. 5.5B). The primary NMR peak occurs between 200 to 10000 ms and the secondary peak exists between 8 and 200 ms. (Fig. 5.5A). The unimodal MIP only show a primary peak between 1 and 200 µm (Fig. 5.5B).

The main pore-type in Group 2 samples is also intergrowth / interdigit growth framework (Figs. 5.5C and D). The samples are characterized by shrubs made up of a nucleus of peloidal micrite aggregates and sparry calcite covering them (Figs. 5.5D). Notice in Fig. 5.5D that the sparry calcite cement is locally micritized. In SEM intrashrub microporosity (< 1 µm) and isolated intergrowth framework pores were observed (Figs. 5.5E and F). The micropores appear isolated due to a non-porous sparry calcite coating (Fig. 5.5G).

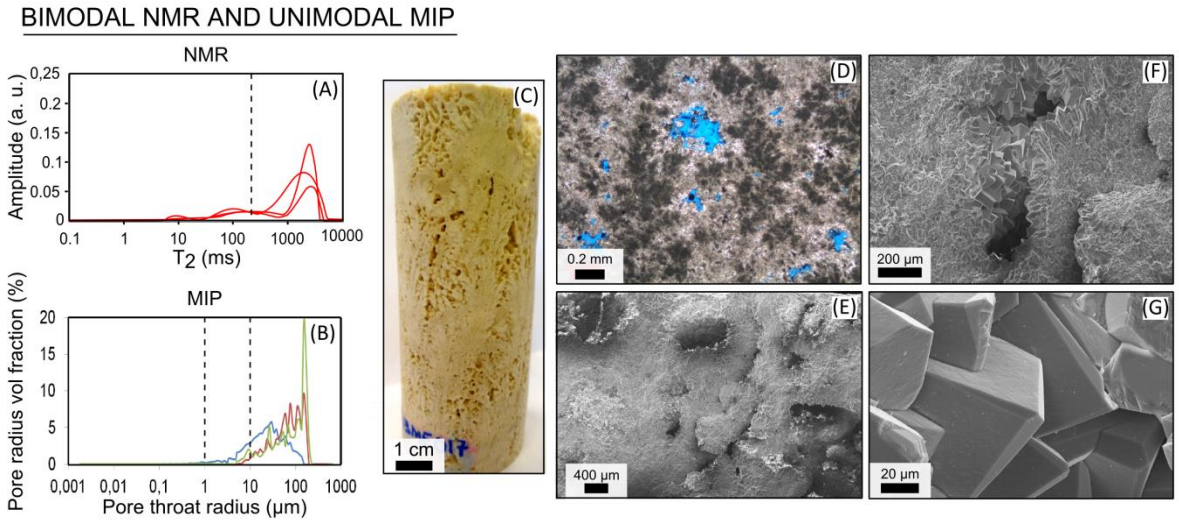

Fig. 5.5: Group 2 of (A) Bimodal NMR and (B) unimodal MIP. (C) Representative sample for Group 2. (D) Microscopy image showing micritization of the shrub structures. Notice that the intershrub growth framework pores are not continuous. (E) SEM images illustrating intrashrub pores. (F) SEM images showing the presence of intercrystalline pores and (G) absence of micropores within sparry calcite cements.

Group 3: Bimodal NMR and MIP curves

For the samples with bimodal distribution curves a secondary peak that corresponds to microporosity occurs between 8 to approximately 200 ms in the NMR distributions (Fig. 5.6A) and 0.01 to 1 µm in the MIP curves (Fig. 5.6B). The primary peak plots between 200 and 10000 ms in NMR (Fig. 5.6A) and between 8 and 200 µm (limit of the technique) in MIP curves (Fig. 5.6B).

The shrubs also possess dominantly intershrub / interdigit growth framework porosity (Figs. 5.6C and D) and are also characterized by peloidal micrite aggregates surrounded by sparry calcite (Figs. 5.6D and E). The sparry calcite that surrounds the peloidal micrite within the shrubs shows dissolution features and intense micritization (Fig. 5.6D). SEM images show abundant micropores in the shrub nucleus (Figs. 5.6E and F) that are associated to rounded to sub-rounded micrite, smaller than 1 µm in size (Fig. 5.6G). Micropores are also observed in the sparry calcite cements.

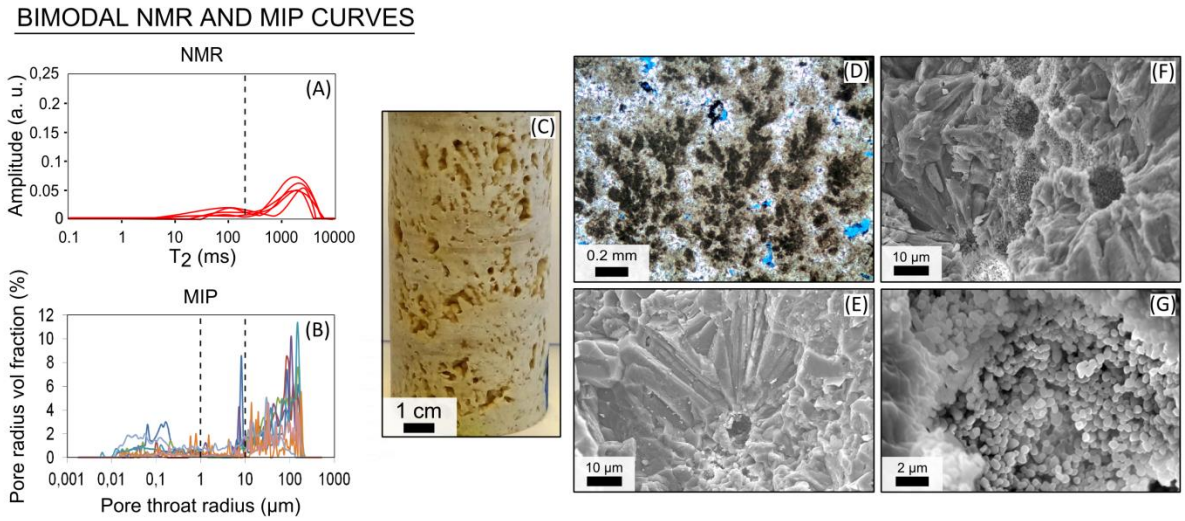

Fig. 5.6: Group 3 (A) bimodal NMR T_2 distribution patterns with a primary peak between 200 and 10000 ms and a secondary peak at relaxation times between 8 and 200 ms; and (B) bimodal MIP distribution patterns with primary peak between 8 and 200 µm and secondary peak between 0.01 to 1 µm. (C) Representative sample for Group 3. Notice growth framework porosity and vuggy pores. (D) Microscopy image showing strongly micritized shrubs (light brown color). (E to F) SEM images showing micropores within shrub structures. (G) SEM images of rounded to sub-rounded micrite (< 1 µm) in the inner part of shrub structure.

NMR curves, with T_2 relaxation times below 200 ms (bimodal distribution curves for NMR), were observed in Group 2 and 3. It is worth to mention that the micropore peaks in NMR present very low frequencies (however extending over a large range). These groups correspond to micropores encountered in SEM images. According to Vincent et al. (2011) and Brigaud et al. (2014), 200 ms T_2-time is therefore considered the upper threshold for microporosity. The corresponding micropores in MIP curves occur below 1 µm. MIP curves show that all samples possess meso- and macropores, however, micropores were only observed in noticeable amounts in Group 3.

Macropores in NMR distribution curves of the analyzed samples occurs below 10000 ms, and for MIP distribution curves below 200 µm (which corresponds to the limit of the technique) pore throat radius. It is remarkable that all samples showed the same T_2 relaxation time range for macro-porosity.

Figure 5.7 illustrates that groups defined on NMR and MIP patterns possess a relationship with permeability. Group 1 yield permeability values vary between 42 to 5255 mD (Fig. 5.7). Group 2 possesses permeabilities values between 8.6 and 148 mD (Fig. 5.7). Group 3 has permeability values varying between 0.001 and 0.2 mD, with an exception of one sample with a permeability value of 1263 mD (Fig. 5.7). All groups thus plot within the same range of porosity, i.e. between 3 and 18 %. However a clear separation is observed between the groups based on their permeability. Group 3 with the highest amount of micropores, possess the

lowest permeability results, followed by the Group 2 samples. Group 1 samples, with non- or very low micropore contribution, yield the highest permeabilities. One sample from Group 3 is plotted with very high permeability (Fig. 5.7). This is because the sample possesses large vugs. Group 1 possesses 4 samples with very low permeability due the high heterogeneity of the pore network.

The NMR and MIP groups do not show any correlation with any specific shrub morpho-type neither do the latter correlate with porosity and permeability results. The clustering of NMR and MIP groups in the porosity and permeability can be attributed to the presence and abundance of micropores, as they influence the porosity and fluid pathways. Sparry calcite cement coatings surround shrub structures and isolate the micropores from the rest of the pore system. Micropores contribute to the porosity, but often not to the connectivity in the sample. Meaning that, at a given sample porosity, higher micro- to macropore ratios will result in lower permeabilities.

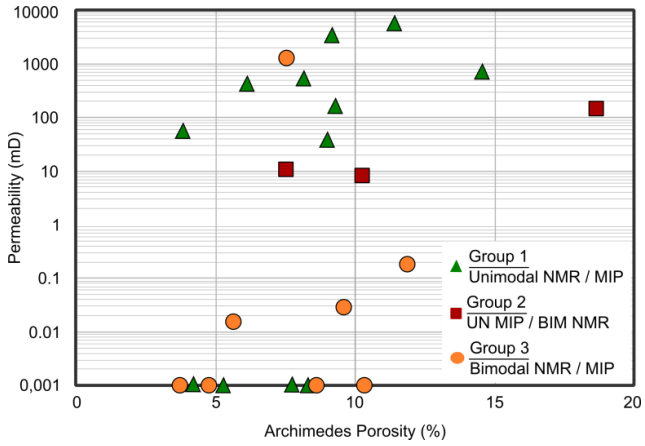

Fig. 5.7: NMR and MIP groups plotted in a porosity versus logarithmic permeability cross plot. Group 1 and 2 with the absent to low amount of micropores possess the highest permeability results, while Group 3 with abundance of micropores presents the lowest permeabilities. Higher amount of micropores are related with lower permeabilities. The micropores from Group 2 are mostly isolated from the macropores by the spary calcite cements that surround the shrub structures.

5.3.3 Correlation between pore parameters and shrub textures

In this section shrub morpho-type textures (i.e. morphologies, packing, size sorting and size), described in Chapter 4, is analyzed in function of pore parameters.

Shrub morpho-types

The log-mean of the transverse relaxation time (T_{2lm}), derived from NMR curves, and the pore radii, inferred from MIP curves, were plotted versus porosity (Figs. 5.8A and C) and permeability (Figs. 5.8B and D) as well as NMR porosity versus average pore throat (APT) (Fig. 5.8E) and, T_{2lm} versus APT (Fig. 5.8F). The T_{2lm} possesses values varying between 352 and 1117 ms, with an average of 838 ms. The APT sizes of the samples comprise values between 14 and 85 µm, with as average 60 µm.

In a graph of T_{2lm} versus porosity (Fig. 5.8A), it can be deduced that larger pore body sizes occur in more porous samples. However, there is no relationship between shrub morpho-types and pore sizes (Fig. 5.8A). The graph $T_{2(lm)}$ values versus permeability (Fig. 5.8B) suggests that larger average pore body sizes yield the highest permeabilities. Samples that plot at 0.001 mD (i.e., pustular, ABT, NDS and FDS) are not plotting along the general trend because of the high pore network heterogeneity within the samples.

Archimedes porosity and NMR porosity versus APT (Figs. 5.8C and E, respectively) demonstrate that higher porosities can go hand in hand with smaller pore throat sizes. APT does not correlate with permeability (Fig. 5.8D), however, the plot indicates that smaller pore throat sizes can have higher permeabilities. APT versus T_{2lm} also does not correlate (Fig. 5.8F), as smaller pore entrances can sometimes relate to larger pore body sizes.

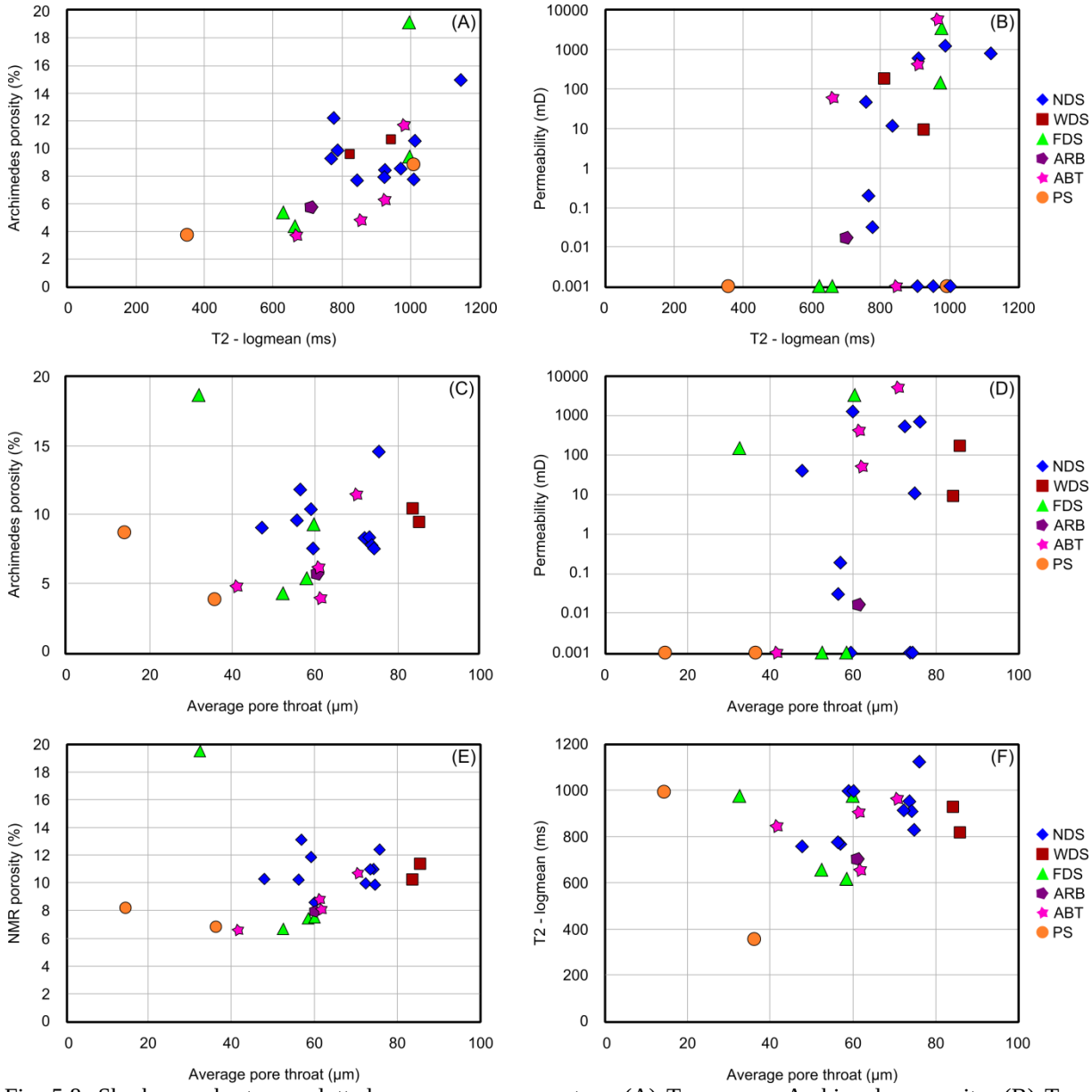

Fig. 5.8: Shrub morpho-types plotted versus pore parameters. (A) T_{2lm} versus Archimedes porosity. (B) T_{2lm} versus logarithmic permeability. (C) APT versus Archimedes porosity. (D) APT versus logarithmic permeability. (E) APT versus NMR porosity. (F) APT versus T_{2lm}. NDS corresponds to narrow dendriform shrub, WDS to wide dendriform shrub, FDS to fili dendriform shrub, ARB to arborescent, ABT to arbustiform and, PS to pustular shrub.

ANOVA statistical analysis was applied in order to test whether shrub morpho-types possess a relationship with T_{2lm} and APT (Figs. 5.9A and B). The variability calculations are based on the differences among the column means (intergroup variability) and differences between the data in each column and the column mean (intra-group variability). The F-statistics for plug scale T_{2lm} and shrub morpho-types equals 0.79 with a p-value of 0.57, while plug scale APT and shrub morpho-types yields a value of 6.81 and a corresponding p-value equal to 0.0012. For p-values below a pre-defined value of 0.05, the null hypothesis can be rejected. Box plots provide the possibility to graphically evaluate differences in the population mean for each shrub morpho-type (Figs. 5.9A and B). Notwithstanding the limited number of samples analyzed, some observations can be made. Box plots of shrub morpho-types in function of T_{2lm} (Fig. 5.9A) demonstrated no relationship with pore body sizes, as the results are overlapping. However, shrub morpho-types seem to display a relationship with pore entrances (Fig. 5.9B),

even though some morpho-types have their results overlapping. To have a statistical representative result, it would be necessary to increase the number of samples for each shrub morpho-type. Multi-comparison test was used to prove whether all shrub morpho-type groups have statistically different means (Figs. 5.10A and B). The result illustrate that the shrub morpho-types have means of T_2 (Fig. 5.10A) not significantly different. However, PS has APT mean (Fig. 5.10B) significantly different from all the others morpho-types.

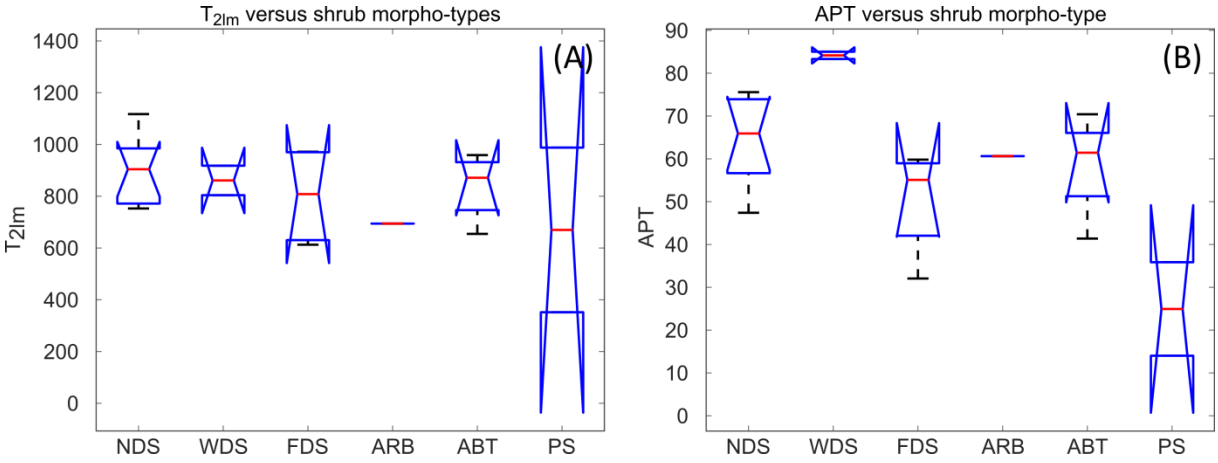

Fig. 5.9: Box plots of shrub morpho-types in function of (A) pore body sizes (T_{2lm}) and (B) average pore throat sizes (APT). NDS corresponds to narrow dendriform shrubs, WDS to wide dendriform shrubs, FDS to fili dendriform shrubs, ARB to arborescent, ABT to arbustiform and PS to pustular shrubs.

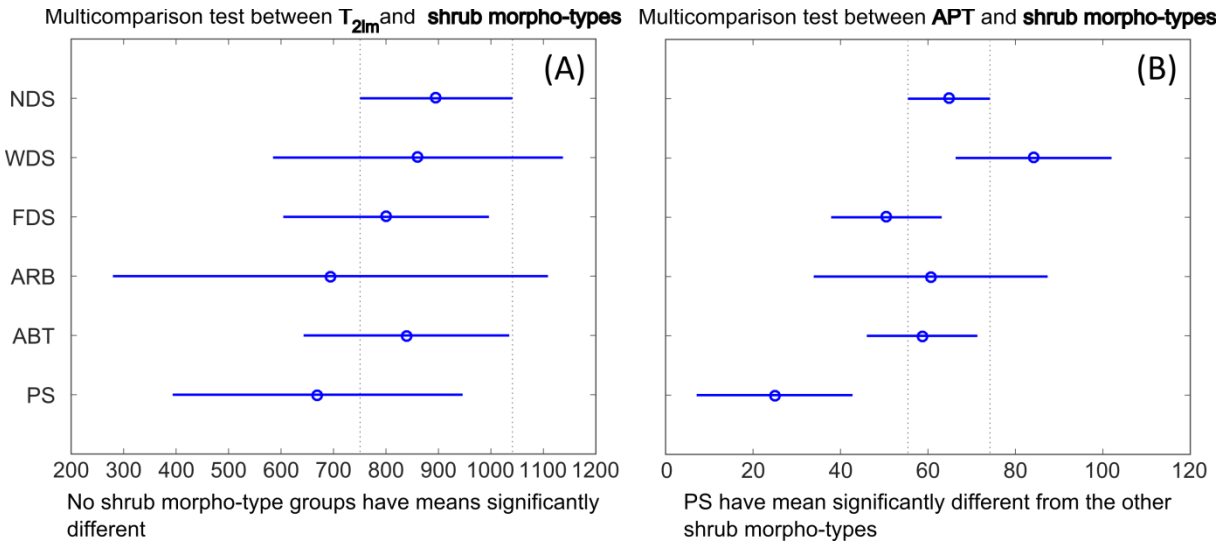

Fig. 5.10: "Multi-comparison" test graphs for shrub morpho-types in function of (A) T_{2lm} and (B) APT. NDS corresponds to narrow dendriform shrubs, WDS to wide dendriform shrubs, FDS to fili dendriform shrubs, ARB to arborescent, ABT to arbustiform and PS to pustular shrub.

When analyzing MIP curves in function of shrub morpho-types (Figs. 5.11A to F), it is possible to observe minute differences in pore throat size. The different shrub morpho-types yield differences in average pore throat sizes, with the largest APT sizes observed in WDS, followed by NDS and ABT shrubs. The smallest APT is encountered in pustular shrubs. The WDS MIP curves show a unimodal distribution, varying between 5 – 200 µm (limit of technique), with the main peak around 150 µm (Fig. 5.11B). FDS also possess MIP curves with unimodal behavior (Fig. 5.11C). Beside ABT being represented by only one sample, NDS and ABT shrubs yield very similar MIP distributions (Figs. 5.11D and E, respectively). They display unimodal curves, with minor to negligible secondary microporosity peaks. The average MIP

distributions plot between 8 to 200 µm (limit of technique), with a second minor contribution of pore radii between 0.01 and 8 µm. ARB and PS with only one measured sample each, possess bimodal curves (Figs. 5.11E and F, respectively), with main peak macropores between 5 to 200 µm (limit of technique) and micropores plotting between 0.01 and 1 µm. Larger pore throats are more abundant in ARB than in PS and the frequency of micropores is higher for PS than for ARB. The amount of smaller pore throats increases from FDS to NDS, ABT, ARB and PS, while they are absent in WDS. The number of samples for the different shrub morpho type populations has to be drastically increased in order to perform a statistical relevant analysis on the influence of shrub morpho-types on APT and T_{2lm}.

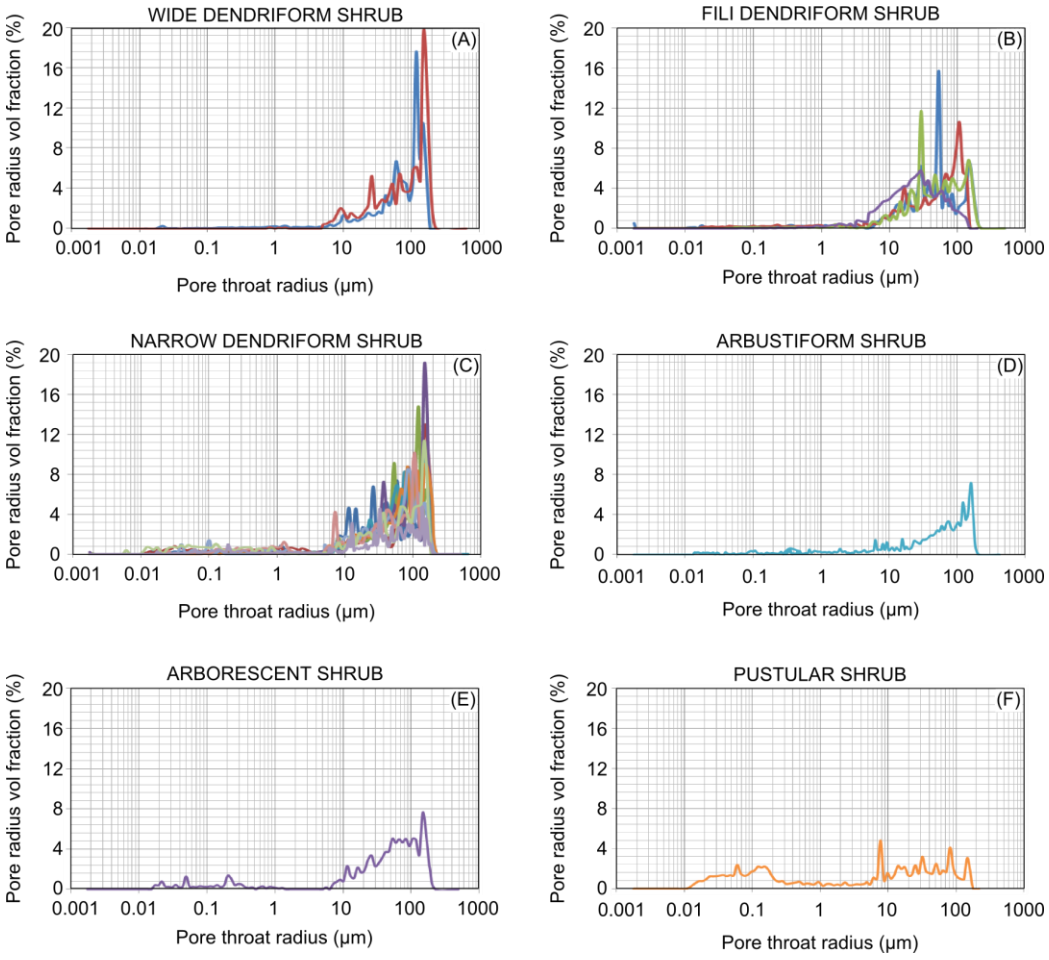

Fig. 5.11: (A) MIP curves for wide dendriform shrub showing a unimodal pattern with higher relative frequencies in comparison to other shrub morpho-types. (B) Fili dendriform shrub with unimodal MIP curve distribution. (C and D) Narrow dendriform and arbustiform shrubs displaying very similar MIP distribution curves. (E and F) Arborescent and pustular shrubs possess bimodal MIP distribution curves. However, arborescent shrub presents the highest frequency of macropores, while pustular shrub displays higher frequency for the micropores.

Shrub packing

The plot of T_{2lm} versus Archimedes porosity indicates that open packing corresponds to higher porosities (Fig. 5.12A). Figure 5.12B suggests that open packing also yields higher permeability and slightly larger pore body sizes. Shrub packing plotted in an APT versus Archimedes porosity plot (Fig. 5.12C) confirms the previously made observations (open packing corresponds to higher porosities) for T_{2lm} versus Archimedes porosity. No relationship is observed between APT and permeability in function of shrub packing (Fig. 5.12D). The APT versus NMR porosity plot (Fig. 5.12E) does not show a clear relationship between shrub packing and porosity. The plot between APT and T_{2lm} (Fig. 5.12F) suggests that higher pore body sizes (T_{2lm}) relate to a more open packing.

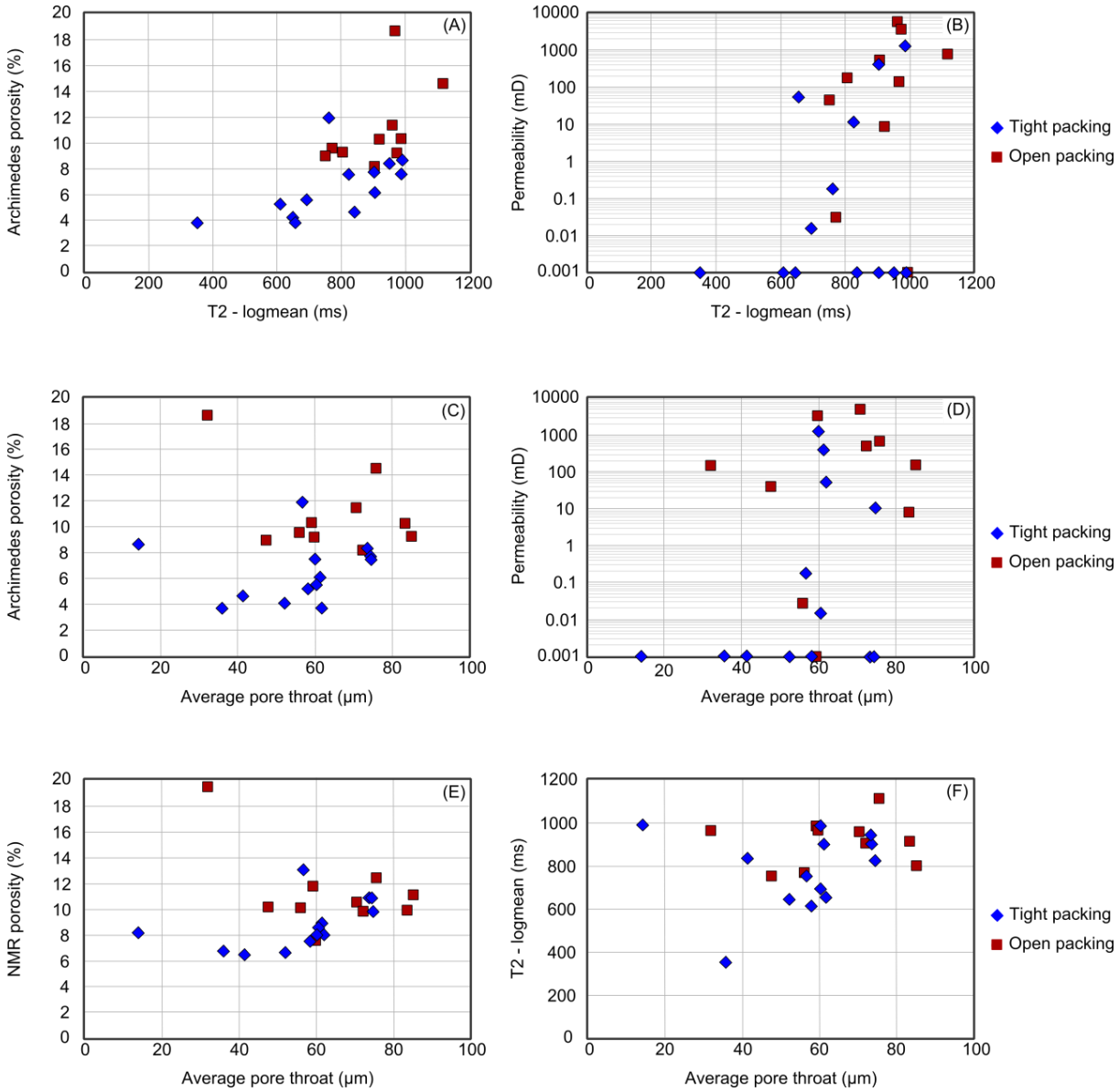

Fig. 5.12: **Shrub packing** plotted versus pore parameters. (A) T_{2lm} versus Archimedes porosity. (B) T_{2lm} versus logarithmic permeability. (C) APT versus Archimedes porosity. (D) APT versus logarithmic permeability. (E) APT versus NMR porosity. (F) APT versus T_{2lm}.

In order to test whether shrub packing exert significant control on pore body size (T_{2lm}) and pore entrances (APT) at plug scale, an ANOVA statistical analysis was applied (Figs. 5.13A and B). The ANOVA box plots statistical analysis for shrub packing in function of T_{2lm} (Fig. 5.13A) indicates that center lines of shrub *open packing* plot above the 75th percentile of the shrub *tight packing*. The box plots of APT in function of shrub packing (Fig. 5.13B) yields a p-value > 0.05, indicating that the null hypothesis of significant differences for the shrub packing and APT, is rejected. "Multi-comparison" test for T_{2lm} in function of shrub packing (Fig. 5.14A) also illustrate that means of open and tight packing are significantly different. Whereas, "multi-comparison" test for APT in function of shrub packing (Fig. 5.14B) show no significant differences.

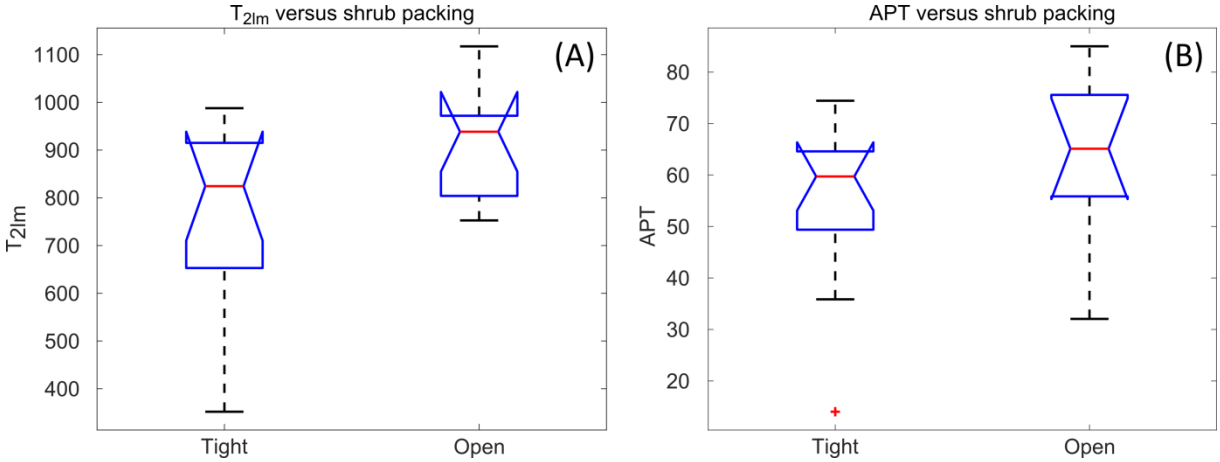

Fig. 5.13: ANOVA statistical box plots for **shrub packing** in function of (A) pore body sizes (T_{2lm}) and (B) average pore throat sizes (APT).

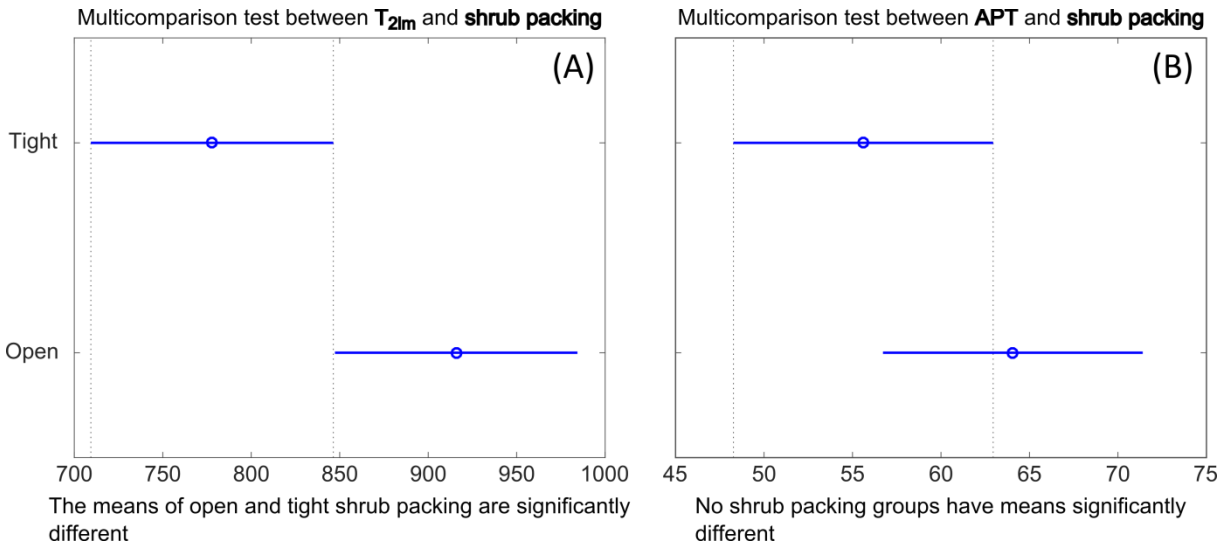

Fig. 5.14: "Multi-comparison" test graphs for **shrub packing** in function of (A) pore body sizes (T_{2lm}) and (B) average pore throat sizes (APT).

Shrub size sorting

The size sorting characteristics of the shrub morpho-types plotted in T_{2lm} versus porosity (Fig. 5.15A) does not clear relationships, however, "well sized sorted" shrub samples suggest slightly higher pore body sizes than "poorly sized sorted" shrubs (Fig. 5.15A). Nevertheless, both "well" and "poorly sized sorted" shrubs can have the same T_{2lm} values. The graph T_{2lm} versus permeability in function of shrub size sorting (Fig. 5.15B) indicates that i.e. "well sized sorted" shrub samples, yield higher permeabilities, and suggest slightly larger pore body sizes. The figure of APT versus Archimedes porosity in function of shrub size sorting (Fig. 5.15C) shows that "well sized sorted" shrubs also results in larger pore entrances. APT versus permeability (Fig. 5.15D) similarly indicates that "well sized sorted" shrubs yields the largest pore throat sizes and highest permeabilities. The graphic APT versus NMR porosity (Fig. 5.15E) only shows a relationship between shrub size sorting and pore entrances. APT versus T_{2lm} (Fig. 5.15F) suggests, despite the occurring overlap, that "well sorted" shrubs possess the largest pore entrances.

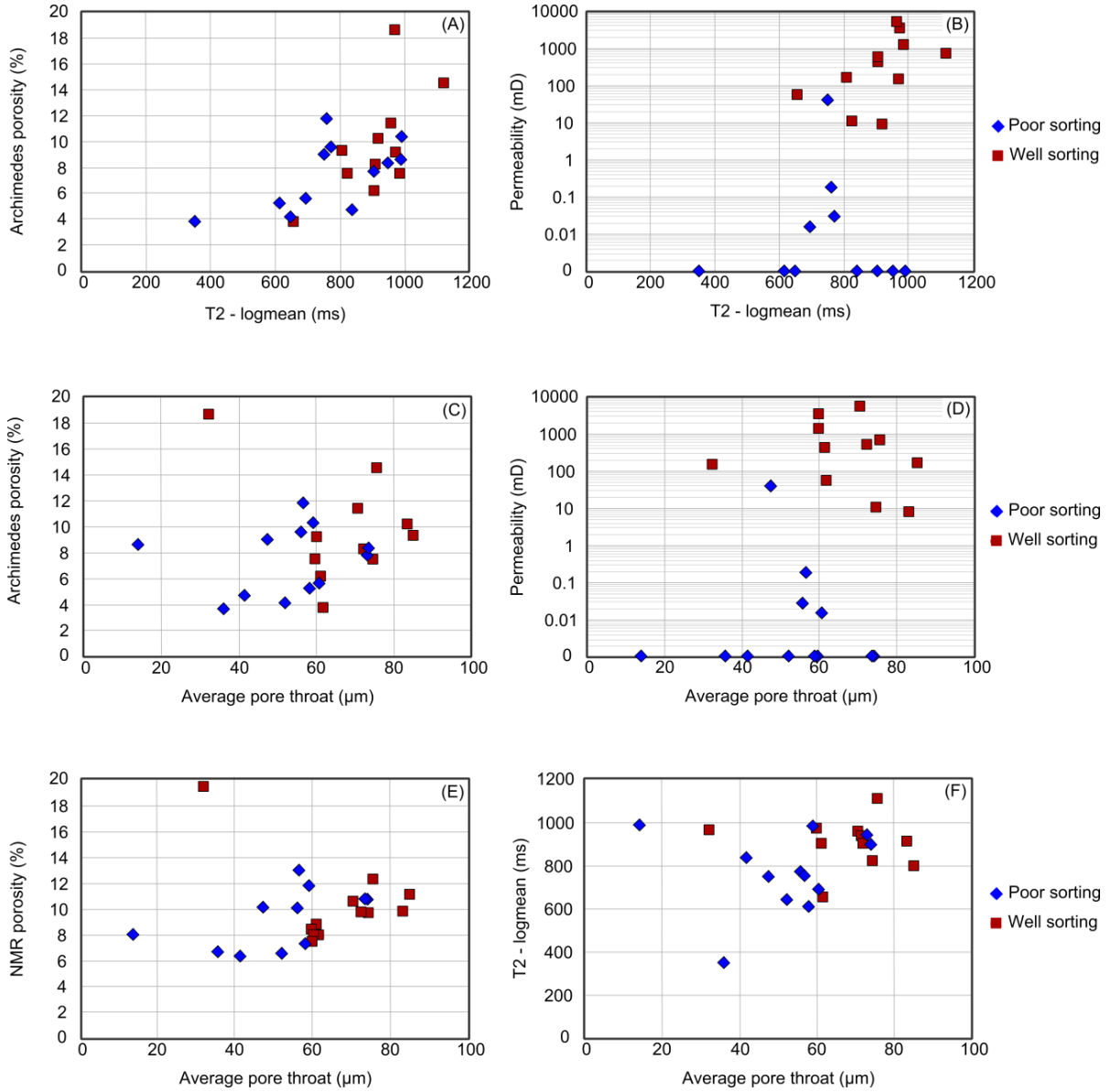

Fig. 5.15: **Shrub size sorting** plotted in pore parameter charts. (A) T_{2lm} versus Archimedes porosity. (B) T_{2lm} versus logarithmic permeability. (C) APT versus Archimedes porosity. (D) APT versus logarithmic permeability. (E) APT versus NMR porosity. (F) APT versus T_{2lm}.

ANOVA statistical analysis was applied to test whether shrub size sorting have significant control on pore body size (T_{2lm}) and pore entrances (APT) on plug scale (Figs. 5.16A and B). The box plots for size sorting and pore body size (Fig. 5.16A) indicate that center lines of the "well sized sorted" shrubs plot above the 75th percentile of the "poorly sorted" ones. This suggests that T_{2lm} is also influenced by shrub size sorting. Box plots of shrub size sorting in function of APT (Fig. 5.16B) attests that for $p<0.05$, the "well sized sorted" shrubs can be distinguished from "poorly sized sorted" shrubs. Larger pore entrances are attributed to "well sized sorted" shrubs (Fig. 5.16B). Multi-comparison test testify that both T_{2lm} and APT in function of shrub size sorting (Fig. 5.17A and B, respectively) indeed possess means of *well*- and *poorly sized sorted* shrubs that significantly differ. These results indicate that shrub size sorting link primarily to pore entrances (APT) and secondarily to pore body sizes (T_{2lm}).

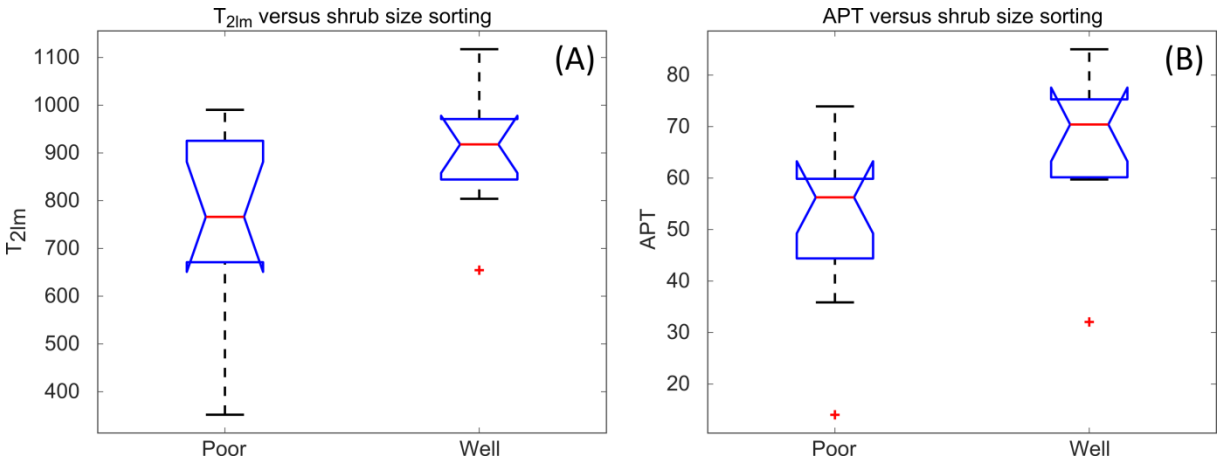

Fig. 5.16: ANOVA statistical box plots data for **shrub size sorting** in function of (A) pore body size (T_{2lm}) and (B) average pore throat sizes (APT).

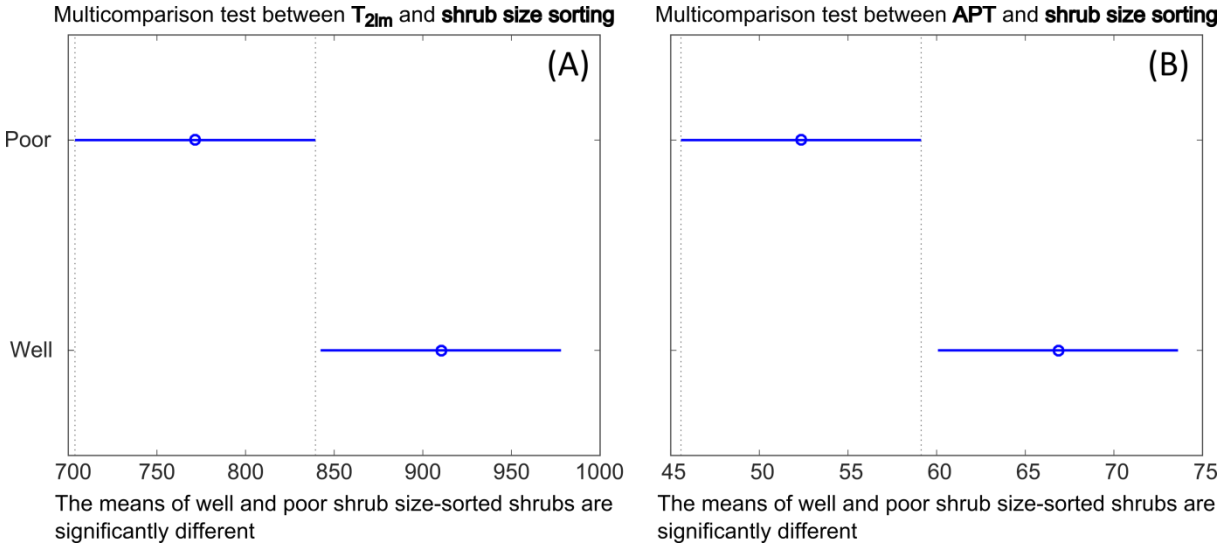

Fig. 5.17: "Multi-comparison" test graphs for **shrub size sorting** in function of (A) pore body sizes (T_{2lm}) and (B) average pore throat sizes (APT).

Shrub size

For the analysis of shrub sizes in function of pore parameters, first of all it has to take into account that only one sample was available with small sized shrubs. As this result has no statistical representativeness, the small shrub results can only be used as an indication compared to the other two groups (medium and large sized), or just for the evaluation of this sample.

Shrub sizes plotted in graphs versus T_{2lm} and Archimedes porosity (Fig. 5.18A) show that large and medium sized shrubs overlap in their distribution (Fig. 5.18A). However, medium sized shrubs possess the highest porosities and pore body sizes (T_{2lm}). The sample with small shrubs possesses the smallest pore body size and the lowest porosity value (Fig. 5.18A). Shrub size plotted in a figure of T_{2lm} versus permeability (Fig. 5.18B) does not show any relationship, but again the only one small sized shrub sample presents the lowest permeability and pore body size. APT versus Archimedes porosity (Fig. 5.18C) indicates that most of the medium sized shrubs possess larger pore entrance values, however an overlap with larger sized shrubs clearly is present. The graph between APT and permeability (Fig. 5.18D) does not display a clear relationship, however, the medium sized shrubs seems to plot in the field with higher permeability and higher pore entrances, but here again some overlap with large sized shrubs exists. APT versus NMR porosity (Fig. 5.18E) do not show an apparent relationship with shrub size, however, most of the medium sized shrubs possess somewhat

larger pore entrances. APT versus T_{2lm} (Fig. 5.18F) does not show an obvious relationship with shrub size, nevertheless the graph suggests that larger pore entrances are mainly associated with medium sized shrubs.

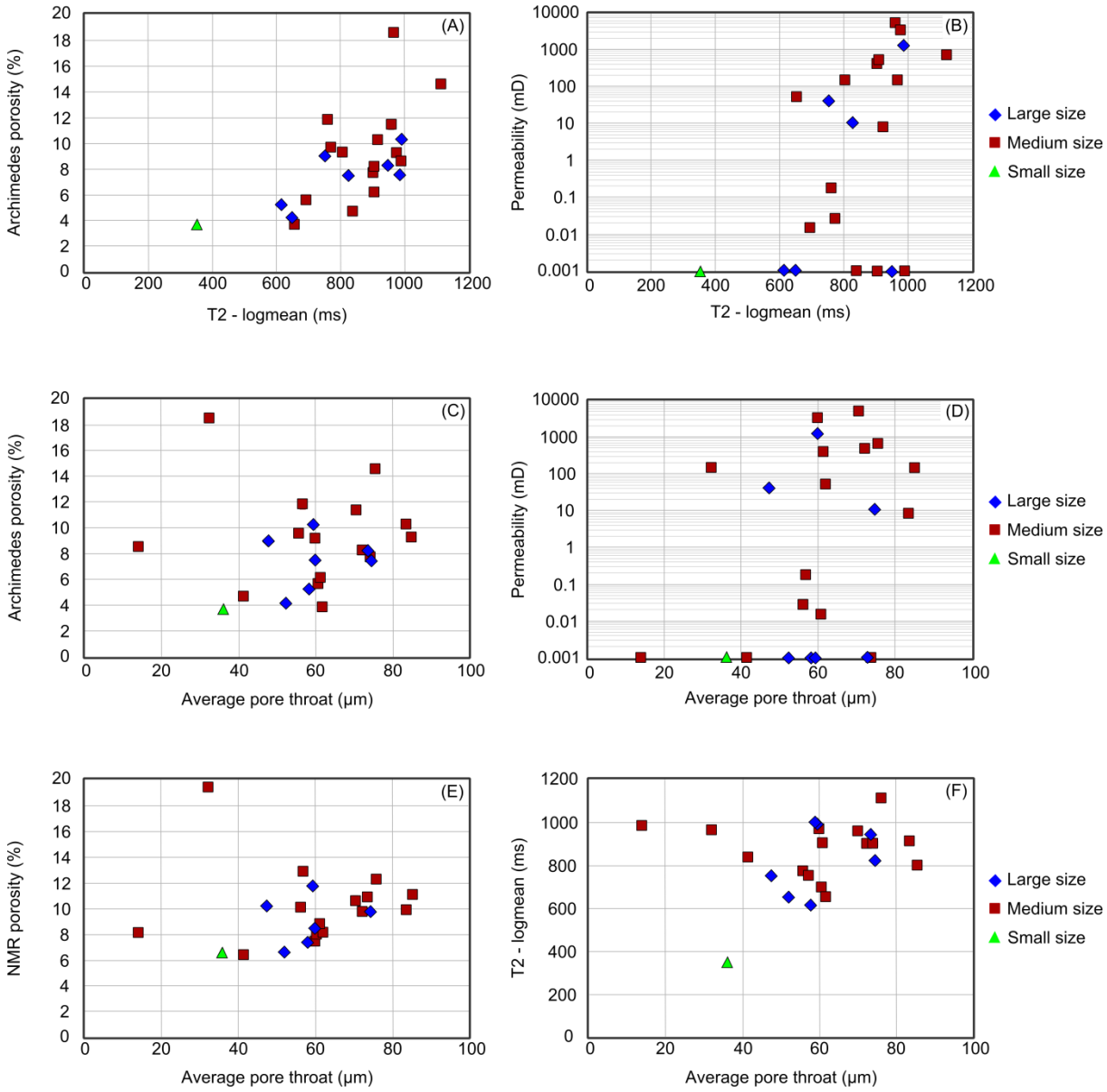

Fig. 5.18: **Shrub sizes** in function of (A) T_{2lm} versus Archimedes porosity, (B) T_{2lm} versus logarithmic permeability, (C) APT versus Archimedes porosity, (D) APT versus logarithmic permeability, (E) APT versus NMR porosity, and (F) APT versus T_{2lm}.

To test whether shrub size possess significant control on pore body size (T_{2lm}) and pore entrances (APT) on plug scale, ANOVA statistical analysis was applied (Figs. 5.19A and B). However, small sized shrub has no statistical representativeness, as mentioned before, because of this it was removed from the statistical analyses. Box plots of shrub size in function of T_{2lm} and APT (Figs. 5.19A and B, respectively) yields a p-value > 0.05, indicating that the null hypothesis of significant differences is rejected. "Multi-comparison" test for T_{2lm} and APT in function of shrub size (Figs. 5.20A and B) shows no significant differences.

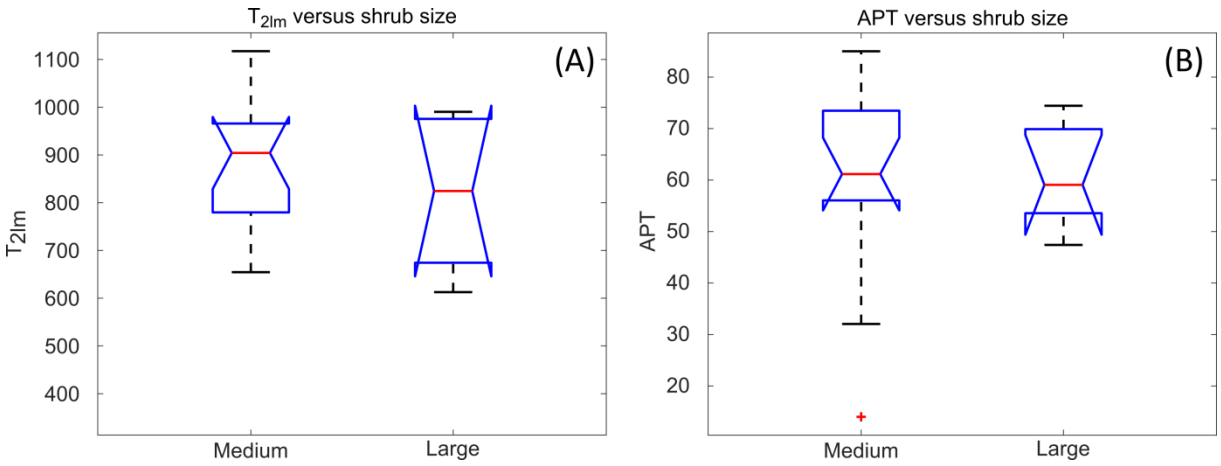

Fig. 5.19: ANOVA statistical box plots data for **shrub size** in function of (A) pore body size (T_{2lm}) and (B) average pore throat sizes (APT).

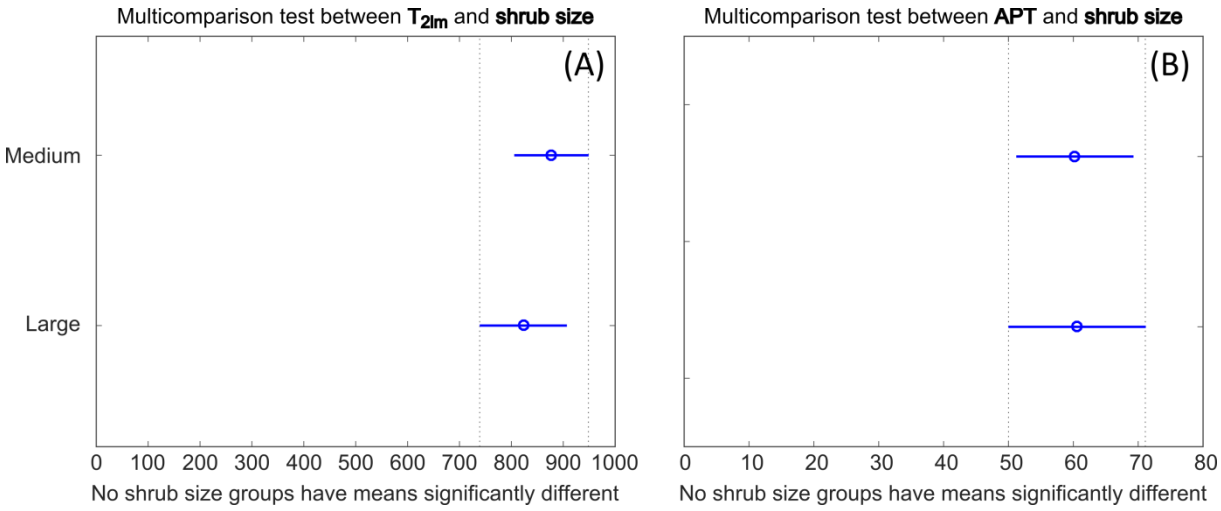

Fig. 5.20: "Multi-comparison" test graphs for **shrub size** in function of (A) pore body sizes (T_{2lm}) and (B) average pore throat sizes (APT).

In Chapter 4, a relationship between shrub packing and porosity and shrub size sorting and permeability was statistically demonstrated. Shrubs with open packing plotted mostly above 10 % of porosity, and well sized sorted shrubs above 10 mD. By applying these 'guiding limits' in the chart of porosity versus permeability in function of pore parameter groups (i.e. MIP and NMR groups), it is possible to observe that PSD- Groups 1 and 2, possess a relationship with well sized sorted shrubs (Fig. 5.21), while Group 3 bimodal samples mainly plot in the poorly sized sorted field with tight packing (Fig. 5.21). These results indicate that not only the micropores (mostly Group 3) influence the pore network connectivity, but also the size sorting of the shrubs. Open packing of the shrubs results in higher porosities but not systematically in higher permeabilities. The permeability is, however, observed for a well sorted shrub sample with an open packing.

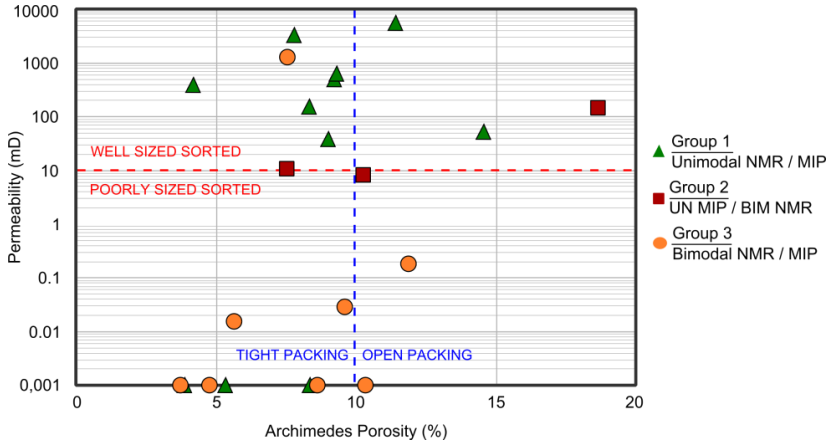

Fig. 5.21: Porosity versus permeability chart in function of NMR and MIP groups (i.e. Group 1, 2 and 3). The results show that Group 3, beside the presence of micropores influencing the flow properties and decreasing permeability, the shrub is also poorly sized sorted, which means the increasing of the flow pathways and decreasing even more the permeability.

5.3.4 Reservoir characteristics – Reservoir Quality Index (RQI) and Flow Zone Indicator (FZI)

Addressing reservoir quality is also an important part of the rock-typing exercise. The methodology for identification and characterization of hydraulic units within lithotypes (Amaefule et al., 1993) helps to identify heterogeneities observed in complex carbonate reservoir.

One hundred and twenty shrub samples were used to define RQI/FZI groups (Fig. 5.22), however, notice that only 23 samples were subjected to NMR and MIP analysis. The detailed RQI and FZI study could therefore only be performed for these 23 samples. The RQI/FZI groups from 120 samples were manually separated so that in each group about the same number of samples occurs (about 20 % of the samples in each group) (Fig. 5.22). As a consequence, the shrubs are separated in 5 RQI (Fig. 5.22) and 5 FZI groups, with group A possessing the lowest RQI and FZI values, and group E the highest (Table 5.9, Fig. 5.23). Group A can be classified as "non reservoir" rocks, while group B display poor reservoir characteristics, group C corresponds to a good reservoir, and group D and E reflects very good and excellent reservoir characteristics, respectively (Table 5.9, Fig. 5.23).

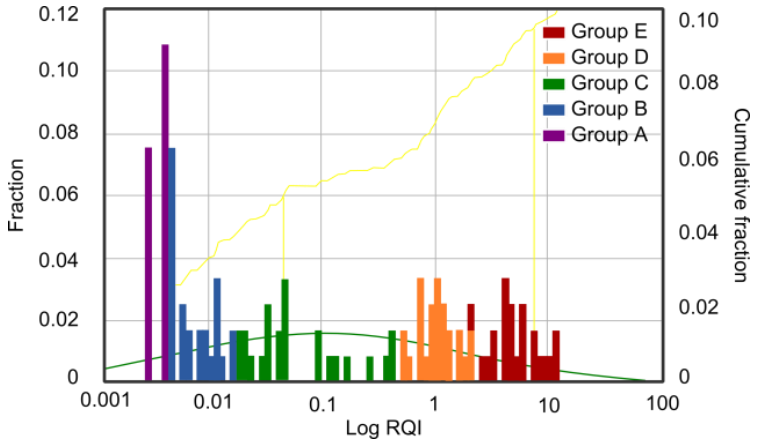

Fig. 5.22: Histogram of RQI groups. One hundred and twenty shrub samples are plotted in this graph, incorporating also the ones without NMR and MIP results.

Samples	Shrub morpho-types	Archimedes porosity (%)	Permeability (mD)	APT (μm)	RQI groups		FZI groups		NMR and MIP groups
QR15B	NDS	9.0	42.69	47.4	0.6	D	5.2	D	Group 1
QR15T	NDS	11.8	0.186	56.7	0.1	C	0.4	C	Group 3
QR17	NDS	7.5	11.06	74.4	0.4	C	4.9	D	Group 2
QR20	NDS	10.3	<0.01	59.1	<0.01	A	0.03	A	Group 3
QR22	NDS	8.3	<0.01	73.3	<0.01	A	0.04	A	Group 1
QR30	NDS	7.7	<0.01	73.9	<0.01	A	0.04	A	Group 1
QR34H	NDS	8.2	543.7	72.1	2.1	D	14.5	D	Group 1
QR35H	NDS	9.5	0.03	55.9	0.02	B	0.1	B	Group 3
QR116H1	NDS	14.5	707.7	75.6	2.2	E	12.8	D	Group 1
QR135H	NDS	7.5	1263	59.7	4.5	E	67.8	E	Group 3
QR31H	WDS	10.2	8.6	83.3	0.3	C	1.8	D	Group 2
QR38H	WDS	9.3	160	85.0	1.4	D	14.7	D	Group 1
QR24V1	FDS	5.3	<0.01	58.1	<0.01	B	0.1	B	Group 1
QR29	FDS	18.6	148	32.1	0.8	D	3.2	D	Group 2
QR33H	FDS	9.2	3409	59.8	4.5	E	22.2	E	Group 1
QR139V	FDS	4.2	<0.01	52.0	<0.01	B	1.4	D	Group 1
QR140H1	ARB	5.6	0.02	60.6	0.02	C	0.5	C	Group 3
QR117H	ABT	11.4	5255	70.4	6.0	E	35.2	E	Group 1
QR138H	ABT	3.8	54.6	61.7	1.3	D	37.4	E	Group 1
QR140H2	ABT	6.1	416.7	61.2	2.5	E	37.1	E	Group 1
QS11B	ABT	4.7	<0.01	41.4	<0.01	B	0.1	B	Group 3
QR103H2	PS	3.7	<0.01	35.9	<0.01	B	0.2	B	Group 3
QS032V	PS	8.6	<0.01	14.0	<0.01	A	0.1	A	Group 3

Table 5.9: Petrophysical properties, RQI, FZI and NMR/MIP groups from different shrub morpho-types (the latter shown in different colors). The letter "V" represents vertical plugs and "H" horizontal plugs.

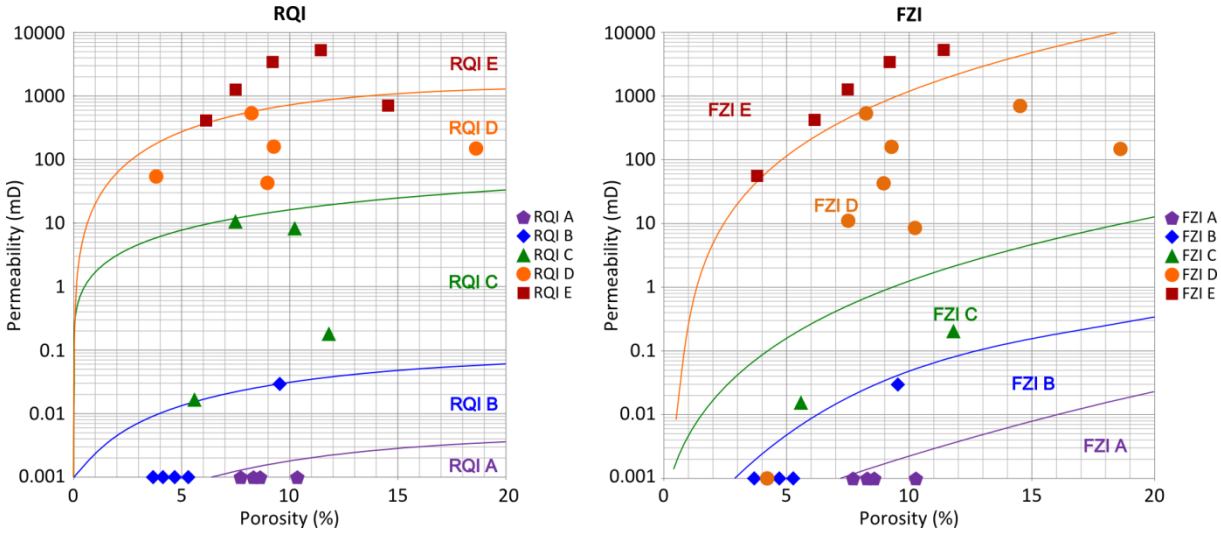

Fig. 5.23: RQI and FZI groups plotted versus porosity and permeability. Notice that group "E" possesses the highest permeability values, while group "A" the lowest values.

The pore throat radius distributions are also separated in 5 groups, in agreement with RQI and FZI zones (Fig. 5.24). The samples, here ordered by increase in hydraulic units, reflect increasing pore throat radii sizes and pore volumes (Fig. 5.24). Bimodal MIP curves, i.e., with micro- and mesopores in distribution, correspond to the groups A, B and C. FZI

groups A, B and C have higher micro- to macropore ratios than group D and E, which directly results in lowered reservoir quality. FZI groups D and E possess unimodal distributions (Fig. 5.24). Larger pore radii are generally more common in these samples, which is evidenced by the larger volume fractions of pore throats > 10 µm.

NMR and MIP PSD types can be distinguished with respect to RQI and FZI (Figs. 5.25A to D). No relationship is observed for NMR/MIP PSD types in the RQI, FZI versus porosity plots (Figs. 5.25A and D). The PSD types do, however, show a good correlation with permeability (Figs. 5.25B and D). It has to be noted that permeability has more influence on FZI and RQI, meaning that better correlations with permeability are expected. NMR/MIP PSD type 1 possesses the highest permeability values and RQI and FZI, followed by type 2. PSD type 3 yields the lowest permeability, RQI and FZI results.

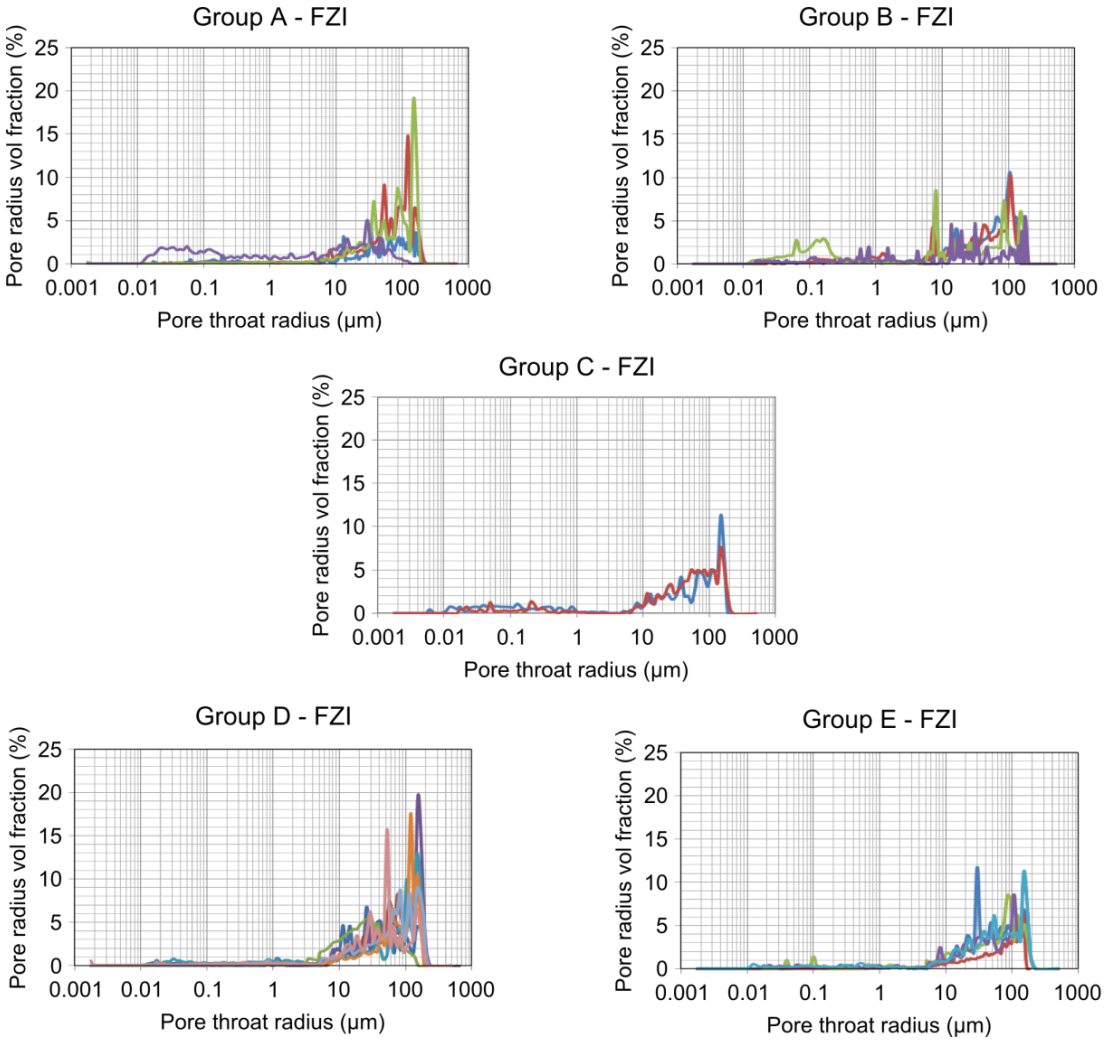

Fig. 5.24: Pore throat radius per hydraulic flow units A, B, C, D and E. Notice that groups A, B and C possess bimodal MIP curves, while groups D and E display unimodal MIP curves.

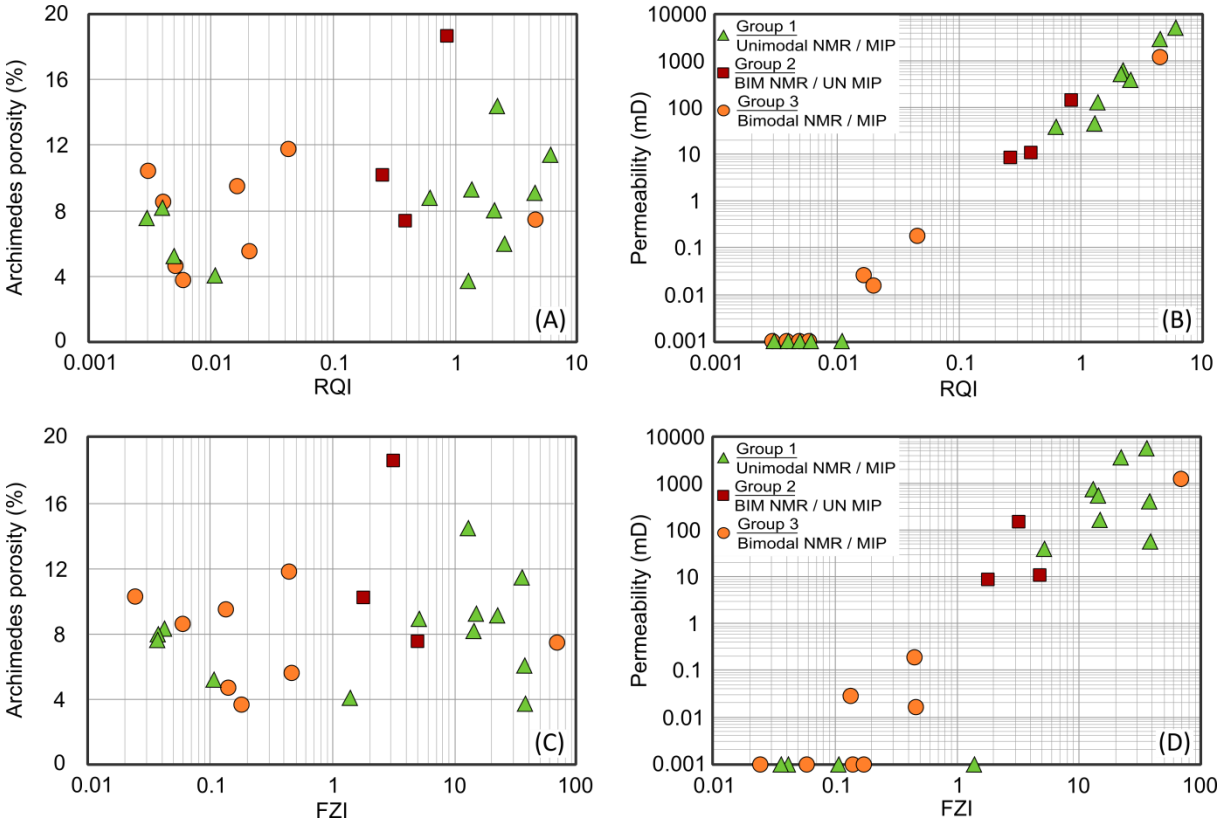

Fig. 5.25: NMR and MIP groups in function of (A) porosity and RQI, (B) logarithmic permeability and RQI, (C) porosity and FZI, and (D) permeability and FZI.

5.4 Discussion

There are no straightforward relationships between shrub morpho-types and their porosity and permeability. This is mainly due to pore network heterogeneities, which originate from complex fabric textures (shrubs and other lithotypes) at plug scale. The pore network alterations by diagenetic processes are considered minor for the studied samples. However, some cementation and dissolution does occur and affects the petrophysical characteristics of the shrubs.

To better understand the pore network heterogeneities and reservoir characteristics of the shrubs, an integrated analysis that incorporates NMR T_2 distribution patterns, MIP pore throat radii distributions, and petrography, is of major importance. Travertine samples are very heterogeneous on µm to mm and cm scale. It can therefore be questioned if 5 cm long plugs are sufficient to capture the Representative Elementary Volume (REV) of these shrub samples. REV results (see Chapter 6, table 6.1) demonstrate that REV was reached despite the heterogeneity of the samples.

5.4.1 Relationship between pore body and pore throat size

The distribution of MIP and NMR curves leads to the interpretation that the different primary shrub morpho-types can have similar pore network characteristics. All samples possess the same T_2 relaxation time range and the primary peak in MIP curves covers the same interval (between 200 and 10000 ms for NMR, and 8 and 200 µm for MIP). Micropores in NMR and MIP distribution curves are evidenced by a secondary peak in the curves. Most of the time, this secondary peak presents very low frequencies (as deduced from NMR and MIP curves). The absence or very low frequency of the secondary peak can be explained in two ways:

1) A very limited amount of micropores, i.e., samples have a low micro- to macropore ratio. 2) Pore compartment coupling depends on the presence of cements that potentially isolate microporous structures.

Three distinct Groups (i.e. 1, 2 and 3) distinguished based on whether or not a secondary peak could be differentiated in

NMR and MIP distribution curves. It was observed that Groups 1, 2 and 3 display a link with permeability, as permeability increases from Group 3 to Group 1. This indicates that the pore network properties quantified by NMR and MIP exert a strong influence on the petrophysical results. The unimodal NMR curve represented by Group 1 can be explained by the dominance of meso- and macropores aside the presence of micropores that mainly occur in the peloidal micritic aggregates in the nucleus of shrubs. The latter are isolated from meso- and macropores by the presence of sparry calcite cement (Fig. 5.26). The latter is sealing the connectivity between micropores and the meso- and macropores (Fig. 5.26). The very low response of NMR and MIP in Group 1 at short relaxation time or at small pore throat sizes respectively, can be explained by equipment noise, but this is a very unlikely option, since this type of error is usually very low, and it did not systematically occurs. Another, more plausible explanation would be that micropores are present in the samples, but in negligible quantities.

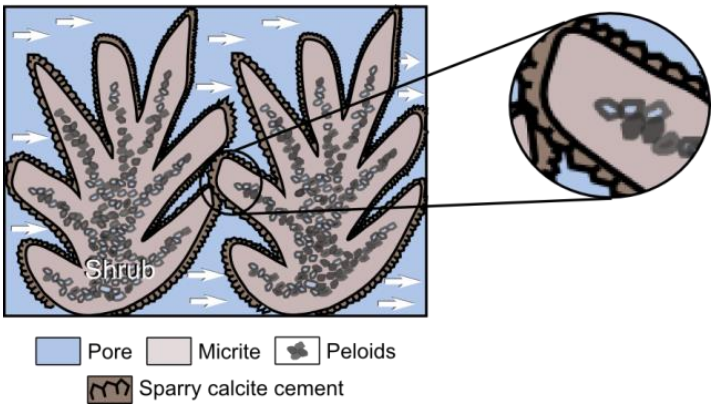

Fig. 5.26: Illustration for Group 1 showing the sparry calcite cement surrounding the shrub structure, isolating the micropores from the peloidal micritic aggregates in the nucleus of the shrub from the meso- and macropores.

In Group 2, the question to be addressed is why MIP curves do not show the presence of micropores, while NMR curves indicate their existence. Micropores were observed on SEM analysis; however, the shrub structures in which the micropores occur were covered by sparry calcite cements, isolating most of the micropores from the rest of the rock. So, it is likely that the volume of the connected micropores accessible for mercury during MIP measurements is very low and under the detection limit of the MIP equipment. It has also to take into account that samples for MIP measurements are 5 times smaller than for NMR measurements. In this way, the limit amount of sample that is used for MIP measurements could be the reason why the volume of micropores did not reach the MIP detection limit. Moreover, NMR secondary peak already show that the amount of micropores is very limited.

Bimodal NMR and MIP samples (Group 3) are attributed to decoupled pore compartments (Soete et al., 2016) detectable for both MIP and NMR techniques. As in Group 2, sparry calcite cement surround shrub structures and decouple the abundant micropore compartments from meso- and macropore compartments and limit the connectivity (< 10 mD). However, alterations of the rock fabric, with for example micritization of calcite rims, occur and might explain why larger volumes of micropores are accessible and thus detectable during MIP measurements. The bimodal pattern of the NMR distributions shows that molecules are not able travel from micropores to larger pore compartments during NMR measurements. So, however accessible during high pressure stages in MIP measurements, the micropores are not sufficiently coupled to provide fluid flow. The decreasing permeability from Group 1 to Group 3 indicates that the ease of flow in shrub samples decreases with increasing microporosity, or in other words with increasing micro- to macropore ratios.

5.4.2 Pore parameters and their relationship with shrub textures

As shown in Chapter 4, shrub morpho-types do not show a relationship with porosity and permeability. In the present chapter it was shown that shrub morpho-types neither possess a relationship with pore body sizes. However, MIP curve patterns for each shrub morpho-types suggest that a relationship with pore throats sizes might exist. Nevertheless, the number of samples per shrub morpho-type is too limited to perform in depth statistical analyses.

In Chapter 4 it was also observed that shrub size sorting and shrub packing has an important influence in permeability and porosity results (respectively). In this chapter it is observed that shrub size sorting and to a lesser extent shrub packing control pore throat sizes and pore body sizes.

Poorly sized sorted shrubs occupy more space per unitary volume, in this way impacting the pore entrances and body size. Consequently, it is likely that the tortuosity also increases in poorly sorted samples (Rezende and Pope, 2015), therefore reducing the permeability. The pore parameter groups (i.e. 1, 2 and 3) are also strongly influenced by shrub size sorting, and thus indirectly by shrub pore entrances and pore body sizes.

Figure 5.21 showed that pore parameter groups (e.g. 1, 2 and 3) and shrub size sorting are coincident. In this example, Group 3 samples, with abundant microporosity, yield the lowest permeability results and are associated with poorly size sorted shrubs. This result indicates not only that the micropores are largely isolated, but also that poor shrub size sorting results in enhanced fluid pathways and tortuosity and associated low permeabilities. Groups 1 and 2, with absence or limited contribution of microporosity, are well sorted and yield higher permeabilities. They are typically associated with lower tortuosities. There is at this point, no proven explanation of why Group 3 samples possess more altered cement rims than the other groups, or why they are related to poorly sorted shrub samples. The reason for the increased alteration could relate to various local environmental parameters as well as to substrate surface rugosity, generated by the poorly sorted, irregular shrubs.

Shrub packing influences only pore body sizes and sample porosities in a statistically significant way by modifying the space between the shrub structures. The parameter increases with increasing openness of the packing. The shrub sizes do not show a relationship with pore network characteristics. Only small sized shrubs can be differentiated in function of pore body sizes in comparison with the other shrub size groups (e.g. medium and large), however small sized shrub has no statistical representativeness (one sample). Rezende and Pope (2015) showed that shrub sizes control pore throat size and also permeability. The shrubs from the Pre-Salt, offshore Brazil, are characterized mainly by arborescent fan-shaped radial fabrics (Rezende and Pope, 2015), while shrubs from Tivoli are predominantly dendritic. It is very likely that the 3D pore network of the Tivoli shrubs is more complex due the presence of the shrub branches that are characteristic for the dendriform morphology. As it was also shown in Chapter 4, the lack of relationship between shrub size and pore network characteristics is mainly due to the texture heterogeneities of the samples, such as shrub morphologies, size sorting and packing.

5.4.3 Reservoir quality

Understanding complex variations in pore geometry within different lithofacies is the key to improve reservoir description and exploitation. Variations in pore geometrical attributes define distinct flow zones (hydraulic units) with similar fluid-flow characteristics (Amaefule et al., 1993). Five FZI groups were identified for the shrub morpho-types in Tivoli. Samples with similar RQI and FZI possess similar pore throat characteristics, and consequently belong to the same hydraulic unit. Similarly, Amaefule et al. (1993) showed that carbonate rocks from West Texas yield a direct relationship between pore throat sizes and FZI. A hydraulic (pore geometrical) unit relates to geologic facies distribution, but do not necessarily coincide with facies boundaries (Hearn et al., 1984). RQI and FZI groups are mainly controlled by permeability. It means that low permeabilities, even with high porosities will result in lower RQI and FZI values.

Groups A, B and C from RQI and FZI possess bimodal MIP curves with a diminishing amount of micropores from group A to group C. While Groups D and E possess unimodal curves, only with meso- and macro-pore throats. These RQI and FZI results demonstrate the impact of microporosity on pore connectivity, and is in agreement with the previously defined pore parameters groups. Samples with lower micro- to macropore ratios possess the best RQI and FZI values. Shrub morpho-types can yield different reservoir characteristics, in accordance with micro- to macropore ratio and the interconnectivity between, on the one hand, the micropore compartment and, on the other hand, the meso- and macropore compartment. The presence of sparry calcite cements that surround the shrubs therefore influence the quality of the reservoir, because it has the potential to isolate microporosity, i.e., disconnecting the micropore compartment by pore shielding. The relationship between RQI and FZI with MIP/NMR groups highlights the complexity of the travertine reservoir. The relationship also helps to understand the pore network by (1) linking the micro- to macropore ratio in a sample to permeability and by (2) providing essential information about the number of pore compartments, their interconnectivity and their link with FZI and RQI.

5.5 Conclusions

The pore network of the shrub morpho-types from Tivoli travertines was assessed by integrating measurements deduced from NMR, MIP, porosity and permeability, petrography and SEM analyses. Based on the results new insights into the complex variations of the pore network were gained.

The shrub structures are mainly characterized by intergrowth and interdigit growth framework porosity. The integration of NMR and MIP curves allowed separating samples into 3 groups based on their pore parameter characteristics: Group 1 is represented by unimodal NMR and MIP curves; Group 2 displays bimodal NMR curves and an unimodal response in MIP curves and; Group 3 displays bimodal curves for both NMR and MIP, with well-developed peaks for both macro- and micro-porosities. The different groups are related to the presence or absence of the secondary peak in NMR and MIP curves, which is associated with micropores that mainly occur in the nucleus of the shrubs and to a far lesser extent in the sparry calcite cement associated to local dissolution.

The absence of the secondary peak (Group 1) or the very low frequency of the secondary peak (Group 2) can be explained by the negligible amount of micropores in the samples. Micropores are furthermore isolated by calcite cements that cover shrub structures. The cements might limit the volume of micropores that is accessible for mercury during MIP measurements. Group 3 have their sparry calcite cements altered by dissolution, and consequently the micropores easier to access during high pressure mercury injection stages. Micropore coupling is, however, not sufficient in the analyzed samples to allow molecules to travel between pore compartments during NMR measurements. Micropores are in NMR still registered as an isolated compartment and are therefore expected to have a negative effect on pore connectivity. Consequently, permeability will decrease with increasing micro- to macropore ratios.

Shrub size sorting and packing influence petrophysical characteristics (i.e. porosity and permeability) as well as pore parameters (e.g. pore body sizes and pore entrances). The shrub size sorting has a major control on pore entrances and permeability, and minor control on pore body sizes and porosity. Shrub packing does not yield a significant control on pore entrances, but do influence pore body sizes and sample porosities. The shrub sizes and morpho-types do not show a clear relationship neither with poro-perm results, nor with pore parameters (i.e. pore body size and pore entrances).

NMR/MIP groups, defined independent of shrub morphologies, display a relationship with permeability and shrub size sorting. Sample with micropores (Group 3) and poorly sized sorted shrubs are associated with decreasing permeability. The absence (Group 1) to very low presence of micropores (Group 2) and well sized sorted shrubs yields the highest permeabilities. Micropores appear as decoupled compartments and are as such not a

strong contributor to the pore network connectivity. Permeability will therefore decrease with increasing micro- to macropore ratios.

The analysis of reservoir quality index and hydraulic units through the RQI and FZI display a relationship with pore parameters, whereby the “unimodal” samples (Group 1) had the best reservoir characteristics. The reservoir quality lowered towards “bimodal” samples (Group 3). The results also evidenced that the amount of microporosity in the pore network decreases the reservoir quality.

Understanding the complex variation of the pore network is key to improved reservoir description and exploitation. Therefore, the integration of NMR / MIP groups together with RQI and FZI are important tools to perform shrub pore-typing and identifying the high heterogeneities of the complex shrub lithotype reservoir. Furthermore, the here applied techniques and tools are valuable to predict the distribution of petrophysical properties in reservoirs and the understanding of the pore network of the rock.

CHAPTER 6 Shrub reservoir characterization – detailed permeability study based on Lattice Boltzmann Method (LBM) simulations and air mini-permeameter measurements – Tivoli study case (Central Italy)

6.1 Introduction

One of the most important challenges that reservoir geoscientists are facing is to improve reservoir study characterization to enhance the understanding of a petroleum field and extending the life of the latter (Amaefule et al., 1993). Numerical simulation of fluid flow and prediction of permeability on small rock samples has important applications in petroleum engineering, environmental studies and core data provide information on various depositional and diagenetic controls on pore geometry and hydrogeology (Mostaghimi et al., 2012). Porosity within a rock type relates to permeability can vary over different orders of magnitude. The latter depends by high petrophysical variability within the reservoir. The production of oil and gas in many reservoirs around the world is seriously affected by their highly heterogeneous and/or anisotropic structure (Ayan et al., 1994). From fluid flow viewpoint, it is well accepted that heterogeneity and anisotropy are two closely related properties. Continental carbonates possess one of the most complex and heterogeneous pore network (Soete et al., 2015; Claes et al., 2016; Erthal et al., 2017). The depositional setting will influence the primary texture of the deposits. However, this texture can also be affected by diagenesis (Eberli et al., 2003).

To model the flow at the pore scale numerically for permeability calculation, the morphology of the pore space needs to be known. The advent of X-ray computed tomography has made it possible to obtain three-dimensional images with a resolution of only a few microns (Flannery et al. 1987; Coenen et al. 2004), which is sufficient to capture the pore space of many reservoir rocks, despite the reconstructing the digital pore networks. The next step is the modeling flow and transport through the reconstructed pore space. The Lattice Boltzmann Method is used for modeling flow in complex geometries (Pan et al. 2001, 2004; Jin et al. 2004; Knackstedt et al. 2004; Kang et al. 2006) because coding is straightforward and it can be readily parallelized (Piller et al. 2009). Although the Lattice Boltzmann is a powerful approach that is widely used, it is computationally demanding and requires the use of massively parallel computing approaches (Mostaghimi et al., 2012). With the aim to better understand the fluid behavior within each shrub morpho-type reservoir, flow modeling was applied by using μCT analysis and Computational Fluid Dynamics (CFD) in Palabos software. In order to characterize the spatial permeability distribution and the relationship with shrub morpho-types at higher scale (upscaling), in situ air mini-permeameter measurements were performed on a quarry wall and on a travertine block (50 cm x 50 cm x 50 cm) to determine permeability. This study investigates the importance of small-scale heterogeneities within different shrub morpho-type reservoir and analyzes micro- and meso-scale fluid flow. The influence of porosity and tortuosity on permeability results, as well as the influence of shrub textures (e.g. size, size sorting and packing) on tortuosity was evaluated.

6.2 Methods

6.2.1 Petrophysical analysis

Petrophysical measurements (see Chapter 3) of porosity and permeability were performed for 17 plug samples of 1 and 1.5 inch wide by 2

inch long of different shrub morpho-types collected from the quarry walls in Tivoli, and 16 plug samples of 1 inch from a travertine block (50 cm x 50 cm x 50 cm) again from a Tivoli quarry. The samples comprise all the shrub morpho-types. The porosity was measured by using Archimedes methodology. The permeability was measured in an UltraPerm 400 from Corelab using nitrogen gas (N_2) as fluid flow.

6.2.2 Micro Computer Tomography (µCT)

The main purpose of applying µCT in the present study is to simulate petrophysical properties. Based on these, the petrophysical parameters are predicted and modeled allowing refining the reservoir characteristics.

A Phoenix Nanotom computed tomography (GE Measurement and Control Solutions, Wunstorf, Germany), equipped with a 180 kV/15 W high-performance nanofocus X-ray tube and a 2304 by 2304 pixel Hamamatsu detector, was used to perform the scans. The plugs were scanned at 120 to 130 kV tube voltages and a current of 220 to 290 µA, and a 0.3 mm thick cupper filter was installed during the scans. Radiographs are reconstructed with the Phoenix datos|x 2.0 reconstruction software (GE Measurement and Control Solutions, Wunstorf, Germany) and images with an isotropic voxel size of respectively 16 µm for areas of ~ 3 cm high by 2.5 cm (1 inch) and 3.8 cm (1.5 inch) diameter plugs were exported. The small analyzed area was selected to characterize only the shrub morpho-types and to avoid the litho- and pore-type heterogeneities of the sample (Fig. 6.1). The µCT slice images were segmented in Matlab. The resulting images were processed in Avizo Fire (v.7), where pores were labeled, rendered in 3D and the Volume of Interest (VOI) was selected.

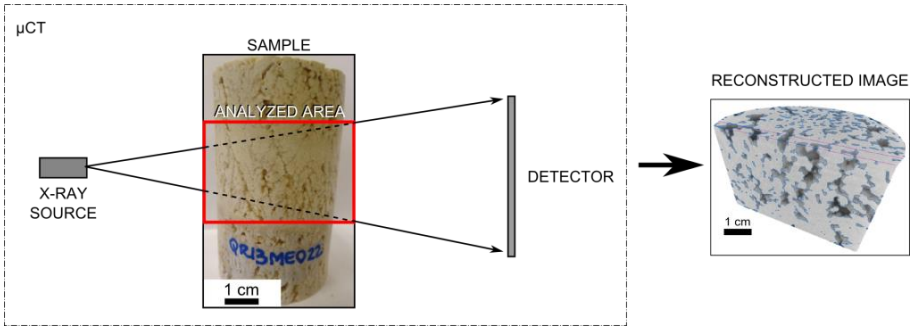

Fig. 6.1: Schematic overview of the µCT methodology that was applied to shrub morpho-types from Tivoli. The shrub plug samples with 2.54 cm (1 inch) and 3.81 cm (1.5 inch) diameter had an area of ~ 3 cm height analyzed to avoid incorporation of non-shrub type heterogeneities of the sample. First the sample was scanned using X-rays generated at the source that traveled through the sample where they were attenuated and finally captured on the detector. Afterwards, the slice images generated by the µCT are reconstructed by using Avizo software.

6.2.3 Representative Elementary Volume (REV)

The concept of Representative Elementary Volume consists of the smallest value which porosity measurements can be taken as a representation for the entire sample area/volume that does not respond to small changes in volume or location (Bear, 1972). The REV is an important concept to evaluate petrophysical properties (Soete et al., 2016). The REV data was determined to evaluate the porosity present in the µCT analysis.

The applied methodology of Claes (2015) to calculate the REV of 17 shrub samples from Tivoli, with scan resolution of 16 µm. This methodology follows the approach of Brown et al. (2000) that a volume falls within the region of the REV if it can be treated as an ergodic stationary function ($Z(x, V_i)$) in the domain R. This corresponds to a second order stationary function in R, defined in equation 6.1

$$E[Z(x, V_i] = constant$$

and (6.1)

$$Cov[Z(x+h, V_i), Z(x, V_i)] = f(h) \rightarrow 0 \; as \; h \rightarrow 0$$

Z remains constant for the first part of the equation, while the second part requires that the covariance between two points is function of the separation distance h in all points x. According to Myers (1989) and Cressie (1992), this last part can be attenuated by using the equation 6.2, if the sample consists of a finite number of observations from a continuous process, which is the case for the porosity parameter.

$$Var[Z(x, V_i)] = constant \quad (6.2)$$

The semi-variogram is characterized by a sill and range. The sill value represents the plateau value and is equal to variance of the data. The range or length of correlation is the distance at which the sill value is reached. In the method from Claes (2015), the semi-variograms of the porosity parameter are calculated based on the segmented datasets. Voxels representing the pore space have a value of one, while the voxels of the rock phase are given a value of zero (Claes, 2015). The semi-variograms are modelled according to the spherical model, which has a linear behavior near the origin and flattens out at larger distances (Isaaks and Srivastana, 1989; Claes, 2015).

The experimental semi-variograms are modelled using a combination of two nested spherical variograms (equation 6.3):

$$f(x) = \begin{cases} n + c_i\left[\frac{3h}{2a_i} - \frac{1}{2}\left(\frac{h}{a_i}\right)^3\right] + c_2\left[\frac{3h}{2a_2} - \frac{1}{2}\left(\frac{h}{a_2}\right)^3\right] & for\ 0 < h \le a_1 \\ n + c_1 + c_2\left[\frac{3h}{2a_2} - \frac{1}{2}\left(\frac{h}{a_2}\right)^3\right] & for\ a_1 < h \le a_2 \\ n + c_1 + c_2 & for\ h > a_2 \end{cases} \quad (6.3)$$

Where, c1 and a1 are sill and range of the first, short range component of the variation, and c2 and a2 are the sill and range of the second. Long range component of the model. The nugget value n is a constant value to each component of equation 6.3.

6.2.4 Permeability simulations by using Lattice Boltzmann Method (LBM)

LBM relates to an equation for simulating flow for Newtonian fluids with collision models (Soete et al., 2016). It simulates a single phase fluid under laminar conditions at low flow rate velocities (< 500) (equation 6.4).

$$Re = \frac{VL\rho}{\mu} \quad (6.4)$$

where,

V = flow velocity (m / s)

L = water depth (m)

P = density

μ = fluid viscosity [$MT^{-1}L^{-1}$]

The permeability equation is defined by Darcy's equation (6.5):

$$K = \frac{\mu V}{\left(\frac{\Delta P}{L}\right)} \quad (6.5)$$

where,

K = permeability (mD)

μ = fluid viscosity [$MT^{-1}L^{-1}$]

V = flow velocity (m / s)

ΔP = pressure difference (psi)

L = length of the pore network

The permeability simulation was carried out in Palabos software. Seventeen samples had their permeability simulation performed along the longest shrub axis (Z-axis). During the simulations, flow direction was restricted to a finite vector set, showing the particle travel direction. The standard Bhatnagar-Gross-Krook (BGK) collision operator was applied together with the D3Q19 lattice. The latter model was selected due the more accurate results. It furthermore possesses more numerical stability and is less complex (Soete et al., 2016). The D3Q19 model possesses 18 discrete lattice velocities for a fluid particle. The initial velocity was considered to be zero. A fixed constant pressure gradient is simulated at the in- and outlet of the pore network, inducing a flow accelerated during the iteration

steps (Soete et al., 2016). According to the latter, the fluid velocity vectors possess an initial and back vector that neutralizes each other, resulting in zero velocity for the displacement towards the solid surface.

The simulations give dimensionless lattice units to describe the fluid flow properties (Latt, 2008; Latt and Krause, 2006, 2015). The dimensionless lattice units are converted to Darcy units by multiplying with the square of the effective length of a voxel size. Equation 6.6 is used to calculate the permeability:

$$K = \frac{\Delta x^2 \, \mu_1 \mathrm{v}}{\left(\frac{\Delta P}{L}\right)} \qquad (6.6)$$

with,

Δx = effective length of a voxel side

μ_1 = lattice viscosity [$MT^{-1}L^{-1}$]

v = fluid flow rate

6.2.5 Tortuosity

The tortuosity factor is a critical parameter that significantly affects reservoir properties. Introduced by Carman (1937), tortuosity is related to a sinusoidal flow path through a porous medium. The tortuosity gives the interconnectivity of the pores in the frame of the pore network. It is also related to the flow differences between pore throat and pore body (Adisoemarta et al., 2000). The complexity of the pore network enhances the pathways (sinuosity) in the pore space that the fluids have to pass.

Various forms of tortuosity have been proposed, such as geometrical, electrical, diffusion and hydraulic (Ziarani and Aguillera, 2012). In the present study, the method for measuring the tortuosity of porous solids was applied on μCT reconstruction images. The method is based on the direct comparison of the geodesic distances calculated from any pore pixel to any limit of the tomogram (Gommes et al., 2009). It requires a preliminary segmentation of the μCT images by which it is defined explicitly which pixels belong to the connected pore network. The tortuosity is defined by equation 6.7:

$$\tau = lim_{L_f} \to \infty \frac{L_f}{L_s} \qquad (6.7)$$

where,

τ = tortuosity

L_f = length of the flow path

L_s = length of the shortest trajectory between a defined inlet and outlet plane in the direction of the applied pressure gradient (Gommes et al., 2009).

A straight path through the sample (Lf = Ls) will have a tortuosity equal to 1, while a cyclic path (Lf>>>Ls) will have tortuosity equals infinite (Gommes et al., 2009).

6.2.6 Air mini-permeameter measurements

Permeability is the single most important factor influencing fluid flow in reservoirs. Mini-permeameters (or probe permeameters) is a gas (nitrogen or air)-based device for measuring permeability in porous rocks. The device is capable of making direct and immediate measurements of rock permeability in both laboratory and field studies. Large numbers of measurements can be assembled to characterize and quantify small-scale permeability heterogeneity distribution within individual lithofacies (Huysmans et al., 2008; Possemiers et al., 2012). One of the main advantages of mini-permeameters is their ability to collect data on various areas. Based on the acquired data the spatial permeability distribution can be characterized (Huysmans et al., 2008).

A “TinyPerm II” mini-permeameter from New England Research (NER) was used. This probe is a portable hand held air mini-permeameter (Fig. 6.3) that measures the rate of air flow through a porous medium from a tip seal placed against the sample/outcrop, or a hole drilled into the outcrop, for a known pressure drop. The device is pressed against the sample/wall and the plunger is depressed to withdraw air from the porous medium (Fig. 6.3). The “TinyPerm II” probe inner tip diameter is 9 mm and the outer tip (sized rubber nozzle) has a diameter of 24 mm. The

measured volume corresponds to a hemisphere with 18 mm radius (Goggin et al., 1988). The probe nozzle is pressed against the sample, and a vacuum is generated in the inner part of the device. A microcontroller unit simultaneously monitors the syringe volume and the transient vacuum pulse created at the sample surface. The microcontroller computes the response function of the sample/instrument system by using a signal processing algorithms.

Fig. 6.3: Minipermeameter device using air injection.

Provided that the flow rate is not too high, and the pore dimensions are not too small (relative to mean free path; gas-slippage effect), gas flow through a porous media is governed by Darcy's law. Therefore, the gas flow rate and gas pressure can be transformed into gas permeability by empirically derived relationships or by using a modified form of Darcy's equation based on the known injection pressure and flow rate, and the geometry of the tip and the rock proposed by Goggin et al. (1988a, b) (equation 6.8):

$$k = \frac{2\mu Q_1 P_1}{G_0^a (P_1^2 - P_2^2)} \qquad (6.8)$$

where:

k = permeability

μ = gas viscosity at atmospheric pressure [$MT^{-1}L^{-1}$]

Q_1 = volumetric flow rate [L^3T^{-1}]

P_1 = injection pressure [$ML^{-1}T^{-1}$]

P_2 = outflow pressure [$ML^{-1}T^{-1}$]

G_0 = Geometrical shape factor [-]

a = internal radius of the tip (seal area) of the mini-permeameter [L]

According to Goggin et al. (1988), the mini-permeameter investigates depths of approximately four times the internal radius of the tip seal. However, Jensen et al. (1994) showed that the measurements only reach depths of two orders of the probe inner radii, i.e. a mean radius varying between 9 and 18 mm.

The air mini-permeameter methodology was applied on a wall in Querciolaie-Rinascente North quarry (QR 3, Fig. 6.4) with dimensions of 40 cm by 30 cm, and on a block with dimensions of 50 by 50 by 50 cm, collected from the quarry Querciolaie-Rinascente South (QR 2, Fig. 6.4). In the quarry wall, 4 profiles were logged, with a spacing of 10 cm between them. The log measurements resulted in a nearly continuous section over 40 cm. Twenty measurements at about 2 cm intervals along its length were performed vertically along each profile, comprising the different shrub morpho-types and associated lithotypes (Fig. 6.5). The measurements are analogous to horizontal permeability measurements in plug samples.

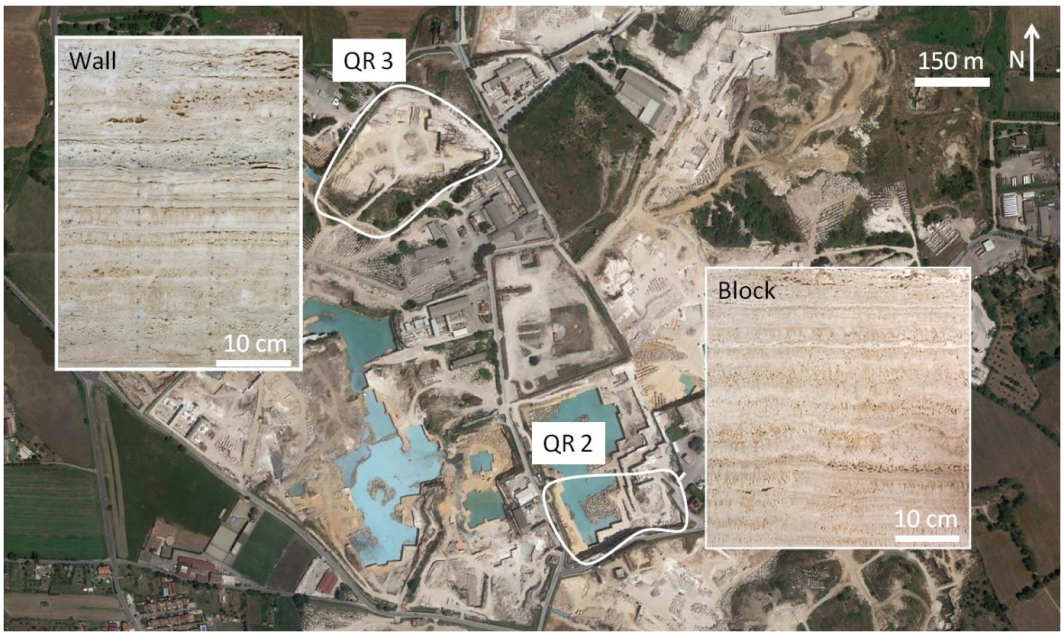

Fig. 6.4: Location of the wall and of the block on which mini-permeability measurements were carried out.

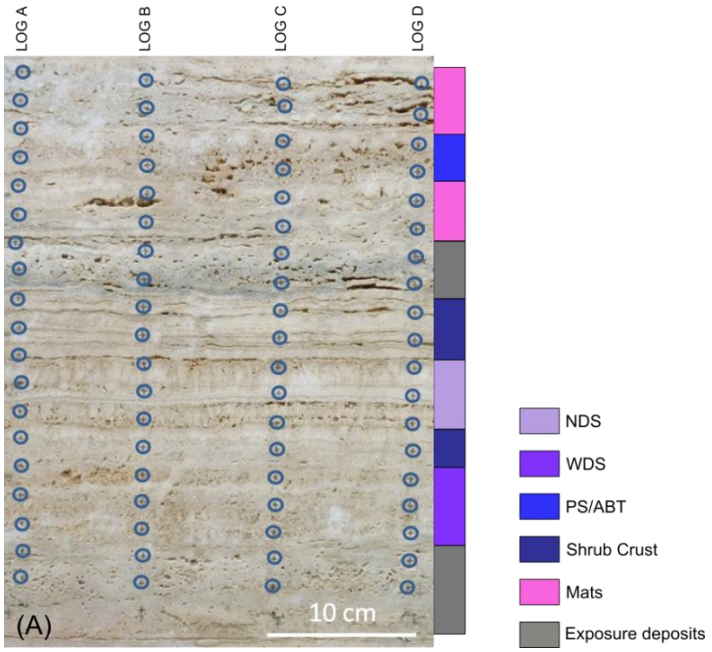

Fig. 6.5: Studied wall in the Querciolaie-Rinascente North quarry (Tivoli area), with NDS corresponding to narrow dendriform shrub, WDS to wide dendriform shrub, PS to pustular shrub, and ABT to arbustiform shrub.

The block was measured on each vertical side in 4 logs, 30 cm long each (15 measurements every 2 cm) and with a spacing of 10 cm between them (Fig. 6.6). On the top and bottom horizontal side of the block, due to its mono-lithological nature, only 4 measurements along each log, with a spacing of 5 cm were carried out (Fig. 6.6). Sixteen samples from one vertical side (Side 1, Logs A and D, Fig. 6.6) of the block were collected for classical porosity and permeability measurements, for comparison with the mini-permeability measurements.

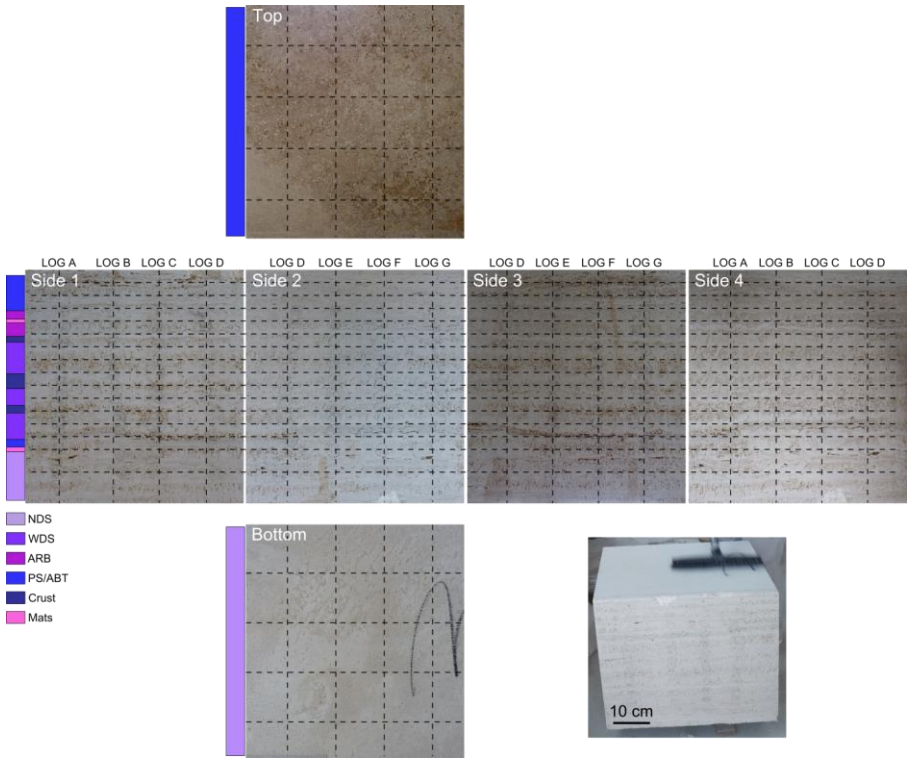

Fig. 6.6: Studied block from Querciolaie-Rinascente South quarry (Tivoli area). The measurements proceeded in 4 logs (10 cm apart) on each side with 15 measurements per log and 16 measurements on top and bottom, with NDS corresponding to narrow dendriform shrub, WDS to wide dendriform shrub, PS to pustular shrub, and ABT to arbustiform shrub.

6.3 Results

6.3.1 Representative Elementary Volume (REV)

When applying pore scale modeling to predict macroscopic parameters, it is of great importance that the underlying model of the pore space is representative of the rock structure at a larger scale. The existence and size of REV at the pore scale has been studied for different porous media (Zhang et al., 2000; Okabe and Oseto, 2006; Al-Raoush and Papadopoulos, 2010). Carbonate reservoir rocks are characterized by their complex pore network due the high heterogeneities within the rock. However, the sample scale is an important factor, since the rocks can be considered as a homogenous continuum in larger samples. The Representative Elementary Volume is defined as the smallest volume that can be assumed at the continuum scale for which the microscopic properties do not change if its dimensions are incremented (Bear 1972). To examine the effect of scale on the porosity REV of 17 µCT scanned plugs (2.5 and 3.8 cm diameter) at a resolution of 16 µm, semi-variograms were calculated (table 6.1) according to the methodology of Claes (2015). The semi-variograms were calculated in 2D, but in 3 directions (x, y, z), allowing to obtain quasi 3D information (table 6.1). The semi-variogram ranges along the principal axes, x, y and z, differ (Table 6.1). It indicates that meso- to macroporosity is heterogeneously distributed for all samples (De Boever et al., 2016). Range 1 provides information about the small pore distribution, while range 2 to larger spatial scale (Claes, 2015) (Table 6.1). From the segmentation the volume of the sample is obtained. If image sizes are smaller than the generated volumes from segmented images, the REV is reached. So, for Range 1 (a1), REV was reached, while for Range 2 (a2) only 3 samples had their REV reached (Table 6.1). The approach was based on assessing the shrub morpho-types and that here at short distances REV was reached. If all lithotypes would be considered to reach REV, larger samples will be needed. This was at this stage out of the scope of the thesis. In the Fig. 6.7, it is possible to observe the pore heterogeneities for each shrub morpho-type, where a color variation (labelled pore network) illustrates the low pore-connectivity for the given resolution.

Sample	Shrub morpho-types	Segmented Volume			Nugget			Range 1 (a1) [mm]			REV achieved	Sill1 (c1)			Range 2 (a2) [mm]			REV achieved	Porosity (%)	Sill2 (c2)		
					x	y	z	x	y	z		x	y	z	x	y	z			x	y	z
QR15	NDS	23.3	21.8	16.7	11878300.0	8666234.6	11171199.4	0.7	0.6	0.7	ok	69616711.1	66063769.0	60407247.3	21.8	4.6	7.6	ok	9.0	15334766.0	9422619.9	13053226.7
QR17	NDS	22.8	22.8	17.0	8775873.7	8263588.7	8637791.4	1.0	0.8	0.9	ok	48368175.8	45682853.8	39643946.2	0.4	6.9	84.8	no	7.5	2882247.4	6193763.9	89953706.5
QR22	NDS	23.1	22.1	17.0	12841599.9	11752611.5	8405282.6	1.1	1.0	0.8	ok	49215026.7	48401973.7	36910079.3	84.8	13.2	84.8	no	8.3	13819547.0	3496624.6	158096161.2
QR26	NDS	23.3	23.1	17.0	39012798.9	39998306.5	33167127.1	0.9	1.0	0.8	ok	159799530.7	171499754.8	151731725.8	84.8	84.7	50.8	no	7.0	126543528.2	72380937.2	200000000.0
QR28	NDS	22.2	22.4	17.0	1353503.7	3773422.6	3055200.2	0.8	1.2	1.0	ok	20191149.3	25993635.5	23212714.1	3.0	84.8	18.5	no	8.9	9488714.8	11902592.4	7786485.3
QR30	NDS	23.3	23.1	17.0	10447398.9	14816724.7	10895259.9	1.0	1.4	1.0	ok	40290897.1	45491972.4	40088042.3	5.6	84.8	84.8	no	7.7	22484670.7	54590734.0	132185305.7
QR34H	NDS	16.4	17.7	15.8	2817760.3	952570.0	1257502.7	1.5	0.8	0.9	ok	19692411.9	13131194.0	13297970.6	9.1	2.7	4.7	ok	8.2	4528750.9	11611087.8	10870447.6
QR35H	NDS	16.8	16.7	15.8	11566089.1	6588267.6	19661436.3	1.2	0.9	1.9	ok	68987104.2	58171626.2	67866549.0	16.4	3.6	79.2	no	9.6	15446550.9	25438917.5	0.0
QR18	WDS	22.6	22.6	17.0	9987596.4	9114215.7	7298853.2	0.9	0.8	0.7	ok	38723141.5	38581167.9	30699480.0	84.8	9.5	84.8	no	5.5	10343023.5	2548473.2	87813009.6
QR31H	WDS	17.1	16.8	15.8	7272004.1	6460666.3	6015402.6	1.0	0.9	0.9	ok	53401330.1	49323222.0	54073252.1	5.9	4.9	79.2	no	10.2	15967951.3	20867271.8	125804767.5
QR38	WDS	22.9	23.5	17.0	12695354.2	7180709.7	9313831.8	1.0	0.6	0.8	ok	43441642.5	38263313.2	48681299.4	38.2	2.7	14.8	no	9.3	25386988.3	21098844.3	6948430.5
QR24	FDS	23.8	21.9	16.7	0.0	16918439.7	18642240.7	0.1	0.7	0.9	ok	29485012.3	50651454.3	48399240.8	0.9	83.3	83.3	no	5.3	38224300.5	0.0	0.0
QR29	FDS	23.3	22.5	17.0	6157355.8	7896130.0	28984694.8	0.5	0.5	2.3	ok	50248613.9	50741135.4	48622177.4	6.1	13.0	0.4	ok	18.6	16392095.3	13396341.4	156233.5
QR139V	FDS	23.1	23.3	16.7	15193665.4	0.0	11985086.7	0.8	0.1	0.6	ok	19449329.7	26953355.6	20781313.0	83.3	3.2	21.3	no	4.2	31970269.8	12733021.2	14010688.1
QS11B	ABT	23.0	23.5	17.0	1384656.1	2099563.0	2719527.6	0.1	0.7	0.8	ok	5962726.8	7340393.0	7494374.5	2.0	84.8	84.4	no	4.7	2907088.6	5155318.6	0.0
QR52	PS	24.6	21.8	17.0	15199644.5	11656030.1	9726303.5	1.3	1.0	0.9	ok	63971704.8	60528372.0	61030039.5	84.8	84.8	84.8	no	9.9	63971704.8	60528372.0	61030039.5
QR32V	PS	17.2	16.4	15.8	9580571.2	6979986.5	5144181.5	1.2	1.1	1.0	ok	123192213.2	109256172.7	87510773.0	79.1	4.3	3.9	no	14.9	82767220.1	31178270.9	56357819.7

Table 6.1: Representative Elementary Volume (REV) calculations. In orange color the REV's that were not reached are indicated. NDS corresponds to narrow dendriform shrubs, WDS to wide dendriform shrubs, FDS to fili dendriform shrubs, ABT to arbustiform shrubs, and PS to pustular shrubs.

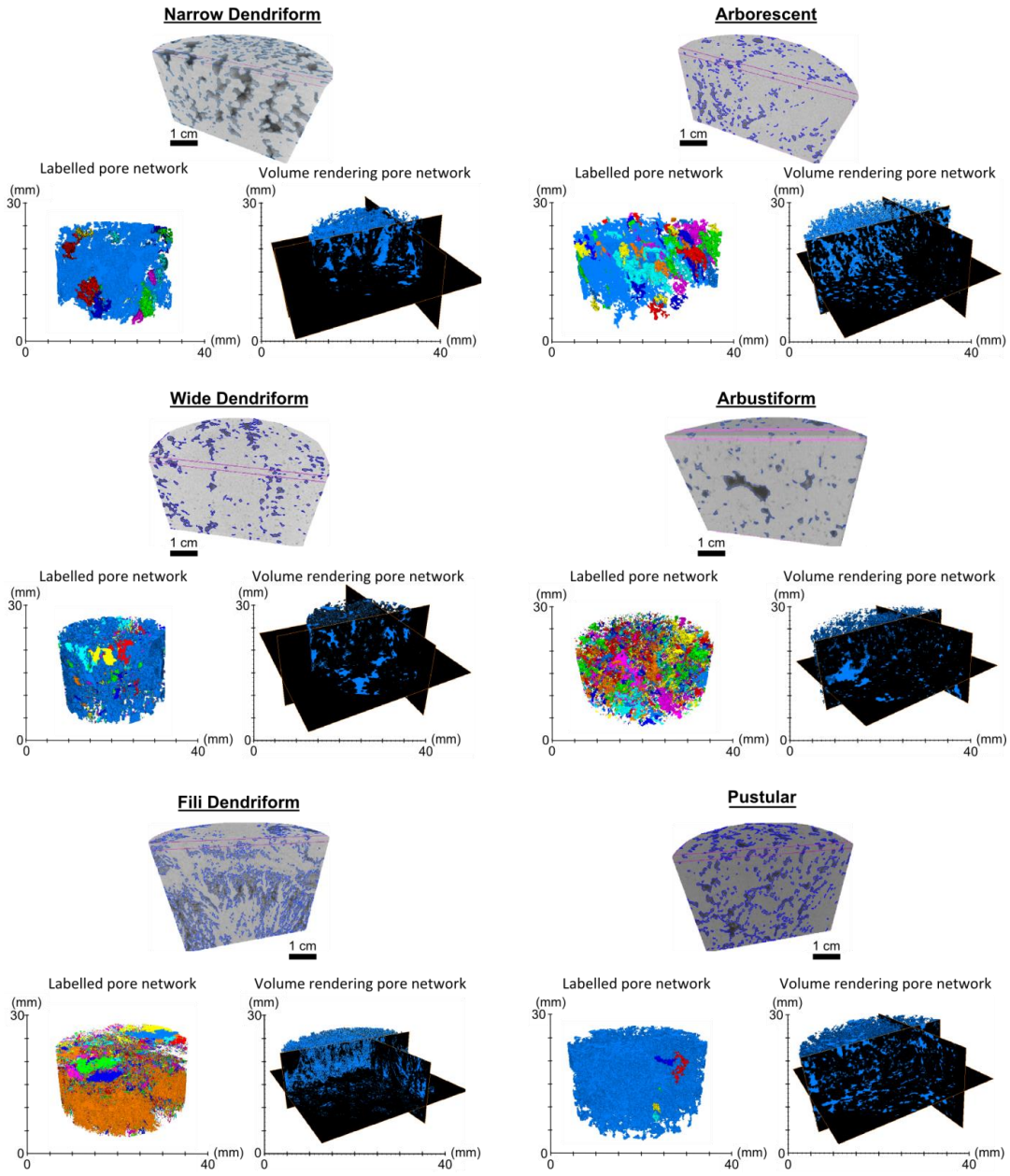

Fig. 6.7: Result of the µCT reconstruction and labeled and volume rendering pore network representative of the 6 shrub morpho-types. The color variation illustrates the low pore-connectivity for the given resolution (16 µm). Pores below this resolution were not taken into account.

6.3.2 Permeability simulations (K_{sim})

Simulated permeability by using Lattice Boltzmann Method (LBM) was applied in order to access the permeability within each shrub morpho-type. 3-D visualization of the streamlines velocity distribution shows a preferential orientation and alignment of the pores in z-axis (Fig. 6.8), and demonstrates the heterogeneous nature of fluid flow through these porous media. This indicates that most of the pores are connected in this z-direction, and permeability simulations could quantify and qualify the connectivity based on the LBM simulations. This type of analysis offers a fast way of visualizing flow heterogeneity in different classes of porous media.

The differences between open pores and total porosity calculated in the z-direction from µCT scanned samples are less than 3% (Chapter 4, Fig. 4.19). Pores below 16 µm resolution were not considered in the present permeability estimations, despite the fact that they could influence flow properties. However, based on SEM analysis, as well as MIP and NMR curve distribution patterns it was inferred that the amount of micropores is very low (Chapter 5).

Among the 6 shrub morpho-types, only 5 gave suitable results (Fig. 6.8), namely i.e. narrow dendriform shrub (NDS), wide dendriform shrub (WDS), fili dendriform shrub (FDS), arbustiform shrub (ABT) and pustular shrub (PS). The arborescent shrub (ARB) µCT scanned samples showed very thin micritic laminae intercalations between the shrubs which created vertical barriers for the porosity connectivity. Consequently, due to the lack of connected pores, the permeability simulation could not be performed in arborescent samples. Analyzing the 3D streamlines velocity distribution in function of each shrub morpho-type (Fig. 6.8), it is possible to observe that each shrub morpho-type possesses differences in the velocity distribution as well as the amount of flow paths. NDS possesses the highest concentration of flow paths, however, in general with low flow velocity magnitude (Fig. 6.8A); WDS shows more localized flow paths, also with low flow velocity magnitude (Fig. 6.8B); FDS displays localized flow paths, with more variations in flow velocity magnitude, showing areas with very low flow velocities and others with very high flow velocities (Fig. 6.8C); PS shows very dense flow paths with moderate to high flow velocity magnitude (Fig. 6.8D); and ABT displays localized flow paths, mainly with low flow velocity magnitude (Fig. 6.8E). The results of permeability simulation (K_{sim}), µCT calculated porosities, and laboratory measurements of porosity and permeability from 17 shrub plug samples (2.5 and 3.8 cm diameter) are given in Table 6.2.

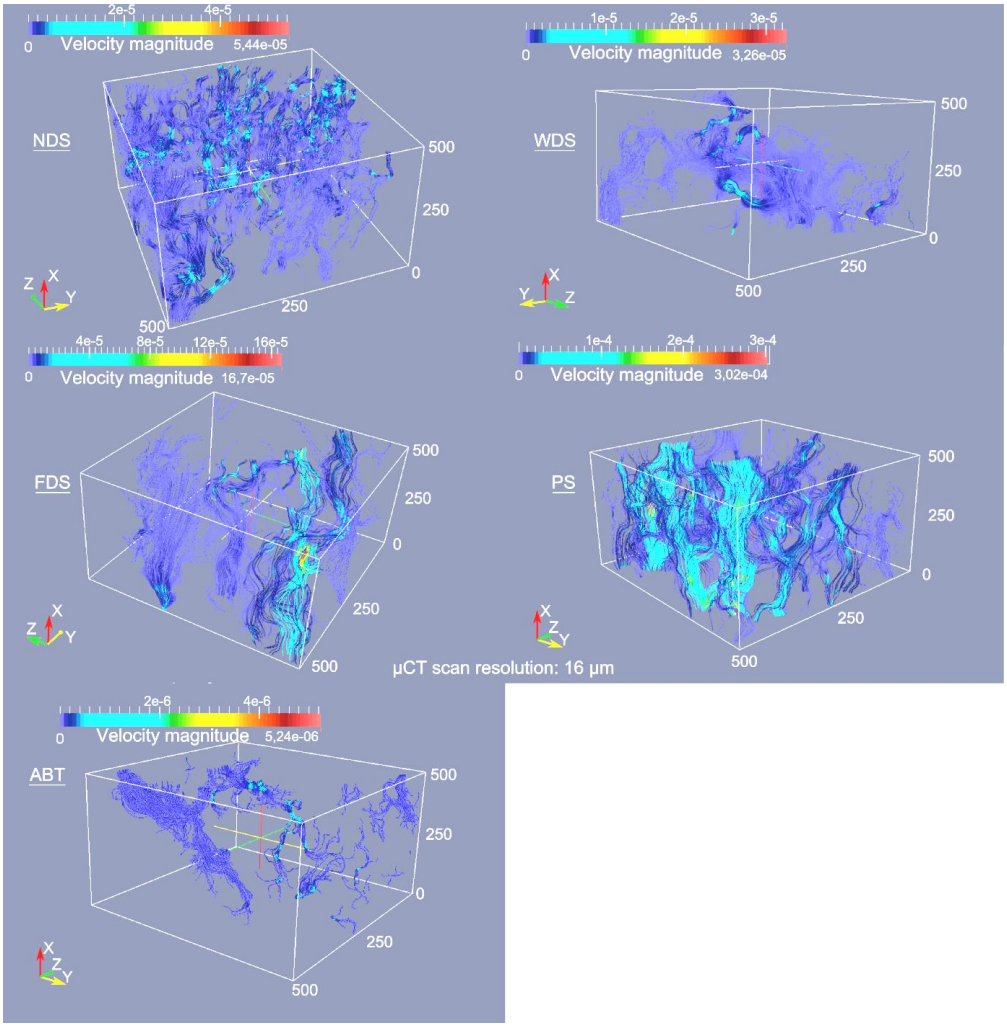

Fig. 6.8: 3D streamlines velocity distribution within narrow dendriform shrub (NDS), wide dendriform shrub (WDS), fili dendriform shrub (FDS) and pustular shrub (PS). The flow is mainly in the z-direction from z = 0 to z = 500 pixels. The lowest velocity magnitude is represented by cold colors and for higher velocities in warm colors.

Table 6.2 presents the results from porosity and permeability measured in the lab and the ones obtained from µCT analysis and permeability simulation (K_{sim}). The latter values correspond to simulations along the vertical axes (z-direction) which represent the main flux flow. The µCT calculated porosity and K_{sim} results are plotted in a chart together with laboratory measurements of porosity and permeability (Fig. 6.9). As can be seen from this figure, the porosity results measured from the lab and the results obtained from µCT present rather similar range. However, simulated permeability (K_{sim}) often possesses higher results in comparison with permeability measured in the lab (Fig. 6.9 and Table 6.2). Nevertheless, the K_{sim} and µCT porosity plotted in the same range as porosity from the lab and the highest permeability results from the lab (Fig. 6.9), validating the results from µCT and the simulated permeability. The volume of the sample for K_{sim} analyzes is ~ 0.5 cm^3, while the volume of the sample for permeability measurements in the lab is between 5 and 10 cm^3, meaning that the rock heterogeneities for K_{sim} analyses, are more limited and consequently the permeability results are higher.

Sample	Shrub morpho-types	Archimedes porosity (%)	µCT porosisty (%)	Permeability (mD)	K_{sim} (mD)	Tortuosity
QR 15B	NDS	9.0	17.8	42.7	1217.8	2.1
QR 17	NDS	7.5	13.2	11.1	705.8	1.9
QR 22	NDS	8.3	8.7	0.001	495.8	2.9
QR 30	NDS	7.7	12.0	0.001	12.5	3.4
QR 34H	NDS	8.2	16.2	543.7	908.2	1.9
QR 35H	NDS	9.5	14.3	0.03	554.7	2.3
QR 26	NDS	7.0	5.5	0.02	168.8	3.7
QR 28	NDS	8.9	17.7	0.001	683.8	2.1
QR 31H	WDS	10.2	10.9	8.6	11.0	3.2
QR 18	WDS	5.5	10.0	161.1	360.3	2.7
QR 38	WDS	9.3	9.2	160.0	291.1	3.0
QR 24V1	FDS	5.3	7.3	0.001	1.2	6.6
QR 29	FDS	18.6	13.3	148.0	11.0	4.0
QR 139V	FDS	4.2	3.3	0.001	0.1	6.3
QS 11B	ABT	4.7	6.0	0.001	11.0	4.5
QR 52	PS	9.9	16.0	463.8	47414.0	2.4
QR 32V	PS	14.9	25.0	496.0	6787.7	1.7

Table 6.2: Seventeen shrub morpho-types have their porosity measured from laboratory and from CT scan analysis (using AVIZO software) and permeability measurements from laboratory and from simulations (K_{sim}) (Palabos software). Shrub morpho-types are indicated as follows: NDS for narrow dendriform shrub, WDS for wide dendriform shrub, FDS for fili dendriform shrub, ABT for arbustiform shrub and PS for pustular shrub.

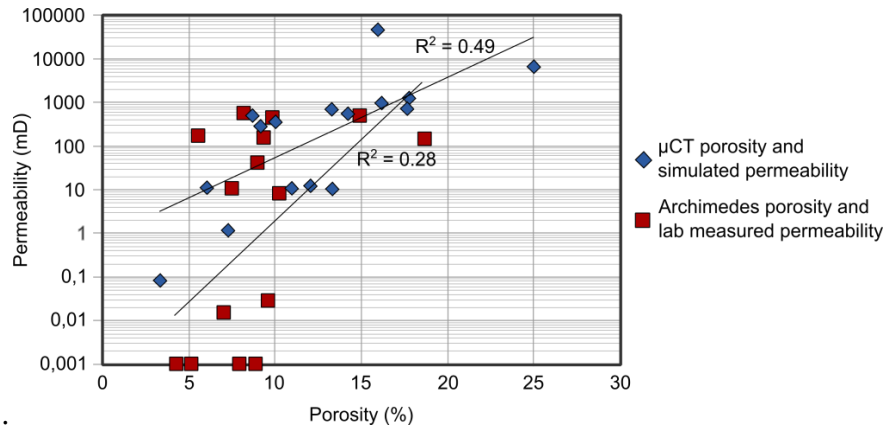

Fig. 6.9: Comparison between results from laboratory measurements and simulated permeability and porosity.

The permeability simulation run for each shrub morpho-types is plotted in function of porosity and µCT porosity. The graphics of K_{sim} versus porosity (Fig. 6.10A) and µCT porosity (Fig. 6.10B), indicate that shrub morpho-types yield different permeability results. PS samples possess the highest K_{sim} values, followed by NDS, WDS, ABT and FDS with the lowest results.

Box plots of shrub morpho-types in function of K_{sim} (Fig. 6.11) illustrate that center lines of shrub morpho-types plot above 75th percentile between them. The box plots are the easiest way to visualize the data, because they are straightforward. The number of samples for each shrub morpho-types has no statistical representativeness, however, the results is used only as an indicator to evaluate the sample.

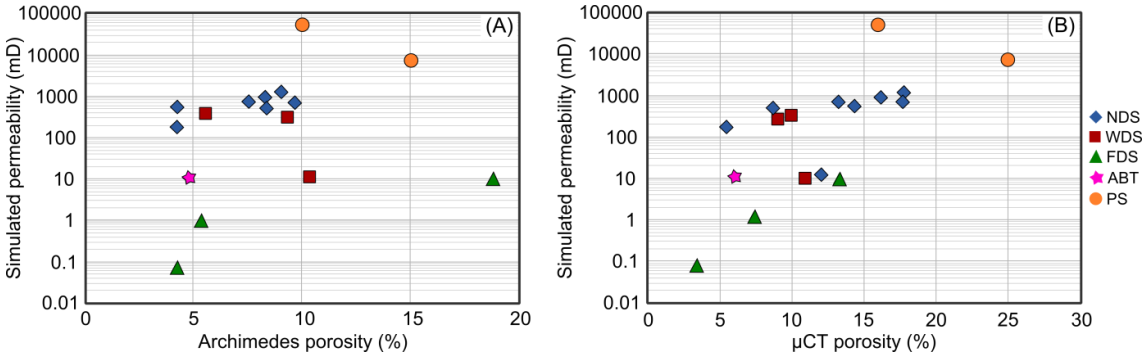

Fig. 6.10: Shrub morpho-types plotted in function of (A) K_{sim} and Archimedes porosity, and (B) K_{sim} and µCT porosity. NDS corresponds to narrow dendriform shrub, WDS to wide dendriform shrub, FDS to fili dendriform shrub, ABT to arbustiform and, PS to pustular shrub.

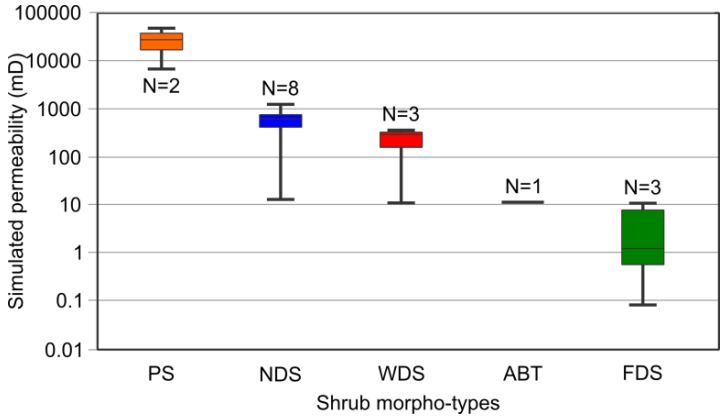

Fig. 6.11: Box plot of simulated permeability (K_{sim}) results per shrub morpho-types. It is possible to observe that the means of each shrub morpho-type plot above 75th percentile between them. Pustular shrub (PS) possess the highest permeability results, followed by narrow dendriform shrub (NDS), wide dendriform shrub (WDS), arbustiform (ABT) and fili dendriform shrub (FDS) with the smallest permeability values.

6.3.3 Tortuosity and K_{sim} in function of shrub textures

Shrub morpho-types

Tortuosity was calculated from µCT and plotted against Archimedes and µCT porosity, permeability measurements and simulated (K_{sim}) from µCT (Fig. 6.12). The plots tortuosity vs. Archimedes and µCT porosity shows that the tortuosity increases as porosity decreases (Figs. 6.12A and B). Tortuosity vs. permeability measurements does not show any relationship (Fig. 6.12C).

The shrub morpho-types do not possess a very clear relationship in the plots of tortuosity versus Archimedes and µCT porosity (Figs. 6.12A and B), neither in the plot of tortuosity versus measured permeability (Fig. 6.12C). Nevertheless, there exists a clear relationship between the shrub morpho-types in the plot tortuosity versus K_{sim} (Fig. 6.12D). PS possesses the lowest tortuosity and the highest permeabilities values, followed by NDS, WDS, ABT and finally FDS with the highest tortuosity results and lowest permeability data (Fig. 6.12D). These results indicate that the

shrub morpho-types itself, without influence of other lithotypes have a relationship with K_{sim} and tortuosity. Without µCT analysis this observation would not be possible, because all the samples present lithotype heterogeneities (i.e. encrusted bubbles or peloidal micritic laminae or rafts) and high texture variability that influence the results of permeability measured in the lab.

The number of samples for the different shrub morpho-types in function of tortuosity is not sufficient for statistical analysis. However, box plots are the best way to visualize the differences between the shrub means in function of tortuosity (Fig. 6.13). The center lines of each shrub morpho-types are plotted above 75th percentile between them.

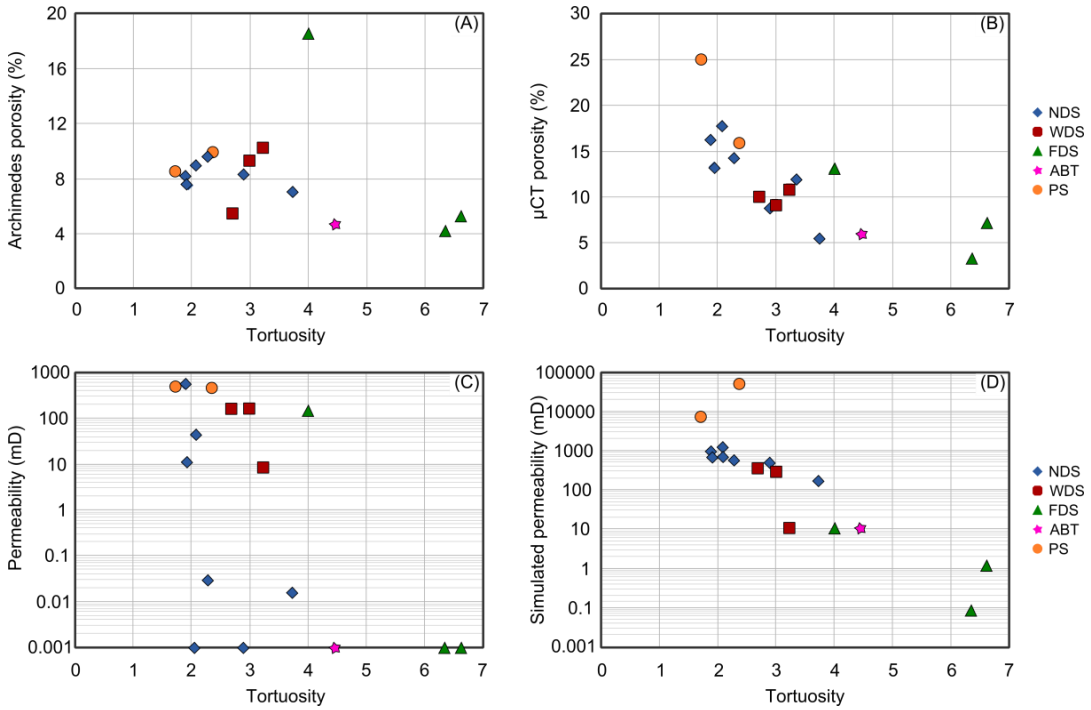

Fig. 6.12: (A) Tortuosity vs. Archimedes porosity and (B) Tortuosity vs. µCT porosity, showing that tortuosity increase while porosity decreases. However, (A) and (B) do not present a clear relationship with shrub morpho-types. (C) Tortuosity vs. Permeability does not display a clear relationship neither, however, (D) Tortuosity vs. simulated permeability (K_{sim}) shows a clear separation according to the shrub morpho-types. NDS corresponds to narrow dendriform shrub, WDS to wide dendriform shrub, FDS to fili dendriform shrub, ABT to arbustiform and, PS to pustular shrub.

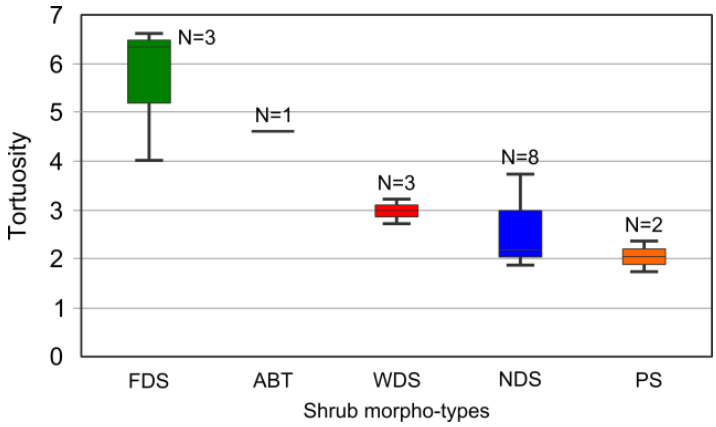

Fig. 6.13: Box plot of tortuosity in function of shrub morpho-types. It is possible to observe that the means of each shrub morpho-type plot above 75th percentile between them. Fili dendriform shrub (FDS) possesses the highest tortuosity values, followed by arbustiform (ABT), wide dendriform shrub (WDS), narrow dendriform shrub (NDS) and pustular shrub (PS).

The plot of tortuosity versus average pore throat size (APT), suggests that each shrub morpho-type yield different tortuosity and also APT results, despite few overlaps (Fig. 6.14). PS possesses the lower tortuosity and APT results. NDS and WDS possess the highest APT results, but not the highest tortuosity results. The highest tortuosity results are observed in FDS samples. These results also indicate that there is no relationship between tortuosity and APT.

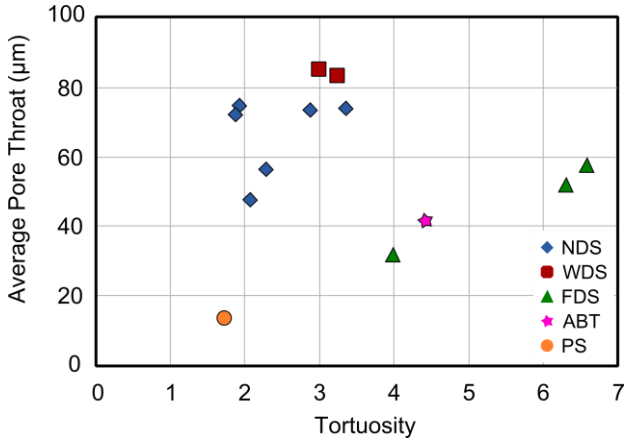

Fig. 6.14: Tortuosity vs. Average Pore Throat showing a clear grouping according to the shrub morpho-types, but without a clear mutual correlation. NDS corresponds to narrow dendriform shrub, WDS to wide dendriform shrub, FDS to fili dendriform shrub, ABT to arbustiform and, PS to pustular shrub.

Shrub packing

The analysis of shrub packing in function of tortuosity versus Archimedes (Fig. 6.15A), µCT porosity (Fig. 6.15B), permeability measurements (Fig. 6.15C) and K_{sim} from µCT (Fig. 6.15D) do not show any relationship.

ANOVA statistical analysis was applied in order to test whether shrub packing possesses a relationship with tortuosity and simulated permeability (K_{sim}) (Tables 6.3 and 6.4). Box plots of shrub packing in function of tortuosity and K_{sim} (Figs. 6.16A and B, respectively) demonstrated no relationship, as the results are overlapping. Multi-comparison test was used to prove whether shrub packing groups have statistically different means (Figs. 5.17A and B). The result illustrates that the shrub packing have means of tortuosity and K_{sim} (Figs. 5.17A and B, respectively) not significantly different.

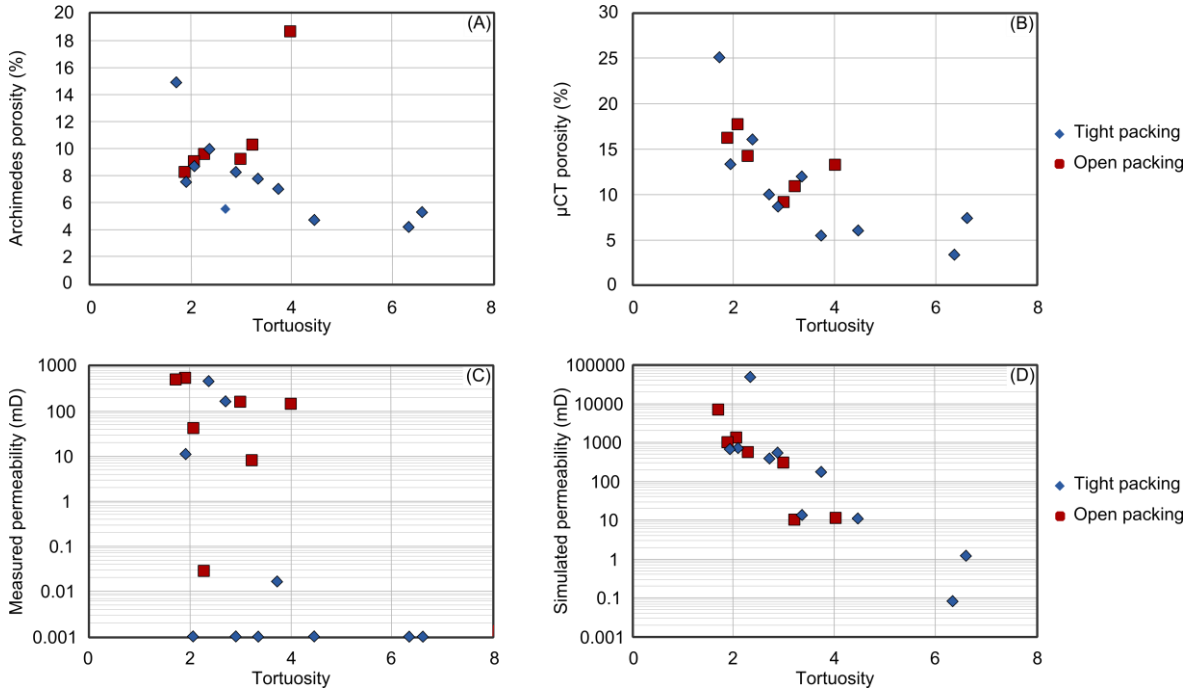

Fig. 6.15: **Shrub packing** plotted in function of (A) tortuosity versus Archimedes porosity, (B) tortuosity versus µCT porosity, (C) tortuosity versus permeability, and (D) tortuosity versus simulated permeability (K_{sim}).

	SS	df	SS/df	F	P
Groups	0.4	1	0.4	2.4	0.2
Error	2.3	15	0.2		
Total	2.6	16			

Table 6.3: ANOVA table for **tortuosity** and **shrub packing**. Sum of Squares (SS), degree of freedom (df), and the Mean Squares (SS/df) for each source. The F-statistic is calculated as the ratio of the mean squares, for p-values below a pre-defined value of 0.05 (Sheskin, 2004).

	SS	df	SS/df	F	P
Groups	6.8	1	6.8	0.6	0.4
Error	164.1	15	10.9		
Total	170.9	16			

Table 6.4: ANOVA table for $\mathbf{K_{sim}}$ and **shrub packing**. Sum of Squares (SS), degree of freedom (df), and the Mean Squares (SS/df) for each source. The F-statistic is calculated as the ratio of the mean squares, for p-values below a pre-defined value of 0.05 (Sheskin, 2004).

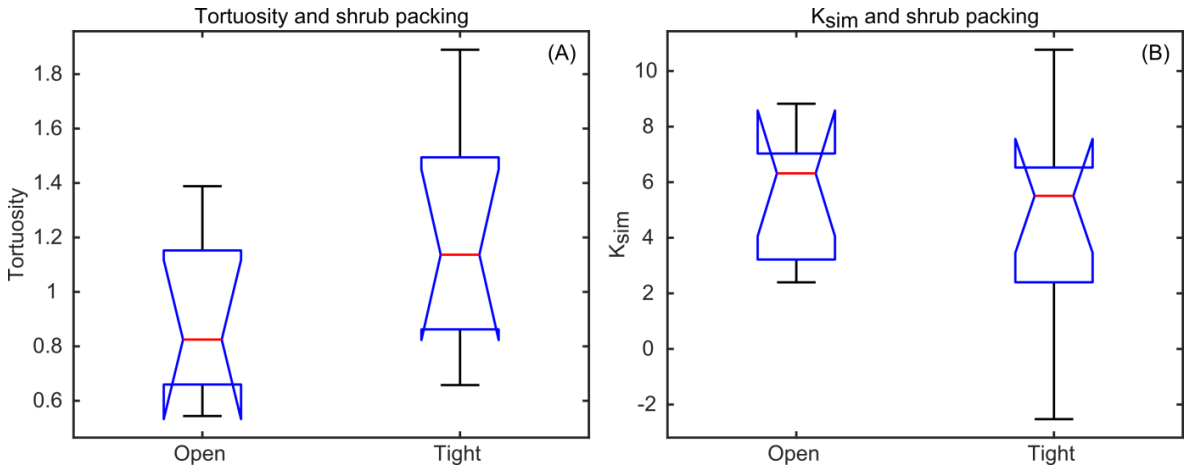

Fig 6.16: ANOVA box plot analysis for **shrub packing** in function of (A) tortuosity and (B) permeability simulation (K_{sim}).

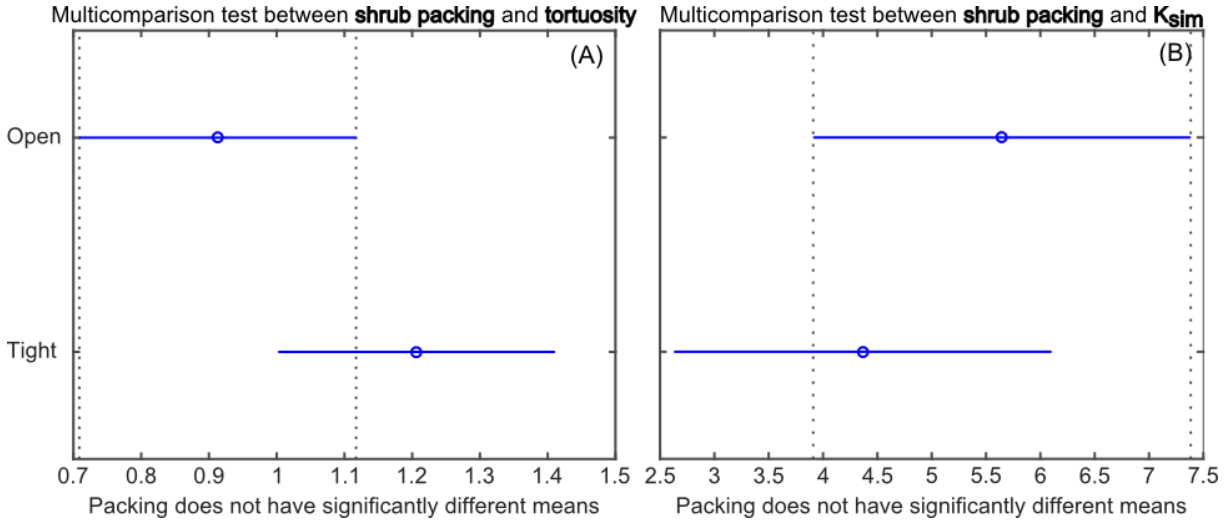

Fig. 6.17: "Multi-comparison" test graphs for **shrub packing** in function of (A) tortuosity and (B) permeability simulation (K_{sim}).

Shrub size sorting

Size sorting samples plotted in graphs of tortuosity versus Archimedes porosity (Fig. 6.18A), µCT porosity (Fig. 6.18B), measured permeability (Fig. 6.18C) and K_{sim} (Fig. 6.18D) do not show a clear relationship. Only Fig. 6.18C suggests a correlation between size sorting and permeability, as it was observed already in Chapter 3.

In order to test whether shrub size sorting control the sample tortuosity (T_{2lm}) and the simulated permeability (K_{sim}) on plug scale, ANOVA statistical analysis was applied (Tables 6.5 and 6.6, respectively). The ANOVA box plots statistical analysis of tortuosity (Fig. 6.19A) and K_{sim} (Fig. 6.19B) in function of shrub size sorting for $p<0.05$ indicate that the null hypothesis of significant differences for the shrub size sorting, tortuosity and K_{sim}, is rejected. "Multi-comparison" test for tortuosity and K_{sim} in function of shrub size sorting (Figs. 6.20A and B) show no significant differences.

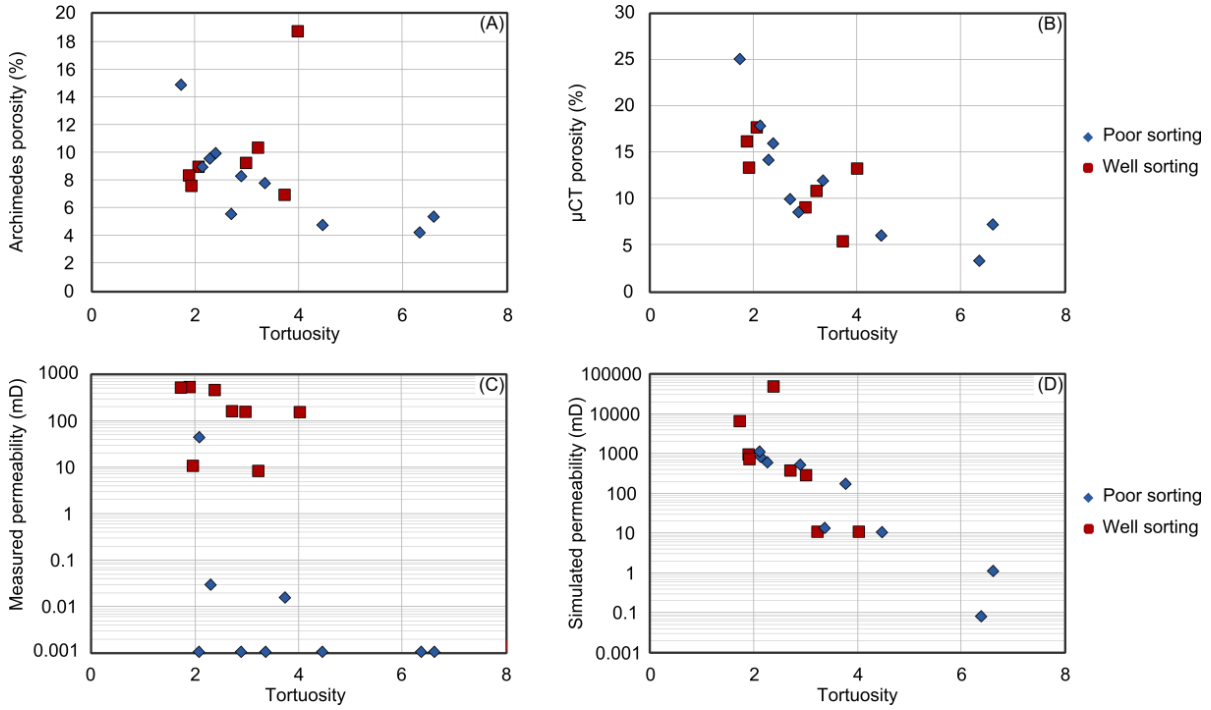

Fig. 6.18: **Shrub size sorting** plotted in graphs of (A) Tortuosity vs. Archimedes porosity, (B) Tortuosity vs. µCT porosity, (C) Tortuosity vs. Permeability, and (D) Tortuosity vs. simulated permeability (K_{sim}).

	SS	df	SS/df	F	P
Groups	0.4	1	0.4	2.9	0.4
Error	2.2	15	0.2		
Total	2.6	16			

Table 6.5: ANOVA table for tortuosity and **shrub size sorting**. Sum of Squares (SS), degree of freedom (df), and the Mean Squares (SS/df) for each source. The F-statistic is calculated as the ratio of the mean squares, for p-values below a pre-defined value of 0.05 (Sheskin, 2004).

	SS	df	SS/df	F	P
Groups	24.4	1	24.4	2.5	0.1
Error	146.4	15	9.8		
Total	170.9	16			

Table 6.6: ANOVA table for K_{sim} and **shrub size sorting**. Sum of Squares (SS), degree of freedom (df), and the Mean Squares (SS/df) for each source. The F-statistic is calculated as the ratio of the mean squares, for p-values below a pre-defined value of 0.05 (Sheskin, 2004).

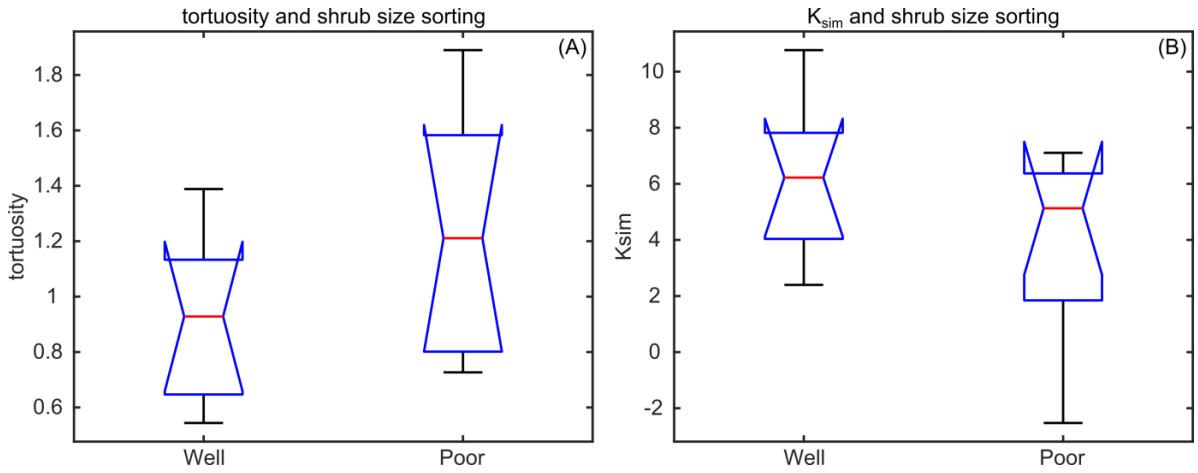

Fig. 6.19: ANOVA box plot analysis for **shrub size sorting** in function of (A) tortuosity and (B) permeability simulation (K_{sim}).

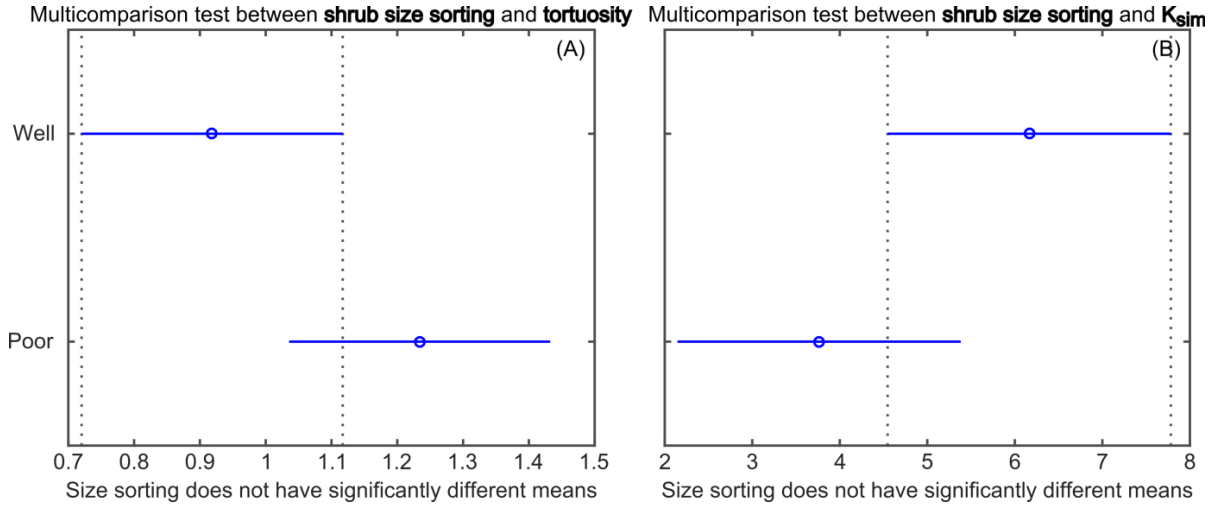

Fig. 6.20: "Multi-comparison" test graphs for **shrub size sorting** in function of (A) tortuosity and (B) permeability simulation (K_{sim}).

Shrub size

The plot of tortuosity versus Archimedes or µCT porosity in function of shrub size, do not exhibit clear relationship (Figs. 6.21A to D). ANOVA statistical analysis tests whether shrub size possesses a relationship with tortuosity and simulated permeability (K_{sim}) (Tables 6.7 and 6.8). The box plots of tortuosity in function of shrub size (Fig. 6.22A) for $p<0.05$ also indicate that the null hypothesis of significant differences for the shrub size and tortuosity, is rejected. However, K_{sim} in function of shrub size (Fig. 6.22B) indicate that center line of small sized shrubs plot above the 75th percentile of the medium and large sized shrubs. "Multi-comparison" test testify that tortuosity in function of shrub size (Fig. 6.23A) show no significant differences. Whereas, "multi-comparison" test for K_{sim} in function of shrub size (Fig. 6.23B) also illustrates that means of small sized shrubs are significantly different from the other shrub sizes. The number of samples for the different shrub size populations has to be drastically increased in order to perform a statistical relevant analysis on the influence of shrub sizes on tortuosity and k_{sim}.

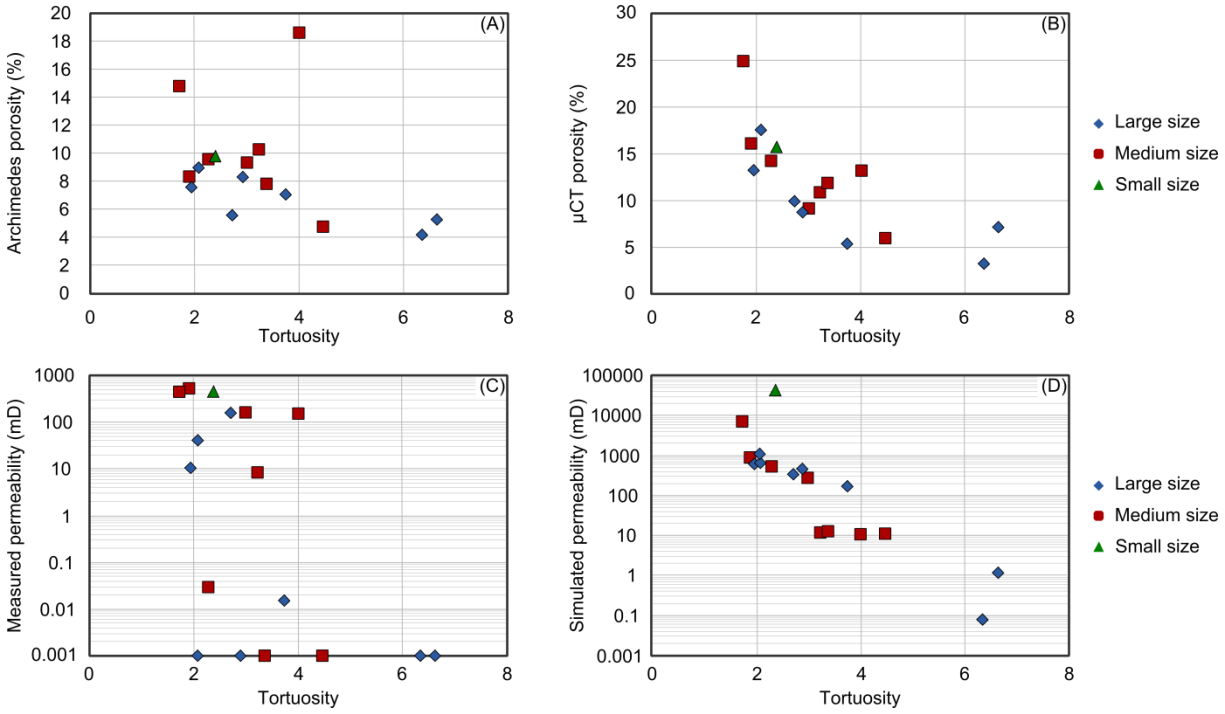

Fig. 6.21: **Shrub size** classes plotted in graphs of (A) Tortuosity vs. Archimedes porosity, (B) Tortuosity vs. µCT porosity, (C) Tortuosity vs. Permeability, and (D) Tortuosity vs. simulated permeability (K_{sim}).

	SS	df	SS/df	F	P
Groups	3.6	2	1.8	0.8	0.5
Error	30.5	14	2.2		
Total	34.1	16			

Table 6.7: ANOVA table for tortuosity and **shrub size**. Sum of Squares (SS), degree of freedom (df), and the Mean Squares (SS/df) for each source. The F-statistic is calculated as the ratio of the mean squares, for p-values below a pre-defined value of 0.05 (Sheskin, 2004).

	SS	df	SS/df	F	P
Groups	54.8	2	27.4	3.3	0.1
Error	115.7	14	8.3		
Total	170.5	16			

Table 6.8: ANOVA table for k_{sim} and **shrub size**. Sum of Squares (SS), degree of freedom (df), and the Mean Squares (SS/df) for each source. The F-statistic is calculated as the ratio of the mean squares, for p-values below a pre-defined value of 0.05 (Sheskin, 2004).

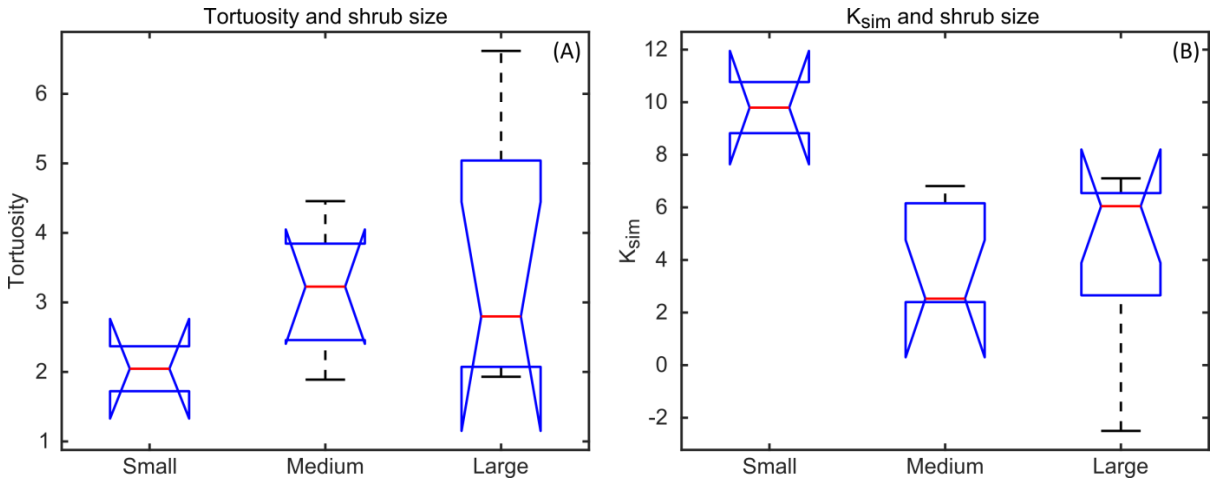

Fig. 6.22: ANOVA box plot analysis for **shrub size** in function of (A) tortuosity and (B) permeability simulation (K_{sim}).

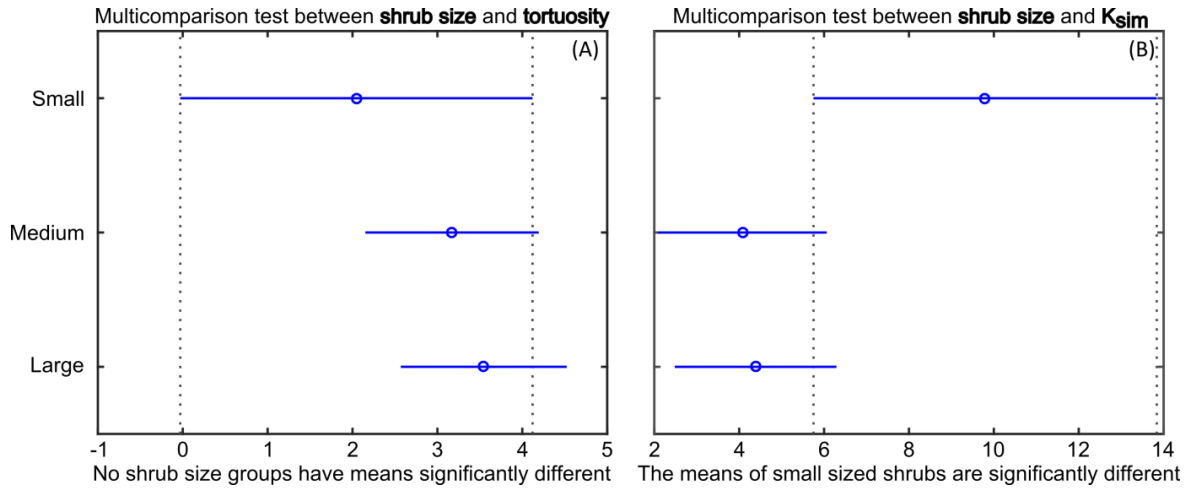

Fig. 6.23: "Multi-comparison" test graphs for **shrub size** in function of (A) tortuosity and (B) permeability simulation (K_{sim}).

6.3.4 Mini-permeameter

Wall measurements

In the quarry wall different shrub morpho-types (NDS, WDS and PS/ABT), crusts, mats and immature palaeosol (intraclast-rich layers) had their permeability measured by using the "TinyPerm II" device (Fig. 6.24A). The permeability plot of the measured grids (40 cm x 30 cm) shows the high permeability variability within one horizontal layer over very short distances (Fig. 6.24B). The results vary between 1 and 31050 mD. The highest permeabilities (> 10000 mD) were observed in intraclast-rich layers, and locally in crust and NDS layers (Figs. 6.24B and 6.25). The lowest permeabilities (< 100 mD) occurred in crust layers (Figs. 6.24B and 6.25). Variogram map (Fig. 6.24C) was calculated for each measured grid, allowing to define the direction of largest continuity. The map (Fig. 6.24C) shows that the main continuity is parallel to the layering, reflecting the anisotropy of the rock. The average mini-permeameter results plotted along the (related-)shrub profile wall (Fig. 6.25) demonstrate that each shrub morpho-types and lithotypes are characterized by distinct permeability averages.

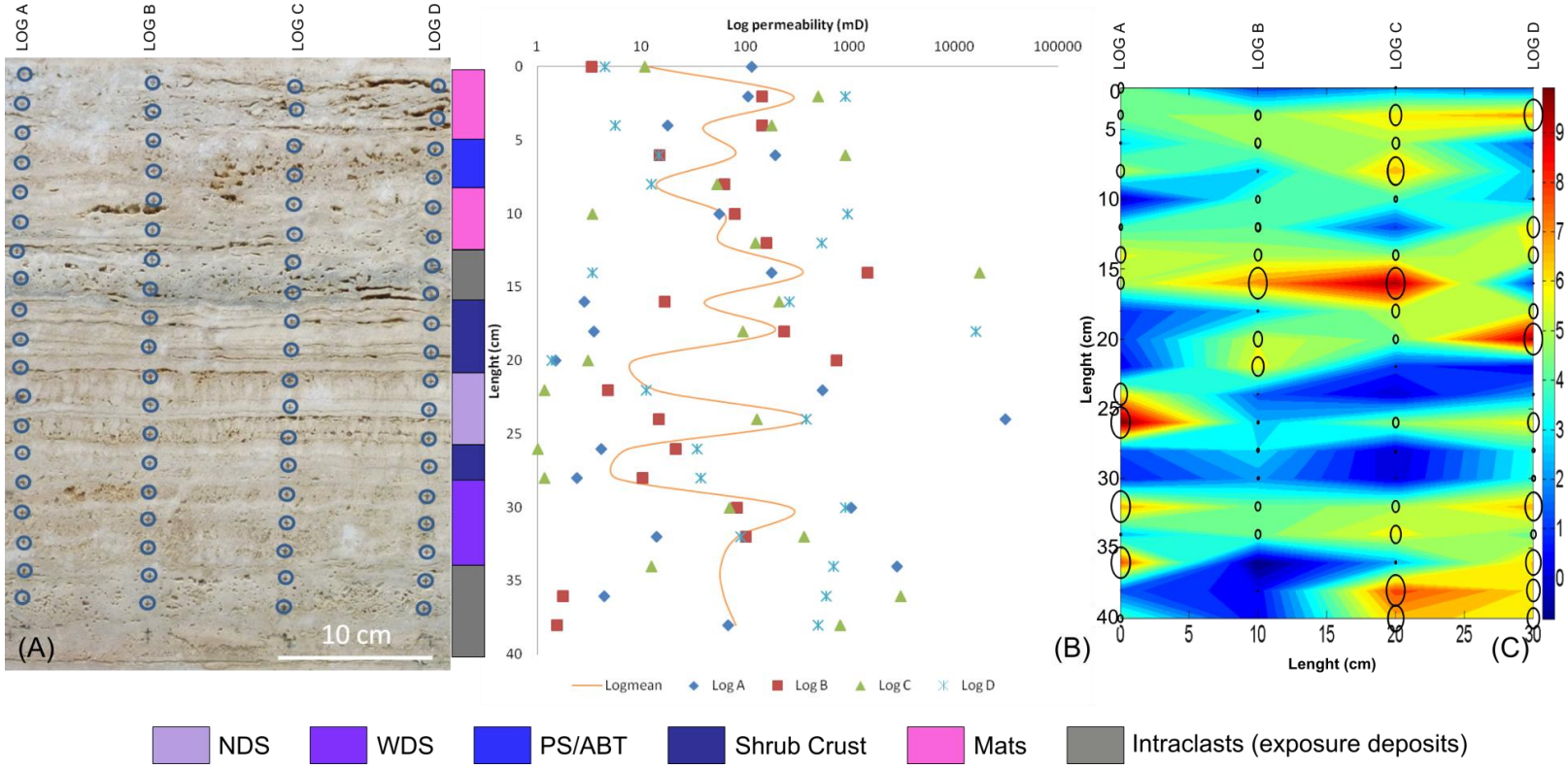

Fig. 6.24: (A) Querciolaie-Rinascente quarry wall with the location of air mini-permeameter measurements. (B) Mini-permeameter results plotted along the length of the profiles. The plots show high horizontal and vertical permeability value variability. (C) Variogram map for each measured grid, showing that the largest continuity is parallel to the layering. It is also possible to notice that within the different shrub morpho-types, mats and intraclast layers possess a clear anisotropy. The lateral anisotropy within the different shrub layers is determined by their lateral texture variation. NDS corresponds to narrow dendriform shrubs, WDS to wide dendriform shrubs, ABT to arbustiform shrubs, and PS to pustular shrubs.

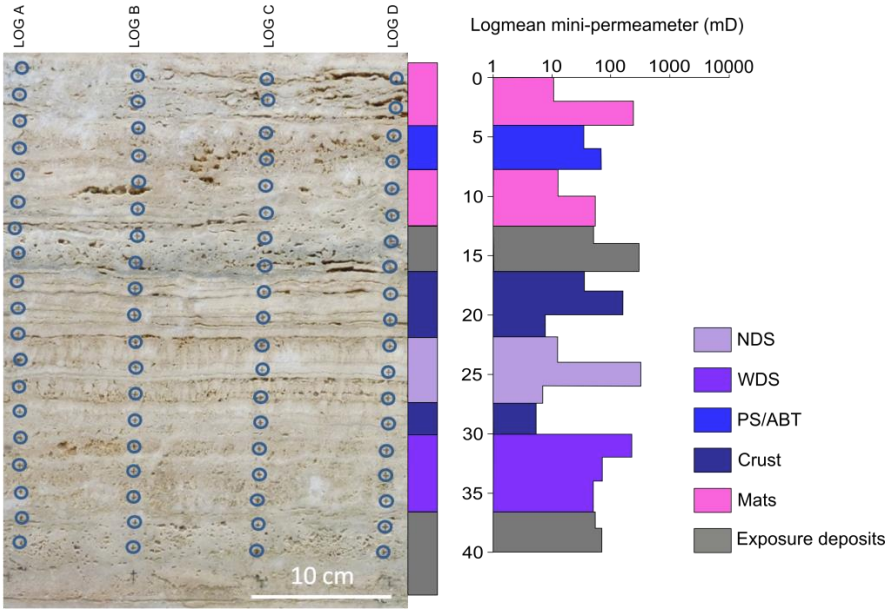

Fig. 6.25: Distribution of average permeability results for the measured grids performed in the quarry wall of Querciolaie-Rinascente. The permeability variation is clearly controlled by the different lithotypes. NDS corresponds to narrow dendriform shrubs, WDS to wide dendriform shrubs, ABT to arbustiform shrubs, and PS to pustular shrubs.

Block measurements

The travertine block from Tivoli, composed of NDS, WDS, ARB, PS/ABT, crust and mats, possesses high horizontal variability in permeability along one layer (Fig. 6.26). The opposite sides of the block show that sides 1 and 4 (Fig. 6.26A) possess very different logmean permeability curve pattern, being only the bottom with similar results. The sides 2 and 3 (Fig. 6.26B) possess similar logmean permeability curve pattern, but with different magnitude order. Variogram maps were also calculated for each measured grid in the block (Fig. 6.27). The directional variogram parallel (Fig. 6.27) to the laminae and perpendicular (top and bottom of the block) (Fig. 6.28) clearly shows large permeability anisotropy within laminae. Fig. 6.29 illustrates the high mini-permeameter logmean variation within different shrub morpho-types and lithotypes laminae.

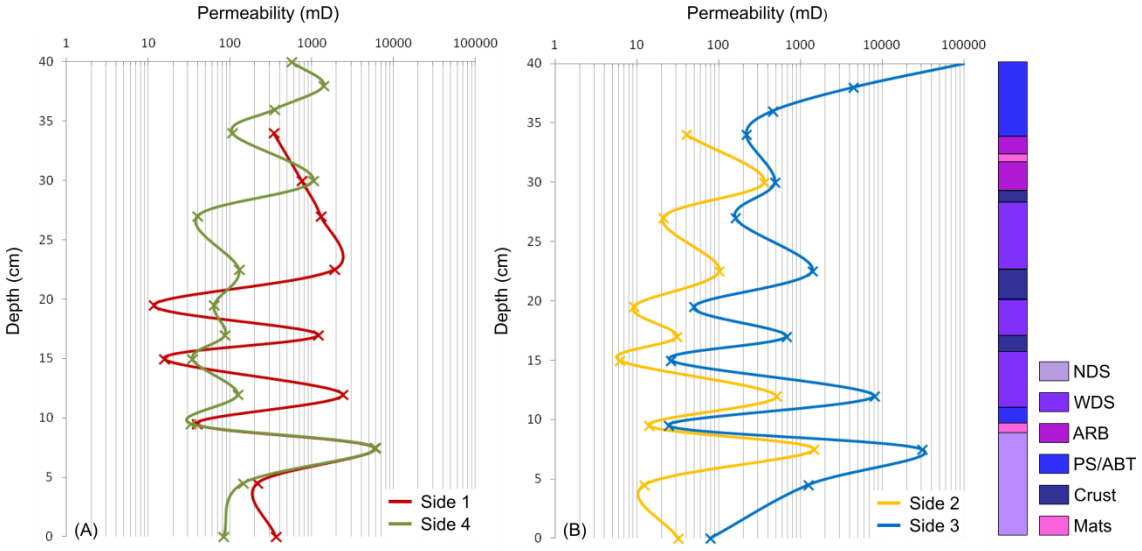

Fig. 6.26: (A) The logmean mini-permeability results from the sides 1 and 4 of the block and (B) sides 2 and 3.

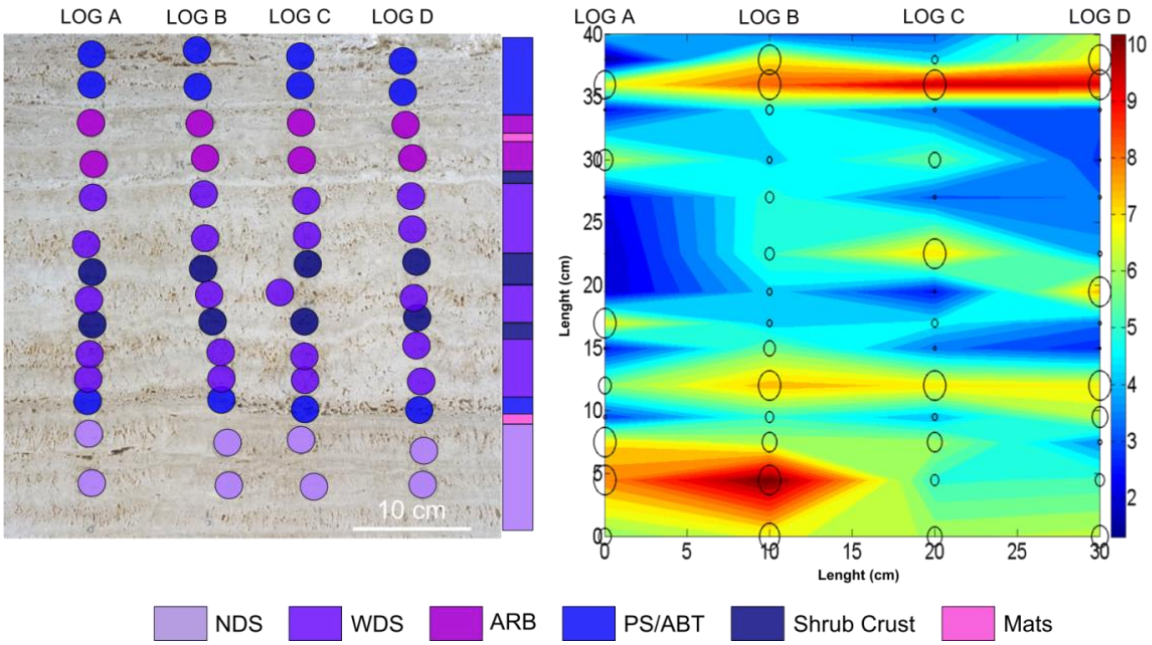

Fig. 6.27: Variogram maps with corresponding grid for side one of the block showing large permeability anisotropy within laminae. NDS corresponds to narrow dendriform shrubs, WDS to wide dendriform shrubs, ARB to arborescent, ABT to arbustiform shrubs, and PS to pustular shrubs.

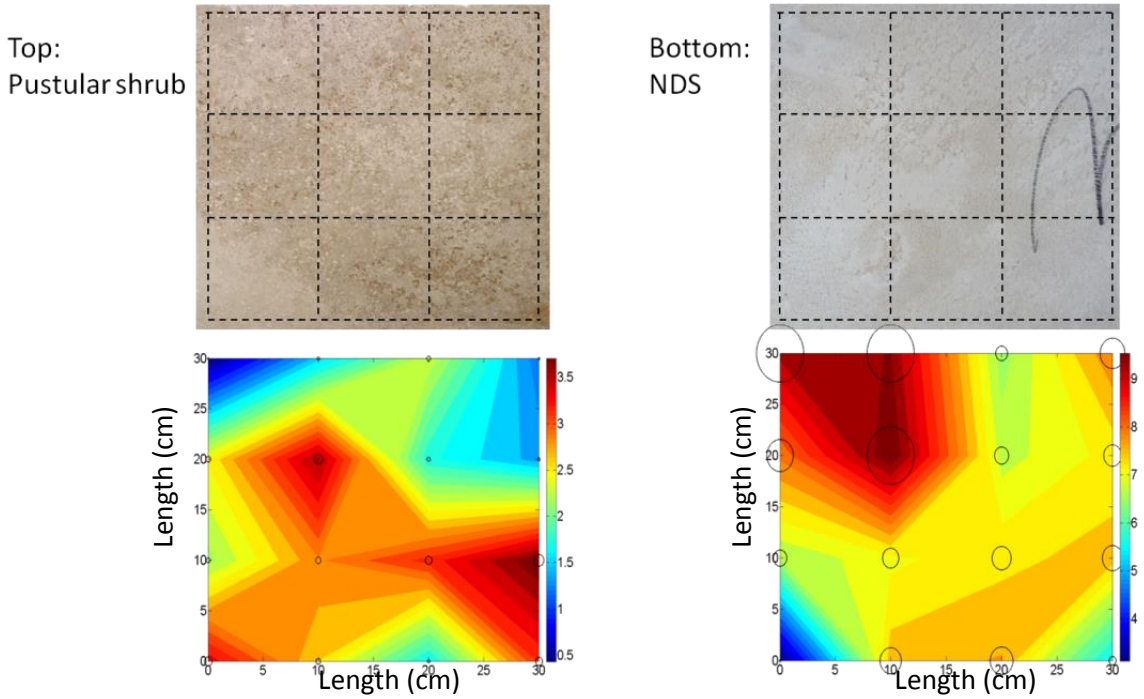

Fig. 6.28: Variogram maps with corresponding grid for top and bottom of the block. This map reflects the permeability anisotropy distribution within a layer.

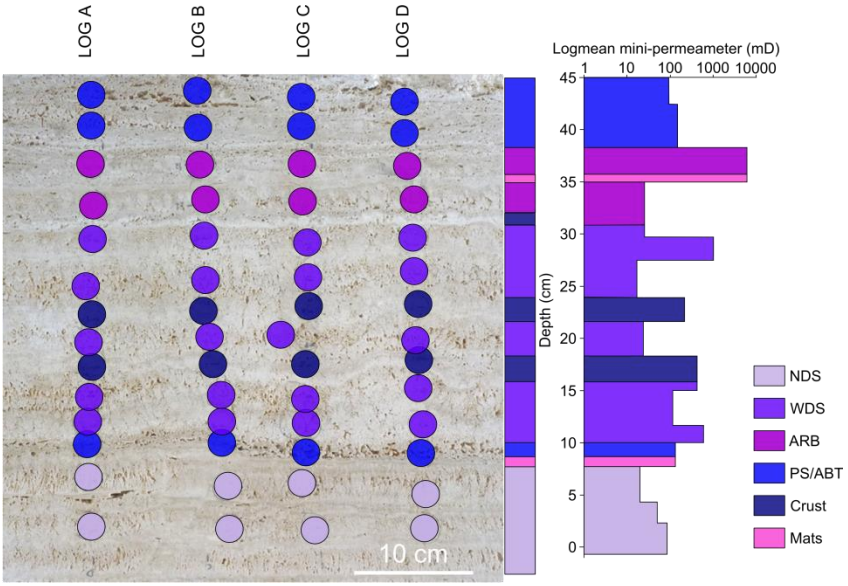

Fig. 6.29: Distribution of the mini-permeameter logmean results for the measured grids performed on side 1 of the block. A clear relationship between permeability and lithotypes becomes apparent. NDS corresponds to narrow dendriform shrubs, WDS to wide dendriform shrubs, ARB to arborescent, ABT to arbustiform shrubs, and PS to pustular shrubs.

In the block, plugs were collected from the same area where the mini-permeameter measurements were performed. The comparison between the (standard) laboratory and "TinyPerm II" measurements (Fig. 6.30) shows very different results for the same analyzed area/sample. In general, mini-permeameter results possess higher permeability values changing from zero to two or three orders of magnitude differences than the lab permeability tests (Fig. 6.31).

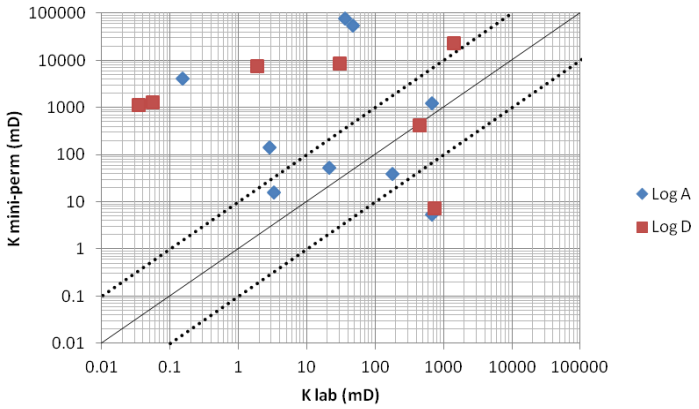

Fig. 6.30: Correlation graph of laboratory permeability log (K lab) versus mini-permeameter log (K mini-perm). Continuous black line corresponds to a perfect correlation, and the dotted ones illustrate an uncertainty of ±1 magnitude order.

Box plots of the mini-permeameter measurement results from the block and the quarry wall (Fig. 6.31) are subdivided according to shrub morpho-types, mats, crust and immature palaeosols. From these box plots it is possible to notice the high variability of the results of mini-permeameter from the block and the quarry wall. Block measurements possess slightly higher mini-permeameter results than from the wall (Fig. 6.31). The means for the shrub morpho-types and lithotypes in function of mini-permeameter results (Fig. 6.31) are not significantly different, as the results are overlapping.

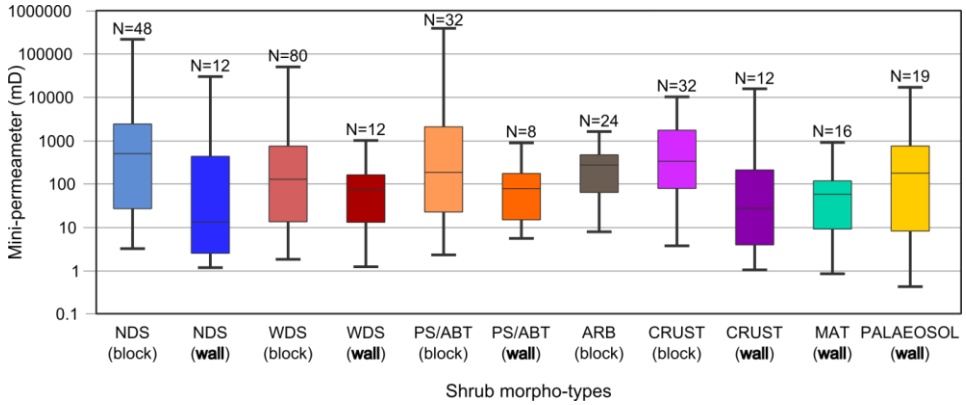

Fig. 6.31: Box plots of all mini-permeameter results from the block and the quarry wall in function of shrub morpho-types, crusts, mats and intraclasts (exposure deposits). N = number of samples. NDS corresponds to narrow dendriform shrubs, WDS to wide dendriform shrubs, ARB to arborescent shrubs, ABT to arbustiform shrubs, and PS to pustular shrubs.

6.3.5 Application of RQI and FZI methodology to the mini-permeameter results

The RQI and FZI methodology for rock typing was applied on the block mini-permeameter measurements, and on the lab measurements. The results show that both methodologies indicate good and excellent RQI and FZI groups (C, D, and E – see Chapter 2) (Table 6.9, Figs. 6.32A to D). However, lab measurements reflect more pessimistic RQI and FZI results (Table 6.9, Figs. 6.32A and B) than the results from the mini-permeameter measurements (Table 6.9, Figs. 6.32C and D). The latter results possess less permeability variation and better RQI and FZI groups in comparison to lab permeability data. Both measurements show differences in reservoir quality along one layer (Figs. 6.32A to D). In general, NDS and WDS possess the highest RQI and FZI results, while crust represents the lowest results (Figs. 6.32A to D).

Sample	Porosity (%)	lab k (mD)	TinyPerm II - side 3 (mD)	RQI (TinyPerm II)	RQI (groups)	FZI (TinyPerm II)	FZI (groups)
A2	19.1	665.9	1249.8	2.5	D	10.8	D
A4	8.0	21.2	53.2	0.8	D	9.2	D
A5	10.0	177.0	39.3	0.6	D	5.6	D
A6	9.5	0.15	4069.9	6.5	E	62.4	E
A8	12.4	3.21	15.9	0.4	C	2.5	D
A9	13.8	660.0	5.4	0.2	C	1.2	D
A12	9.6	2.82	142.8	1.2	D	11.5	D
A14	16.4	47.1	55262.2	18.2	E	92.7	E
A15	8.3	35.7	78967.5	30.7	E	340.3	E
D4	10.2	723.0	7.2	0.3	C	2.3	D
D5	10.4	444.4	416.7	1.9	D	17.2	E
D8	11.2	1.84	7653.4	8.2	E	64.7	E
D9	11.8	30.3	8779.7	8.6	E	64.3	E
D12	6.5	0.001	1119.8	4.1	E	59.7	E
D14	11.4	0.05	1284.6	3.3	E	25.9	E
D15	14.3	1381.1	23591.9	12.8	E	76.7	E

Table 6.9: Permeability data set of 16 studied plugs collected from side one of the block, measured with conventional laboratory device and with the "TinyPerm II" device. The samples started with the letter "A" and "D" corresponds to the plugs from the log A and D respectively.

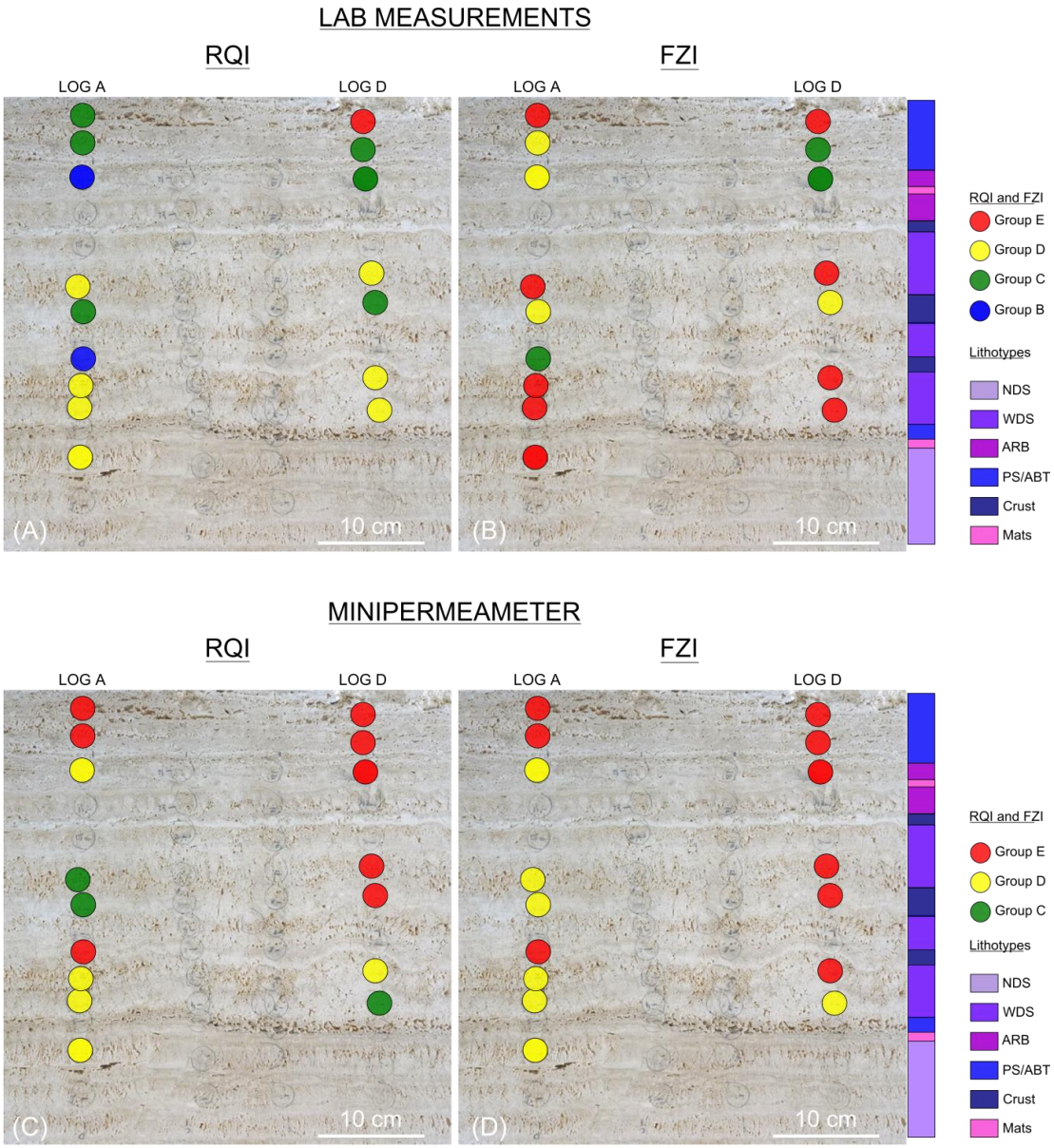

Fig. 6.32: Flow zone indicator (FZI) and reservoir quality index (RQI) results based on the lab measurements applied on the block results (A and B) and on the mini-permeameter measurements (C and D). FZI and RQI comprise only groups C, D and E that corresponds to good and excellent reservoir quality (see Chapter 2). NDS corresponds to narrow dendriform shrubs, WDS to wide dendriform shrubs, ARB to arborescent, ABT to arbustiform shrubs, and PS to pustular shrubs.

6.4 Discussion

The shrub textures and their petrophysical and pore network relationship were analyzed and discussed already in Chapters 4 and 5. As it was discussed in the latter chapters, plug measurements have their permeability results strongly influenced by the heterogeneities encountered in the samples. The permeability simulation and mini-permeameter measurements allowed to reach different reservoir scales (upscaling), improving the characterization and knowledge about the shrub reservoirs.

6.4.1 Permeability simulation and Tortuosity

The study of permeability is very important for understanding and predicting reservoir behavior. Permeability is the capability of a porous rock or sediment to allow flow of fluids through its pore spaces. In other words, it represents the connectivity between the pores and how the fluids will flow within them. By applying µCT analysis in specific areas within the studied plug samples, it was possible to refine and observe the permeable nature of the shrub morpho-types,

avoiding the rock heterogeneities, since the analysis can be carried out at a scale relevant for that purpose. To better characterize the differences in reservoir behavior, the multi-method approach that combines µCT analysis with permeability simulations and hydraulic unit calculations was applied. The results were satisfactory and realistic.

The use of µCT analysis gave the possibility to study in detail the pore network of the shrubs. The resolution used was ~ 16 µm, in plugs of 2.5 cm (1 inch) and 3.8 cm (1.5 inch) diameter. This clearly does not reach the resolution for characterizing microporosity (< 1 µm). As addressed in Chapters 4 and 5, micropores are almost absent in most of the samples, and when they are present, their importance is limited.

The relationship observed in Chapter 4 between porosity and permeability in function of shrub morpho-types, and in the present Chapter 6 between simulated permeability (K_{sim}) and µCT porosity in function of shrub morpho-types showed very different results. In the first study (Chapter 4), no relationship between shrub morpho-types and poro-perm laboratory measurement results were observed. However, µCT analysis and simulated permeability allowed to evaluate in detail the poro-perm characteristics of the shrub morpho-types that showed a relationship. The number of analyzed samples for each shrub morpho-type has to be taken into account since most of them have no statistical representativeness, however, the results can be used as an indicator to evaluate the sample and the potential of the methodology.

Looking into the results in more detail, PS possesses the best reservoir characteristics (with lowest tortuosity and higher K_{sim} results), being followed (in decreasing order of reservoir performance) by NDS, WDS, ABT and FDS (with higher tortuosity and lower K_{sim} results). Very different results were obtained in the measured samples from the laboratory (Chapter 4). The latter show that for e.g. PS possess the lowest poro-perm results, while WDS the highest. The explanation here relates to the work scale and sample heterogeneities. The target of µCT analysis for the present study was to characterize the shrub morpho-types. For this purpose a very detailed area (0.5 cm^3) was selected of the scanned plugs. In this way, most of the heterogeneities between shrub layers could be avoided, allowing studying the characteristics of shrub morpho-types in particular. The influence of micropores cannot explain the differences in measured and simulated permeability, because their importance within the shrubs is very low if not absent (see Chapters 4 and 5). It is likely that the exclusion of other lithotypes that possess a different pore network and that interfere in the final result from the permeability analysis will be more straightforward to the shrub morpho-type results. If each morpho-types and lithotypes can be characterized and distinguished between each other, it will help to understand the reservoir behavior and predict future problems in the production of water or hydrocarbons. The pore network is not simplified by this method, it rather relates to the analyzed area that is very specific.

The heterogeneities within the rock likely increase the sinuosity and tortuosity of fluid flow and consequently negatively affect the permeability (Torabi and Fossen, 2009), as it was observed in the analyzed sample, while simulated permeability and µCT porosity results decreases, tortuosity increases. The presence of branches, observed in dendriform shrubs, will favor higher tortuosity pathways.

In contrary to the poro-perm laboratory measurements, the µCT porosity and K_{sim} do not show a relationship either with shrub packing, size sorting or size. The reason again may be due to the scale of the measurements. Possibly, in larger samples (plug size) the texture heterogeneities will display a stronger control on poro-perm results, as it was observed in Chapters 4 and 5.

6.4.2 Mini-permeameter

The upscaling of the spatial distribution of permeability and the better understanding of the shrub reservoir behavior was reached by analyzing the air-driven mini-permeability measurements. The results show that the vertical variation was very high and lateral continuity existed, be it also with some variation at cm-scale displaying the high anisotropy within these horizons. This means that the permeability continuity is larger in the direction parallel to the laminae than in the perpendicular direction (Possemiers et al., 2012). Also, the small scale

texture variation (heterogeneities) within the shrub morpho-types and other lithotypes is responsible for the high permeability variation values within laminae.

The comparison between the measured permeability in the laboratory (K lab) and the ones gathered by using the air mini-permeameter device (K mini-perm) is significant, with the second possessing higher permeabilities and reaching two or three orders of magnitude of difference. It is very likely that the main reason for this distinction between the two methods is due to the sample-size limitation (Torabi and Fossen, 2009). The plug samples that are measured in laboratory have their surrounding encapsulated by a rubber sleeve, limiting the horizontal percolation of the gas flow. The perpendicular lithological barriers, especially compartmentalizing porosity in vertical plugs, also cause the permeability to very low values. The mini-permeameter investigates some depths of approximately two to four times the internal radius of the tip seal (Goggin et al., 1988). Here air has space to escape in all directions and if there is a barrier in a vertical way the air can still escape in a different direction. Huysmans et al. (2008) already attributed higher average permeability values due the measurement scale. Another reasons for this difference are 1) K lab possesses confinement pressure, while K mini-perm does not; 2) K mini-perm was executed on a block and quarry wall in environmental conditions (the pores can keep a small amount of irreducible water), while in the lab the samples are dried; 3) the open area to flow is different (lab and environmental conditions) and in heterogeneous rocks this can be critical. It is also possible that more than one reason can influence the differences in permeability results.

This methodology illustrates the lateral heterogeneous complexity of the different shrub morpho-types and lithotypes.

The experimental use of Reservoir Quality Index (RQI) and Flow Zone Index (FZI) methodology (Amaefule et al., 1993) applied to the studied block allowed to observe the parallel and perpendicular flow zones within the shrub morpho-types. Flow units are strongly dependent on the permeability distribution (Aminian et al., 2002). The results showed small variability of reservoir quality. It means that different shrub morpho-types present similar reservoir behavior and because of this they receive a similar flow zone index (good and excellent FZI). This seems contradictory, because as it was discussed before (Chapters 4, 5 and 6) small-scale heterogeneities within laminae do influence the permeability anisotropy. However, what it is observed in the present study is that the heterogeneities do not influence significantly the reservoir quality, and this can be explained by the fact that facies heterogeneities occur localized.

6.5 Conclusions

To understand the flow and porosity in the complex shrub structures, the use of computer tomography and Lattice Boltzmann Method permeability simulations was necessary, since a 2D study is very limited. These methodologies were applied to obtain 3D quantifications of the pore network and flow paths. The results proved that there exists a relationship between μCT porosity and simulated permeability, as well as with tortuosity and pore throat sizes in function of shrub morpho-types. PS possesses the lowest tortuosity and the highest permeability values, followed by NDS, WDS, ABT and finally FDS with the highest tortuosity results and lowest permeability data. Thanks to the detailed scale at which the shrubs were analyzed, rock heterogeneities could be avoided. Besides, shrub size sorting and packing has no influence in the μCT porosity and permeability simulation results. The velocity distribution is preferentially oriented and aligned along the z-axis (Fig. 6.8), in agreement with the main pore type (growth framework porosity). The geostatistic results as well as the 3D streamlines velocity distribution demonstrate how heterogeneous the shrub structures are.

The use of the Tiny-permeameter II device allowed unraveling the permeability distribution within a reservoir with different shrub morpho-types at large scale. Vertical permeability variation was very high as well as high lateral permeability variation is observed at cm-scale. High anisotropy occurs within laminae, with larger permeability continuity in the direction parallel to the laminae. Textural heterogeneities are responsible for the high permeability variation values within laminae. The comparison between the measured permeability in the

laboratory and by using the air mini-permeameter device shows that the first possesses higher permeabilities reaching two or three orders of magnitude of difference. The application of RQI/FZI methodology on the mini-permeameter results pointed out that shrub-dominated reservoir would have similar flow zone index (good and excellent reservoirs) despite the small-scale heterogeneities within laminae.

Understanding complex variation in pore network is the key to improve reservoir description and exploitation. The multi-method and multi-scale workflow allowed a better characterization and understanding of the reservoir characteristics of the different shrub morpho-types. Therefore, LBM and mini-permeameter methodologies have a large potential in rock-typing of complex reservoirs. The applied workflow has the potential to substitute the laboratory permeability measurements on large core samples, which is rather expensive and because of this, not so often used.

CHAPTER 7 Acoustic properties in shrub morpho-types from Tivoli (Central Italy): relation to porosity-pore-types and comparison with continental carbonate results from Turkey and Hungary

7.1 Introduction

Carbonate rocks possess a complex pore system. The variety of pore-types is large when compared to siliciclastic. Continental carbonate rocks possess very heterogeneous textures and pore-types mainly due to the depositional environment in various facies and to diagenetic overprinting. The impact of diagenesis can modify significantly the mineralogy and the pore structure within carbonate rocks (Anselmetti and Eberli, 1993; Xu and Payne, 2009). Cementation and dissolution are diagenetic modifiers that can reduce or enhance the porosity (Eberli et al., 2003). Besides, the travertine deposits are well known for their complex pore network characteristics (Pentecost, 1990; Soete et al., 2015; Claes et al., 2015; De Boever et al., 2016) and for the fact that similar lithofacies can possess very different three-dimensional pore shapes (Soete et al., 2015; Claes et al., 2015; Erthal et al., 2017; Claes et al., 2017). Different pore shapes influence the elastic properties of the rock and, therefore, the sonic velocity (Anselmetti and Eberli, 1993; Xu and Payne, 2009; Soete et al., 2015). Xu and Payne (2009) demonstrated that rounded pores (i.e. mouldic, intraframe and vuggy) possess faster compressional-wave velocities (Vp) than flatter pores. Usually, the wave velocity propagation is calculated by the relation between the sample length size and the time that wave spends to travel through the sample (Morschbacker et al., 2010).

Shrub-like fabrics are one of the most common features encountered in travertines from Tivoli (central Italy). They are important constituents since similar fabrics and pore-types were reported as one of the best reservoir lithotypes present in the gigantic oil reservoirs from offshore Brazil and Africa (Dias, 1998, 2005; Rezende and Pope, 2015).

It is also worth mentioning that the different shrub morpho-types for Tivoli travertines were first discriminated by Erthal et al. (2017) according to the 3D arrangement of the different morphologies, taking into account their complex pore network system.

Identification of travertine rocks in seismic lines is still not straightforward. The latter can be easily misinterpreted as other types of carbonate deposits. Data on the acoustic wave velocity for travertine rocks are still scarce in literature. Recently, Soete et al. (2015) published a study about acoustic wave velocity from the Turkish and Hungarian travertines. The seismic lines related with travertines display in general a dome morphology with reflectors displaying an aggradational pattern, formed on an escarpment created by syn-depositional faulting (Buckley et al., 2013). The interpretation of seismic lines is often one of the first actions to be carried out for the exploration of oil/gas reservoirs. A better understanding of how these deposits occur on seismic is thus necessary.

For this purpose, the present study concerns to check the acoustic wave velocity of Tivoli travertine shrubs and to compare them with the results from Turkish and Hungarian travertines according to Soete et al. (2015). The present research combines acoustic-wave velocity measurements, petrography and SEM analysis.

7.2 Methods

7.2.1 Acoustic velocity measurements

Ultrasonic pulse propagation velocity analyses were performed on 24 plug samples of 1 and 1.5 inches diameter. The measurements were performed on dry samples. The analyses were performed with the Autolab 500 equipment

(NER: www.ner.com) from New England Research, which contains three cylindrical transducers that generate, separately, a compressional wave (P) and two orthogonally polarized shear waves (S1 and S2). The frequency of these transducers is 700 kHz.

The propagation velocities of elastic waves in rocks are calculated by dividing the length of the sample (L), by the time (Δt), effectively, spent by the wave to cross the entire sample (as a one-way travel time) (equation 7.1).

$$V = \frac{L}{\Delta t} \qquad (7.1)$$

The transit time, as observed in Fig. 7.1, of the wave in the sample is equal to the time observed in the equipment minus the system time or delay time (t_0), intrinsic to the measurement system. The latter corresponds to the time spent by the signal on the electronic part and on the metal heads, with no sample inserted between them (equation 7.2):

$$\Delta t = t - t_0 \qquad (7.2)$$

The following pressure trajectory for the hydrostatic tests performed on the Autolab equipment was used: unloading (psi): 5000 – 4500 – 4000 – 3500 – 3000 – 2500 – 2000 – 1500 – 1000.

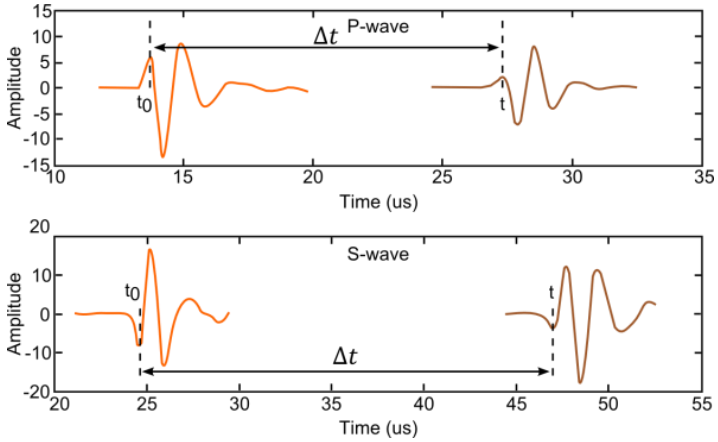

Fig. 7.1: Compressional (P-wave) and shear (S-wave) waveforms, showing the correlation of the system time signal (orange curve) and the sample curve (brown curve) (Morschbacker et al., 2010).

7.3 Results and discussions

7.3.1 Acoustic velocity measurements and petrophysical properties

Acoustic properties of 23 travertine plug samples from Tivoli quarries (central Italy) were measured. The dataset consisted of 10 narrow dendriform shrubs (NDS), 2 wide dendriform shrubs (WDS), 3 fili dendriform shrubs (FDS), 1 arborescent shrub (ARB), 3 arbustiform shrubs (ABT) and 4 pustular shrubs (PS) (Table 7.1). All analyzed samples consisted of calcite (XRD results).

Different kinds of complementary petrophysical measurements were carried out, such as Archimedes porosity, permeability, grain density, bulk density, compressional-wave velocity (Vp), shear-wave velocity (Vs) and acoustic impedance was calculated (Table 7.1). Grain and bulk density range from 2.53 to 2.69 g/cm^3 and 2.07 to 2.51 g/cm^3 respectively. Archimedes porosity varies between 3.7 to 18.6 % (mean value of 8.1 %) and permeability between 0.001 to 5254.6 mD. Vp values vary between 4836 to 5958 m/s, while Vs plots between 2675 to 3178 m/s. For a given sample, the lowering in Vp does not lower Vs in the same proportion (Fig. 7.2). As the travertine has a compact, rigid frame, it is expected that its rigidity is high, then the shear wave velocity is less sensitive as compared to the compressional wave velocity. The latter depends on the inverse of the compressibility. As porosity increases, once there is less solid material, the velocity decreases. On the one hand, as porosity decreases (and velocity increases) the Vp/Vs ratio approaches the value of pure calcite, i.e. Vp/Vs=1.93. In sum, Vp increases when porosity decreases, in this way, Vp/Vs tend to reach the pure limestone value that is Vp/Vs=1.93.

The plot Vp versus Vp/Vs ratio (Fig. 7.2) illustrates that the range in Vp/Vs ratio is very limited and varies between 1.8 to 1.9. Thus, these results show that the velocity ranges do not vary much. These values correspond to indurated samples, suggesting that artificial compaction was limited during the analysis and that the samples were strong enough for the shear stresses applied (Anselmetti and Eberli, 1993; Soete et al., 2015). According to Soete et al. (2015), the travertines, even under limited burial conditions, developed rigid rock frames that allow them, to a certain degree, to withstand compaction. The Vp/Vs ratio explains the primary porosity preservation that was reported for Pre-Salt continental carbonate reservoirs (Thompson et al., 2015). The latter, likely preserves their primary porosity in a similar way as travertines, due to the rigidity of the rock frame (Soete et al., 2015).

Sample	Permability (mD)	Archimedes porosity (%)	Grain density (g/cc)	Bulk density (g/cc)	Vp (m/s)	Vs (m/s)	Vp / Vs	Acoustic Impedance	Shrub morpho types
QR 15B	10.80	8.96	2.60	2.33	5568	3043	1.83	12.97	NDS
QR 15T	9.10	11.81	2.59	2.28	5359	2976	1.80	12.21	NDS
QR 17	7.30	7.49	2.54	2.36	5533	3029	1.83	13.05	NDS
QR 20	10.70	10.28	2.60	2.29	5379	2986	1.80	12.32	NDS
QR 22	7.90	8.28	2.56	2.33	5456	2994	1.82	12.71	NDS
QR 30	8.60	7.74	2.53	2.32	5521	3021	1.83	12.83	NDS
QR 34H	12.50	8.24	2.63	2.41	5584	3002	1.86	13.47	NDS
QR 35H	10.80	9.55	2.67	2.35	5587	2999	1.86	13.14	NDS
QR 116H1	14.60	14.52	2.60	2.18	5617	3089	1.82	12.25	NDS
QR 135H	6.20	7.49	2.60	2.41	5952	3184	1.87	14.33	NDS
QR 31H	12.60	10.23	2.69	2.28	5924	3137	1.89	13.48	WDS
QR 38H	8.50	9.26	2.53	2.27	5617	3092	1.82	12.75	WDS
QR 24V1	4.30	5.27	2.55	2.42	5692	3114	1.83	13.78	FDS
QR 29	20.90	18.62	2.58	2.07	4836	2675	1.81	10.03	FDS
QR 139V	0.80	4.17	2.56	2.48	5631	3098	1.82	13.97	FDS
QR 140H1	4.10	5.59	2.63	2.46	5958	3178	1.87	14.66	ARB
QR 117H	14.50	11.40	2.67	2.21	5840	3149	1.85	12.93	ABT
QR 138H	3.30	3.80	2.61	2.50	5933	3181	1.87	14.82	ABT
QR 140H2	6.40	6.13	2.64	2.45	5814	3150	1.85	14.22	ABT
QS 11B	3.60	4.69	2.62	2.47	5851	3159	1.85	14.43	PS
QS 11T	3.80	3.80	2.62	2.51	5812	3168	1.83	14.58	PS
QR 32V	6.30	8.59	2.60	2.39	5536	3055	1.81	13.24	PS
QR 103H2	3.10	3.70	2.62	2.49	5726	3091	1.85	14.24	PS

Table 7.1: Petrophysical and acoustic velocity measurements of 23 shrub samples from Tivoli.

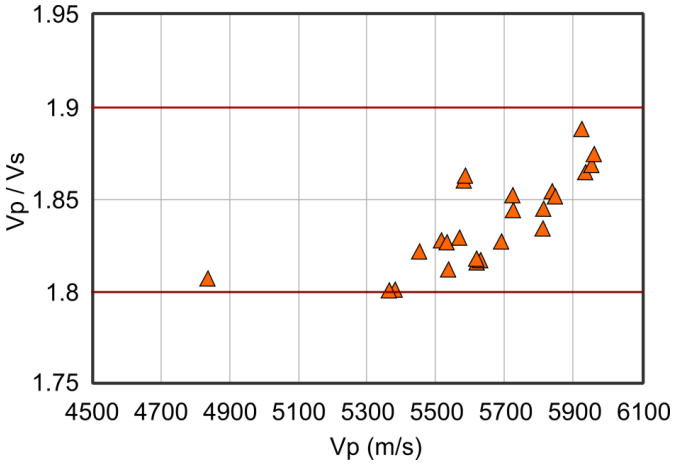

Fig. 7.2: Plot of Vp vs. Vp/Vs ratio showing that the range in Vp/Vs ratio is very limited and is varying between 1.8 to 1.9.

Vp and Vs plotted against Archimedes porosity shows that all the samples plot within the same trend (Fig. 7.3). Despite the restricted velocity range, it is still possible to observe a clear inverse trend, whereby an increase in velocity corresponds to a decrease in porosity (Fig. 7.3). Besides, grain density values of the samples reflect almost the same values, and bulk density is, therefore directly related to the acoustic velocities (Kearey et al., 2002) and it is also dependent on porosity (Soete et al., 2015).

The dominant calcite nature of these shrub travertine samples suggests that the mineralogy did not influence the body wave propagation velocities, and therefore most likely shrub fabric, texture and pore-types play an important role in the propagation speed of P- and S-waves (Anselmetti and Eberli, 1993; Verwer et al., 2008; Soete et al., 2015).

The plot of the shrub morpho-types in a Vp versus Archimedes porosity plot suggests a separation between the types involved (Fig. 7.4). However, there are similar morpho-types with very different Vp and porosity results, suggesting that pore-types play a complex role in the acoustic-wave velocity results.

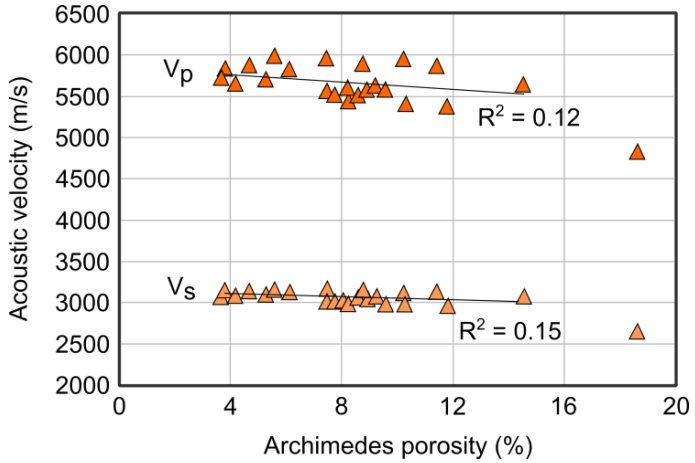

Fig. 7.3: Plot of Vp and Vs versus Archimedes porosity. An inversed correlation between both parameters is observed, with Vp and Vs decreasing while porosity increases. Removing the outliers, there is no correlation.

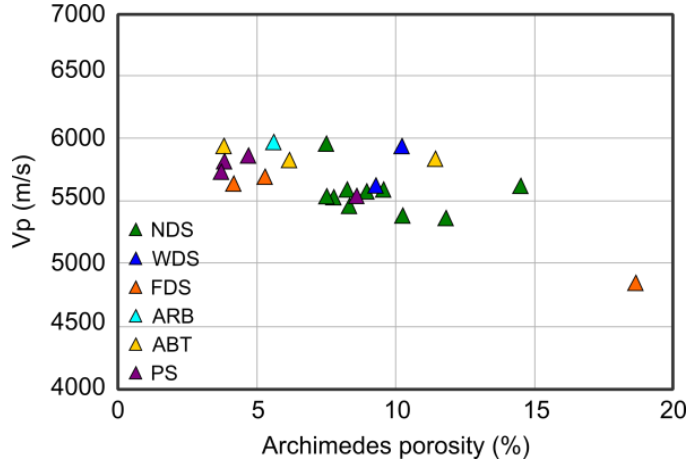

Fig. 7.4: Vp vs. Archimedes porosity in function of shrub morpho-types with different morpho-types clustering in groups. Pustular shrubs (PS) possess the highest Vp values and the lowest porosity results, followed by fili dendriform (FDS), arborescent (ARB), arbustiform (ABT), narrow dendriform (NDS) and wide dendriform shrubs (WDS). However, the lowest Vp value and the highest porosity value correspond to one FDS sample.

Moreover, the plot of pore-types in the velocity-porosity diagram displays some clustering (Fig. 7.5). It seems that the pore-types are more related with porosity than with Vp results. However, samples with similar porosity display slightly different velocities (Vp). The main pore-type observed in all shrub morpho-types consists of intershrub growth framework, yet the associations with other different dominant pore-types explain the different clusters in the velocity-porosity diagram. The pore-types groups (Fig. 7.5) are: 1) mouldic, 2) encrusted bubble, 3) vuggy, 4) interdigit, vuggy and, 5) interdigit, interlaminar, microvuggy.

Samples with **mouldic** pores possess high velocities, between 5631 to 5958 m/s and low porosities, between 3.7 to 6.1 %. **Encrusted bubble** porosity samples possess high Vp results, between 5521 and 5952 m/s, and porosities between 7.5 and 7.7 %. **Vuggy** porosity dominated samples possess Vp results that vary between 5456 and 5840 m/s and porosities varying from 8.2 and 11.4 %. Samples with **vuggy** and with **interdigit** porosities possess Vp values between 5359 and 5924 m/s and porosities of 10.2 and 14.5 %. **Microvuggy** associated with **interlaminar** porosity bearing samples possess the lowest Vp value of 4836 m/s and a porosity of 18.6 %. The pore-types that plot above the regression line comprise more cemented samples.

Samples with vuggy pore-types, associated or not with other pore-types, plot in the lower velocity area with higher porosity values, being above, on and below the regression line, because pores in these lithologies vary greatly in size (μm to dm scale diameter) and shapes, giving rise to large specific pore surfaces (Soete et al., 2015). Whereas, mouldic and encrusted bubble pore-type dominating samples plot in higher velocity areas with lower porosity values.

Several authors (Anselmetti and Eberli, 1993; Eberli et al., 2003; Fournier and Borgomano, 2007; Soete et al., 2015) already reported that velocity increase is associated with mouldic pores because they possess a rigid frame that allows fast travel times for the acoustic-wave velocity. Microporosity, on the contrary, is responsible for a decrease in acoustic velocity (Anselmetti and Eberli, 1993; Eberli et al., 2003; Fournier and Borgomano, 2007; Soete et al., 2015). However, as they are not abundant in Tivoli samples, their influence is minimal. Travertines are well known for the abundance of macropores, consequently, they cause a decrease in acoustic velocity. According to Anselmetti and Eberli (1993) and Eberli et al. (2003), in carbonate rocks, pore-type is as important as porosity in controlling sonic velocity.

ANOVA statistical analysis was applied in order to test whether shrub pore-type groups possess a relationship with V_p and/or porosity (Figs. 7.6A and B). The ANOVA box plots statistical analysis for **pore-types groups** in function of V_p (Fig. 7.6A) indicate that center line of the *interdigit, interlaminar, microvuggy group* plot below the 25th percentile of the others pore-type groups. ANOVA box plots of **pore-types groups** in function of porosity (Fig. 7.6B) illustrate that center lines of pore-type groups plot above 75th percentile between them. Multi-comparison test for $\mathbf{V_p}$ in function of **pore-type groups** indeed indicates that means of the *interdigit, interlaminar, microvuggy group* are significantly different (Fig. 7.7A) from the others pore-type groups. While, multi-comparison for **pore-type groups** in function of **porosity** testify that the means of the different **pore-type groups** indeed possess significantly different means (Fig. 7.7B).

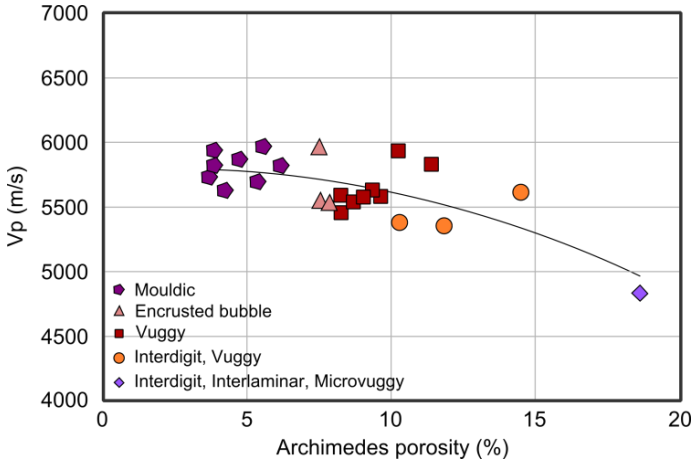

Fig. 7.5: Plot of Vp vs. Archimedes porosity of various pore-types with an exponential best-fit curve through the data for reference. The pore-types are clustered according to the second dominant pore type apart from the dominant intershrub growth framework porosity.

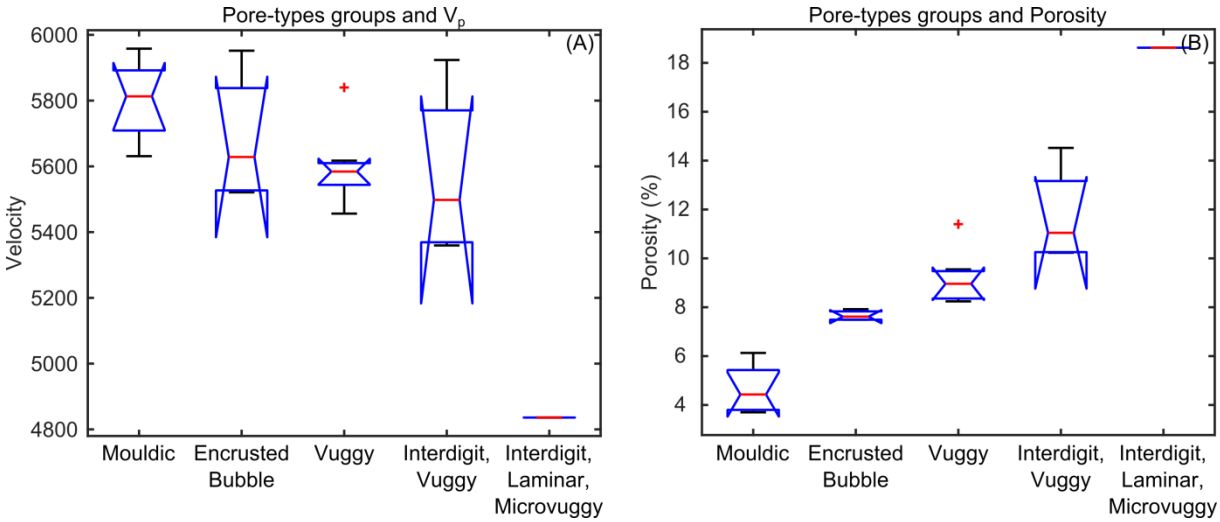

Fig. 7.6: ANOVA statistical box plots data for pore-types groups in function of (A) V_p and (B) porosity.

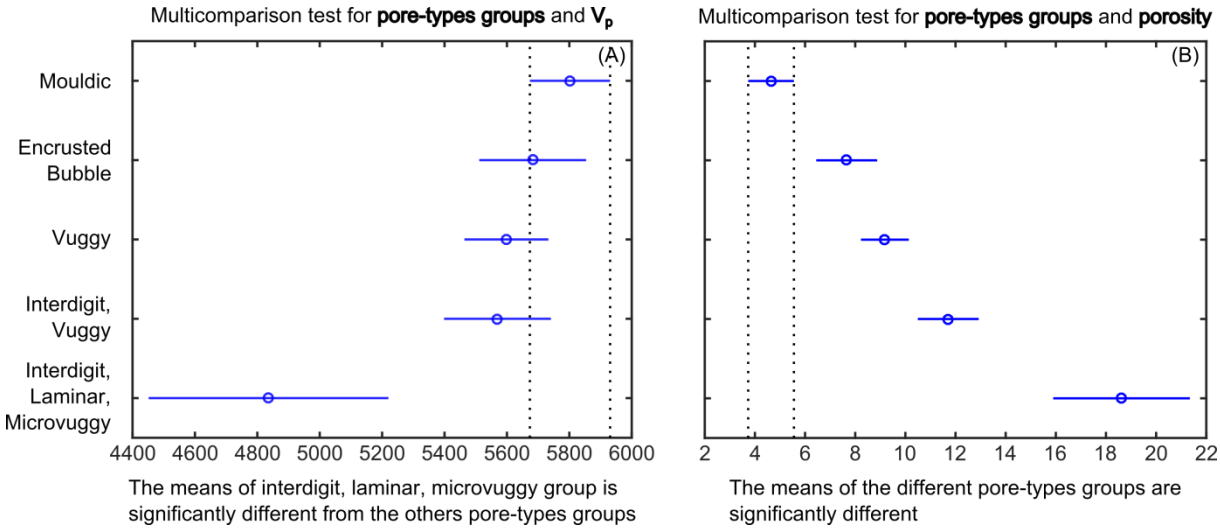

Fig. 7.7: "Multi-comparison" test graphs for pore-types groups in function of (A) V_p and (B) porosity.

Whether the pore framework is reduced or enhanced is also of importance as can be seen in figure 7.8. It is very clear that reduced porosity relates to samples that contain primary, compact and tight packing textures of the shrubs, besides cementation. These samples are associated with higher Vp results and lower porosity values (Fig. 7.8). Samples with porosity enhanced by dissolution possess lower Vp values (Fig. 7.8) and higher porosity results. Petrographically, it is clear that these samples possess very well developed depositional porosity (open packing textures) that is enhanced by dissolution that, however, did not change much the primary porosity. Primary connections between rock constituents in samples with higher porosities (> 10%) were less established and cements, when occurring, connected the individual constituents (Soete et al., 2015). The accompanied increase of the bulk modulus resulted in higher body wave velocities.

Cementation occurs in all samples, however, in the ones that initially are more compact and tightly packed, its effect may be more meaningful by relatively more decreasing the porosity of the rock and, consequently, increasing the acoustic-wave velocity. According to Eberli et al. (2003), the weak relationship between porosity and velocity in carbonates is caused by the cements and by the peculiar depositional fabrics that can enhance the elastic properties without filling completely the pore space.

No reminiscent of aragonite or any other mineral phase was observed in the samples. Therefore, the influence of different mineralogy affecting the velocity results is excluded. Thus, primary textures, diagenesis (cementation and dissolution) and pore-types determine the acoustic-wave velocity behavior of the rock for Tivoli shrubs.

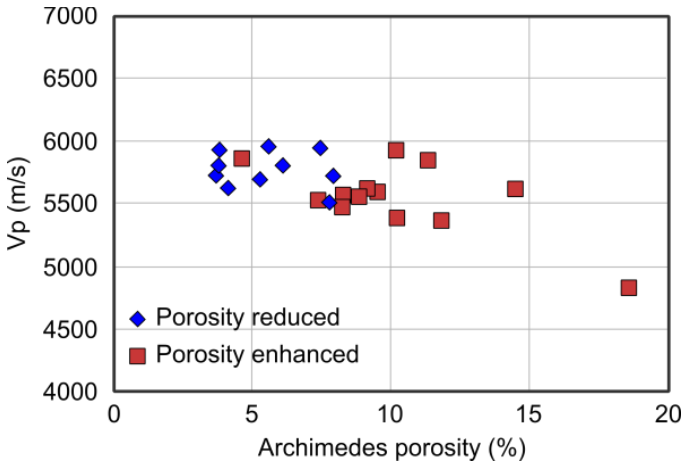

Fig. 7.8: Plot Vp vs. Archimedes porosity with assessment of the influence of diagenesis. Samples with porosity that was classified as reduced (with primary, compact, tight packing textures, besides cementation) possess higher Vp data and lower porosities, while samples with solution enhanced porosity possess lower Vp values and higher porosities.

Acoustic impedance (or seismic) of the medium in which body waves travel, is the product of the P-wave velocity and bulk density of the sample. The data possess values between 10 and 14.8 x 10^6 Ns/m^3. In plots of the latter variable versus Archimedes porosity, a strong inversed trend can be seen with a correlation coefficient of 0.83 (Fig. 7.9). The acoustic impedance is the product of the compressive-wave velocity (V_p) and bulk density. Although the spread in values does not relate to the mineralogy of the sample, it is mainly controlled by porosity and pore-type. What is of importance here is the fact that seismic reflectors in this type of pure carbonate will reflect the combined effect of porosity and pore-types of the geobody (Soete et al., 2015).

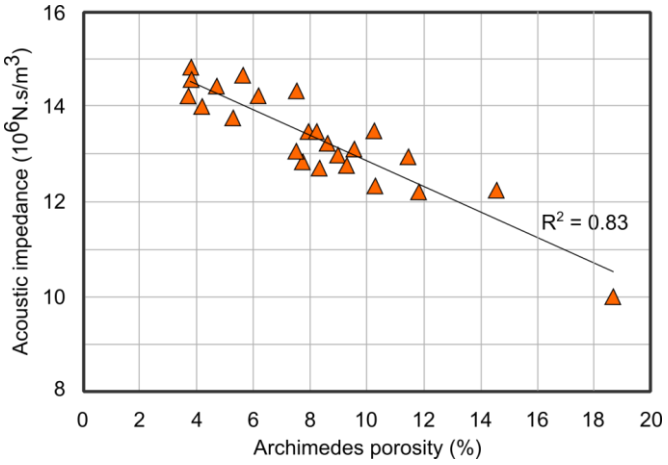

Fig. 7.9: Plot of acoustic impedance vs. Archimedes porosity showing a strong correlation. The data display a linear and inversed correlation.

7.4 Comparison between Tivoli travertines with Turkey and Hungary travertines

Soete et al. (2015) analyzed 60, 1.5 inch diameter plugs from travertines from quarries near Denizli (Turkey) and from Süttő and Budakalász (Hungary). XRD analyses confirmed that the samples are composed of well over 90 % of calcite, in contrast to Tivoli samples that are 100 % calcite. The analyzed samples from Turkey and Hungary comprise more lithofacies (i.e. sub-horizontal, cascade, waterfall, reed and marl) than the ones described from Tivoli samples (i.e. sub-horizontal lithofacies). In this way, there are some differences in the observed pore-types. The samples from Tivoli shrubs possess 5 different pore-types, while the samples from Turkey and Hungary were grouped into 7 dominant pore-types (Soete et al., 2015), namely: 1) **microporosity**, 2) **interpeloidal** porosity, 3) **interlaminar** porosity, 4) **mouldic** porosity, 5) **micro-mouldic** porosity, 6) **vuggy** porosity and 7) **framework** porosity. The **framework** porosity reported by Soete et al. (2015) corresponds to the intershrub and interdigit growth framework porosity from this study. However, this pore-type is reported in Soete et al. (2015) to be associated with dendritic crust lithotype. Besides, the dendritic texture on micro-scale, the crusts does not comprise a morpho-type for Tivoli. Moreover, the framework porosity is the most common and abundant pore-type described for Tivoli shrubs, and for this reason this porosity was not used to differentiate between the different pore-types. **Microporosity** was reported to occur between micritic particles and structures in the Turkish and Hungarian samples, while in Tivoli samples they are observed associated with intrashrub porosity. **Mouldic** porosity described from Tivoli possesses smaller sizes (between 10 to 100 µm) than the ones described from Turkey and Hungary (between 10 to 500 µm). It is very likely that they correspond to different plant types. **Vuggy** porosity was described in the three case study areas and possesses the same definition: non-fabric selective secondary solution-enlarged pores (Choquette and Pray, 1970; Lønøy, 2006). Moreover, **interlaminar** porosity is described by Soete et al. (2015) as pores that occur between dendritic crusts, while in the present study, this type of porosity characterizes pores between laminae of shrubs. Soete et al. (2015) also described **interpeloidal** porosity related to samples displaying a peloidal framework which are often associated with lamination on macroscale. Yet, this pore-type is not dominant in shrub morpho-type samples from Tivoli. Moreover, **encrusted bubble** porosity that was described as one of the main pore-types in Tivoli is not mentioned in the Turkish and Hungarian cases.

The samples from Turkey and Hungary are more porous (ranging between 2.8 and 34.7 %) (Soete et al., 2015) than the Tivoli samples (ranging between 3.7 to 18.62 %). Permeability results from the Turkish and Hungarian travertines are higher (between 0.05 and 18000 mD) (Soete et al., 2015) than the results from travertines from Tivoli (between 0.001 to 5254 mD).

Grain and bulk density range from 2.56 to 2.72 g/cm^3 and 1.77 to 2.57 g/cm^3, respectively, for

the Turkish and Hungarian samples (Soete et al., 2015), while for the Tivoli travertines, it ranges from 2.53 to 2.69 g/cm^3 (for grain density) and 2.07 to 2.51 g/cm^3 (for bulk density). The velocity range is higher for the Turkish and Hungarian samples than for the ones from Tivoli. Compressional-wave velocity (Vp) and shear-wave velocity (Vs) values vary between 3695 to 6097 m/s and 2037 to 3140 m/s, respectively, for the Turkish and Hungarian samples (Soete et al., 2015), while for the Tivoli samples the values vary between 4836 to 5958 m/s and 2675 to 3178 m/s, respectively. The plot Vp versus Vp/Vs ratio (Fig. 7.10) shows that the range in Vp/Vs ratio is very limited for both studies, varying, for the Turkish and Hungarian case, between 1.8 and 2.0 and, for Tivoli samples between 1.8 and 1.9.

When all the data from Denizli, Süttő, Budakalász and Tivoli are plotted in a graph with Vp and Vs versus Archimedes porosity, a similar trend for all locations can be seen (Fig. 7.11). The plot of acoustic impedance versus Archimedes porosity with all the 3 areas also shows correlation, with correlation value of 0.90 (Fig. 7.12).

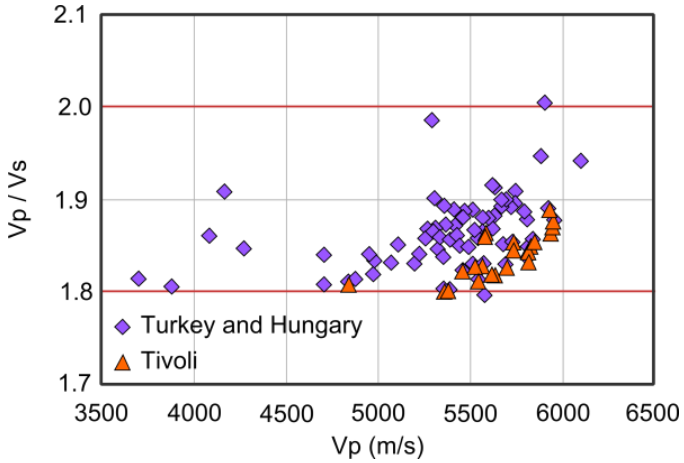

Fig. 7.10: Plot Vp vs. Vp/Vs ratio of samples from Turkey and Hungary and Tivoli. Notice that the Vp/Vs range is more restricted for the Tivoli samples and varies between 1.8 and 1.9, while for the Turkish and Hungarian samples, it ranges between 1.8 and 2.0.

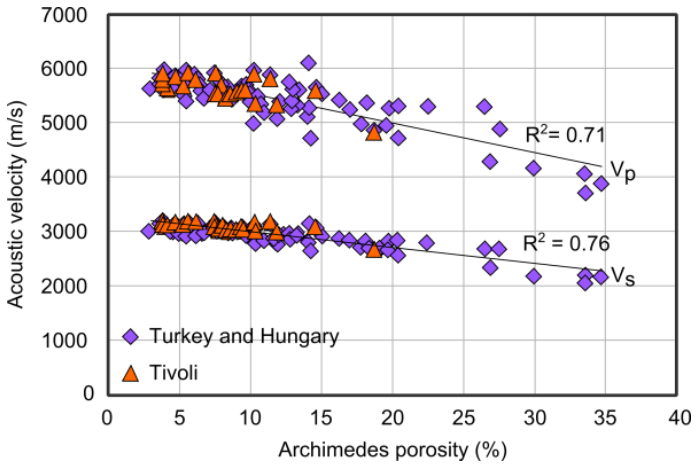

Fig. 7.11: Acoustic velocity vs. Archimedes porosity of Turkish, Hungarian and Tivoli samples. All the studied areas are plotting along the same Vp and Vs trends. The mentioned correlation coefficient is for the Turkish and Hungarian samples.

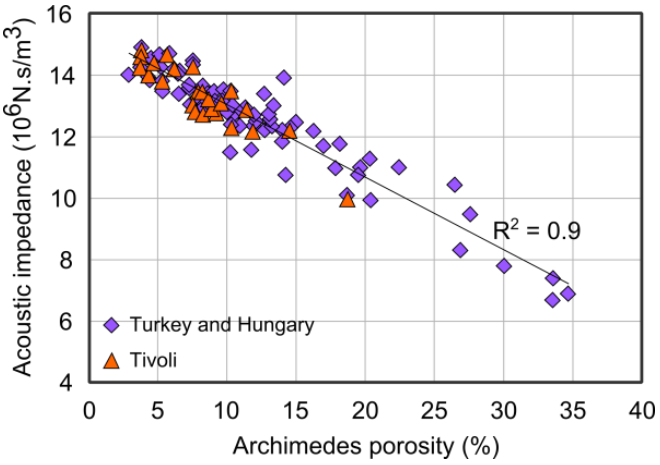

Fig 7.12: Plot of acoustic impedance vs. Archimedes porosity of Turkish, Hungarian and Tivoli samples. The samples are plotted along the same linear and an inverse correlation is present. The mentioned correlation coefficient (0.9) is for all the samples.

Soete et al. (2015) demonstrated by comparing results from Turkish and Hungarian travertine data and different marine carbonate results from literature that they possess very different acoustic velocity results (Fig. 7.13). An inverse exponential correlation illustrated the relationship between sample porosity and compressional-wave velocities. With increasing porosity, travertine Vp values become gradually higher than marine carbonates with similar porosity (Fig. 7.13) even with different mineralogy (dominantly calcite, but also dolomite and aragonite) (Soete et al., 2015). The data show that the P waves propagate faster in travertine then in classical marine reservoir rocks. The travertine trend line exhibits a generally less steep slope and is clearly deviating from reported marine trend lines, moving further into more stiff pores. The fabric, texture and pore-types of the travertine and marine carbonate furthermore control the velocity differences. This difference is attributed to the fact that travertines are precipitates that possess a rigid rock frame with large primary pores. After minor burial or even at the surface, the travertine rocks possess considerable high compressive and shear strength (Soete et al., 2015). On the other hand, marine carbonates mostly consist of transported sediment (e.g. bioclast fragments), with cementation, creating a rock frame with slower wave propagation when compared to travertine rocks (Soete et al., 2015). Furthermore pores can become modified by diagenesis, e.g. cementation. In contrast the studied shrubs are often covered by a calcite cement which is gluing all the shrub branches together. It therefore is likely that especially the P-waves are preferentially travelling along these pore lining fabric stabilizing cements, and thus they do "not see" the matrix (peloids) with their microporosity, neither are they influenced by the meso- and macroporosity since the waves can propagate around them.

Other differences that might influence wave velocities in marine carbonate are the uniformity of grain size distribution versus the varying of crystal sizes (micrite and sparite) (Eberli et al., 2003; Soete et al., 2015). The variations in crystal size in travertines give rise to changes in grain densities which affect the small scale velocity variations (Samsuri and Herianto, 2005; Wichtmann and Triantafyllidis, 2010; Soete et al., 2015).

Results from Tivoli travertines follow the same trend line as travertines from Turkey and Hungary (green line Fig. 7.13) because they possess a similar porosity-velocity relationship, as it was observed above (Figs. 7.11 and 7.12).

Despite the absence of Pre-Salt publications on this topic, it is very likely that the acoustic velocities for the Pre-Salt continental carbonate deposits also possess very similar results as the travertines from Turkey, Hungary and Italy, because of their similar texture and pore morphology. Besides, they also display the cement coverage, which also explains why these reservoir rocks have less been affected by physical and chemical compaction when compared to marine reservoir rocks that are encountered at similar depth. Possibly, they preserved their primary porosity in a similar way as the studied travertines, due to the rigidity of

the rock frame (Thompson et al., 2015; Soete et al., 2015). But as said to translate the documented acoustic behavior from our study to real cases in pre-salt settings is not straightforward, especially since the experimental set-up used in our study differs from the real case situation. However, this was not the aim of this study.

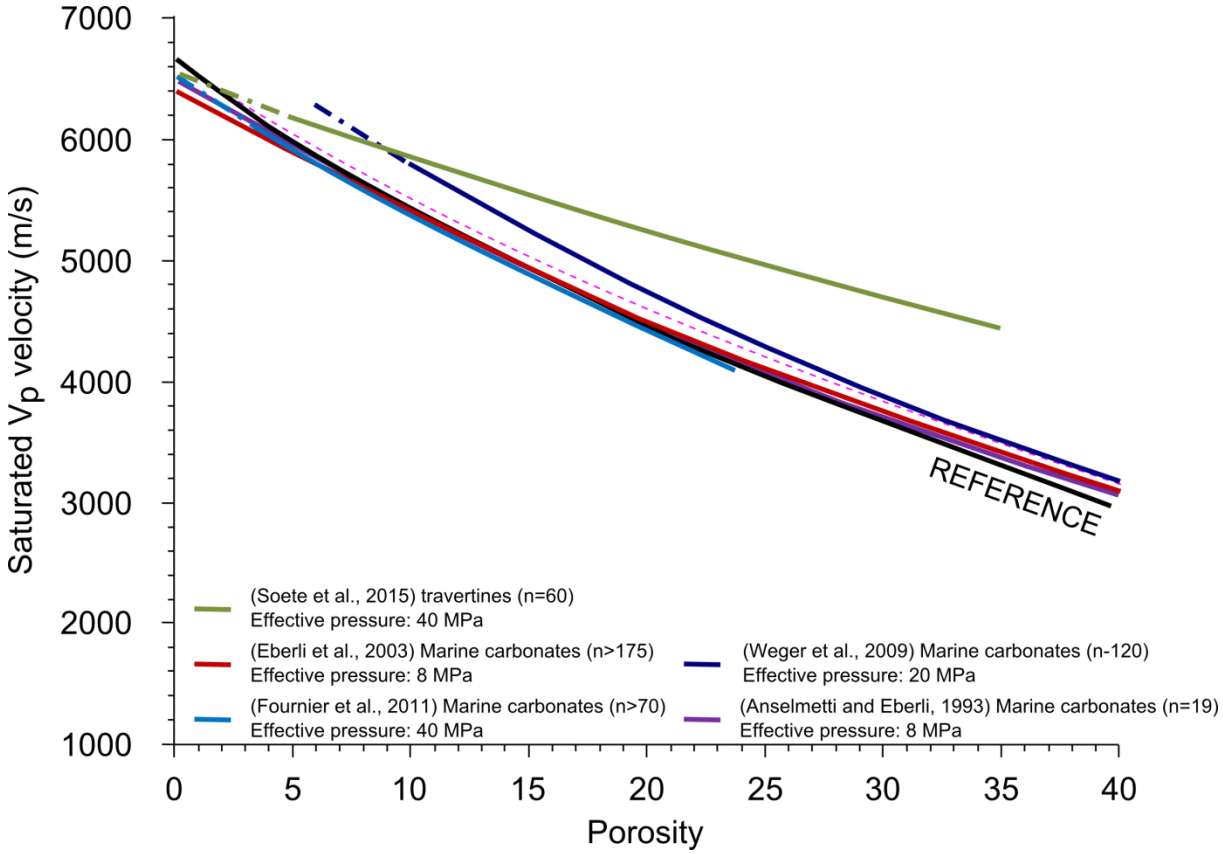

Fig. 7.13: Inverse porosity-acoustic velocity trend lines for marine (red, purple and blue lines) and travertines from Turkey and Hungary (green line), plotted in a model of Xu and Payne (2009) (extracted from Soete et al., 2015). The red (Anselmetti and Eberli, 1993) and purple (Eberli et al., 2003) trend lines correspond to limestones with micropores, vuggy, mouldic and framework porosity. The light blue (Fournier et al., 2011) trend line corresponds to limestones rich in micropores. The dark blue (Weger et al., 2009) trend line relates to vug-dominated limestone.

7.5 Conclusions

Travertine shrub morpho-type samples from quarries in Tivoli (Italy) display a relationship of morpho-types and pore-types with acoustic wave velocities and porosity. Intershrub growth framework is the main pore-type observed in all shrub morpho-type samples. For this reason, a different pore-type classification was used in this study. The pore-types were grouped in: 1) mouldic, 2) encrusted bubble, 3) vug, 4) interdigit, vug and, 5) interdigit, interlaminar, microvug. These groups result in distinct porosity-velocity clusters and the influence of pore-types on acoustic-wave velocity is very clear. What is more, samples with frame-forming pore-types as mouldic pores or encrusted bubbles show higher velocity values and lower porosities than samples with no frame-forming pores as vuggy pores, what results in lower velocity values and higher porosities. Besides, based on the analyzed samples, velocity decreases while porosity increases.

Furthemore, seismic lines for mono-mineralic carbonate deposits can possess seismic reflectors in function of porosity and pore-types, and not caused by non-carbonate intercalations.

Despite the fact that samples from Denizli (Turkey) and from Süttő and Budakalász (Hungary) comprise a bigger variety of travertine lithofacies (i.e. sub-horizontal, cascade, waterfall, reed and marl) than the samples analyzed from Tivoli (i.e. sub-

horizontal lithofacies), the acoustic-wave velocity results are remarkable similar. On the other hand, the comparison with marine carbonate shows that compressional-wave velocity follows a very different trajectory (Soete et al., 2015). The fabric, texture and pore-types of travertines and marine carbonates are decisive in the velocity differences. This difference is attributed to the fact that travertines are precipitates that possess a rigid rock frame with large primary pores, while marine carbonates rocks mostly consist of cemented transported sediment (e.g. bioclast or allochem fragments), which creates a rock frame with slower wave propagation.

Acoustic wave velocity analysis can serve as a tool bridging the information from outcrops to subsurface, providing insights and understanding about the parameters (e.g. fabric, texture, pore-types) that can influence the subsurface seismic reflector results. On plug scale a greater small scale heterogeneity is expected while on seismic scale the data are expected to display more subtle variations, given the scale of observation. This, however, does not invalidate the laboratory-scale observations (plug, core), which are useful for qualitative interpretations and for a better understanding the effect of e.g. facies and pore-types on seismic scale, especially if associated within "conceptual geological models".

Until recently, no data on the acoustic behavior of travertines were available. Furthermore a relevant question that yet was not addressed is whether shrub-morpho-types control the acoustic behavior, and whether this is different or similar to marine carbonates. Traditionally the first step to do in this type of research is to study the acoustic behavior of dry plugs at different confining pressure. This allowed to infer how acoustic properties behave in function of porosity, pore types, diagenetic overprinting, etc. However, these results cannot blindly be used to interpret seismic responses, since used frequencies and pore filling status are different, among other parameters. The translation of our results towards seismic interpretation therefore is out of the scope of this study.

CHAPTER 8 General conclusions

Travertine shrub structures from Tivoli were studied as a potential sedimentological and petrophysical analogue for the so-called Pre-Salt reservoirs (offshore Brazil and Angola) because of their textural and pore morphological similarities as well as spatial distribution. Dimensions of travertine deposits correspond to a small reservoir oil field size. The purpose of this study was to unravel the genesis and depositional setting of shrub morpho-types, as well as to address their relationship with pore network and poro-perm characteristics. The organization of each chapter reflects the workflow followed in the understanding and characterization of this potential travertine shrub reservoir analogue.

To unravel the shrub reservoir properties the different shrub textures were characterized. Paleoenvironments and processes responsible for their development were identified. The sedimentological characterization of the shrub textures were carried out at different scale (Chapter 2). The travertine shrubs from Tivoli are laterally very continuous (i.e. they can be followed over hundreds of square meters). It is possible to state that they comprise the largest present-day known outcrop area where these structures can be found. This makes the study of the Tivoli shrubs even more important as an analogue for the Pre-Salt deposits.

In Chapter 2, shrubs mapped in the quarries were analysed individually in 2D (petrography) and 3D (Micro-Computer Tomography analyses). This allowed to identify and characterize six main shrub morphologies i.e., narrow dendriform (NDS), wide dendriform (WDS), fili dendriform (FDS), arborescent (ARB), arbustiform (ABT) and pustular (PS). The dendriform shrub structures (i.e. NDS, WDS, and FDS) comprise the most abundant morphologies observed in the studied area. They can be distinguished basically according to the arrangement of their branches. The framework of the Tivoli shrubs largely consists of peloidal micritic aggregates which are covered by thin sparry calcite cement, with the shrubs ranging on average from 1 to 3 cm in height. They rarely show crystalline characteristics. Under SEM, the peloidal micritic aggregates are formed by micrometric rounded to sub-rounded spheres (< 1 μm-sized), interpreted as bacterial related bodies.

The characteristics of the different shrub morphologies indicate a close relationship of the hydrodynamic conditions and microbial influence in the development of these structures. Changes in the hydrodynamic conditions with episodes of stagnancy probably influenced the precipitation rate of the calcite, as well as controlled the abundance of microbes (i.e., bacteria), both affected the shrub morphologies making them very variegated. The shrubs are interpreted to have been developed in very shallow extensive waterlogged, slightly inclined flat areas, changing laterally into a slope system with crusts as the main lithotype. The hydrodynamic conditions associated with the shrub morphologies can be summarized as follow: 1) in fast flowing water more dense and tight packed shrub structures developed, and crusts are the most abundant lithotype; 2) fast to moderate flowing waters promoted NDS and WDS morphologies. NDS reflect faster flowing conditions compared to WDS, in line with the denser fabric of the former; 3) slow to stagnant waters allowed the development of FDS and ARB, ABT and PS morpho-types, with the last three likely being more influenced by evaporative processes based on their petrographic fabrics, associated rafts textures and calcite encrusted bubbles, and because of the lack of stratification, overall resembling low energy flowing-to-standing water conditions. The microbial influence is interpreted to increase from NDS, over WDS,

FDS, ARB, ABT to PS, according to the decrease in flow velocity.

The shrub morpho-types in the studied outcrops make up three sedimentary sequences that are limited by major exposure surfaces associated with immature palaeosol development. The palaeosols clearly indicate a lowering of the water table, however, whether they reflect more arid conditions or just some changes in vent location(s) or water discharge(s) in relation to tectonic activity is unclear. The sequences display from north to the south an aggradational to progradational stacking pattern. Shrubs are more abundant in the northern part of the studied quarry area where the deposits are more horizontally flat, passing gradually into crust lithotypes in a slope system located in the central part of the quarries area, and finally change into mats that predominate the southern area of the Tivoli quarries. Immature paleosols are better developed in the northern area of the studied quarries.

To better understand the origin of the precipitated fluids and the environmental conditions in which the shrubs precipitated, a geochemical study (e.g. Sr, C and O isotopes and elemental analysis) was carried out (Chapter 3). Major and minor/trace element analysis was useful to comprehend the genesis and processes that promote carbonate precipitation, depositional water temperatures, CO_2—origin and source rocks of the fluids. QEMSCAN analyses brought insights of the less than 1% mineralogies present in the sample, allowing the understanding how individual elements are related each other and supporting the interpretation of the detrital versus authigenic origin of these traces.

The geochemical signature of the shrubs was mainly related to the characteristics of the fluids. The C and O stable isotopes of the shrub morpho-types do not allow any geochemical distinction between them. Only crusts can be isotopically differentiated from the shrub morphologies, because they possess a heavier carbon and lighter oxygen signature, indicating the predominance of CO_2 degassing over other processes. The precipitation of the shrub morphologies and their geochemical signature support similar physico-chemical conditions being mainly influenced by degassing and evaporation processes. The latter interpretation is in agreement with the very flat waterlogged depositional setting proposed in Chapter 2. The very high C stable isotope signature encountered in these shrub structures is not only attributed to abiotic (CO_2 degassing and evaporation), but also photosynthetic processes which preferentially extracted $^{12}CO_2$ and enriched the water in $^{13}CO_2$.

The Sr isotopic signature normally reflects the signature of the parent rock precipitating fluids. $^{87}Sr/^{86}Sr$ ratios that cluster around 0.708, a ratio similar to that measured in several Mesozoic limestone formations of central Italy (Minissale, 2002, 2004). The basal Triassic anhydrite unit (Anidrite di ‘‘Burano’’ Fm) contains considerably more Sr than the Mesozoic limestone unit (Barbieri et al., 1979). Because anhydrite is soluble in water (at relatively low temperature), and because anhydrite is located at the base of the Mesozoic limestones, elevated Sr elemental concentrations in the studied travertines suggest that the source groundwaters were deeply circulating (Minissale, 2004). The $\delta^{13}C_{CO2}$ re-calculated values show that the main source of CO_2 in the Tivoli area is related to the thermo-metamorphic decarbonatation of the Mesozoic carbonate rocks. Water temperatures calculated from the $\delta^{18}O_{PDB}$ signatures of the shrubs, assuming disequilibrium fractionation, plot in a range of 17.3°C to 31.9°C (with average of 25.6°C).

After the characterization and understanding of the sedimentology and geochemistry of the shrubs from Tivoli, their pore network was studied. Porosity and permeability studies were evaluated in function of shrub morphologies, but, no clear relationships were observed (Chapter 4). However, the study of other shrub texture attributes such as size sorting, packing and size do show some relationship with the poro-perm results. The shrub size sorting which comprises the complexity of the shrub sizes within a sample, strongly influences permeability and reflect a minor contribution to porosity. Shrub packing is related to the ratio between shrub width and adjacent spacing. The latter is the main control on porosity, but also has a minor influence on permeability. Shrub size sorting influences permeability by enhancing or reducing the

tortuosity of the flow path, while packing influences porosity by modifying the space between the shrubs. So, textures with open packing and well sized sorted shrubs are associated with higher porosities and permeability in comparison with tight packed and poorly size sorted shrubs. Shrub sizes (i.e. small, medium and large) correspond to the longer vertical length of the shrubs, and they seem to have a relationship with porosity, however, results are strongly influenced by the shrub size sorting and packing. Here, the medium sized shrubs possess the highest porosity results, which more often correspond to open packing and well sized sorted shrubs, while large sized shrubs possess lower porosities corresponding more often to tight packed shrubs and poorly sized sorted shrubs.

Differences in pore-types and shape, and their connectivity help to explain differences in porosity and permeability results, allowing to characterize the pore network accurately in 3D, which will, consequently, influence the hydraulic quality units that are controlled by pore geometry as a function of rock textures (Chapter 4). Intershrub and interdigit growth framework porosities are the most abundant pore-types. But other pore-types were also observed associated with the latter, such as intrashrub growth framework, interlaminar, encrusted bubble, mouldic, vuggy, shelter, intercrystalline, intracrystalline porosities, besides microporosity. µCT analysis showed that shrub morphologies possess high pore network connectivity which can be differentiated based on their pore shape volume. The pore shape analysis was based in this study on the 3D pore classification developed by the PhD thesis of Steven Claes at KU Leuven (2015). This approach allowed to characterize the different pore shapes by using 3D micro computer tomography analysis. The study of pore shapes in the shrub morpho-types from Tivoli showed that higher porosities are observed in samples dominated by cube-like pore shapes that are mainly associated with vuggy pores, while lower porosities are related with plate- and cuboid-like shapes, which are linked with intergrowth and interdigit growth framework porosity. This means that decreasing porosities link to decreasing vuggy porosities and increasing amounts of intergrowth framework porosity. Besides, the shrub textures, i.e. size and packing also display a relationship between pore shapes and porosity. Cube shaped pores possess a relationship with medium sized shrubs and higher porosities, while blade and cuboid pore shapes present mainly large shrubs with tight packing texture and low porosities. Both blade- and cuboid-like pore shape volumes are also observed associated with well size sorted shrubs and permeability. Therefore, blade- and cuboid-like pore shapes mainly influence pore connectivity (permeability results) due their flattened and elongated shapes (respectively), which creates longer pathways, connecting permeable zones in the studied samples.

In order to understand the petrophysical characteristics studied in Chapter 4, and to have a better understanding of the pore network and connectivity among the different shrub morpho-types, pore size distributions were analyzed by using NMR and MIP measurements, which allowed to assess the different pore compartments (Chapter 5). This study allowed performing a rock-typing of the different shrub morpho-types recognized in the Tivoli travertines. The rock-typing study considers not only lithological aspects (composition, texture, structure), but also petrophysical aspects (porosity and permeability), which directly influence the fluid flow capacity. Here, distinct lithological aspects with similar porosity-permeability characteristics will be grouped in the same rock-type. The shrub samples were subdivided into 3 groups in accordance with their pore parameter characteristics: Group 1 is represented by unimodal NMR and MIP curves; Group 2 displays bimodal NMR curves and an unimodal response in MIP curves; Group 3 displays bimodal curves for both NMR and MIP, with well-developed peaks for both macro- and micro-porosities. The groups are not dominated by any specific shrub morpho-type. The different groups are related to the presence or absence of the secondary peak in NMR and/or MIP curves, which is associated with micropores that mainly occur in the nucleus of the shrubs and to a far lesser extent in the sparry calcite cement, where they are associated to local dissolution.

Group 1 and Group 2 can be explained by the negligible amount of micropores in the samples. Micropores occur mostly isolated by the cements that cover the shrub structures,

which limit the volume of micropores that is accessible for mercury during MIP measurements. Group 3 is attributed to decoupled pore compartments detectable for both MIP and NMR analysis. The sparry calcite cement that surrounds the shrub structures decouples the abundant micropore compartments from meso- and macropores and limit its connectivity (< 10mD). Micropores are in NMR still registered as an isolated compartment and are therefore expected to have a negative effect on pore connectivity. Therefore, Group 3 possesses the lowest permeability values, while Group 1 the highest.

Shrub textures (e.g. size sorting and packing) also influence pore parameters (e.g. pore body sizes and pore entrances). The shrub size sorting has a major control on pore entrances, and it has a minor effect on pore body sizes, while shrub packing mainly influences pore body sizes. The shrub sizes and morpho-types do not show a clear relationship neither with poro-perm results, nor with pore parameters (i.e. pore body size and pore entrances). A relationship between NMR and MIP groups with shrub size sorting was also observed. Group 3 is mainly related to poorly size-sorted shrubs and associated with lower permeabilities. Group 1 and Group 2 represent well size sorted shrubs and yield the highest permeabilities. Micropores appear as decoupled compartments and are as such not a strong contributor to the pore network connectivity. Permeability will therefore decrease with increasing micro- to macropore ratios.

The Reservoir Quality Index (RQI) and Flow Zone Indicator (FZI) of the samples, a methodology developed by Amaefule et al. (1983), was calculated with the aim to replicate the shrub morpho-types behavior as a reservoir (Chapter 5). The analysis allowed to identify heterogeneities observed in complex carbonate reservoirs. The shrub samples could be separated into 5 RQI and 5 FZI groups, with group A possessing the lowest RQI and FZI values, and group E the highest. Low permeabilities comprise the lowest RQI and FZI values, while high permeabilities possess the highest RQI and FZI. The RQI and FZI results also display a relationship with pore parameters. Samples with similar RQI and FZI possess similar pore throat characteristics, and consequently belong to the same hydraulic unit. Groups A, B and C possess bimodal MIP curves with a diminishing amount of micropores from group A to group C. While Groups D and E possess unimodal curves, only with meso- and macro-pore throats. The results evidenced that the amount of microporosity in the pore network affects negatively the reservoir quality. The sparry calcite cements that surround the shrubs had an important influence in the reservoir quality, since the latter shield micro-porosity, in the center of the shrub, from meso-/macro-porosity.

For the understanding of the fluid behavior within the shrub structures, flow modelling by applying the Lattice Boltzmann Method (LBM) based on μCT images was used (Chapter 6). The characterization of the spatial permeability distribution allowed to better understand the importance of small-scale heterogeneities within the different shrub morpho-types. The 3D datasets allowed to simulate the permeable nature of each shrub morpho-types and also to obtain the tortuosity of the samples, since the latter cannot be obtained from 2D observations. Porosity and permeability in function of shrub morpho-types studied in Chapter 4 did not show any clear relationship, however, in Chapter 6, μCT analysis and simulated permeability allowed to evaluate in detail the poro-perm characteristics of the shrub morpho-types that showed a relationship. The results from tortuosity also presented a relationship with shrub morpho-types. In sum, PS possesses the best reservoir characteristics (with lowest tortuosity and higher K_{sim} results), being followed (in decreasing order of reservoir performance) by NDS, WDS, ABT and FDS (with higher tortuosity and lower K_{sim} results). The higher tortuosity pathways are due the presence of branches. The geostatic results as well as the 3D streamline velocity distribution demonstrate how heterogeneous the shrub structures are at small-scale (0.5 cm^3). These results cannot be assessed by using standard laboratory data.

Nevertheless, in contrary to the poro-perm laboratory measurements, the μCT porosity and K_{sim} do not show a relationship either with shrub packing, size sorting or size. The reason may be due to the scale of the measurements. Possibly, in larger samples (plug size) the

texture heterogeneities will display a stronger control on poro-perm results, as it was observed in Chapters 4 and 5.

To do the upscaling and to visualize the spatial permeability distribution of the shrub structures, in situ air mini-permeameter measurements were performed (Chapter 6). The use of the Tiny-permeameter II allowed to observe the high anisotropy within laminae, with larger permeability continuity in the direction parallel to the laminae. Vertical as well as lateral permeability variation was respectively very high. Textural heterogeneities are responsible for the high permeability variation values within laminae.

The comparison between the measured permeability in the laboratory and by using the air mini-permeameter device was significant, with the first possessing higher permeabilities and reaching two or three orders of magnitude of difference. The application of RQI/FZI methodology allowed assessing the reservoir quality on large scale of the different shrub morpho-types. Besides the differences between the shrub structures due their complex textures (morphologies, size sorting, packing and size) and small-scale heterogeneities, all the morpho-types yielded good to excellent reservoir characteristics. Plug measurements have their permeability results strongly influenced by the heterogeneities encountered in the samples. The permeability simulation and mini-permeameter measurements allowed to reach different reservoir scales (upscaling), improving the characterization and knowledge about the shrub reservoirs.

In sum, the complexity of the shrub textures were accessed and highlighted in the present thesis at different scales. What it is important to mention and keep in mind here is that depending on which scale one is working, the influence of heterogeneities will increase or decrease. With the upscaling study, the different shrubs structures with their different textures such as: morpho-types, packing, size-sorting and size, proved that they possess similar reservoir behavior (on larger scale) and heterogeneities do not influence significantly the reservoir quality at lithotype level. This may be explained by the fact that facies heterogeneities occur localized.

For a future seismic forward modeling, analysis of the acoustic wave velocities showed a relationship with shrub morpho-type and their pore types (Chapter 7). The pore types were grouped in: 1) mouldic, 2) encrusted bubble, 3) vug, 4) interdigit, vug and, 5) interdigit, interlaminar, microvug. They displayed distinct porosity-velocity characteristics. Samples with frame-forming pore-types such as mouldic pores or encrusted bubbles showed higher velocity values and lower porosities, than samples with no frame-forming pores as vuggy pores, which resulted in lower velocity values and higher porosities. The acoustic-wave velocity results from Tivoli showed remarkable similarity with the results from Denizli (Turkey) and Süttő and Budakalász (Hungary) samples. In contrast, the comparison with marine carbonates pointed out (or indicate) that compressional-wave velocity follows a very different trajectory (Soete et al., 2015).

Understanding complex variation in pore network is the key to improve reservoir description and exploitation. The multi-method and multi-scale workflow applied in this study allowed a better characterization and understanding of the travertine shrub lithotype as a reservoir. This workflow is valuable to predict the pore network characteristics and distribution of the rock, first by understanding the depositional setting, and subsequently by characterizing the pore network. The use of 3D image analysis not only allowed a better understanding between texture (e.g. morphologies, size, size sorting and packing), pore-shapes and porosity but also provided quantitative tools. Besides, LBM simulations and mini-permeameter measurements both have the potential to substitute the expensive laboratory permeability measurements on large core samples.

This methodology can be applied both for Exploration and Reservoir Characterization. However, depending on what is the main purpose of the study, some tools are more important than others.

At an exploration scale the following workflow is suggested:

- Detailed fieldwork,
- Thin section petrographic descriptions,
- Stable isotopic analyses,

- QEMSCAN,
- Element analyses,
- Petrophysical characterization, including porosity and permeability study, NMR and MIP analyses,
- Acoustic property characterization for upscaling from plug-scale to seismic.

And for a reservoir scale characterization, which was the purpose of my thesis, it is suggested to add to the workflow previously described:

- the study of simulated permeability and air mini-permeameter measurements for flow modelling as well as
- the characterization of the Reservoir Quality Index (RQI) and Flow Zone Indicator (FZI).

Anyway, what is indispensible for any of these approaches are a good petrographic description/characterization and petrophysical measurements.

For future research I would propose:

- To apply the same methodology to more representative samples of each of the shrub morpho-types.
- To collect samples along more than one log, preferentially in the same wall with horizontal sampling along the same layer level and at decimeter scale. The following analyses should be performed on samples: elemental analysis, C and O stable isotope analysis, porosity and permeability measurements. This will bring a better correlation of the results, a more accurate understanding of the depositional setting and detailed reservoir characteristics will be provided.
- Sampling travertines from the most northern and southern Tivoli quarries, allowing to perform geochemical analysis (trace elements, C and O stable isotopes), that could result in a better understanding of the possible vent location(s).
- To reconstruct a 3D geobody architecture and to populate the model with geochemical data (this is in fact embedded in the PhD of Alessandro Mancini).
- To analyse biomarkers since the shrubs from Tivoli possess some indications of microbial influence in the carbonate precipitation.
- To scan by µCT smaller samples to reach higher resolution for a better characterization of the pore network by including the meso- and micropores.
- To apply the Lattice Boltzmann Method on a higher number of samples, for the different lithotypes, and use different scales. I would also suggest the use of different methods and software for permeability simulation to compare the results.
- To apply the Tiny-permeameter method in larger areas to improve the methodology and the understanding of the complex carbonate pore network.
- Finally, for a better and complete reservoir characterization, the same methodology should be applied not only on the shrub morpho-types, but also on the different other lithotypes.

REFERENCES

A

Acocella, V., Funiciello, R., 2002. Transverse structures and volcanic activity along the Tyrrhenian margin of central Italy. Bollettino della Società Geologica Italiana, V. Speciale, 1, 739-747.

Acocella, V., Funicello, R., 2006. Transverse systems along the extensional Tyrrhenian margin of central Italy and their influence on volcanism. Tectonics, 25, 2, 1-24. http://dx.doi.org/10.1029/2005TC001845 .

Adisoemarta, P.S., Anderson, G.A., Frailey, S.M., Asquith, G.B., 2000. Historical use of m and a in well log interpretation: is convemtional wisdom backwards. Society of Petroleum Engineers – SPE Permian Basin Oil and Gas Recovery Conference, 21-23 March, Midland, Texas. DOI: http://dx.doi.org/10.2118/59699-MS.

Al-Raoush, R., Papadopoulos, A., 2010. Representative elementary volume analysis of porous media using X-ray computed tomography. Powder technology, 200, 69-77.

Allan, J. R., Matthews, R.K., 1982. Isotope signatures associated with early meteoric diagenesis. Sedimentology, 29, 797-817.

Alfonsi, L., Funiciello, R., Mattei, M., Girotti, O., Maiorani, A., Preite Martinez, M., Trudu, C., Turi, B., 1991. Structural and geochemical features of the Sabina strike–slip fault (Central Apennines). Bollettino della Società Geologica Italiana, 110, 217-230.

Alonso-Zarza, A.M., Wright, V.M., 2010. Palustrine carbonates. In: Alonso-Zarza, A.M., Tanner, L.H. (Eds), Carbonates in Continental Settings: Facies, Environments and Processes. Developments in Sedimentology (Elsevier, Amsterdam), 61, 103-132.

Amabeoku, M. O., Funk, J. J., Al-Dossary, S. M., Al-Ali, H. A., 2001. Calibration of Permeability Derived from NMR Logs in Carbonate Reservoirs. Society of Petroleum Engineers. doi:10.2118/68085-MS.

Amaefule, J.O., Altunbay, M., Tiab, D., Kersey, D.G., Keelan, D.K., 1993. Enhanced Reservoir Description: Using core and log data to identify hydraulic (flow) units and predict permeability in uncored Intervals/Wells, 68th Annual Technical Conference and Exhibition of the Society of Petroleum Engineers held in Houston, TX Paper SPE26435.

Amieux, P., Bernier, P., Dalongeville, R., de Medwecki, V., 1989. Cathodoluminescence of carbonate-cemented Holocene beachrock from the Togo coastline (West Africa): An approach to early diagenesis. Sedimentary Geology, 65, 261-272.

Aminian, K., Thomas, B., Ameri, S., Bilgesu, H.I., 2002. A new approach for reservoir characterization. SPE Eastern Regional Meeting. Society of Petroleum Engineers.

Andres, M.S., Sumner, D.Y., Pamela Reid, R., Swart, P.K., 2006. Isotopic fingerprints of microbial respiration in aragonite from Bahamian stromatolites. Geology, 34, 973-976.

Anselmetti, F.S., Eberli, G.P., 1993. Controls on sonic velocity in carbonates. Experimental Techniques in Mineral and Rock Physics, 141, 287-323.

Ausbrooks, R., Hurley, N.F., May, A., Neese, D.G., 1999. Pore-Size distributions in vuggy carbonates from core images, NMR, and capillary pressure. Presented at the SPE Annual Technical Conference and Exhibition, Houston, October 3-6. SPE-56506-MS.

http://dx.doi.org/10.2118/56506-MS.

Ayan, C., Colley, N., Cowan, G., Ezekwe, E., Wannell, M., Goode, P., Halford, F., Joseph, J., Mongini, A., Obondoko, G., Pop, J., 1994. Measuring permeability anisotropy: The latest approach. Oilfield Review, 6, 4, 24-35.

B

Barchi, M., 2010. The Neogene-Quaternary evolution of the Northern Apennines: crustal structure, style of deformation and seismicity. In: Beltrando M., Peccerillo A., Mattei M., Conticelli S., Doglioni C. (Eds.), Journal of the Virtual Explorer, 36. http://dx.doi.org/10.3809/jvirtex.2009.00220.

Barbieri, M., Masi, U., Tolomeo, L., 1979. Origin and distribution of strontium in the travertines of Latium (Central Italy). Chemical Geology, 24, 181–188.

Bear, J., 1972. Dynamics of fluids in porous materials. Society of Petroleum Engineers.

Billi, A., Valle, A., Brilli, M., Faccenna, C., Funiciello, R., 2007. Fracture-controlled fluid circulation and dissolution weathering in sinkhole-prone carbonate rocks from central Italy. Journal of Structural Geology, 29, 3, 385-395.

Boquet, E., Boronat, A., Ramos-Cormenzana, A., 1973. Production of calcite (calcium carbonate) crystals by soil bacteria is a general phenomenon: Nature, 246, 527-528.

Brasier, A.T., 2011. Searching for travertines, calcretes and speleothems in deep time: Processes, appearances, predictions and the impact of plants. Earth-Science Reviews, 104, 213-239.

Brasier, A.T., Andrews, J.E., Kendall, A.C., 2011. Diagenesis or dire genesis? The origin of columnar spar in tufa stromatolites of Central Greece and the role of chironomid larvae. Sedimentology, 58, 1283-1302.

Brasier, A.T., Salminen, P.E., Melezhik, V.A., Fallick, A.E., 2013. Earth's earliest travertines. Chapter 7.9 terrestrial environments, In: Melezhik, et al. (Eds.), Reading the Archive of Earth's Oxygenation, Global Events and the Fennoscandian Arctic Russia – Drilling Early Earth Project, vol. 3, Springer Verlag, Berlin Heidelberg. http://dx.doi.org/10.1007/978-3-642-29670-3_9.

Brehm, U., Krumbein, W.E., Palinska, K.A., 2006. Biomicrospheres generate ooids in the laboratory. Geomicrobiology Journal, 23, 7, 545-550. http://www.tandfonline.com/loi/ugmb20.

Brehm, U., Palinska, K.A., Krumbein, W.E., 2004. Laboratory cultures of calcifying biomicrospheres generate ooids – A contribution to the origin of oolites. Carnets de Géologie / Notebooks on Geology – Letter 2004/03 (CG2003_L03), 1-6. http://paleopolis.rediris.es/cg/CG2004_L03/.

Brigaud, B., Vincent, B., Durlet, C., Deconinck, J.F., Jobard, E., Pickard, N., Yven, B., Landrein, P., 2014. Characterization and origin of permeability-porosity heterogeneity in shallow-marine carbonates: From core scale to 3D reservoir dimension (Middle Jurassic, Paris Basin, France). Marine and Petroleum Geology, 57, 631-651.

Brock, G., Pihur, V., Datta, S., Datta, S., 2008. Cl Valid: an R package for cluster validation. Journal of statistical software, 25 ($). http://www.jstatsoft.org/v25/i04

Brogi, A., Liotta, D., 2008. Highly extended terrains, lateral segmentation of the substratum, and basin development: The Middle-Late Miocene Radicondoli Basin (inner northern Apennines, Italy). Tectonics, 27, TC5002, 1-20.

Brogi, A., Liotta, D.K., Ruggieri, G., Capezzuoli, E., Meccheri, M., Dini, A., 2016. An overview on the characteristics of geothermal carbonate reservoirs in southern Tuscany. Italian Journal of Geosciences, 135, 1, 17-29.

Brown, G. O., Hsieh, H. T., Lucero, D. A., 2000. Evaluation of laboratory dolomite core sample size using representative elementary volume concepts. Water resources research, 36, 1199-1207.

Brownstein, K.R., Tarr, C.E., 1979. Importance of classical diffusion in NMR studies of water in biological cells. Physical Review A, 19, 6, 2446-2453. https://doi.org/10.1103/PhysRevA.19.2446

Brunet, C., Monie, P., Jolivet, L., Cadet, J.P., 2000. Migration of compression and extension in the Tyrrhenian Sea, insights from $^{40}Ar/^{39}Ar$ ages on micas along a transect from Corsica to Tuscany. Tectonophysics, 321, 127-155.

Buczynski, C., Chafetz, H.S., 1991. Habit of bacterially induced precipitates of calcium carbonate and the influence of medium viscosity on mineralogy: Journal of Sedimentary Research, 61, 226-233.

C

Cantrell, D.L., Hagerty, R.M., 1999. Microporosity in Arab Formation Carbonates, Saudi Arabia. GeoArabia, 4, 2, 129-154.

Capelli, G., Mazza, R., Taviani, S., 2005. Studi idrologici per la definizioni degli strumenti operativi del piano stralcio per l'uso compatibile delle risorse idriche sotterranee nell'ambito dei sistemi acquiferi prospicienti i territori vulcanici laziali. Relazione inedita, Università degli Studi di Roma III, dipartimento di Scienze Geologiche, Laboratorio di Idrogeologia.

Capezzuoli, E., Gandin, A., Dandrelli, F., 2008. Evidence of associated deposition of travertine and calcareous tufa in the Quaternary carbonates of Valdelsa Basin (Tuscany). II Quaternario. Italian Journal of Quaternary Sciences 21, 113–124.

Capezzuoli, E., Gandin, A., Pedley, M., 2014. Decoding tufa and travertine (fresh water carbonates) in the sedimentary record: The state of the art. Sedimentology, 61, 1-21.

Carman, P.C., 1937. Fluid flow through granular beds. Transactions – Institution of Chemical Engineers, 5, 150-166.

Carminatti, M., Wolff, B., Gamboa, L., 2008. New exploratory frontiers in Brazil, in 19th World Petroleum Congress: World Petroleum Council.

Carminatti, M., Dias, J.L., Wolff, B., 2009. From turbidites to carbonates: breaking paradigms in deep waters: Offshore Technology Conference, 4-7.

Carucci, V., Petitta, M., Aravena, R., 2012. Interaction between shallow and deep aquifers in the Tivoli Plain (Central Italy) enhanced by groundwater extraction: A multi-isotope approach and geochemical modeling. Applied Geochemistry, 27, 266-280.

Chafetz, H.S., 1986. Marine peloids: a product of bacterially induced precipitation of calcite. Journal of Sedimentary Petrology, 56, 6, 812-817.

Chafetz, H.S., 2013. Porosity in bacterially induced carbonates: focus on micropores. American Association of Petroleum Geologists Bulletin 97, 2103-2111.

Chafetz, H.S., Folk, R.L., 1984. Continental carbonates: depositional, morphology and the bacterially constructed constituents. J. Sediment. Petrol., 54, 289-316.

Chafetz, H.S., Guidry, S.A., 1999. Bacterial shrubs, crystal shrubs, and ray-crystal shrubs: Bacterial vs. abiotic precipitation. Sediment. Geol., 126, 57-74.

Chafetz, H.S., Lawrence, J.R., 1994, Stable isotope variability within modern travertine:Géographie Physique et Quaternaire, 48, 257–273.

Chafetz, H.S., Meredith, J.C., 1983. Recent travertine pisolites (pisoids) from southeastern Idaho, U.S.A. In: Coated Grains (Ed. T.M. Peryt), 450-455. Springer-Verlag, New York.

Chafetz, H.S., Rush, P.F., Utech, N.M., 1991a.

Microenvironmental controls on mineralogy and habit of $CaCO_3$ precipitates: an example from an active travertine system. Sedimentology, 38, 107-126.

Chafetz, H.S., Utech, N.M., Fitzmaurice, S.P., 1991b. Differences in the $\delta^{18}O$ and $\delta^{13}C$ signatures of seasonal laminae comprising travertine stromatolites: Journal Sedimentary Petrology, 61, 1015-1028.

Chafetz, H.S., Akdim, B., Julia, R., Reid, A., 1998. Mn- and Fe-rich black travertine shrubs: bacterially (and nanobacterially) induced precipitates. Journal of Sedimentary Research, 68, 3, 404-414.

Chen, S., Georgi, D.T., 1997. Improving the accuracy of NMR relaxation distribution analysis in clay-rich reservoirs and core samples. SCA 9702, International Symposium Proceedings: Society of Professional Well Log Analysts, Society of Core Analysts Chapter-at-large, 10p.

Chiodini, G., Cardellini, C., Amato, A., Boschi, E., Caliro, S., Frondini, F., Ventura, G., 2004. Carbon dioxide Earth degassing and seismogenesis in central and southern Italy. Geophys. Res. Lett., 31, 1-4.

Choquette, P., Pray, L., 1970. Geologic nomenclature and classification of porosity in sedimentary carbonates. AAPG Bull., 2, 207-250.

Claes, H., 2015. Sediment-petrological and geochemical characterization of travertine. Thesis presented in pursuit of the degree of Doctor in Sciences, Department Geography-Geology, Faculty of Sciences, KULeuven, Belgium, 2015.

Claes, H., Degros, M., Soete, J., Claes, S., Kele, S., Mindszenty, A., Török, Á., El Desouky, H., Vanhaecke, F., Swennen, R., 2016a. Geobody architeture, genesis and petrophysical characteristics of the Budakalász travertines, Buda Hills (Hungary). Quaternary International, http://dx.doi.org/10.1016/j.quaint.2016.09.007.

Claes, H., Erthal, M.M., Soete, J., Özkul, M., Swennen, R., 2017. Shrub and pore type classification Petrography of travertine shrubs from the Ballık-Belevi area (Denizli, SW Turkey). Quaternary Geology, 437, 147-163. http://dx.doi.org/10.1016/j.quaint.2016.11.002.

Claes, H., Soete, J., Van Noten, K., El Desouky, H., Erthal, M. M., Vanhaecke, F., Özkul, M., Swennen, R., 2015. Sedimentology, three-dimensional geobody reconstruction and carbon dioxide origin of Pleistocene continental carbonate deposits in the Ballık area (south-west Turkey). Sedimentology, 62, 1408-1445.

Claes, S., 2015. Pore classification system and upscaling strategy in travertine reservoir rocks. Thesis presented in pursuit of the degree of Doctor in Sciences, Department Geography-Geology, Faculty of Sciences, KULeuven, Belgium, 2015-2016.

Claes, S., Soete, J., Cnudde, V., Swennen, R., 2016b. A three-dimensional classification for mathematical pore shape description in complex carbonate reservoir rocks. International Association for Mathematical Geosciences, 48, 619p. http://dx.doi.org/10.1007/s11004-016-9636-z.

Coates, G.R., Xiao, L., Prammer, M. G., 2001. NMR Logging: Principles and Applications. Houston: Halliburton Energy Services. Gulf Professional Publishing.

Coenen, J., Tchouparova, E., Jing, X., 2004. Measurement parameters and resolution aspects of micro X-ray tomography for advanced core analysis. In proceedings of International Symposium of the Society of Core Analysts.

Craig, H., 1963. The isotopic geochemistry of water and carbon geothermal areas. Nuclear Geology Areas, 17-53.

Cressie, N. 1992. Statistics for spatial data. Terra Nova, 4, 613-617.

Croci, A., Della Porta, G., Capezzuoli, E.,

2016. Depositional architecture of a mixed travertine-terrigenous system in a fault-controlled continental extensional basin (Messinian, Southern Tuscany, Central Italy). Sedimentary Geology, 332, 13–39.

D

Data, S., Datta, S., 2003. Comparisons and validation of statistical clustering techniques for microarray gene expression data. Bioinformatics, 19, 459-466.

De Boever, E., Fouber, A., Lopez, B., Swennen, R., Jaworowski, C., Özkul, M., Virgone, A., 2016. Comparative study of the Pleistocene Cakmak quarry (Denizli Basin, Turkey) and modern Mammoth Hot Springs deposits (Yellowstone National Park, USA), Quaternary international, http://dx.doi.org/10.1016/j.quaint.2016.09.011.

De Filippis, L., Faccenna, C., Billi, A., Anzalone, E., Brilli, M., Soligo, M., Tuccimei, P., 2013. Plateau versus fissure ridge continental carbonates from Quaternary geothermal springs of Italy and Turkey: Interactions and feedbacks between fluid discharge, paleoclimate, and tectonics. Earth-Science Rev., 123, 35-52.

Della Porta, G., 2015. Carbonate build-ups in lacustrine, hydrothermal and fluvial settings: comparing depositional geometry, fabric types and geochemical signature. Microbial Carbonates in Space and Time: Implications for Global Exploration and Production. Geological Society, London, Special Publications 418. http://dx.doi.org/10.1144/SP418.4.

De Rita, D., Faccenna, C., Funiciello, R., Rosa, C., 1995. Structural and geological evolution of the Colli Albani volcanic district. In: Trigila, R. (Ed.), The Volcano of the Alban Hills. Tipografia SGS, Rome, 33-71.

De Rita, D., Funiciello, R., Parotto, M., 1988. Geological map of the Colli Albani volcanic complex, 1:50,000 scale. SELCA, Florence.

Dias, J.L., 1998. Analise sedimentológica e estratigráfica do Andar Aptiano em parte da margem leste do Brasil e no platô das Malvinas - consideraçoes sobre as primeiras incursões e ingressões marinhas do Oceano Atlântico sul Meridional: Universidade federal do Rio Grande Do Sul, 399p.

Dias, J.L., 2004. A New Gas Province in South Atlantic Region: Recent Gas Discoveries in Santos Basin, Offshore Brazil: 2004 AAPG International Conference: October 24-27; Cancun, Mexico, 20031p.

Dias, J.L., 2005. Tectônica, estratigrafia e sedimentação no Andar Aptiano da margem leste brasileira. Boletim de Geociências da Petrobras, 13, 7-25.

Dini, A., Mazzarini, F., Musumeci, G., Rocchi, S., 2008. Multiple hydro-fracturing by boron-rich fluids in the Late Miocene contact aureole of eastern Elba Island (Tuscany, Italy). Terra Nova, 20, 318-326.

Dupraz, C., Reid, R.P., Braissant, O., Decho, A.W., Norman, R.S., Visscher, P.T., 2009. Processes of carbonate precipitation in modern microbial mats. Earth-Science Rev., 96, 141-162.

Dupraz, C., Visscher, P.T., Baumgartner, L.K., Reid, R.P., 2004. Microbe-mineral interactions: Early carbonate precipitation in a hypersaline lake (Eleuthera Island, Bahamas). Sedimentology, 51, 745-765.

E

Ebanks, W.J., 1982. Integrated approach to reservoir description for engineering projects. (abstract only) AAPG Abstract Flow Unit Concept.

Eberli, G.P., Anselmetti, F.S., Incze, M.L., 2003. Factors controlling elastic properties in carbonate sediments and rocks. The Leading Edge, 654-660.

Ehrlich, H.L., 1996. How microbes influence mineral growth and dissolution: Chemical Geology, 132, 5-9.

El Desouky, H., Soete, J., Claes, H., Özkul, M., Vanhaecke, F., Swennen, R., 2015. Novel applications of fluid inclusions and isotope geochemistry in unravelling the genesis of fossil travertine systems. Sedimentology, 62, 27-56.

Enos, P., Sawatsky, L.H., 1981. Pore networks in Holocene carbonate sediments. Journal of Sedimentary Research, 51, 961-985.

Erthal, M.M., Capezzuoli, E., Mancini, A., Claes, H., Soete, J., Swennen, R., 2017. Shrub morpho-types as indicator for the water flow energy-Tivoli travertine case (Central Italy). Sedimentary Geology, 347, 79-99.

F

Faccenna, C., Funiciello, R., Bruni, A., Mattei, M., Sagnotti, L., 1994a. Evolution of a transfer-related basin: the Ardea basin (Latium, Central Italy), Basin Research, 6, 1, 35-46.

Faccenna, C., Funiciello, R., Mattei, M., 1994b. Late Pleistocene N-S shear zones along the Latium Tyrrhenian margin: structural characters and volcanological implications. Bollettino di Geofisica Teorica ed Applicata, 36, 141-44, 507-522.

Faccenna, C., Soligo, M., Billi, A., De Filippis, L., Funiciello, R., Rossetti, C., Tuccimei, P., 2008. Late Pleistocene depositional cycles of the Lapis Tiburtinus continental carbonate (Tivoli, Central Italy): Possible influence of climate and fault activity. Global and Planetary Change, 63, 4, 299-308.

Fairchild, I.J., Treble, P.C., 2009. Trace elements in speleothems as recorders of environmental change. Quat. Sci. Rev. 28, 449–468.

Faÿ-Gomord, O., Soete, J., Katika, K., Galaup, S., Caline, B., Descamps, F., Lasseur, E., Fabricius, I.L., Saïag, J., Swennen, R., Vandycke, S., 2016. New insight into the microtexture of chalks from NMR analysis. Marine and Petroleum, 75, 252-271.

Flannery, B. P., Deckman, H. W., Roberge, W. G., d'Amico, K. L., 1987. Three-dimensional X-ray microtomography. Science, 237, 1439-1444.

Fleury, M., 2007. NMR surface relaxivity determination using NMR apparent diffusion curves and BET measurements. International Symposium of the Society of Core Analysts Held in Calgary, Canada, September 10-12, 1-12.

Folk, R.L., 1994. Interaction between bacteria, nannobacteria, and mineral precipitation in hot springs of Central Italy. Géographie physique et Quaternarie, 48, 233-246.

Folk, R.L., Chafetz, H.S., 1983. Pisoliths (pisoids) in Quaternary travertines of Tivoli, Italy. In: Coated grains. Springer Berlin Heidelberg, 474-487.

Folk, R.L., Chafetz, H.S., Tiezzi, P.A., 1985. Bizarre forms of depositional and diagenetic calcite in hot-spring travertines, central Italy: The Society of Economic Paleontologists and Mineralogists, 36, 349-369.

Ford, T.D., Pedley, H.M., 1996. A review of tufa and travertine deposits of the world. Earth-Science Reviews, 41, 117-175.

Fouke, B.W., 2011. Hot-spring systems geobiology: abiotic and biotic influences on travertine formation at Mammoth Hot Springs, Yellowstone National Park, USA. Sedimentology, 58, 170-219.

Fouke, B.W., 2001. Depositional facies and aqueous-solid geochemistry of travertine-depositing hot springs (Angel Terrace, Mammoth Hot Springs, Yellowstone National Park, U.S.A.) – Reply. J. Sediment. Res., 71, 497-500.

Fouke, B.W., Bonheyo, G.T., Sanzenbacher, B., Frias-Lopez, J., 2003. Partitioning of bacterial communities between travertine depositional facies at mammoth hot springs, Yellowstone National Park,

U.S.A. Can. J. Earth Sci., 40, 1531-1548.

Fouke, B.W., Farmer, J.D., Des Marais, D.D., Pratt, L., Sturchio, N.C., Burns, P.C., Discipulo, M.K., 2000. Depositional facies and aqueous-solid geochemistry of travertine-depositing hot springs (Angel Terrace, Mammoth Hot Springs, Yellowstone National Park, U.S.A.). Journal of Sedimentary Research, 70, 3, 565-585.

Fournier, F., Borgomano, J., 2007. Geological significance of seismic reflections and imaging of the reservoir architecture in the Malampaya gas field (Philippines). AAPG Bull.

Fournier, F., Leonide, P., Biscarrat, K., 2011. Elastic properties of microporous cemented grainstones. Geophysics 76, 6, 211-226.

Frank, S., Narayanan, R., Hansen, P.M., Allen, D., Albrechtsee, T., Steinhardt, H., Raven, M., Fordham, E., Bize, E., Rose, D., 2005. Carbonate rock typing using NMR data: a case study from Al Shaheen field, offshore Qatar. In: International Petroleum Technology Conference, Doha.

Friedman, I., 1970. Some investigations of the deposition of travertine from Hot Springs – I. The isotopic chemistry of a travertine-depositing spring. Geochimica et Cosmochimica Acta, 34, 1303-1315.

Fritz, P., 1965. Composizione isotopica dell'ossigeno e del carbonio nei travertine della Toscana. Bol. Geof. Teor. Applic., 7, 25p.

Funiciello, R., Giordano, G., De Rita, D., 2003. The Albano maar lake (Colli Albani Volcano, Italy): recent volcanic activity and evidence of pre-Roman Age catastrophic lahar events. Journal of Volcanology and Geothermal Research, 123, 43-61.

Funiciello, R., Locardi, E., Lombardi, G., Parotto, M., 1976. The sedimentary ejecta from pheatomagmatic activity and their use for location of potential geothermal areas. In: Proceedings Geothermal Energy, International Congress on Thermal Waters, Geothermal Energy and Vulcanism of the Mediterranean Area, Athens, 227-240.

G

Gandin, A., Capezzuoli, E., 2008. Travertine versus calcareous tufa: distinctive petrologic features and related stable isotopes signature. II Quaternario Italian Journal of Quaternary Sciences, 21, 1B, 125-136.

Gandin, A., Capezzuoli, E., 2014. Travertine: Distinctive depositional fabrics of carbonates from thermal spring systems. Sedimentology, 61, 264-290.

Gasparini, C., Di Maro, R., Pagliuca, N., Pirro, M., Marchetti, A., 2002. Recent seismicity of the "Acque Albule" travertine basin. Annals of Geophysics, 45, 537-550.

Gerundo, M., Schwartz, G.L., 1949. The role of denitrifying bacteria in the genesis of formations found in the Carlsbad Caverns: Texas Journal of Science, 1, 58-61.

Giesche, H., 2006. Mercury Porosimetry: A General (Practical) Overview. Particle & Particle Systems Characterization, 23, 1, 9-19.

Giraud, R., Goni. J., Rémond, G., 1968. Possibilités de la microanalyse par sonde électronique dans la détection des éléments en traces, applications de la cathodoluminescence à l'étude de la localisation des élements en traces dans les minéraux. In: Dosage des éléments à l'état de traces dans les roches et autres substances minérales naturelles. Colloq. Cent. Nat. Rech. Sci., 923, 413-432.

Goggin, D.J., Chandles, M.A., Kocurec, G., Lake, L.W., 1988a. Patterns of permeability in eolian deposits: Page Sandstone (Jurassic), NE Arizona. SPE Formation Evaluation, 3, 297-306.

Goggin, D.J., Thrasher, R.L., Lake, L.W., 1988b. A theoretical and experimental analysis of minipermeameter response

including gas slippage and high velocity flow effects. In Situ;(United States), 12.

Gommes, C.J., Bons, A., Blacher, S., Dunsmuir, J.H., Tsou, H., 2009. Practical methods for measuring the tortuosity of porous materials from binary or gray-tone tomographic reconstructions. American Institute of Chemical Engineering, 55, 8, 2000-2012.

Gonfiantini, R., Panichi, C., Tongiorgi, E., 1968. Isotopic disequilibrium in travertine deposition. Earth and Planetary Science Letters, 5, 55-58.

Guo, L., Riding, R., 1992. Aragonite laminae in hot water continental carbonate crusts, Rapolano Terme, Italy. Sedimentology, 39, 1067-1079.

Guo, L., Riding, R., 1994. Origin and diagenesis of Quternary continental carbonate shrub fabrics, Rapolano Terme, central Italy. Sedimentology 41, 499–520. doi:10.1111/j.1365-3091.1994.tb02008.x.

Guo, L., Andrews, J., Riding, R., Dennis, P., Dresser, Q., 1996. Possible microbial effects on stable carbonisotopes in hot-spring travertines. Journal of Sedimentary Research, 66, 468-473.

Guo, L., Riding, R., 1998. Hot-spring continental carbonate facies and sequences, Late Pleistocene, Rapolano Terme, Italy. Sedimentology, 45, 163-180.

Guo, L., Riding, R., 1999. Rapid facies changes in Holocene fissure ridge hot spring travertines, Rapolano Terme, Italy. Sedimentology 46, 1145–1158.

H

Hearn, E.L., Ebanks, W.J., Tye, R.S., Ranganathan, V., 1984. Geological factors influencing reservoir performance of the Hartzog Draw Field, Wyoming. JPT, 36, 9, 1335-1344.

Huysmans, M., Peeters, L., Moermans, G., Dassargues, A., 2008. Relating small-scale sedimentary structures and permeability in a cross-bedded aquifer. Journal of Hydrology, 361, 41-51.

I

Isaaks, E. H., Srivastava, R. M., 1989. An introduction to applied geostatistics.

J

Jahnert, R.J., Collins, L.B., 2013. Controls on microbial activity and tidal flat evolution in Shark Bay, Western Australia. Sedimentology, 60, 1071-1099.

Janssen, A., Swennen, R., Podoor, N., Keppens, E., 1999. Biological and diagenetic influence in recent and fossil tufa from Belgium. Sedimentary Geology, 126, 74-95.

Jensen, J.L., Glasbey, C.A., Corbett, P.W.M., 1994. On the Interaction of geology, measurements, and statistical-analysis of small-scale permeability measurements. Terra Nova, 6, 4, 397-403.

Jin, G., Patzek, T. W., Silin, D. B., 2004. Direct prediction of the absolute permeability of unconsolidated and consolidated reservoir rock. In SPE Annual Technical Conference and Exhibition. Society of Petroleum Engineers.

Jolivet, L., Faccenna, C., Goffé, B., Mattei, M., Rossetti, F., Brunet, C., Storti, F., Funiciello, R., Cadet, J. P., D'Agostino, N., Parra, T., 1998. Midcrustal shear zones in postorogenic extension: example from the northern Tyrrhenian Sea. Journal of Geophysical Research: Solid Earth, 103, 12, B6, 12123-12160.

Jones, B., Kahle, C.F., 1986. Dendritic calcite crystals formed by calcification of algal filaments in vadose environment. Journal of Sedimentary Petrology, 56, 217-227.

Jones, B., Kahle, C.F., 1993. Morphology, Relation, and Origin of Fiber and Dendrite Calcite Crystals. Journal of

Sedimentary Research, 63, 1018-1031.

Jones, B., Renaut, R.W., 1995. Noncrystallographic Calcite Dendrites from Hot-Spring Deposits at Lake Bogoria, Kenya. Journal of Sedimentary Research, 65A, 154-169. doi:10.1306/D4268059-2B26-11D7-8648000102C1865D

Jones, B., Renaut, R.W., 1996. Skeletal crystals of calcite and trona from hotspring deposits in Kenya and New Zealand. Journal of Sedimentary Research, 66, 265-274.

Jones, B., Renaut, R.W. , 1998. Origin of platy calcite crystals in hot-spring deposits of the Kenya Rift Valley. Journal of Sedimentary Research, 69, 913-926.

Jones, B., Renaut, R.W., 2008. Cyclic development of large, complex, calcite dendrite crystals in the Clinton continental carbonate, Interior British Columbia, Canada. Sedimentary Geology, 203, 17-35.

Jones, B., Renaut, R.W., 2010. Calcareous spring deposits in continental settings. In: Carbonates in Continental Settings. Eds A.M. Alonso-Zarza and L.H. Tanner. Developments in Sedimentology, 61, 177–224.

Jones, B., Renaut, R.W., Owen, R.B., Torfasons, H., 2005. Growth patterns and implications of complex dendrites in calcite continental carbonates from Lysuholl, Snaefellsnes, Iceland. Sedimentology, 52, 1277-1301.

Jones, B., Renaut, R.W., Rosen, M.R., 2000. Trigonal dendritic calcite crystals forming from hot spring waters at Waikite, North Island, New Zealand. Journal of Sedimentary Research, 70, 586-603. doi:10.1306/2DC4092A-0E47-11D7-8643000102C1865D.

K

Kahle, F., 1977. Origin of subaerial Holocene calcareous crusts: role of algae, fungi and sparmicritization. Sedimentology, 24, 413-435.

Knackstedt, M. A., Arns, C. H., Limaye, A., Sakellariou, A., Senden, T. J., Sheppard, A. P., Bunn, G. F., 2004. Digital Core Laboratory: Properties of reservoir core derived from 3D images. In SPE Asia Pacific Conference on Integrated Modelling for Asset Management. Society of Petroleum Engineers.

Kang, Q., Lichtner, P. C., Zhang, D., 2006. Lattice Boltzmann pore-scale model for multicomponent reactive transport in porous media. Journal of Geophysical Research: Solid Earth, 111.

Kano, A., Takashima, C., Ohtsuka, S., 2006. Hot-springs in eastern Kyushu and their related sedimentation and microbial processes. In: Ito, M., Yagishita, K., Matsuda, H. (Eds.), 17th International Sedimentological Congress, 2006, Fukuoka. Field Excursion Guide book FE-A10. The Sedimentological Society of Japan, 10p.

Kearey, P., Brooks, M., Hill, I., 2002. An Introduction to Geophysical Exploration. Blackwell Publishing.

Keith, H.D., Padden, F.J., 1964. Spherulitic crystallization from the melt, I: Fractionation and impurity segregation and their influence on crystalline morphology: Journal of Applied Physics, 35, 1270-1285.

Kele, S., Breitenbach, S.F.M., Capezzuoli, E., Meckler, A.N., Ziegler, M., Millan, I.M., Kluge, T., Deák, J., Hanselmann, K., John, C.M., Yan, H., Liu, Z., Bernasconi, S.M., 2015. Temperature dependence of oxygen- and clumped isotope fractionation in carbonates: a study of travertines and tufas in the 6-95°C temperature range. Geochemica et Cosmochimica Acta, 168, 172-192.

Kele, S., Özkul, M., Fórizs, I., Gökgöz, A., Baykara, M.O., Alçiçek, M.C., Németh, T., 2011. Stable isotope geochemical and facies study of Pamukkale travertines: new evidences of low temperature non-equilibrium calcite-water fractionation. Sedimentary Geology, 238, 191-212.

Kellerman, K.F., Smith, N.R., 1914. Bacterial precipitation of calcium carbonate: Journal of the Washington Academy of Science, 4, 400-402.

Kenyon, W.E., 1992. Nuclear magnetic resonance as a petrophysical measurement. Nuclear Geophysics, 6, 153-171.

Kenyon, W.E., Day, P.I., Straley, C., Willemsen, J.F., 1988. A three-part study of NMR longitudinal relaxation studies of water saturated sandstones. SPE Formation Evaluation, 3, 3, 622-636. SPE-15643-PA. http://dx.doi.org/10.2118/15643-PA

Kenyon, W.E., Kolleeny, J.A., 1995. NMR surface relaxivity of calcite with adsorbed Mn^{2+}. Journal of Colloid and Interface Science, 170, 502-514.

Kim, S.T., O'Neil, J.R., 1997. Equilibrium and nonequilibrium oxygen isotope effects in synthetic carbonates. Geochemica et Cosmochimica Acta, 61, 3461-3475.

Kitano, Y., 1963. Geochemistry of calcareous deposits found in hot springs. J. Earth Sci. Nagoya Univ., II, 68-100.

Kleinberg, R.L., 1996. Utility of NMR T_2 distributions, connection with capillary pressure, clay effect, and determination of the surface relaxativity parameter ρ_2. Magnetic Resonance Imaging, 14, 7-8, 761-767.

Kleinberg, R.L., Jackson, J.A., 2001. An introduction to the history of NMR well logging. Concepts in Magnetic Resonance, 13, 6, 340-342.

Koban, C.G., Schweigert, G., 1993. Microbial origin of travertine fabrics – two examples from southern Germany (Pleistocene Stuttgart travertines and Miocene Riedöschingen travertine). Facies, 29, 251-264.

Krumbein, W.E., 1979a. Photolithotrophic and chemoorganotrophic activity of bacteria and algae as related to Beachrock formation and degradation (Gulf of Aqaba, Sinai): Geomicrobiology Journal, 1, 139-203.

Krumbein, W.E., Cohen, Y., Shilo, M., 1977. Solar Lake (Sinai): 4. Stromatolitic cyanobacterial mats: Limnology and Oceanography, 22, 635-656.

L

Lalou, C., 1957. Studies on bacterial precipitation of carbonates in sea water: Journal of Sedimentary Petrology, 27, 190-195.

Latt, J., Krause, M.J., 2006-2015. OpenLB User Guide. http://optilb.com/openlb.

Latt, J., 2008. Choice of units in lattice Boltzmann simulations. Available at: www.lbmethod.org.

Lenormand, R., 2003. Interpretation of Mercury injection curves to derive pore size distribution. In: International Symposium of the Society of Core Analysts. Pp. SCA2003-52

Liotta, D., Brogi, A., Meccheri, M., Dini, A., Bianco, C., Ruggieri, G., 2015. Coexistence of low-angle normal and high-angle strike- to oblique-slip faults during Late Miocene mineralization in eastern Elba Island (Italy). Tectonophysics, 660, 17-34.

Lofgren, G., 1974. An experimental study of plagiodase crystal morphology: isothermal crys- tallization: American Journal of Science, 274, 243-273.

Lofgren, G. 1980. Experimental studies on the dynamic crystallization of silicate melts, in Haegraves, R.B., ed., Physics of Magmatic Processes: Princeton, New Jersey, Princeton University Press, 487-551.

Lønøy, A., 2006. Making sense of carbonate pore systems. AAPG Bull. 90, 9, 1381-1405.

Lucia, F.J., 1983. Petrophysical parameters estimated from visual description of carbonate rocks. A field classification of carbonate pore space. Journal of Petroleum Technology, 35, 626-637.

Lucia, F.J., 1995. Rock-fabric/petrophisical classification of carbonate pore space for reservoir characterization. AAPG Bulletin, 79, 9, 1275-1300.

M

Manfra, L., Masi, U., Turi, B., 1974b. Effetti isotopici nelladiagenesi dei travertini. Geol. Romana, 13, 147-155.

Manfra, L., Masi, U., Turi, B., 1976. La composizione isotopica dei travertini del Lazio. Geol. Romana, 15, 127-174.

Marshall, D. J., 1988. Cathodoluminescence of geological materials. Unwin Hyman, London, 146p.

Marschall, D., Gardner, J.S., Mardon, D., Coates, G.R., 1995. Method for correlating NMR relaxometry and mercury injection data. Presented at the Society of Core Analysts International Symposium, San Francisco, California, USA, September 12-14. SCA-9511.

Martini, I.P., Sagri, M., 1993. Tectono-sedimentary characteristics of late Miocene-Quaternary extensional basins of the northern Apennines, Italy. Earth-Science Reviews, 34, 3, 197-233.

Maxia, C., 1950. Il Bacino delle Acque Albule. Contributi di Scienze Geologiche, 20. CNR, Rome.

McArthur, J.M., Howarth, R.J., 2004. Sr-isotope stratigraphy: the Phanerozoic 87Sr/86Sr-curve and explanatory notes. In: A Geological Timescale (Eds F. Gradstein, J. G. Ogg and A.G. Smith), 96-105. Cambridge University press, Mouscron.

Melim, L.A., Anselmetti, F.S., Eberli, G.P., 2001. The importance of pore type on permeability of Neogene carbonates, Great Bahama Bank. In Subsurface Geology of a Prograding Carbonate Margin, Great Bahama Bank: Results of the Bahamas Drilling Project (ed. Ginsburg, R.N.), SEPM Special Publication, 70, 217-240.

Mendonça Filho, J.G., Chagas, R.B.A., Menezes, T.R., Mendonça, J.O., da Silva, F.S., Sabadini-Santos, E., 2010. Organic facies of the Oligocene lacustrine system in the Cenozoic Taubaté basin, Southern Brazil. International Journal of Coal Geology, 84, 166-178.

Mendonça Filho, J.G., Menezes, T.R., Mendonça Filho, J.O., Oliveira, A.D., Silva, T.F., Rondon, N.F., Silva, F.S., 2012. Organic Facies: Palynofacies and Organic Geochemistry Approaches, Geochemistry - Earth's System Processes, Dr. Dionisi os Panagiotaras (Ed.), ISBN: 978-953-51-0586-2, InTech, Available from: http://www.intechopen.com/books/geochemistry-earth-s-system-processes/organic-facies-palynofacies-and-organic-geochemistry-approaches.

Mettraux, M., Homewood, P., Balushi, S.A., Erthal, M.M., Matsuda, N.S., 2014. Neoproterozoic microbialites in outcrops of the Qarn Alam salt dome, central Oman. GeoArabia, 19, 3, 17-76.

Minissale, A., 2004. Origin, transport and discharge of CO_2 in central Italy. Earth-Science Reviews, 66, 89-141. doi:10.1016/j.earscirev.2003.09.001.

Minissale, A.A., Duchi, V., 1988. Geothermometry on fluids circulating in a carbonate reservoir in north-central Italy. Journal of Volcanology and Geothermal Research, 35, 237-252.

Minissale, A., Kerrick, D.M., Magro, G., Murrell, M.T., Paladini, M., Rihs, S., Sturchio, N.C., Tassi, F., Vaselli, O., 2002. Geochemistry of Quaternary continental carbonates in the region north of Rome (Italy): Structural, hydrologic and paleoclimatic implications. Earth Planet. Sci. Lett. 203, 709-728. doi:10.1016/S0012-821X(02)00875-0.

Minissale, A., Magro, G., Martinelli, G., Vaselli, O., Tassi, F., 2000. Fluid geochemical transect in the Northern Apennines (central – northern Italy): fluid genesis and migration and tectonic implications. Tectonophysics, 319, 199-222.

Minissale, A., Sturchio, N.C., 2004. Travertines of Tuscany and Latium (Central Italy). Field trip guide book, 25p.

Molli, G., 2008. Northern Apennine–Corsica orogenic system: an updated overview. Geological Society, London, Special Publications, 298, 413-442.

Mohnke, O., 2014. Jointly deriving NMR surface relaxativity and pore-size distributions by NMR relaxation experiments on partially desaturated rocks. American Geophysical Union, 50, 6, 5309-5321.

Morschbacher, M.J., Vasquez, G.F., Justen, J.C.R., 2010. Metodologias de estimativa das velocidades sísmicas em ensaios de laboratório. 4º Simpósio Brasileiro da Sociedade Brasileira de Geofísica, Brasília

Mostaghimi, P., Bijeljic, B., Blunt, M., 2012. Simulation of flow and dispersion on pore-space images. SPE Journal, 17, 1-131.

Myers, D. E., 1989. To be or not to be... stationary? That is the question. Mathematical Geology, 21, 347-362.

O

Okabe, H., Oseto K., 2006. Pore-scale heterogeneity assessed by the lattice-Boltzmann method. In: Proceedings of the international symposium of the society of core analysts, Trondheim, Norway, 2006-44.

Okumura, T., Takashima, C., Shiraishi, F., Akmaluddin, Kano, A., 2012. Textural transition in an aragonite continental carbonate formed under various flow conditions at Pancuran Pitu, Central Java, Indonesia. Sediment. Geol., 265-266, 195-209.

Özkul, M., Varol, B., Alçiçek, M.C., 2002. Depositional environments and petrography of denizli travertines. Bulletin of the Mineral Research and Exploration, 125, 13-29.

P

Pan, C., Hilpert, M., Miller, C. T., 2001. Pore-scale modeling of saturated permeabilities in random sphere packings. Physical Review E, 64.

Pan, C., Hilpert, M., Miller, C. T., 2004. Lattice-Boltzmann simulation of two-phase flow in porous media. Water Resources Research, 40.

Panichi, C., Tongiorgi, E., 1976. Carbon isotopic composition of CO_2 from springs, fumaroles, mofettes and travertines of central and southern Italy: a preliminary rospection method of geothermal areas. Proceedings of the 2nd U.N. Symposium on the Development and Use of Geothermal Energy, San Francisco, 20-29 May 1975, 815-825.

Patacca, E., Sartori, R., Scandone, P., 1992. Tyrrhenian basin and Apenninic arcs: kinematic relations since late Tortonian times. Mem. Soc. Geol. Ital., 45, 425-451.

Pedley, M., 1990. Classification and environmental models of cool freshwater tufas. Sedimentary Geology, 68, 143-154.

Pedley, M., 2009. Tufas and travertines of the Mediterranean region: a testing ground for freshwater carbonate concepts and developments. Sedimentology, 56, 221-246.

Pedley, M., Rogerson, M., 2010. Introduction to tufas and speleothems. Geological Society, London, Special Publications, 336, 1-5.

Pentecost, A., 1990. The formation of continental carbonate shrubs: Mammoth Hot springs, Wyoming. Geological Magazine, 127, 159-168. doi:10.1017/S0016756800013844.

Pentecost, A., 2005. Continental carbonate: London, Springer-Verlag, 445p.

Pentecost, A., Viles, H., 1994. A Review and Reassessment of Travertine Classification. Géographie physique et Quaternaire, 48, 3, 305-314.

Piller, M., Schena, G., Nolich, M., Favretto, S., Radaelli, F., Rossi, E., 2009. Analysis of hydraulic permeability in porous media: from high resolution X-ray tomography to direct numerical simulation. Transport in porous media, 80, 57-78.

Possemiers, M., Huysmans, M., Peeters, L., Batelaan, O., Dassargues, A., 2012. Relation between sedimentary features and permeability at different scales in Brussels sands. Geologica Belgica, 13, 3, 156-164.

Pursell, V.J., 1985. The petrology and diagenesis of Pleistocene and recent travertines from Gardiner, Montana, and Yellowstone National Park, Wyoming. Unpubl. M.S. thesis, University of Texas, Austin, TX.

R

Rainey, D. K., Jones, B., 2009. Abiotic versus biotic controls on the development of the Fairmont Hot Spring carbonate deposit, British Columbia, Canada. Sedimentology, 56, 1832-1857.

Rémond, G., Cesbron, F., Chapoulie, R., Ohnenstetter, D., Roques-Carmes, C., Schvoerer, M., 1992. Cathodoluminescence applied to the microcharacterization of mineral materials: a present status in experimentation and interpretation. Scanning Microscopy, 6, 23-68.

Renaut, R.W., Owen, R.B., Jones, B., Tiercelin, J.J., Tarits, C., Ego, J.K., Konhauser, K.O., 2013. Impact of lakelevel changes on the formation of thermogene travertine in continental rifts: evidence from Lake Bogoria, Kenya Rift Valley. Sedimentology, 60, 428-468.

Rezende, M.F., Pope, M.C., 2015. Importance of depositional texture in pore characterization of subsalt microbialite carbonates, offshore Brazil. Geological Society, London, Special Publications, 418, 1, 193-207. doi:10.1144/SP418.2.

Riding, R., 1991. Classification of microbial carbonates. In: Calcareous algae and stromatolites, ed. By R. Riding, 21-51. Springer-Verlag, Berlin.

Rigby, S.P., Gladden, L.F., 2000. Deconvolving pore shielding effects in mercury porosimetry data using NMR techniques. Chemical Engineering Science, 55p.

Rios, E.H., Stael, G.C., Ramos, P.F.O., Machado, V.F., Forecchi, R.B., Azeredo, R.B.V., 2010. Caracterização Petrofísica de Rochas Reservatório por Ressonância Magnética Nuclear. IV Simpósio Brasileiro de Geofísica, novembro 14-17.

Rollinson, H.R., 1993. Using Geochemical Data: Evaluation, Presentation, Interpretation, Longman Geochemistry Series. Longman Group UK Limited, Pearson Education Limited, Oxfordshire, UK.

Ronchi, P., Cruciani, F., 2015. Continental carbonates as a hydrocarbon reservoir, an analog case study from the travertine of Saturnia, Italy. AAPG Bulletin, 99, 711-734.

Rousseeuw, P.J., 1987. Silhouettes: a graphical aid to the interpretation and validation of cluster analysis. Journal of computational and applied mathematics, 53-65.

S

Saller, A., Rushton, S., Buambua, L., Inman, K., McNeil, R., Dickson, J.A.D., 2016. Presalt stratigraphy and depositional system in the Kwanza Basin, offshore Angola. AAPG Bulletin, 100, 1135-1164.

Salminen, R., Reeder, S., De Vivo, B., Demetriades, A., Pirc, S., Batista, M.J., Marsina, K., Ottesen, R.T., O'Connor, P.J., Bidovec, M., Lima, A., Siewers, U., Smith, B., Taylor, H., Shaw, R., Salpeteur, I., Gregorauskiene, V., Halamic, J., Slaninka, I., Lax, K., Gravesen, P., Birke, M., Breward, N., Ander, E.L., Jordan, G., Duris, M., Klein, P., Locutura, J., Bellan, A., Pasieczna, A., Lis, J., Mazreku, A., Gilucis, A.,

Heitzmann, P., Klaver, G., Petersell, V., 2006. Geochemical atlas of Europe. Part 2 - Interpretation of Geochemical Maps, Additional tables, Figures, Maps, and related Publications. Geological Survey of Finland.

Schröder, S., Ibekwe, A., Saunderes, M., Dixon, R., Fisher, A., 2016. Algal-microbial carbonates of the Namibe Basin (Albian, Angola): Implications for microbial carbonate mound development in the South Atlantic. Petroleum Geoscience, 22, 71-90.

Seevers, D.O., 1966. A nuclear magnetic method for determining the permeability of sandstones. Presented at the SPWLA 7th Annual Logging Symposium, Tulsa, May 8-11. Paper L.

Skalinski, M., Kenter, J.A.M., 2015. Carbonate petrophysical rock typing: integrating geological attributes and petrophysical properties while linking with dynamic behavior. Geological Society, London, Special Publications, 406, 229-259.

Soete, J., Kleipool, L.M., Claes, H., Claes, S., Hamaekers, H., Kele, S., Özkul, M., Foubert, A., Reijmer, J.J.G., Swennen, R., 2015. Acoustic properties in travertines and their relation to porosity and pore types. Mar. Pet. Geol. 59, 320-335. doi:10.1016/j.marpetgeo.2014.09.004.

Soete, J., 2016. Pore network characterization in complex carbonate system. Thesis presented in pursuit of the degree of Doctor in Sciences, Department Geography-Geology, Faculty of Sciences, KULeuven, Belgium, 2016.

Soete, J., Claes, S., Claes, H., Janssens, N., Cnudde, V., Huysmans, M., Swennen, R. (Accepted). Lattice Boltzmann simulations of fluid flow in continental carbonate reservoir rocks and in upscaled rock models generated with multiple-point geostatistics. Geofluids, Special issue: Flow and Transport in Porous Media: A Multiscale Focus.

Stalinski, M., Kenter, J., Jenkins, S., 2009. Rock type definition and pore type classification of a carbonate platform, Tengiz field, Republic of Kazakhstan. SPWLA 50th Annual Logging Symposium.

Straley, C., Morriss, C.E., Kennyon, W.E., Howard, J.J., 1995. NMR in partially saturated rocks: laboratory insights on free fluid index and comparison with borehole logs. The Log Analyst, 36, 40-56.

T

Teboul, P.A., Durlet, C., Gaucher, E.C., Virgone, A., Girard, J.P., Curie, J., Lopez, B., Camoin, G.F., 2016. Origins of elements building travertine and tufa: new perspectives provided by isotopic and geochemical tracers. Sedimentary Geology, 334, 97-114.

Terra, G.J.S., Spadini, A.R., França, A.B., Sombra, C.L., Zambonato, E.E., da Silva Juschaks, L.C., Arienti, L.M., Erthal, M.M., Blauth, M., Franco, M.P., Matsuda, N.S., Carramal da Silva, N.G., Moretti Júnior, P.A., D'Avila, R.S.F., Schiffer de Souza, R., Tonietto, S.N., Couto dos Anjos, S. M., Campinho, V.S., Winter, W.R., José, G., Terra, S., Leite, C., Costa, L., Goulart, N., Augusto, P., Junior, M., Francisco, R.S., Avila, D., Souza, R.S., De Maria, S., 2009. Carbonate rock classification applied to brazilian sedimentary basins. Bol. Geociencias da Petrobras, 18, 9-29.

Timur, A., 1969. Effective porosity and permeability of sandstones investigated through nuclear magnetic principles. The Log Analyst, 10, 1, 3p.

Timur, A., 1969. Pulsed nuclear magnetic resonance studies of porosity, movable fluid, and permeability of sandstones. Journal of Petroleum Technology, 21, 6, 775-786. SPE-2045-PA. http://dx.doi.org/10.2118/2045-PA

Thompson, D.L., Stilwell, J.D., Hall, M., 2015. Lacustrine carbonate reservoirs from Early Cretaceous rift lakes of western

Gondwana: Pre-Salt coquinas of Brazil and West Africa. Gondwana Research, 28, 26-51.

Torabi, A., Fossen, H., 2009. Spatial variation of microstructure and petrophysical properties along deformation bands in reservoir sandstones. AAPG Bulletin, 93, 7, 919-938.

Torrey, H.C., 1956. Bloch equations with diffusion terms. APS Journals Archieve, 104, 3, 563-565. https://doi.org/10.1103/PhysRev.104.563

Tucker, M.E., Wright, V.P., 1990. Carbonate sedimentology. Blackwell Scientific Publications, Oxford, 482p.

Turi, B., 1986. Stable isotope geochemistry of travertines, in: Fritz, B.P., Fontes, J.C. (Eds.), Handbook of Environmental Isotope Geochemistry. Elsevier, Amsterdam, pp. 207–235.

Turner, E.C., Jones, B., 2005. Microscopic calcite dendrites in cold-water tufa: implications for nucleation of micrite and cement. Sedimentology, 52, 1043-1066. doi:10.1111/j.1365-3091.2005.00741.x

V

Vasconcelos, C., Dittrich, M., McKenzie, J. A., 2013. Evidence of microbiocoenosis in the formation of laminae in modern stromatolites. Facies, 60, 3-13.

Vasconcelos, C., McKenzie, J.A., 1997. Microbial mediation of modern dolomite precipitation and diagenesis under anoxic conditions (Lagoa Vermelha, Rio de Janeiro, Brazil). Journal of Sedimentary Research, 67, 378-390.

Vasconcelos, C., Warthmann, R., McKenzie, J.A., Visscher, P.Z., Bittermann, A.G., van Lith, Y., 2006. Lithifying microbial mats in Lagoa Vermelha, Brazil: Modern Precambrian relics? Sedimentary geology, 185, 175-183.

Verwer, K., Braaksma, H., Kenter, J.A.M., 2008. Case History Acoustic properties of carbonates: Effects of rock texture and implications for fluid substitution. Geophysics, 73, B51-B65.

Vincent, B., Fleury, M., Santerre, Y., Brigaud, B., 2011. NMR relaxation of neritic carbonates: An integrated petrophysical and petrographical approach. Journal of Applied Geophysics, 74, 1, 38-58.

W

Weger, R.J., Eberli, G.P., Baechle, G.T., Massaferro, J.L., Sun, Y.F., 2009. Quantification of pore structure and its effect on sonic velocity and permeability in carbonates. AAPG Bull. 93, 10, 1297-1317.

Westphal, H., Surholt, I., Kiesl, C., Thern, H. F., Kruspe, T., 2005. NMR measurements in carbonate rocks: problems and an approach to a solution. Pure and Applied Geophysics, 162, 549-570. Doi: 10.1007/s00024-004-2621-3.

Wichtmann, T., Triantafyllidis, T., 2010. On the influence of the grain size distribution curve on P-wave velocity, constrained elastic modulus M max and Poisson's ratio of quartz sands. Soil Dynamics and Earthquake Engineering, 30, 757-766.

Wright, V.P., Tucker, M.E., 1991. Calcretes: an introduction. In: Wright, V.P., Tucker, M.E. (Eds), Calcretes. IAS Reprint Series, 2. Blackwell Scientific Publications, Oxford, 1222p.

Wright, V.P., 2012. Lacustrine carbonates in rift settings: the interaction of volcanic and microbial processes on carbonate deposition. Geological Society of London, Special Publication, 39-47. doi:10.1144/SP370.2.

Wright, V.P., Barnett, A.J., 2015. An abiotic model for the development of textures in some South Atlantic early Cretaceous lacustrine carbonates Cretaceous (part): Microbial Carbonates in Space and Time: Implications for Global Exploration and Production, 418p.

X

Xu, S., Payne, M.A., 2009. Modeling elastic properties in carbonate rocks. The Leading Edge, 28, 1, 66-74.

Y

Yeung, K.Y., Haynor, D.R., Ruzzo, W.L., 2001. Validating clustering for gene expression data. Bioinformatics, 17, 309-318.

Z

Zhang, Y., Xia, P., Yu, Y., 2000. Review of nuclear magnetic resonace magnet for oil well logging. IEEE Trans. Supercond., 10, 763-766.

Ziarani, A.S., Aguilera, R., 2012. Pore-throat radius and tortuosity estimation from formation resistivity data for tight-gas sandstone reservoirs. Journal of Applied Geophysics, 83, 65-73.

Zinszner, B., Pellerin, F., 2007. A geoscientist's guide to petrophysics. IFP Publications.

APPENDIX 1 – Shrub and pore type classification: petrography of travertine shrubs from the Ballik-Belevi area (Denizli, SW Turkey)

Based on Claes, H., Erthal, M.M., Soete, J., Özkul, M., Swennen, R., 2017. Shrub and pore type classification Petrography of travertine shrubs from the Ballık-Belevi area (Denizli, SW Turkey). Quaternary Geology, 437, 147-163. http://dx.doi.org/10.1016/j.quaint.2016.11.002

Erthal M.M. contributed with 50% of the writing, gathering of samples in the field, petrography, working out the shrub classification, interpretation and discussion of the results. The matter of importance, she is also the first author of the present publication.

A.1 Introduction

In 2006 the giant Tupi oil field, now known as the Lula oil field, was discovered offshore Brazil in a salt-sealed reservoir that on average lies 5.485 m below sea level (Beasley et al., 2010). Temperatures in the reservoir vary from 60 °C to locally more than 80 °C (Alves et al., 2009). Similar discoveries, both offshore the eastern coast of South America as well as offshore West Africa (Borsato et al., 2012; Saller et al., 2016), have resulted in an increased interest in this so-called Pre-Salt play. The lacustrine source rocks and the excellent, sometimes more than 2000 m thick, evaporite seal are the subject of numerous studies (Pasley and Wilson, 1998; Meisling et al., 2001; Thompson and Oftebro, 2011). The reservoir rocks, however, are non-conventional, heterogeneous and poorly understood (Nakano et al., 2009; Beasley et al., 2010). Their thickness is variable, from less than 55 to more than 500 meters (Wright and Barnett, 2015). The reservoir rocks are described as shallow water microbial carbonates (Carminatti et al., 2008, 2009) and more specifically as "stromatolites", spherulites and laminites (Dias, 1998; Terra et al., 2010). Their classification as "stromatolites" refers to the micro-lamination of the structures. Recently, the "stromatolites" are also described as "shrub framestones" (Alabi et al., 2014) or "shrubby boundstones" (Saller et al., 2016). However, their formation, within a lacustrine or marine sedimentological environment and possible microbial origin are under discussion (Dorobek et al., 2012; Wright, 2012; Mancini et al., 2013; Wright and Barnett, 2015).

In particular, the occurrence and formation of "microbial" aggradational carbonate build-ups (Carminatti et al., 2008, 2009; Wright, 2012; Buckley et al., 2013; Schröder et al., 2015) remains poorly understood. Tufa and travertines share several common features with stromatolites of marine origin (Pentecost, 1990) and they are sometimes even referred to as freshwater stromatolites (Freytet and Verrecchia, 1998). If travertine precipitating waters discharge sub-aerially, they can create topographic features like mounds and ridges (Bargar, 1978; Chafetz and Folk, 1984; Wright, 2012). In the onshore time equivalent of the Namibe Basin (Angola), fracture fed mound-like morphologies are linked to fissure ridge and "dam and cascade" travertines (Sharp et al., 2013). Sub-aerial carbonates and their relation with volcanic activity have attracted Pre-Salt exploration in West Africa, the focus being on geological reconstruction of the potential Pre-Salt target in the Kwanza Basin (Lottaroli et al., 2012; Sharp et al., 2012). Furthermore, Wright (2012) indicated that shrub-like travertine fabrics, observed in lacustrine, i.e. sub-aqueous travertines (Chafetz and Guidry, 1999), are remarkably similar to the microbialite fabrics encountered in the Pre-Salt of the Campos and Santos Basin (Dias, 1998; Terra et al., 2010). In conclusion, understanding of travertine development, including the differences with regard to sub-aerial and sub-aqueous formation, is crucial in the exploration for, and development of, carbonate reservoirs in rift basins (Mancini et al., 2013). Recently, several travertines have been studied as potential reservoir analogues (e.g. Ronchi and Francesco, 2015; Claes et al., 2016; Török et al., 2016). The travertine dome inside the Ballık-Belevi area, as described by Claes et al. (2015), is a transitional occurrence of a sub-aqueous and sub-aerial thin water film system, and provides excellent outcropping conditions due to ongoing

excavation. The aim of this paper is to develop a reservoir oriented classification of the Turkish Ballık-Belevi shrubs, including morphology, size and fabric. In addition, the related pore-types are distinguished and some reconnaissance porosity and permeability measurements are performed.

A.1.1 Terminology

Before focusing on description and classification, it is essential to clarify some terminology.

A.1.1.1 Shrub or dendrite? Or both?

The term "shrub" was introduced for travertines by Kitano (1963) but is commonly in use since the study of Chafetz and Folk (1984). Although they related the term immediately to bacterially influenced fabrics, it was introduced solely to describe the "*gross morphologic similarities with low, usually several stemmed, woody plants*". Shrubs are described as "*the shrub-like or fern-like arborescent growths that branch upward to form colonies*" (Chafetz and Folk, 1984). Throughout literature the term "shrub" is often combined or confused with "dendrite" and related terms like "dendrolite", "dendrititic" and "dendroid", that are derived from the Greek "dendron" meaning "tree". A similar term is "arborescent" that is derived from Latin "arborescere" meaning "to grow into a tree". Dendritic and arborescent are used, also in other scientific fields, to describe the branching nature of structures. Shrubby, dendritic and arborescent thus all refer to very similar structures. The fact that Chafetz and Folk (1984) described *shrubs* as having "the appearance of a succession of miniature *forests*" and resembling the "micro*trees*" of Christie and Floodgate (1966), illustrates the miscellaneous use.

The term shrub, however, originally was mainly related to the outer appearance of the structures. It is in this way that the term is applied in this manuscript, i.e. shrub as descriptive morphological term for the outer appearance of millimetre to centimetre scaled structures. It thus does not apply to the internal texture, that, as will be illustrated, can be fully sparitic, peloidal, dendritic (branching) and even stromatolitic, i.e. thinly laminated. Prime examples of macro-scale shrubs are given in Fig. 1. Recognizing shrubs, however, is not always straightforward, as will be clear from the examples that will be presented.

A.1.1.2 Micrite

Folk (1959) described micrite for the first time as "microcrystalline calcite ooze" considering crystal sizes between 1 – 4 µm, characteristic for low-energy deposits. According to Friedman and Sanders (1978) micrite may be defined as "lithified lime mud". Milliman et al. (1985) classify tiny calcite crystals as microcrystalline or cryptocrystalline. In contrast, micrite is considered an intimate mixture of aphanocrystalline (1 – 4 µm) matrices and microspar with very finely crystalline matrices (16 - 4 µm) (Folk, 1959; Tucker and Wright, 1990; Dupraz et al., 2009). It is clear that the term "micrite" or "micritic" is defined and applied differently in literature. Some authors base their definition on crystal size, while others also include genesis. For this study, the definition of Tucker and Wright (1990) is applied, where micrite is defined as fine calcite crystals less than 4 µm in size.

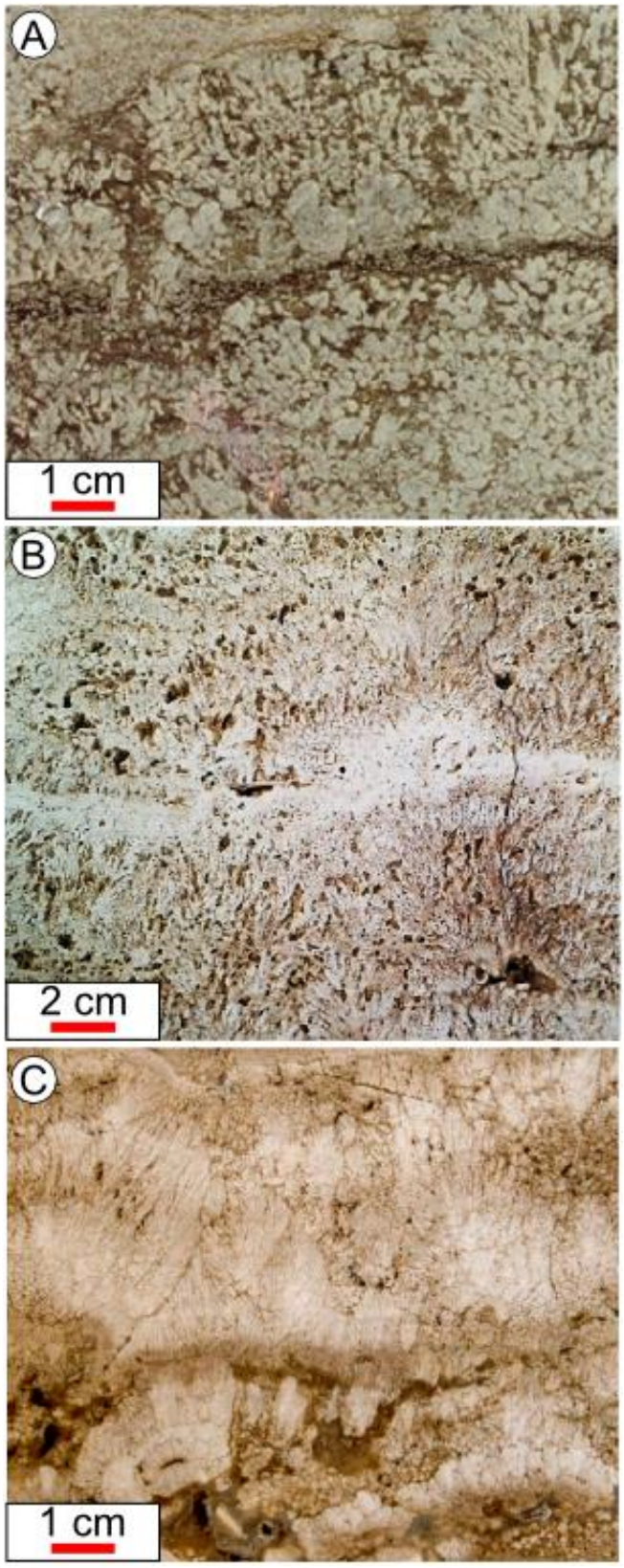

Figure 1: Prime examples of dendriform shrubs: A) an example cropped from Dias (2005) of the Upper Aptian of the Campos Basin described as “dendritic/bush-shaped stromatolites”, B) an example from Italy, in this case from Acquasanta, but similarly described for Tivoli as shrubs by Chafetz and Folk (1984) and C) an example of shrubs from the Ballık-Belevi area in Turkey.

A.2 Geological Setting

The extensional Denizli Basin in the south-west of Turkey is well-known for its numerous fossil and active travertine occurrences (Özkul et al., 2013). The relation between the tectonical, seismic and hydrothermal settings is pointed out by multiple authors (De Filippis et al., 2012; Kaypak and Gökkaya, 2012; Van Noten et al., 2013). Travertine precipitation is mainly related to CO_2-degassing and occurred along basin-bounding faults. The oldest travertine age (>1.1 Ma; Lebatard et al., 2014) is reported for the Ballık-Belevi area (Figure 2), the largest travertine deposit of the Denizli Basin (Özkul et al., 2013). This area has been the subject of multiple studies, in particular within the Killik dome. The domal structure provides excellent outcropping conditions due to on-going excavation mainly in the Ece, Faber, Çakmak, İlik and Alimoğlu quarries (Figure 2). Van Noten et al. (2013) performed a structural analysis of the Ballık area, while El Desouky et al. (2015) combined oxygen, carbon and strontium isotope data on travertine samples from the Çakmak quarry with results from a fluid inclusion study in order to deduce the parent carbonate source rocks. The Lycian Nappes carbonates were proposed as source rocks for the travertine dome by El Desouky et al. (2015) and Claes et al. (2015). A minimum and maximum domal travertine age of 1.10 Ma and 1.78 Ma was deduced as part of a study to determine the age of the *Homo erectus* fossil (Lebatard et al., 2014). Based on age and thickness, a precipitation rate of roughly 10 m per 100 ka was concluded (Lebatard et al., 2014).

The calculated mean precipitation temperature deduced based on stable oxygen isotopes is estimated between 26 and 35 °C (Claes et al., 2015). Active continental carbonate precipitation still takes place today in the Kaklık cave, in the SE of the Ballık area (Figure 2). The present-day temperature of this thermal spring is 22.8 °C (Özkul et al., 2013). The hottest present-day active thermal spring in the Denizli Basin is the Çukurbağ spring (57.1 °C) on the Pamukkale site (Özkul et al., 2013). Özkul et al. (2002, 2013) provided a concise general macroscopic and microscopic description of the Denizli travertines in combination with stable isotopic data and provided a stratigraphical section of the İlik quarry. Khatib et al. (2014) performed a mineralogical and sedimentological analysis of lithologies exposed in the Faber quarry. They focused mainly on the non-travertine lithologies in the frame of paleomagnetic dating. The Ballık travertines consist almost purely of a calcite mineralogy (>94%), with minor amounts of detrital quartz, amorphous phases organic matter and clays (Khatib et al., 2014; Soete et al., 2015). The sedimentology, including a 3D sedimentological geobody reconstruction, formed the focus of the study on the Ece and Faber quarry by Claes et al. (2015), providing insight in the architecture of this potential reservoir analogue. The Çakmak quarry was part of a sedimentological comparative study with the modern Mammoth Hot Springs (De Boever et al., 2016a). Petrophysical properties of the Ballık travertines have been addressed in Khatib et al. (2014), Soete et al. (2015) and De Boever et al. (2016b). Travertine quarries around the Killik dome were also the subject of several studies. Samples from the Kömürcüoğlu quarry (Figure 2) for example were analysed for stable isotopes (Özkul et al., 2013) and were together with samples from the Belevi quarries dated by thermoluminescence (490±50 ka and 510±50 ka respectively; Özkul et al., 2004).

The well-exposed, well-studied and transitional nature of the Ballık-Belevi travertines from sub-aqueous sub-horizontal to sub-aerial domal deposits, in combination with their presumed similarities to the travertines in Angola and the Pre-Salt microbialites makes them ideal as study object.

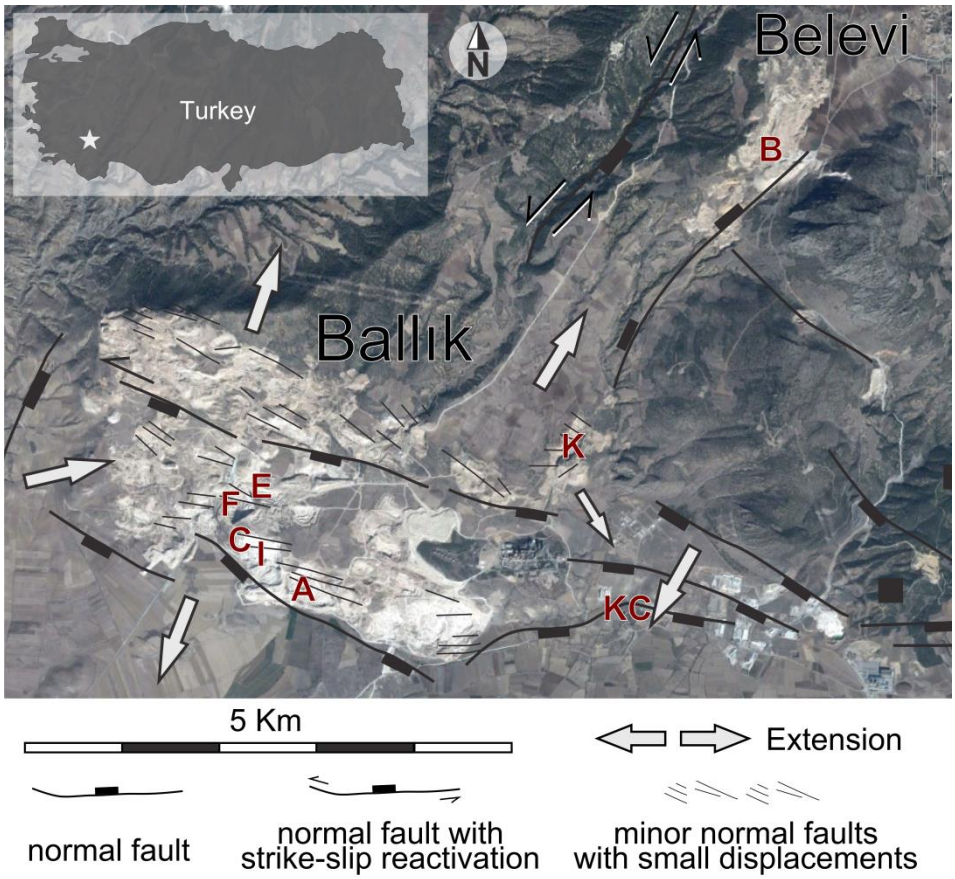

Figure 2: Overview of the Ballık-Belevi area in SW Turkey (modified from Van Noten et al., 2013). Some of the localities are indicated with their initials; The E = Ece, F= Faber, C = Çakmak, I = İlik, and A = Alimoğlu quarries that excavate the Killik dome. The K = Kömürcüoğlu and B = Belevi quarries. KC= Kaklık cave.

A.3 Methodology

A.3.1 Petrography

Because of the fragility of travertine, particularly at pore edges, the samples were doubly impregnated under vacuum with resin for thin-section preparation. For some thin-sections a fluorescent dye was used in order to easily distinguish (micro-)porosity with incident fluorescent light microscopy. For other thin-sections blue dye was used. Petrographic characterization was conducted on an Olympus BX60 (Olympus Corporation, Tokyo, Japan) and Leica DM LP Parallel (Leica Microsystems, Wetzlar, Germany) and Crossed Polarizer Optical and Fluorescence microscope (PPM, CPM and FM respectively). A Zeiss Axio Imager Z1m microscope with adapted filter set (EX BP365/12 EM LP397, EX G 365 EM LP 420 and EX BP 450-490 EM LP 515) was used to examine the auto-fluorescence (Zeiss Group, Oberkochen, Germany). A Nikon OptiPhot microscope (Nikon Corporation, Tokyo, Japan) with a modified Technosyn Model 8200 Mark II stage was used for Cold Cathodoluminescence (CCL) observations.

A.3.2 Porosity - Permeability

A conventional core analysis was carried out on 1 and ~1.5 inch diameter plugs. The effective porosity is measured with helium expansion porosimetry. The specific gas permeability is measured in a steady state permeameter with nitrogen gas.

A.3.3 Computed Tomography (CT)

Cores of ~10 cm diameter were scanned with a Siemens Somatom Flash medical CT scanner (Siemens AG, Berlin, Germany) at 140 kV and 46 kW. The data are reconstructed with filtered back projection using a very sharp convolution (B70f). The resulting voxel resolution is 0.3 x 0.3 x 0.5 mm³. The CT images were segmented in Matlab (MathWorks Inc., Natick,

Massachusetts, USA), by dual thresholding. The pore network was rendered in 3D and labelled in Avizo Fire 7.0 (FEI Visualization Sciences Group, Hillsboro, Oregon, USA). Further data-processing on pore shape parameters was executed in Matlab.

A.4 Results

A.4.1 Petrography

Because of the characteristic branching nature of their micro-fabrics, the main shrub types of the Ballık travertines were classified as dendritic lithotypes by Claes et al. (2015). To the center of the Ballık travertine dome, the lower sub-horizontal facies, flat pool facies (Van Noten et al., 2013), or extended pond facies (De Boever et al., 2016a) is dominated by dendrites. In the Çakmak quarry for example, the more than 6 m thick sub-horizontal, dendrite dominated facies can be followed laterally over more than 300 m. Of importance is that lithological variations can be studied in three dimensions based on the excavated quarry walls. Macroscopically dense, very white, relatively straight laminated, dendritic crusts evolve laterally and vertically into more crenulating crusts (e.g. Figure 3A), shrubby, micritic dendrite travertine (e.g. Figure 1C). The dendritic organisation of their internal fabrics is most clear when the rocks are (slightly) weathered (e.g. weathered crust in Figure 3B). High porosities result mainly from inter-laminar porosity due to the cyclic alternation with porous peloidal micrite and dissolution enhanced porosity along the laminae (Figure 3A). Remarkably, the largest macro-scale dendritic shrubs are found at the bottom of primary caves (Figure 3D-F). In the vicinity of these caves also large straight branching feather-like crystals occur (Figure 3G), referred to as "crystal shrubs" by Chafetz and Guidry (1999).

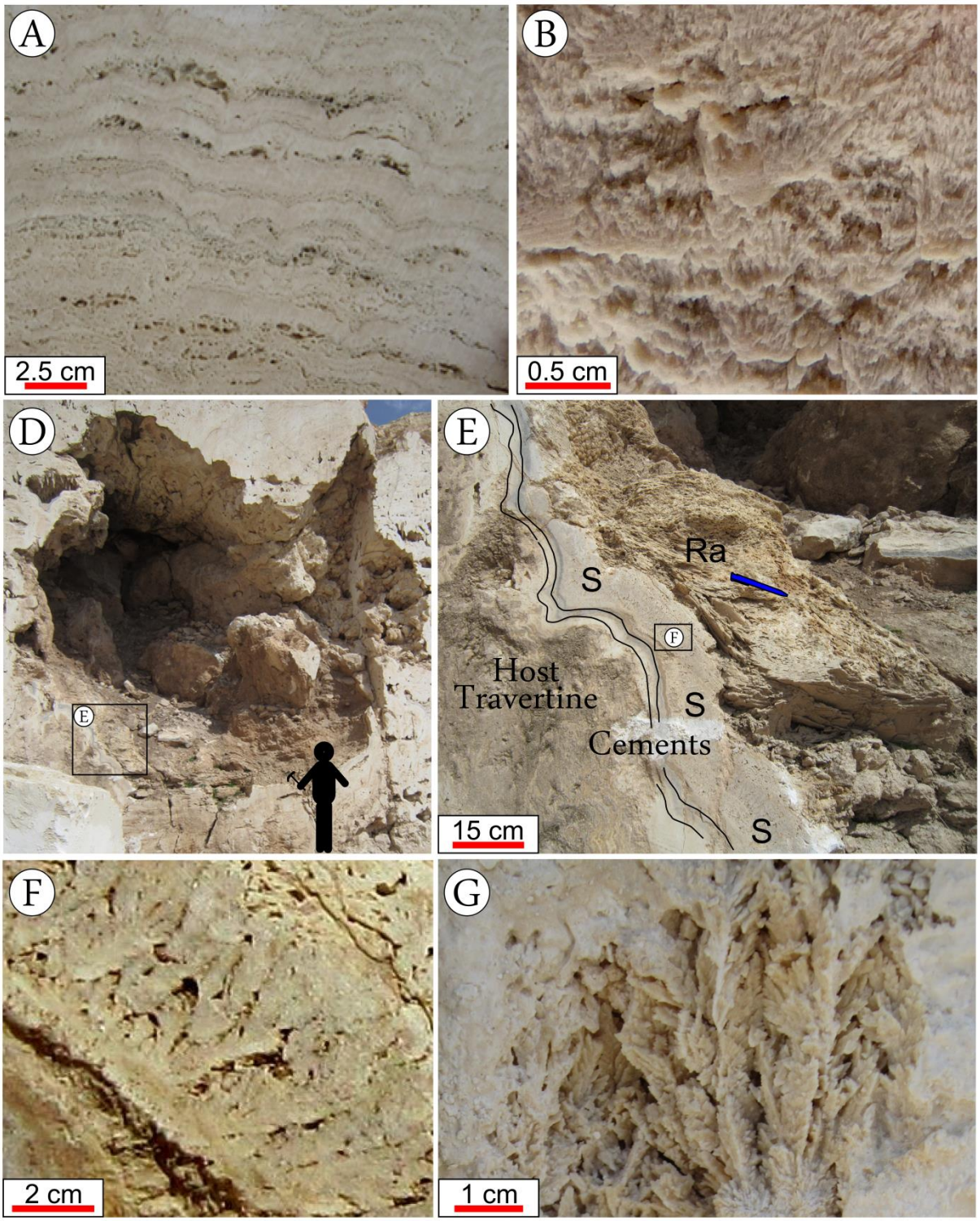

Figure 3: A) Macroscopically dense, very white, relatively straight laminated, dendritic crusts (c) laterally and vertically transition into more crenulating, shrubby, micritic dendrite travertine (s). B) Weathering of the crusts and shrubs, shown in (A), reveals their internal dendritic fabrics. C) Inter-laminar porosity due to the cyclic alternation of dendritic crusts with, sometimes dissolution enhanced, porous peloidal micrite. D) Primary cave that was enlarged by secondary collapse. E) Zoom on D. Edge of primary cave with cement bands that coated the host travertine before shrubs (s) and subsequently rafts (Ra) formed. F) Zoom on the shrubs in E. G) Straight branching feather-like crystals found in the vicinity of primary caves.

In order to develop a classification that is applicable from a reservoir engineering point of view, with a link to petrophysical properties, the classification of the shrub related lithotypes described by Claes et al. (2015) has been re-evaluated. Here a refined classification is established that takes the different scales of investigation into account as well as the different fabrics and morphologies (Figure 4). The classification of shrub-related lithotypes is mainly based on morphology. The morphologies described by Terra et al. (2010) are incorporated in the proposed classification. Depending on the direction of sample cutting, the 2D shape of the shrubs can also be very different. For these cases it is important to take the three dimensions into account, e.g. with computed tomography. The different types are first described on micro-scale and subsequently on macro-scale. The photographs of the classification in Figure 4 are morphological prime examples. Additional realistic micro- and macro-scale examples of the Ballık-Belevi travertines are given in Figures 5 and 6 respectively, illustrating that recognising shrub types might not always be straightforward. Based on macro-scale alone, the shrub shape might not always be evident and the internal features are not always clear, making a combined micro- and macro-classification a necessity.

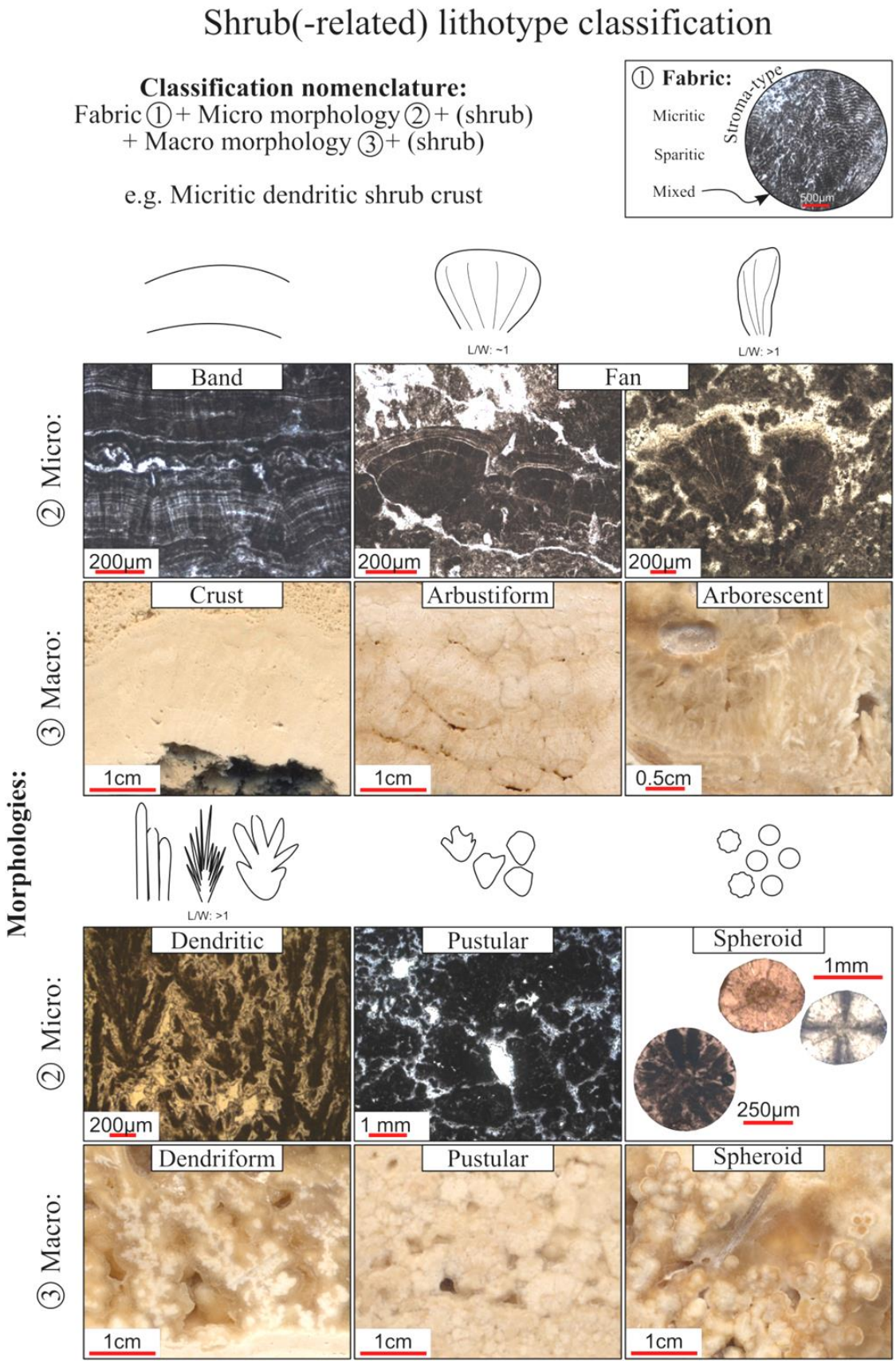

Figure 4: Classification of shrub-related morphologies. The pictures are taken as cross-cuts parallel to the growth direction of the structures. Micro-scale photos are taken under plain polarized light. Micro-scale classification is independent of the macro-scale classification.

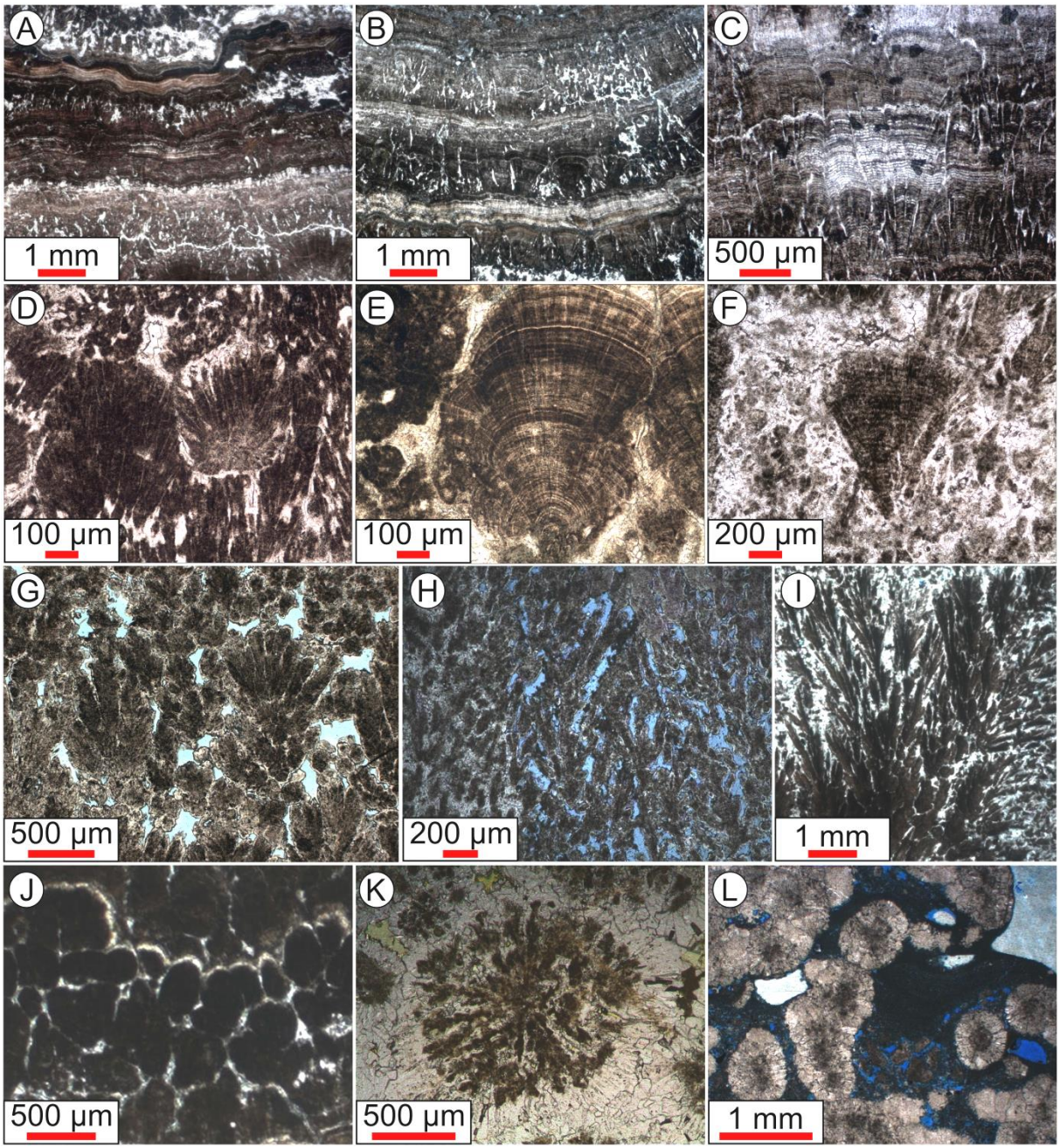

Figure 5: Most common micro-scale shrub-related morphologies observed in the Ballık-Belevi travertines. A), B) and C) show three examples of bands, consisting of alternating micrite and sparite lamina, with changing crystal size and varying amount of organic matter. Internally, locally, some branching structures can be observed. D), E) and F) are examples of fan shrubs. For (D) the branching nature towards the top of the shrub is clear. For (E) and (F) a clear micro-lamination can be observed. G), H) and I) illustrate the dendritic shrubs. (G) is an example of the dominantly micritic, knobby shrub type. The primary pores are preserved. (H) and particularly (J) show more straight branching, featherlike dendritic shrubs. Branching in (I) is dominantly crystallographic. Preferential dissolution of the sparite coating in (H) leads to very porous framework structures. J) Micritic pustular shrubs, with only a slight preferential orientation in their growth orientation, are here shown cemented together. (K) Spheroid rosette of radial dendritic shrubs. L) Amalgamated spheroids.

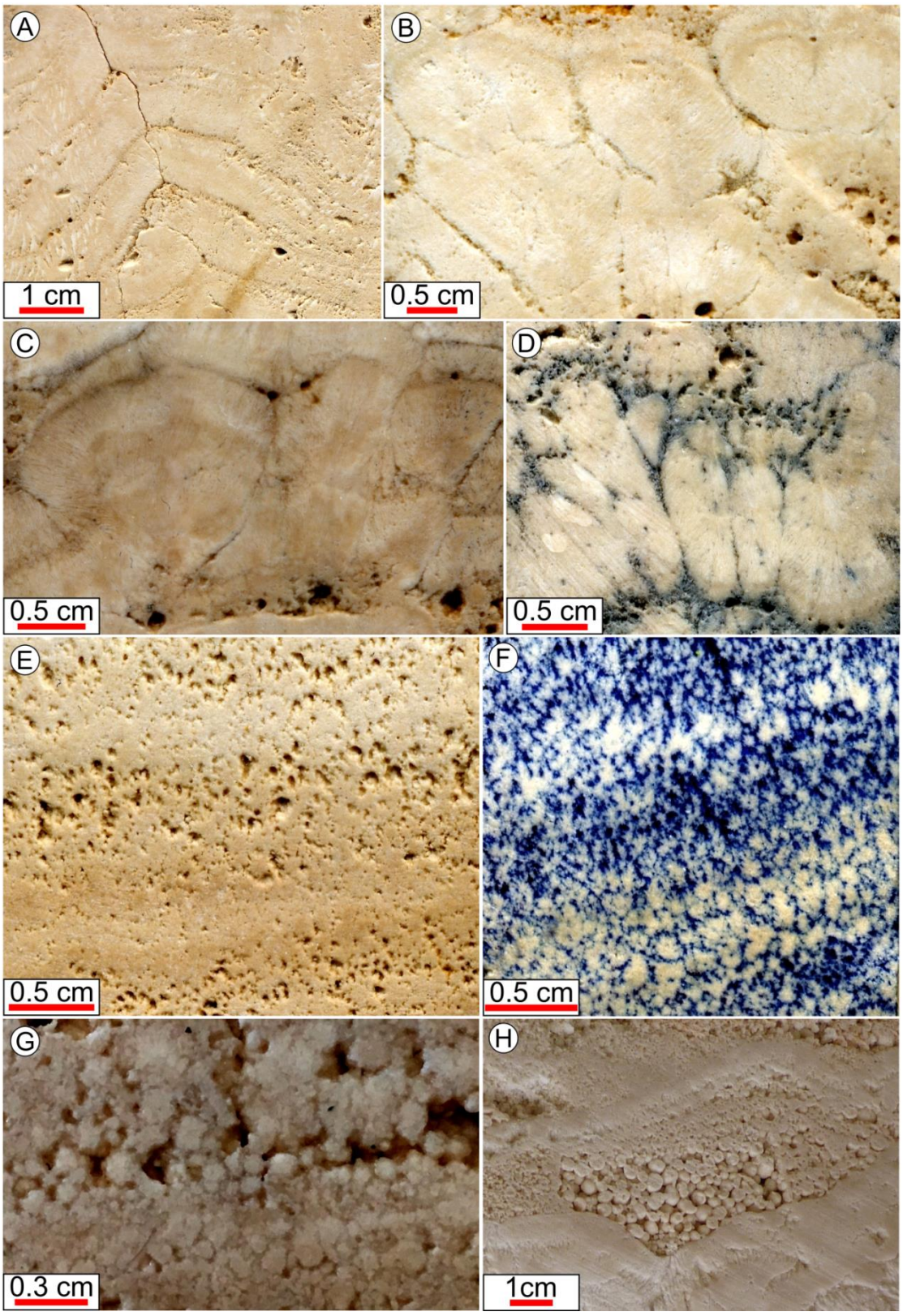

Figure 6: Most common macro-scale shrub-related lithotypes observed in the Ballık-Belevi travertines. A) (Dendritic shrub) Crust. Internal dendrites difficult to observe, except when weathered like in Figure 3B. B) and C) show arbustiform shrubs. D) Arborescent shrubs emphasised by (light) weathering and oxidation along the edges. E) and F) Dendriform shrubs. The dendriform morphologies become more apparent when impregnated like in (G). H) Sparite cemented pustular shrubs. I) Spheroids between dendritic crusts.

A.4.1.1 Micro-scale

On micro-scale, bands are distinguished from fan, dendritic and pustular shrubs and from spheroids.

The mm to cm-thick dense *bands* show a characteristic micro-scale banding, i.e. a millimetre to micrometre scale lamination (Figures 5A-C). The lamination is most apparent due to the difference in opacity/transparency. This is related to changes in crystal size, i.e. the alternation of micrite with sparite or bands of coarse to fine fibrous elongated calcite crystals, but could also be partially related to minor organic matter layering. Usually the bands are isopachous and have a wavy overall outline. This lithotype shows similarities to shrubs due to the merged fan-like, radial fibrous, calcite crystals that are readily recognisable by the undulose extinction patterns under crossed polarisers. They are considered under the shrub-related lithotype classification since they can form the interior of macro-scale shrubs. In addition, they occur vertically and horizontally lateral to the other shrub types, e.g. Figures 5B and C, where locally some branching within the bands can be observed. Crusts can also consist of an alternation of these micrite and (micro-)sparite bands. In this case, the lithotype does not show a shrub morphology on the macro-scale, nor on the micro-scale, and thus by definition cannot be considered as shrubs.

Fan shrubs (Figure 5D-F) consist of coarse, individual but often densely packed, fan-shaped, calcite (composite) crystals. They are most commonly composed of a mixed fabric of dominantly micrite and (micro-)sparite (Figure 5D-F) or they are purely fascicular calcite spars. The fan shrubs are 1 mm to 1 cm in height. Characteristic is their undulose extinction over the fans under crossed polarisers. A slight branching nature of their interior fabrics can sometimes be observed, as if the digits are squeezed together. Towards the tips of the shrub the branching becomes more apparent (e.g. Figure 5D). At the initiation point of the shrubs different kinds of nuclei are observed, e.g. plant relicts and spherulites. Wide and narrower fan shrubs occur together. The fan shrubs often occur as cement rims in a meteoric-vadose environment.

Dendritic shrubs (Figure 5G-I) show an internal upward branching growth pattern. They can be fully crystalline or consist of knob-shaped, dominantly micritic, aggregates. For micritic dendritic shrubs, it is the micrite fabric that shows a branching organization. Their outer morphology varies from a digitated glove of dominantly irregular micritic dendrites (e.g. Figure 5G) that can be surrounded by an isopachous micro-sparite calcite coating, to fibrous tightly, relatively straight, packed dendrites (e.g. Figure 5I). Particularly the latter type shows undulose extinction under crossed polarisers. The shrub morphology of crystalline dendritic shrubs can be marked by dark inclusions or micrite at the crystal edges. The calcite crystals are oriented with the shrub growth axis perpendicular to the substrate. The crystalline shrubs have a sweeping extinction under crossed polarisers. Cementation occurs locally for all fabric types of dendritic shrubs but it is difficult to distinguish these fabrics when they also are crystalline in nature. Length to width ratios of the dendritic shrubs in general fluctuate around two, with typical widths in the order of 500 to 1000 µm. A planar cut of dendritic shrubs will make them resemble pustular shrubs, so care should be taken to check the third dimension and to the orientation of the thin-section.

Pustular shrubs (Figures 4 and 5J) can sometimes look similar to spheroids. Their morphology, however, is not spherical and their surfaces vary from smooth to irregular. They show a preferential growth direction, but their length to width ratio (L/W) is close to 1. The pustular shrubs usually are smaller than 2 cm. Their fabric can be composed of pure micrite or pure sparite or a mixture of both. Micritic pustular shrubs with irregular shapes regularly possess a thrombolitic clotted micro-texture.

Spheroids (Figure 5K-J), which generally are smaller than 2 mm, occur as radial fibrous calcite spheres or as micritic rosettes. The rosettes can be considered as radial dendrites or radial shrubs (Figure 5K). The radial fibrous spheres (Figure 5L) do not present a shrub morphology on micro-scale, nor on macro-scale. They occur, however, associated with different types of shrubs. Next to the dispersed, isolated or amalgamated occurrence in the rock, spheroids also can occur as shrub nuclei. The spheroids also can show very similar fabrics to the shrubs, but in the former case, they are always radially organized. Spheroids usually

grew around a nucleus, which can consist of a micritic core or any kind of grain. The spheres sometimes show a concentric microscopic lamination and have sharp or lobate rims. They can consist of homogeneous micrite, bladed or fibrous amalgamated calcite crystals, or sparite coated micritic petals. Independent of the fabrics, a typical extinction in sectors or as an undulose cross is observed under crossed polarisers. Crystalline spheroids often show small micrite inclusions.

All of the here reported shrub-related lithotypes can show a pronounced micro-lamination, caused by the alternation of almost isopachous micrite and micro-sparite laminae (e.g. Figure 5C, E and F). This characteristic can be stressed by adding the adjective *"stroma"* (from Greek meaning "layer(ed)") to the classification nomenclature (Figure 4). The micritic laminae tend to be slightly more associated with organic material. TOC values, however, are low (<0.35%). For the bands the thin lamination can be crinkly, giving them a vague shrub/fan-like morphology, even when observed under parallel polarisers (Figure 5B and C). To emphasize the fabrics of the shrub morphology type, terms like "micritic" or "sparitic" can be added to the classification nomenclature (example in Figure 4).

A.4.1.2 Macro-scale

The shrub morphologies observed on micro-scale are often not evident on macro-scale. In addition, similar micro-morphologies can have a different macro-appearance and vice versa. Therefore, the overall macroscopic morphology is classified independently from the microstructures. The macro-classification types can then be combined with terminology of the micro-classification, giving a more precise and complete description (see Figure 4). Additional examples of the macro-scale shrub morphologies are given in Figure 6. Weathering, etching and impregnation of the sample can help to emphasize the internal and external structures.

Macroscopically, crusts are distinguished from arborescent, arbustiform, dendriform, pustular shrubs and spheroids. *Crusts* (Figure 6A) consist of thickly laminated to thinly bedded deposits of densely packed shrubs. The crusts can correspond to the macro-scale appearance of bands, densely packed fan, dendritic and pustular shrubs. They can be made of purely sparite calcite crystals or show a millimetre scale alternation of micrite with sparite. Shrub growth is perpendicular to the depositional surface. Due to weathering, or higher shrub spacing, their individual morphology on macro-scale becomes more apparent. In line with Terra et al. (2010), *arborescent* and *dendriform shrubs* are differentiated from *arbustiform shrubs* based on their L/W. Arbustiform shrubs (Figure 6B and C) have a length to width ratio (L/W) of ~1. Arborescent and dendriform have a L/W >1. Arborescent shrubs (Figure 6D) are elongated and fan-shaped (on macro-scale). Their top often shows some branching. Dendriform shrubs, in contrast, show an elongated branching over their whole structure (Figure 1 and 6E-F). In addition to Terra et al. (2010), also *pustular shrubs* are differentiated. Pustular shrubs form around a nucleus and are rounded. In contrast to spheroids, they also show a preferential growth orientation, and often a more variable size (compare Figure 6G with 6H).

The different morphology types are observed in close associations, making these rocks highly heterogeneous on different scales, from fabric as well as pore network point of view. Arborescent, arbustiform, dendriform and pustular macro-shrubs can on micro-scale consist of fan-like, dendritic or pustular micro-shrubs. It should be stressed that the macroscopic classification is independent of the microscopic classification, for which pustular shrubs and spheroids can be considered an exception. On macro-scale the latter are often difficult to distinguish one from another. On micro-scale the distinction is evident.

A.4.2 Pore type classification

Shrubs are associated with typical pore types (Figure 7), schematically represented in Figure 7A. The first pore type corresponds to the *intershrub growth framework porosity* (Figure 7A-C, number 1), that exists between the shrubs. A second type of growth framework porosity is observed between the shrub digits or branches, and is hence referred to as *interdigit growth framework porosity* (Figure 7A and D, number 2). The pore size for the growth framework types depends on the shrub size, e.g. since larger shrubs can simply give rise to larger intershrub

growth framework pores. Intershrub growth framework pores can thus range from sub-millimetre to centimetre scale. Interdigit growth framework porosity will be slightly smaller related to the size of the branches. Commonly, however, they are below millimetre scale. Both growth framework pore types are oriented more or less perpendicular to the growth substrate, unless a good connection along the layer exists. In the latter case the growth framework pores of neighbouring shrubs will be connected, creating horizontal pores. *Interlaminar porosity* (Figure 7A and C, number 3) can be observed between different generations of shrub laminae. Interlaminar pores can reach a vertical diameter of up to 1/3rd of the shrub laminae, but most commonly are less than 1 millimetre high. Their longest diameter, however, is along the laminae and reaches up to centimetre scale, but commonly is about 3-10 times the vertical height. The *intrashrub growth framework porosity* (Figure 7A and E, number 4) is observed inside the shrub structure. Often it can be related to the stroma, i.e. micro-laminated, lithotypes, where dissolution is observed mainly related to micritic laminae. Intrashrub pore sizes are dominantly below 100 µm. For micritic shrubs, fluorescence microscopy of fluorescent resin impregnated samples and SEM reveal the presence of these *micropores*, here defined as pores smaller than the thin-section thickness, i.e. <30 µm (Figure 7A, F and G, number 5). When fabric selective decay of the organic substrate of the shrubs or plants between the shrubs takes place, they are referred to as *mouldic pores* (Figure 7A and H, number 6). This fabric selective decay results in pore morphologies with the shape and size of the former plants or constituents (Choquette and Pray, 1970; Lønøy, 2006), and can thus be very variable.

The manifestation of the pore types is dependent on the morphology of the shrubs. Dense crusts and bands seem practically non-porous. From the moment that individual morphologies, i.e. arborescent, arbustiform, dendriform (on micro-scale: fan and dendritic) or pustular shrubs occur, intershrub growth framework porosity appears. Spheroids analogously can present interspheroid porosity. Interdigit growth framework porosity is inherently related to branching structures. Fan shrubs, for example, will not display this pore type. Towards the center of the dendritic shrubs, digits are observed to be more tightly packed, while towards the sides and top of the shrubs interdigit growth framework porosity increases. Microporosity, intra-framework and mouldic porosity develop independently of the outer shrub morphology. Usually growth framework pore types are sparite reduced. Furthermore, minor dissolution is evident from the rounded edges of these sparites. Although these shrub associated pores can be differentiated according to type, they often are connected, forming a semi-continuous pore network.

Most of the shrubs from the Ballık-Belevi area on macro-scale appear as crusts or show arborescent and arbustiform patterns. The shrubs show a relatively tight packing, with low to moderate pore network connectivity. The presence of growth framework porosity gives rise to vertically elongated pores.

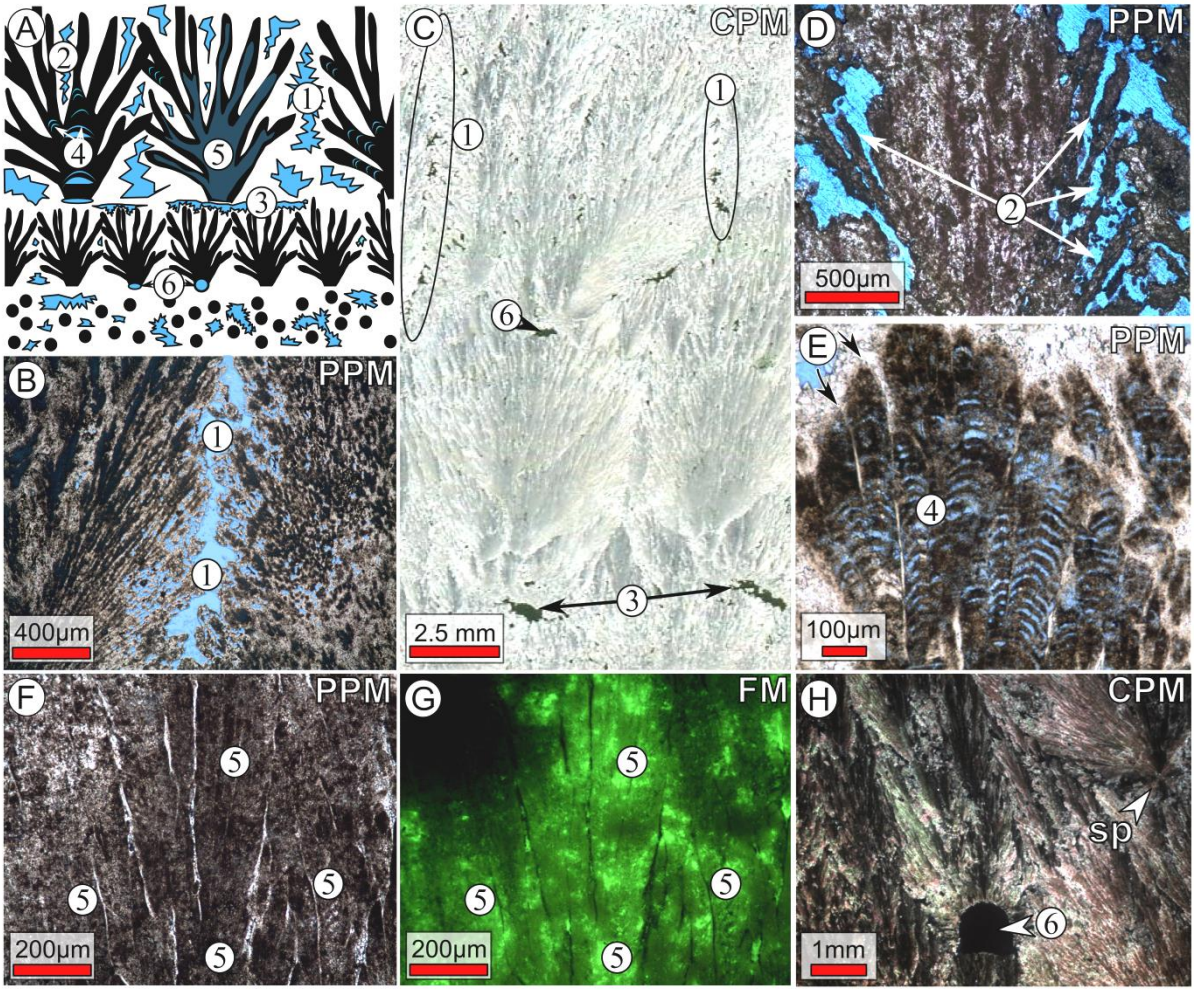

Figure 7: Pore types related to shrubs: (1) intershrub growth framework porosity, (2) interdigit growth framework porosity, (3) interlaminar porosity, (4) intrashrub growth framework porosity, (5) microporosity, (6) mouldic porosity. Microscopy images under parallel polarisers (PPM), crossed polarisers (CPM) and fluorescent light (FM). A) Schematic representation of the different pore types. B) Intershrub growth framework porosity, in this case emphasised by dissolution. C) Crossed polarised thin-section scan showing the intershrub growth framework porosity, interlaminar porosity and local mouldic porosity related to the shrubs. D) Interdigit growth framework porosity of dendritic shrubs. E) Intrashrub growth framework porosity related along micro-laminae. Arrows indicate the angular crystal terminations. F and G) PPM and FM image illustrating how fluorescent resin impregnated samples help to reveal micro-porosity under fluorescent light. H) Shrub growth nucleated from a plant stem that decayed and now is represented by a rounded mouldic pore. Spheroids can also serve as a nucleation point for shrub growth (sp).

A.4.2.1 Porosity-Permeability measurements

Different shrub types occur together in vertical and/or lateral arrangements on centimetre scale. It is therefore difficult, if not impossible, to take a plug that is made up of only one shrub type suited for helium porosimetry and specific gas permeability measurements. In addition, due to the occurrence of shrubs as thin laminae or as individual shrubs between other lithotypes, it is even impossible to take a full plug of one lithotype. Despite this drawback, 12 plugs with shrub dominance were selected (Table 1).

The porosity-permeability data are plotted in Figure 8. Effective porosities range between 3 and 15 % (Table 1). Permeabilities range from 0 to 15 mD, with one exception of 505 mD (Table 1). The low permeabilities on plug-scale are mainly related to the dense growth of the shrubs. In addition, sparite phases further strongly reduce the pore space. Horizontal plugs show a higher permeability, due to a higher connectivity parallel to the laminae with growth framework and/or interlaminar porosity in combination with lower shrub type heterogeneity. This is particularly pronounced in the sample with the lowest effective porosity (3.3 %), which shows a

considerable horizontal permeability of 14.7 mD. The highest porosity (14.9 %) and permeability (505 mD) are measured for a horizontal sample dominated by horizontally well-connected slightly dissolution enlarged growth framework porosity.

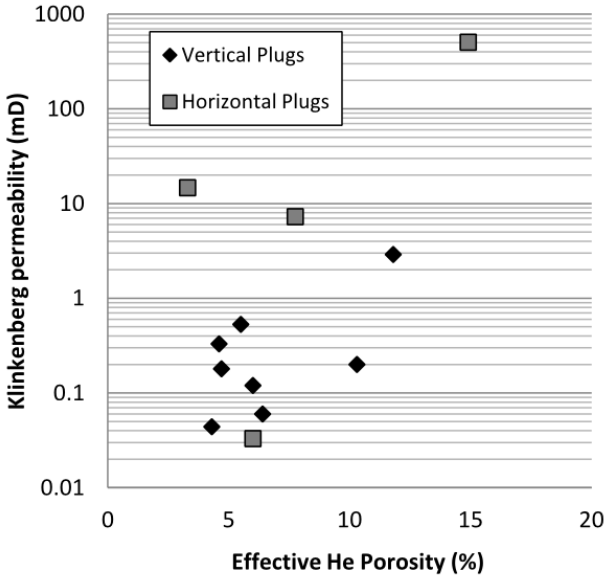

Figure 8: Porosity-Permeability plot of Ballık-Belevi shrub samples

	Sample	Macro-classification	Micro-classification	% Other lithotypes	Macroscopically dominant pore type	Plug Size (inch)	Ambient He Porosity (%)	Empirical Klinkenberg Corrected Gas Permeability (mD)	Grain Density (g/cm³)	Plug orientation
1	CK12HC001_1	Crust, Arborescent, Arbustiform	Dendritic	5	Mouldic	1.5	5.5	0.53	2.64	vertical
2	CK12HC001_2	Crust, Arborescent, Arbustiform	Dendritic	0	Mouldic	1.5	4.6	0.33	2.64	vertical
3	CK12HC002_1	Crust, Arborescent, Arbustiform	Dendritic	30	Intergranular	1.5	4.7	0.18	2.61	vertical
4	CK12HC002_2	Crust, Arborescent, Arbustiform	Dendritic	30	Intergranular	1.5	6	0.12	2.64	vertical
5	CK12HC002_3	Crust, Arborescent, Arbustiform	Dendritic	20	Dissolution vug in shrubs, intergranular	1.5	6.4	0.06	2.63	vertical
6	CA13ME013	Crust, Arborescent	Dendritic	5	Growth framework porosity	1.5	14.9	505	2.63	horizontal
7	CA13ME022	Crust, Arbustiform, Pustular	Dendritic, Pustular	65	Mouldic (dissolution enlarged)	1.5	7.75	7.27	2.64	horizontal
8	BE13ME002	Arbustiform, Pustular	Fan, dendritic	40	Mouldic	1	3.3	14.7	2.65	horizontal
9	BE13ME004	Crust	Fan, dendritic (+stroma)	0	Non-porous	1	6	0.03	2.66	horizontal
10	BE13ME007	Crust, Dendriform	Band, dendritic (+stroma)	<5	Small moulds, Growth framework	1	4.3	0.04	2.61	vertical
11	AL11HC063_1*	Crust, Dendriform	Dendritic	0	Growth framework porosity	1.5	11.8	2.9	2.28	vertical
12	AL11HC063_2**	Crust, Dendriform	Dendritic	0	Growth framework porosity	1.5	10.3	0.2	2.31	vertical

Table 1: Results from porosity-permeability analysis of 1 and 1.5 inch plugs. * & **: These results were previously reported accompanied by Vp-Vs data, respectively sample "AL15" and "AL16" (Soete et al., 2015).

A.4.3 Computed Tomography

In order to obtain 3D quantitative pore network data and to assess the connectivity in 3D, cores were scanned by means of medical CT. An example is given in Figure 9, in which dense dendritic shrub crust layers alternate with more porous dendriform shrubs. For this example, the 3D reconstructed images enable a clear observation of these two shrub lithotypes. In addition, related pore types can be distinguished. Figure 9 shows the intershrub growth framework porosity that has a preferential orientation and connection perpendicular to the layering. Interlaminar porosity can also be observed. Based on the developed 3D pore shape classification (Claes et al., 2016; Soete et al., 2015), the shape of these pores can be quantified, based on the projection of a spheroid projected inside the pores (Figure 10). The sample is dominated by cube, rod and cuboid growth framework pores and cube and platy interlaminar porosity. In Figure 9C, the pore network is labelled for connectivity. All connected pores have the same colour. The high colour variation illustrates the low pore-connectivity for the given resolution (0.3*0.3*0.5 mm). Pores below this resolution will not be taken into account. By applying micro-CT, the resolution challenge can be addressed. Multi-scale CT imaging, i.e. combining CT reconstructions at different resolutions enables an upscaling approach for porosity characterization by applying Multiple Point geo-Statistics (MPS, research in progress).

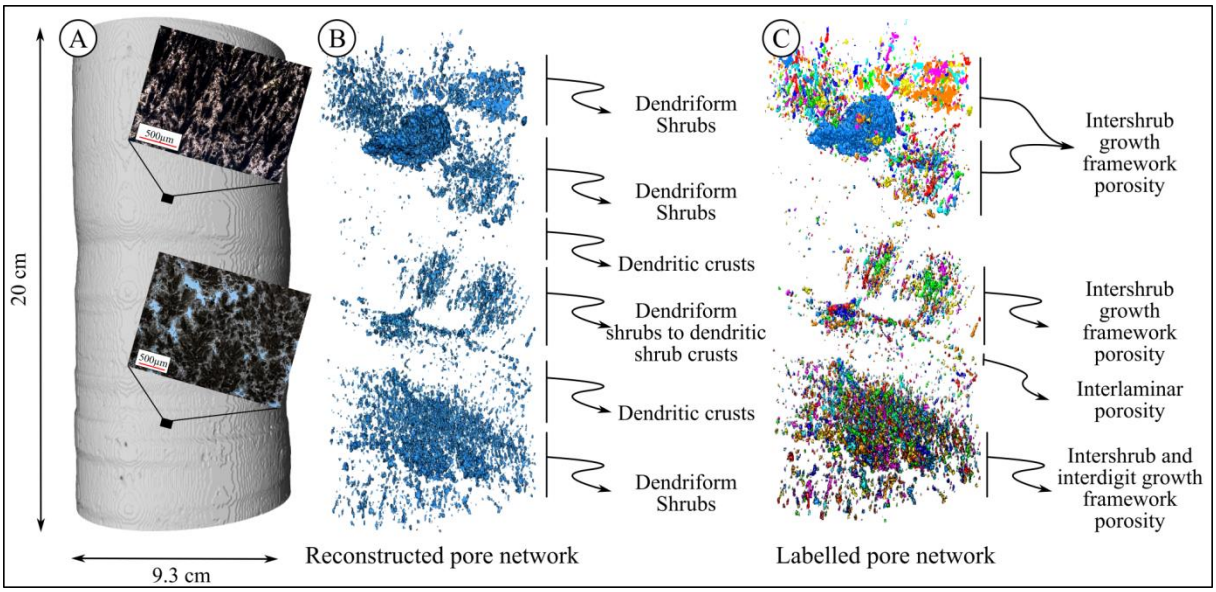

Figure 9: (A) Reconstructed Medical CT scan image of a shrub core, with the upper microscopy image showing micritic dendritic shrub crusts under parallel polars and the lower microscopy image showing micritic dendriform shrubs under parallel polars. (B) Reconstructed pore network. (C) Labelled pore network, in which connected pores are indicated in the same colour. Different pore types can be observed related to the shrub lithotypes. The crusts are characterized by an absence to very low occurrence of pores (on the resolution of the scan 0.3x0.3x0.5). Dendriform shrubs are associated with intershrub and interdigit growth framework porosity.

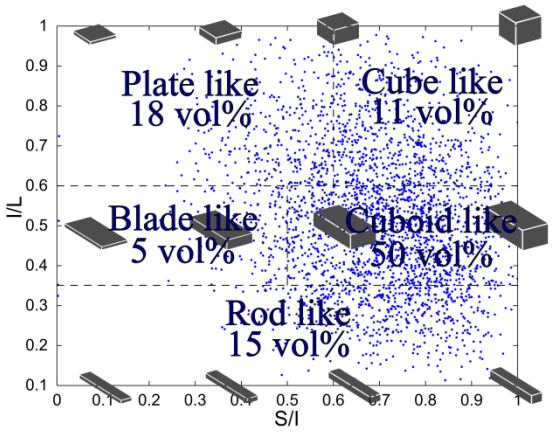

Figure 10: Pore-shape distribution plotted on I/L-S/I diagram adapted from Claes et al. (2016) and Soete et al. (2015) for the core example shown in Figure 8. S, I and L represent respectively the shortest, intermediate and longest axes of the ellipsoids fitted into the pores.

A.5 Discussion

A.5.1 Morphology and size

Due to the difficulties to recognise the internal features of macro-scale shrubs, and to the complexity of the shrub structures on different scales, it was necessary to add a separate micro-classification of the morphology types. The shrub facies can be strongly heterogeneous, with different shrub shapes and sizes both on macro- and micro-scale. In addition, the lateral and vertical spacing between the shrubs and the layer thickness varies strongly. In the Ballık-Belevi area, the crusts are the most common (~85 %), whereas the other types, especially the dendriform shrubs, are rarer. Oil-impregnation, clay coatings, and surface weathering/dissolution of crusts can make their interior morphologies more apparent (e.g. Figure 6D and F). Depending on the degree of dissolution, the primary morphologies can be extensively modified. An arborescent morphology, for example, can get a dendriform resemblance, illustrating how diagenesis could affect the morphology.

A.5.2 Fabrics and crystal sizes

The origin of shrub fabrics in continental carbonates is controversial (Chafetz et al., 1994; Freytet and Verrecchia, 1998; Brasier et al., 2011). Their primary mineralogy like almost all travertine most commonly consists of aragonite (e.g. Rodríguez-Berriguete et al., 2012) and/or calcite (e.g. Chafetz and Folk, 1984). Concerning crystal size, however, shrubs can precipitate as micrites, as sparites or as a mixture of both, depending on the physico-chemical environmental conditions (pH, temperature, saturation, pCO_2, Eh, ...) and the microbial communities involved in precipitation (Freytet and Verrecchia, 1998). The Extracellular Polymeric Substance (EPS) biofilm, for example, could result in the precipitation of micritic micro-peloidal structures and could serve as a substrate for physico-chemical precipitation of sparite as reported by Dupraz et al. (2004). Moreover, diagenesis can lead to both micritization and sparitisation. Chafetz et al. (1994) provided ghost structures as evidence of sparmicritization. Guo and Riding (1994) reported on recent and fossil travertines and saw a clear increase in dark micrite fabrics with age, pointing to sparmicritization. The original fabric can be completely converted from micritic or spar rhombohedrons to uniform micritic.

Based on the angular crystal terminations (e.g. Figure 7E, see arrows), in contrast to square stepped terminations which would point to former aragonite, it is concluded that the Ballık-Belevi calcite crystals preserved their original mineralogy (Ross, 1991). The frequent occurrence of micrite in the majority of the Ballık-Belevi travertines in combination with their undulose extinction under crossed polarisers (e.g. Figure 11), stimulated discussion on whether recrystallisation could overprint micritic centers, or whether micritisation could have altered the primary sparite fabric. Due to the small size of the calcite crystals, micritic shrub crystals were not expected to display the observed undulose extinctions (Figure 11; Movie 1). For some samples, it can be argued that “extinction” will be due to the presence of (opaque) organic matter. TOC values, however are low (<0.35% and usually below 0.1%) and based on petrographic observation, it is mainly the crystal size that results in the darker appearance of micrite. The common undulose extinction of the micrite crystals (Movie 1) and over both micrite and sparite reveals a crystal (re)organization on a larger crystal scale (> 4µm and often more than several 100’s of µm). The extinction over both sparite and micrite is even

clearer for sparite dominated fabrics (Figure 12). They could be referred to as a kind of ghost structures (similar to Boggs, 2009), since it becomes only clear under crossed polarisers that they are part of larger structures (e.g. Figure 12E-F). The undulose extinction on a scale larger than the micrite crystals, even over both micrite and sparite, and the ghost structures cannot be explained only by the entrapment of micrite, or organic matter and subsequent micritisation, in sparitic overgrowths. Micritisation alone would remove the optical continuity within the micrite zones of the crystals. Therefore, the majority of the shrubs were deposited with a general crystalline sparite fabric, subsequently micritized and later again recrystallized (illustrated in Figure 13). Shrubs with a clear predominance of sparite were only minorly micritized (e.g. Figure 11E-F).

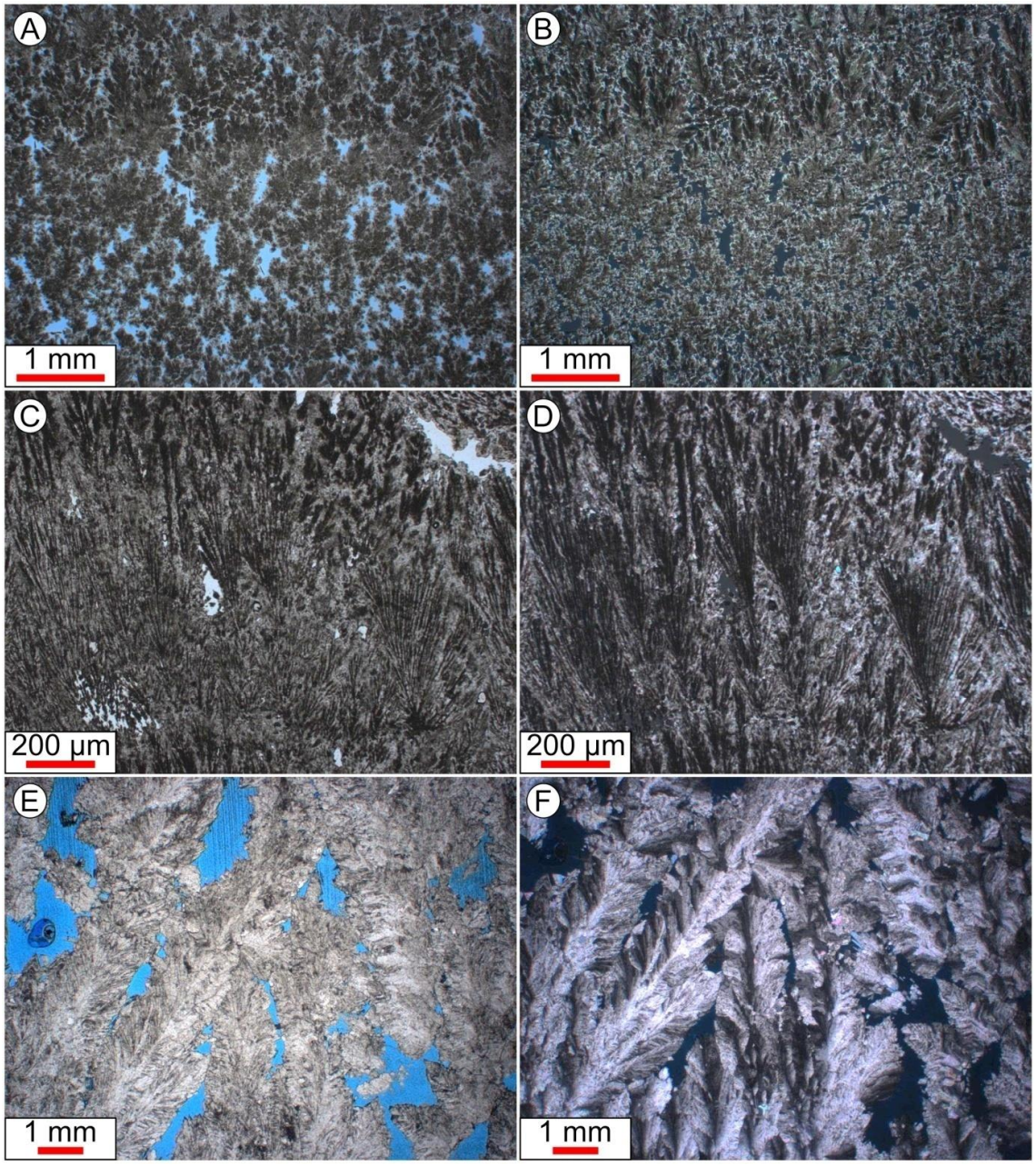

Figure 11: Plain Polarized Light (A, C and E) and Crossed Polarized Light (B, D and F) images of typical shrub fabric occurrences in the Ballık-Belevi travertines illustrating their extinction patterns. A) and B) show knobby, clotted micrite dominated dendritic shrubs. C) and D) show straight branching, featherlike dendritic shrubs, observed related to crusts. E) and F) show almost purely sparitic shrubs with micrite inclusions.

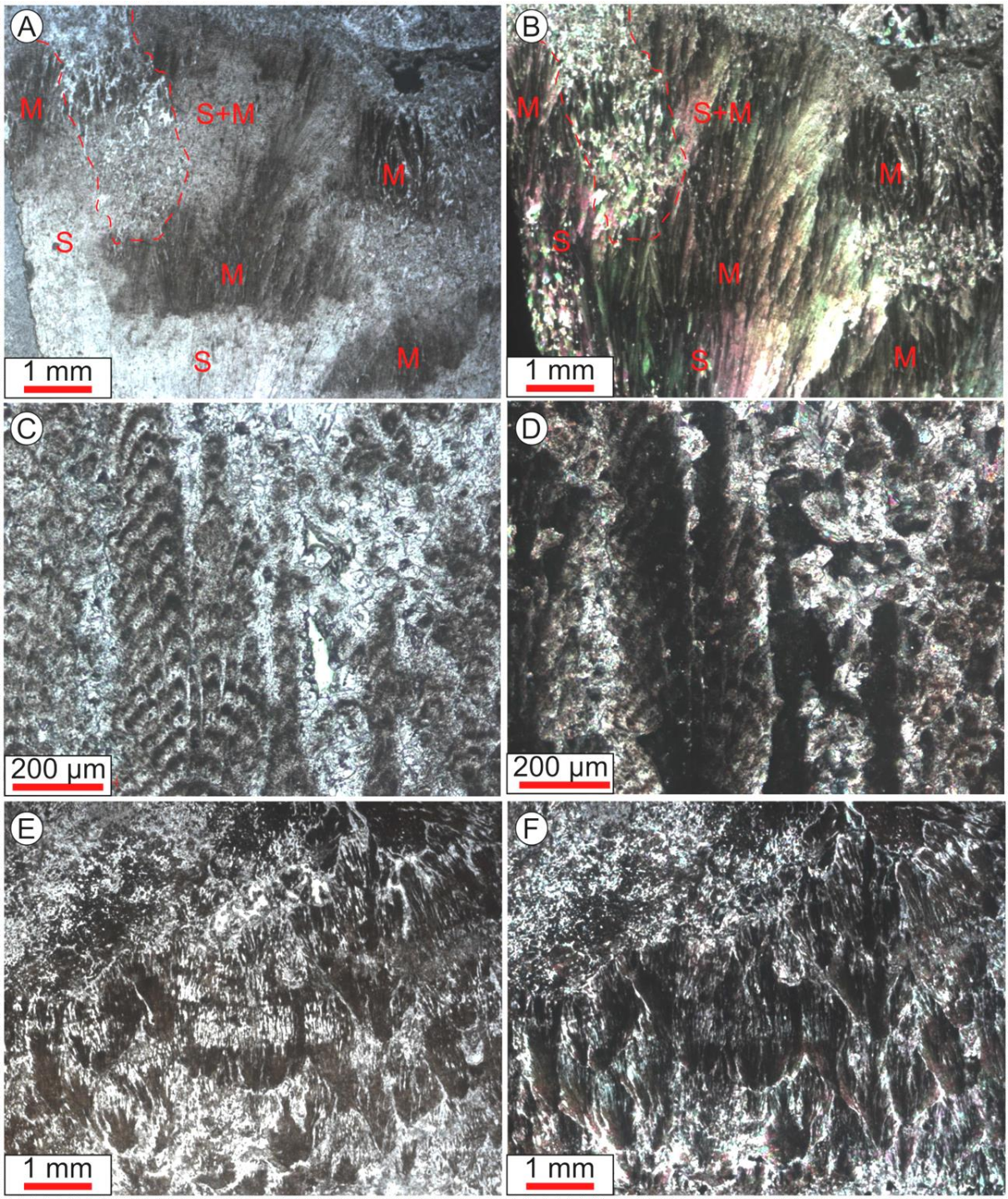

Figure 12: Continuous extinction patterns over micrite and sparite in sparite dominated fabrics. A), C) and E): Images taken under Plain Polarized Light conditions. B), D) and F): The equivalents of (A), (C) and (E) under Crossed Polarized Light conditions. M = Micrite. S = Sparite. The images under Crossed Polarized Light reveal that the micritic structures are part of larger structures.

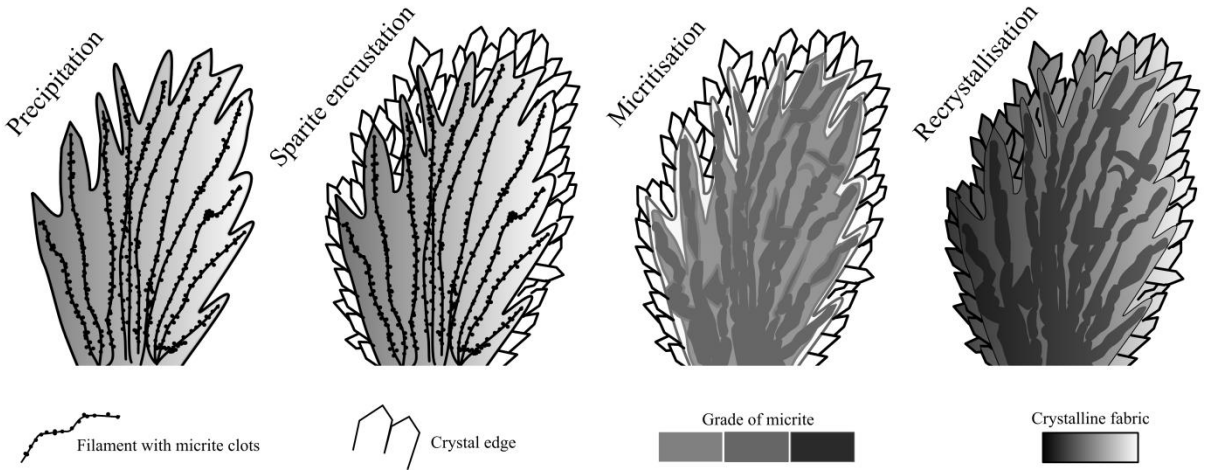

Figure 13: Genesis of the Turkish micritic dendritic shrubs. (A) Sparite crystalline shrub precipitation around a dendritic, organic-rich, filamentous framework (Claes et al., 2015); (B) Syngenetic (micro-)sparite encrustation around the shrub crystals; (C) Early micritisation related to the decay of the organic matter of the dendritic framework; (D) Recrystallisation, overprinting the previous fabrics.

A.5.3 Process-dependent shrub types

Many factors, from sedimentary conditions to diagenetic modifiers, influence the shrub morphologies and their fabrics. The primary controls are related to the dominant processes during precipitation, hence the actual discussion on precipitation rate and biotic versus abiotic precipitation. For continental carbonates this more concretely considers microbial mediation versus evaporation and degassing. Fast precipitation is considered to result in an abiotic dominance, while 'less fast' precipitation allows microbes to have a higher influence or even control on the fabrics (Dupraz et al., 2009). Shrub structures related to abiotic conditions are reported by Pentecost (1990), Jones and Renaut (1995, 2008) and Jones et al. (2000, 2005). However, shrubs whose growth shape show a clear biotic influence are reported by Chafetz and Folk (1984), Chafetz and Guidry (1999) and Guo and Riding (1994). Chafetz and Guidry (1999) made a subdivision between "bacterial shrubs" in which bacteria played a dominant part in controlling the shrub morphology, and "crystal shrubs" that formed at sites of high saturation where shrub morphology was dominated by crystallographic effects.

Often Ballık-Belevi shrub crusts, as well as dendriform, arborescent and arbustiform shrubs are found in sloping facies, related to fast, turbulence-induced, CO_2 degassing and precipitation. These shrub types correspond to thin water film formed "abiotic" shrubs that most closely resemble the Pre-Salt shrub-like calcites (Wright and Barnett, 2015). However, it is the internal fabric organization of the shrubs and the presence of particular bio-related structures that are diagnostic for a biotic influence. Non-crystallographic branching (e.g. Figure 14), alternation of micro-sparite and micrite micro-laminae (i.e. stroma-type, e.g. Figures 5E and 12C-D), clotted fabrics (e.g. Figures 5G and 14) and filaments or bacteriform shapes (Claes et al., 2015) are observed in the Ballık-Belevi shrubs. The ensemble of these features suggests that their formation was not always purely abiotic. In literature, micro-rhythmic laminae (of the stroma-shrubs) are reported to represent daily cycles (Chafetz and Folk, 1984; Folk et al., 1985; Okumura et al., 2011). Dupraz et al. (2009) explained the formation of micritic laminae by microbial mediation. Photosynthesis removed CO_2 from the system and EPS inhibited calcite precipitation, resulting in rods (Dupraz et al., 2004; Okumura et al., 2011). The micro-sparitic laminae can be caused by microbes changing local conditions, such as alkalinity and supersaturation (Dupraz et al., 2009). Even though, precipitation is thus likely dominantly controlled by supersaturation and degassing, some biotic influence is considered for the Ballık-Belevi shrub types. A higher vertical ion-diffusion during the biologically-influenced mineralization (Dupraz et al., 2009), which is characteristic for fast precipitation rates, will result in fascicular aggregates.

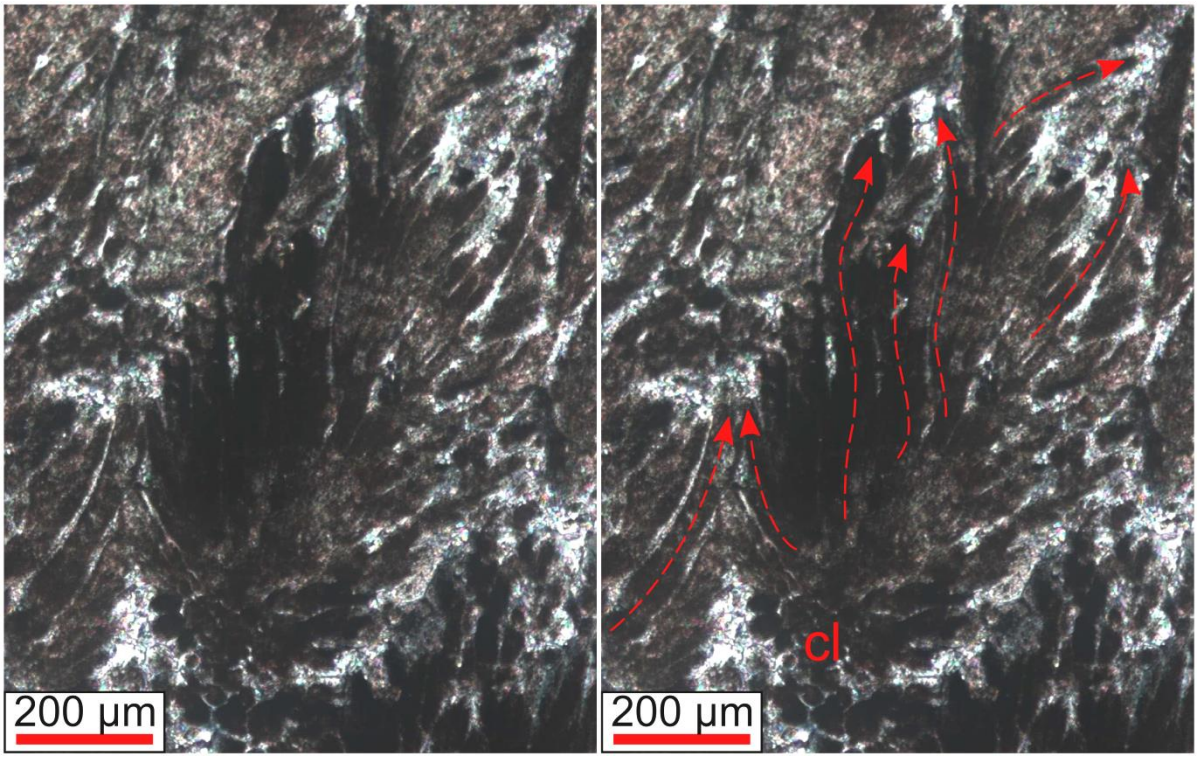

Figure 14: Pronounced non-crystallographic branching of a shrub structure, emphasised by the red arrows in the right image. At the base of the shrub clotted fabrics (Cl) can be observed.

Occurrences of larger shrubs (up to 3 cm), inside Ballık-Belevi travertine caves (Figure 3D-F), yield higher porosities (not included in the porosity-permeability data) and macro-scale branching. They represent the tallest shrub structures described from this area. These crystalline dendriform cave shrubs are very local and restricted to the bottom of primary caves. However, their restricted presence perhaps contains some valuable information. The primary caves provided unique micro-environments, unsuitable for macrophyte or bryophyte growth, where micro-organisms could have a higher influence on the precipitation. Evaporation should have been the main process for CO_2 degassing. El Desouky et al. (2015) reported a more saline hot fluid being responsible for the late dark cements that coat fractures and faults but sometimes also caves. Possibly, these more saline hot fluids that formed static pools at cave bottoms, provided a harsh environment scenario, that should be taken into consideration for the carbonate reservoir formation conditions. The maximal water depth should have been slightly deeper than the largest shrub.

Pustular fabrics are reported related to biotic action when the excess of fine carbonate particles discourages structured growth (Jahnert and Collins, 2013). In the case of excessive fine carbonate, however, the pustular fabrics become embedded in micrite-rich fabrics, in contrast to the observed Ballık-Belevi examples. Pustular fabrics also can grow abiotically related to evaporative conditions or CO_2 degassing by high flux flow (Jahnert and Collins, 2013). The morphology will be limited by the water depth. In analogy to Dias (1998), pustular or arbustiform shrubs could be the initial growth stage of dendriform or arborescent types that due to local physical-chemical-biological conditions were not able to fully develop their branches.

Spheroids can form in several settings and under several conditions, from a spring to lake or reef setting or they can be the result of pedogenesis or speleothem development. They are mentioned to occur organically mediated, within an EPS matrix with or without bacterial cells present (Dupraz et al., 2009). Abiotic formation processes are also reported, where supersaturation with respect to Mg^{2+} can produce spherulitic morphologies (Fernández-Díaz et al., 1996). Spheroids can also be formed inside the sediment (Rainey and Jones, 2009). In the Ballık-Belevi case, spheroids occur as shrub

nuclei (e.g. Figure 7H sp), developing into arbustiform and arborescent shrubs. This can be explained by the increase in water saturation with respect to calcium and the increase in CO_2 degassing rates. Alternatively, this can be explained by the availability of growth space. Spheroids, for example, could have formed inside a matrix, while shrubs formed at the sediment-water interface. Spheroids also occur as amalgamated cement structures, attributed here to be formed in the later stages of drying pools where evaporation is the main process controlling calcite precipitation. Calcite nucleation driven by evaporation within gels has been reported to result in spherulitic textures (Wright and Barnett, 2015).

A.5.4 Petrophysical properties

Unless the depositional fabric is destroyed, petrophysical characteristics depend on the building blocks and the corresponding growth fabrics (Ahr et al., 2011). The limited diagenesis of the Ballık-Belevi travertines (Claes et al., 2015) allowed them to preserve, to a major extent, the primary porosity and permeability characteristics. Consequently, in the shrub facies, it should be the type of shrub with its associated pore structure that will determine the petrophysical characteristics. The presented shrub classification incorporates their fabric and, particularly important from a petrophysical point of view, their size, morphology and packing. The size, size sorting and packing of the shrub structures are the main controls on porosity and permeability (Rezende and Pope, 2015). The shrub morphology has an impact on the porosity, as illustrated by the associated pore type classification, but will also influence the permeability of the sample. More complex pore networks will result in lower permeabilities. From this point of view, it is also clear that the occurrence of multiple shrub types in one sample will have a negative influence on the permeability. The presented classification incorporates the complexity of the overall shrub structures. For shrub types of equal size, excluding the presence of matrix or diagenetic modifiers, the reservoir quality should enhance from crust to arbustiform and arborescent, to dendriform and pustular shrubs.

The Ballık-Belevi shrubs generally have relatively low porosities and permeabilities, because of the high occurrence of crusts, arbustiform and arborescent shrubs with a dense shrub packing. Consequently, they will rather act as local barriers when intercalated with other shrub morphologies. This is in contrast with e.g. travertines from Tivoli (Chafetz et al., 1984) that are dominated by dendriform shrubs. Dendriform structures have better porosities in comparison to arborescent and arbustiform structures, due to their interdigit growth framework porosity. Pustular shrubs and spheroids, as a main constituent, without matrix, would have the best petrophysical characteristics, similar to other detrital rocks (e.g. oolitic carbonates). For the Ballık-Belevi shrubs, however, the latter usually occur in a micrite matrix and porosity is further reduced by sparite overgrowths.

For most of the shrubs in the Ballık-Belevi area, the diagenesis did not have a significant impact and the depositional network was maintained. Nonetheless, the highest porosities and permeabilities are reported related to dissolution that slightly enlarged the growth framework pores. In addition, the intrashrub growth framework porosity is multi-genetic. Thin organic-rich laminae are, for example, prone to decay, which leads to pore-creation. Associated with the decay of organic matter is also the formation of organic acids (Chafetz and Folk, 1984). These can create dissolution enhanced porosity. Decay and dissolution on smaller scale can also explain the creation of microporosity related to the micritic shrubs. The importance of microporosity and quantification approach are discussed by De Boever et al. (2016b).

A.6 Conclusions

The following conclusions can be drawn:

- A new shrub-related lithotype classification, considering the different scales as well as the different fabrics and morphologies, is presented. Within this classification macro-structures are combined with micro-scale characteristics, providing a more precise and complete description. To emphasize the fabrics of the shrub morphology type, terms like “micritic”, “sparitic” and “mixed fabric” can be added to the classification nomenclature.

- Shrubs largely preserved their original calcite mineralogy. In general the Ballık-Belevi travertines show a high presence of micrite fabrics.

- Depositional pore types were largely preserved and control the porosity-permeability properties of the shrubs. The diagenetic overprint is minor. Growth framework and interlaminar porosity result in a strong anisotropy in the permeability. The highest porosity and permeability are related to horizontal samples with well-connected, slightly dissolution enhanced, growth framework porosity.

- Horizontal permeabilities in general are higher than vertical permeabilities. In addition, moulds and microporosity have been observed.

- Shrubs from the Ballık-Belevi are complex from a fabric as well as pore network point of view on macro- and micro-scale. The presented pore type classification is applicable to shrub reservoirs worldwide. From both points of view, the Ballık-Belevi travertines can be used to develop and optimize a petrophysical characterization methodology following an upscaling philosophy.

A.7 References

Ahr, W. M., E. A. Mancini, and W. C. Parcell, 2011, Pore Characteristics in Microbial Carbonate Reservoirs: Search and discovery, no. Article #30167.

Alabi, G., R. Kasten, V. Chitale, S. Yadavalli, and L. Piccoli, 2014, The value of petrophysical measurements across multiple scales. A lacustrine carbonate example from Campos Basin, Brazil, *in* SPWLA 55th Annual Logging Symposium: p. 1–12.

Alves, I., A. Aragão, B. Bastos, J. Falcão, and E. Fartes, 2009, Pre-Salt Santos Basin — Well Construction Learning Curve Acceleration, *in* Offshore Technology Conference: p. 1–12.

Bargar, K. E., 1978, Geology and thermal history of Mammoth Hot Springs, Yellowstone National Park, Wyoming: U.S. Geological Survey Bulletin, v. 1444, p. 1–55.

Beasley, C. J., J. C. Fiduk, E. Bize, A. Boyd, M. Frydman, A. Zerilli, J. R. Dribus, J. L. P. Moreira, and A. C. Capeleiro Pinto, 2010, Brazil's Presalt Play: Oilfield Review, v. 22, no. 3, p. 28–37.

De Boever, E., A. Foubert, B. Lopez, R. Swennen, C. Jaworowski, M. Özkul, and A. Virgone, 2016, Comparative study of the Pleistocene Cakmak Quarry (Denizli Basin, Turkey) and Modern Mammoth Hot Springs deposits (Yellowstone National Park, USA): Towards an integrated Travertine Depositional Facies Model? Quaternary International, doi:10.1016/j.quaint.2016.09.011.

De Boever, E., A. Foubert, D. Oligschlaeger, S. Claes, J. Soete, P. Bertier, M. Özkul, A. Virgone, and R. Swennen, 2016, Multiscale approach to (micro)porosity quantification in continental spring carbonate facies: Case study from the Cakmak quarry (Denizli, Turkey): Geochemistry, Geophysics, Geosystems, doi:10.1002/2016GC006382.

Boggs, S., 2009, Petrology of sedimentary rocks.

Borsato, R., W. Jones, J. Greenhalgh, M. Martin, R. Roberson, C. Fontes, P. Markwick, and A. Quallington, 2012, South Atlantic Conjugate Margin: An Exploration Strategy: First Break, v. 30, no. December, p. 79–84.

Brasier, A. T., J. E. Andrews, and A. C. Kendall, 2011, Diagenesis or dire genesis? The origin of columnar spar in tufa stromatolites of central Greece and the role of chironomid larvae: Sedimentology, v. 58, no. 5, p. 1283–1302, doi:10.1111/j.1365-3091.2010.01208.x.

Buckley, J. P., C. Elders, and J. Mann, 2013, Carbonate Buildups in the Santos Basin, Offshore Brazil, *in* Microbial Carbonates in Space and Time: Implications for Global Exploration and Production: The Geological Society of London, p. 37–38.

Carminatti, M., J. L. Dias, and B. Wolff, 2009, From turbidites to carbonates: breaking paradigms in deep waters: Offshore Technology Conference, no. May, p. 4–7.

Carminatti, M., B. Wolff, and L. Gamboa, 2008, New exploratory frontiers in Brazil, *in*

19th World Petroleum Congress: World Petroleum Council.

Chafetz, H., and R. Folk, 1984, Travertines: depositional morphology and the bacterially constructed constituents: Journal of Sedimentary Petrology, v. 54, no. 1, p. 0289–0316.

Chafetz, H. S., and S. A. Guidry, 1999, Bacterial shrubs, crystal shrubs, and ray-crystal shrubs: bacterial vs. abiotic precipitation: Sedimentary Geology, v. 126, p. 57–74.

Chafetz, H. S., D. Srdoc, and N. Horvatincic, 1994, Early Diagenesis of Plitvice Lakes Waterfall and Barrier Treavertine Deposits: Géographie physique et Quaternaire, v. 48, no. 3, p. 247, doi:10.7202/033006ar.

Choquette, P. W., and L. C. Pray, 1970, Geologic nomenclature and classification of porosity in sedimentary carbonates: AAPG Bulletin, v. 54, no. 2, p. 207–244.

Christie, A. O., and G. D. Floodgate, 1966, Formation of microtrees on surfaces submerged by the sea: Science, v. 212, p. 308–310.

Claes, H., M. Degros, J. Soete, S. Claes, S. Kele, A. Mindszenty, Á. Török, H. El Desouky, F. Vanhaecke, and R. Swennen, 2016, Geobody architecture, genesis and petrophysical characteristics of the Budakalász travertines, Buda Hills (Hungary): Quaternary International, doi:10.1016/j.quaint.2016.09.007.

Claes, S., J. Soete, V. Cnudde, and R. Swennen, n.d., A 3D classification for mathematical pore shape description in complex carbonate reservoir rocks: Mathematical Geology.

Claes, H., J. Soete, K. Van Noten, H. El Desouky, M. Marques Erthal, F. Vanhaecke, M. Özkul, and R. Swennen, 2015, Sedimentology, three-dimensional geobody reconstruction and carbon dioxide origin of Pleistocene travertine deposits in the Ballık area (south-west Turkey): Sedimentology, v. 62, no. 5, p. 1408–1445, doi:10.1111/sed.12188.

El Desouky, H., J. Soete, H. Claes, M. Özkul, F. Vanhaecke, and R. Swennen, 2015, Novel applications of fluid inclusions and isotope geochemistry in unravelling the genesis of fossil travertine systems: Sedimentology, v. 62, p. 27–56, doi:10.1111/sed.12137.

Dias, J. L., 1998, Analise sedimentológica e estratigráfica do Andar Aptiano em parte da margem leste do Brasil e no platô das Malvinas - consideraçoes sobre as primeiras incursões e ingressões marinhas do Oceano Atlântico sul Meridional: Universidade federal do Rio Grande Do Sul, 399 p.

Dias, J. L., 2005, Tectônica, estratigrafia e sedimentação no Andar Aptiano da margem leste brasileira: Boletim de Geociências da PETROBRAS, v. 13, no. nov. 2004/maio 2005, p. 7–25.

Dorobek, S., L. Piccoli, B. Coffey, and A. Adams, 2012, Carbonate Rock-Forming Processes in the Pre-salt "Sag" Successions of Campos Basin, Offshore Brazil: Evidence for Seasonal, Dominantly Abiotic Carbonate Precipitation, Substrate Controls, and Broader Geologic Implications, *in* AAPG Hedberg Conference "Microbial carbonate reservoir characterization": p. 4–5.

Dupraz, S., M. Parmentier, B. Ménez, and F. Guyot, 2009, Experimental and numerical modeling of bacterially induced pH increase and calcite precipitation in saline aquifers: Chemical Geology, v. 265, no. 1–2, p. 44–53, doi:10.1016/j.chemgeo.2009.05.003.

Dupraz, C., R. P. Reid, O. Braissant, A. W. Decho, R. S. Norman, and P. T. Visscher, 2009, Processes of carbonate precipitation in modern microbial mats: Earth-Science Reviews, v. 96, no. 3, p. 141–162, doi:10.1016/j.earscirev.2008.10.005.

Dupraz, C., P. T. Visscher, L. K. Baumgartner, and R. P. Reid, 2004, Microbe-mineral interactions: early carbonate precipitation in a hypersaline lake (Eleuthera Island, Bahamas): Sedimentology, v. 51, no. 4, p. 745–765, doi:10.1111/j.1365-3091.2004.00649.x.

Fernández-Díaz, L., A. Putnis, M. Prieto, and C. V. Putnis, 1996, The Role of Magnesium in the Crystallization of Calcite and Aragonite in a Porous Medium: SEPM Journal of Sedimentary Research, v. Vol. 66, no. 3, p. 482–491, doi:10.1306/D4268388-2B26-11D7-

8648000102C1865D.

De Filippis, L., C. Faccenna, A. Billi, E. Anzalone, M. Brilli, M. Ozkul, M. Soligo, P. Tuccimei, and I. M. Villa, 2012, Growth of fissure ridge travertines from geothermal springs of Denizli Basin, western Turkey: Geological Society of America Bulletin, v. 124, no. 9–10, p. 1629–1645, doi:10.1130/B30606.1.

Folk, R. L., 1959, Practical petrographic classification of limestones: American Association of Petroleum Geologists Bulletin, v. 43, p. 1–38.

Folk, R. L., H. S. Chafetz, and P. A. Tiezzi, 1985, Bizarre forms of depositional and diagenetic calcite in hot-spring travertines, central Italy: The Society of Economic Paleontologists and Mineralogists, p. 349–369.

Freytet, P., and E. P. Verrecchia, 1998, Freshwater organisms that build stromatolites: a synopsis of biocrystallization by prokaryotic and eukaryotic algae: Sedimentology, doi:10.1046/j.1365-3091.1998.00155.x.

Friedman, G. M., and J. E. Sanders, 1978, Principles of Sedimentology: New York, Wiley, 792 p.

Guo, L., and R. Riding, 1994, Origin and diagenesis of Quaternary travertine shrub fabrics, Rapolano Terme, central Italy: Sedimentology, v. 41, p. 499–520.

Jahnert, R. J., and L. B. Collins, 2013, Controls on microbial activity and tidal flat evolution in Shark Bay, Western Australia: Sedimentology, v. 60, no. 4, p. 1071–1099, doi:10.1111/sed.12023.

Jones, B., and R. W. Renaut, 2008, Cyclic development of large, complex, calcite dendrite crystals in the Clinton travertine, Interior British Columbia, Canada: Sedimentary Geology, v. 203, no. 1–2, p. 17–35, doi:10.1016/j.sedgeo.2007.10.002.

Jones, B., and R. W. Renaut, 1995, Noncrystallographic Calcite Dendrites from Hot-Spring Deposits at Lake Bogoria, Kenya: SEPM Journal of Sedimentary Research, v. Vol. 65A, p. 154–169, doi:10.1306/D4268059-2B26-11D7-8648000102C1865D.

Jones, B., R. W. Renaut, R. Bernhart Owen, and H. Torfason, 2005, Growth patterns and implications of complex dendrites in calcite travertines from Lýsuhóll, Snaefellsnes, Iceland: Sedimentology, v. 52, no. 6, p. 1277–1301, doi:10.1007/s00198-005-1960-y.

Jones, B., R. W. Renaut, and M. R. Rosen, 2000, Trigonal Dendritic Calcite Crystals Forming from Hot Spring Waters at Waikite, North Island, New Zealand: Journal of Sedimentary Research, v. 70, no. 3, p. 586–603, doi:10.1306/2DC4092A-0E47-11D7-8643000102C1865D.

Kaypak, B., and G. Gökkaya, 2012, 3-D imaging of the upper crust beneath the Denizli geothermal region by local earthquake tomography, western Turkey: Journal of Volcanology and Geothermal Research, v. 211–212, p. 47–60, doi:10.1016/j.jvolgeores.2011.10.006.

Khatib, S., P. Rochette, M. C. Alçiçek, A.-E. Lebatard, F. Demory, and T. Saos, 2014, Études stratigraphique, sédimentologique et paléomagnétique des travertins de Kocabaş, Bassin de Denizli, Anatolie, Turquie, contenant des restes fossiles quaternaires: L'Anthropologie, p. 1–18, doi:10.1016/j.anthro.2014.01.005.

Lebatard, A. et al., 2014, Dating the Homo erectus bearing travertine from Kocabaş (Denizli, Turkey) at at least 1.1 Ma: Earth and Planetary Science Letters, v. 390, p. 8–18.

Lønøy, A., 2006, Making sense of carbonate pore systems: AAPG Bulletin, v. 90, no. 9, p. 1381–1405, doi:10.1306/03130605104.

Lottaroli, F., L. Meciani, P. Andreotti, and F. Cornaggia, 2012, West Africa Pre-salt Exploration: Background and Perspective of the West African "Tupi" Myth, *in* New understanding of the Petroleum Systems of Continental Margins of the World: GCS SEPM, p. 460–468.

Mancini, E. A., W. A. Morgan, P. M. (Mitch) Harris, and W. C. Parcell, 2013, Introduction: AAPG Hedberg Research Conference on Microbial Carbonate Reservoir Characterization—Conference summary and selected papers: AAPG Bulletin, v. 97, no. 11, p. 1835–1847, doi:10.1306/intro070913.

Meisling, K. E., P. R. Cobbold, and V. S. Mount, 2001, Segmentation of an obliquely rifted margin, Campos and Santos basins, southeastern Brazil: AAPG bulletin, v. 85, no. 11, p. 1903–1924.

Milliman, J. D., J. A. Hook, and S. Golubić, 1985, Meaning and usage of micrite cement and matrix-reply to discussion: Journal of Sedimentary Petrology, v. 55, p. 777–784.

Nakano, C. M. F., A. C. C. Pinto, J. L. Marcusso, and K. Minami, 2009, Pre-Salt Santos Basin-Extended Well Test and Production Pilot in the Tupi Area-The Planning Phase, *in* Offshore Technology Conference: p. 1–8.

Van Noten, K., H. Claes, J. Soete, A. Foubert, M. Özkul, and R. Swennen, 2013, Fracture networks and strike – slip deformation along reactivated normal faults in Quaternary travertine deposits , Denizli Basin , western Turkey: Tectonophysics, v. 588, p. 154–170, doi:10.1016/j.tecto.2012.12.018.

Van Noten, K., S. Topal, M. O. Baykara, M. Özkul, and R. Swennen, n.d., Pleistocene deformation history of the Ballik travertine along the NE margin of the Denizli Graben-Horst System (SW Turkey): Tectonophysics.

Okumura, T., C. Takashima, F. Shiraishi, S. Nishida, K. Yukimura, T. Naganuma, H. Koike, G. Arp, and A. Kano, 2011, Microbial Processes Forming Daily Lamination in an Aragonite Travertine, Nagano-yu Hot Spring, Southwest Japan: Geomicrobiology Journal, v. 28, no. 2, p. 135–148, doi:10.1080/01490451003743275.

Özkul, M., B. Engin, M. Alçiçek, T. Koralay, and H. Demirtaş, 2004, Thermoluminescence dating of Quaternary hot spring travertines and some implications on graben evolution, Denizli, western Turkey: 32nd International Geological ….

Özkul, M., S. Kele, A. Gökgöz, C.-C. Shen, B. Jones, M. O. Baykara, I. Fórizs, T. Németh, Y.-W. Chang, and M. C. Alçiçek, 2013, Comparison of the Quaternary travertine sites in the Denizli extensional basin based on their depositional and geochemical data: Sedimentary Geology, v. 294, p. 179–204, doi:10.1016/j.sedgeo.2013.05.018.

Özkul, M., B. Varol, and M. C. Alçiçek, 2002, Depositional environments and petrography of Denizli travertines: Mineral Res. Expl. Bul., v. 125, p. 13–29.

Pasley, M. A., and E. N. Wilson, 1998, Lower Cretaceous Stratigraphy and Source Rock Distribution in Pre-salt of the South Atlantic: Comparison of Angola and Southern Brazil, *in* ABGP/AAPG International Conference and Exhibition.

Pentecost, A., 1990, Travertine Dating, *in* Travertine: p. 243–251.

Rainey, D. K., and B. Jones, 2009, Abiotic versus biotic controls on the development of the Fairmont Hot Springs carbonate deposit, British Columbia, Canada: Sedimentology, v. 56, no. 6, p. 1832–1857, doi:10.1111/j.1365-3091.2009.01059.x.

Rezende, M. F., and M. C. Pope, 2015, Importance of depositional texture in pore characterization of subsalt microbialite carbonates, offshore Brazil: Geological Society, London, Special Publications, v. 418, doi:10.1144/SP418.2.

Rodríguez-Berriguete, a., a. M. Alonso-Zarza, M. C. Cabrera, and a. Rodriguez-Gonzalez, 2012, The Azuaje travertine: an example of aragonite deposition in a recent volcanic setting, N Gran Canaria Island, Spain: Sedimentary Geology, v. 277–278, p. 61–71, doi:10.1016/j.sedgeo.2012.07.010.

Ronchi, P., and C. Francesco, 2015, Continental carbonates as hydrocarbon Reservoir, an analog case study from the travertine of Saturnia, Italy: AAPG Bulletin, v. 4, no. April 2015, p. 711–734, doi:10.1306/10021414026.

Ross, D. J., 1991, Botryoidal High-Magnesium Calcite Marine Cements from the Upper Cretaceous of the Mediterranean Region: Journal of Sedimentary Research, v. Vol. 61, no. 3, p. 349–353, doi:10.1306/D4267708-2B26-11D7-8648000102C1865D.

Saller, A., S. Rushton, L. Buambua, K. Inman, R. Mcneil, and J. A. D. T. Dickson, 2016, Presalt stratigraphy and depositional

systems in the Kwanza Basin , offshore Angola: v. 7, no. 7, p. 1135–1164, doi:10.1306/02111615216.

Schröder, S., A. Ibekwe, M. Saunders, R. Dixon, and A. Fisher, 2015, Algal–microbial carbonates of the Namibe Basin (Albian, Angola): implications for microbial carbonate mound development in the South Atlantic: Petroleum Geoscience, p. 2014–83, doi:10.1144/petgeo2014-083.

Sharp, I. et al., 2013, Pre- and Post-Salt Non-Marine Carbonates of the Namibe Basin, Angola, *in* Microbial Carbonates in Space and Time: Implications for Global Exploration and Production: The Geological Society of London, p. 52–53.

Sharp, I. et al., 2012, Pre- and Post-Salt Non-Marine Carbonates of the Namibe Basin, Angola, *in* AAPG Annual Convention and Exhibition: AAPG Search and Discovery.

Soete, J., M. Huysmans, H. Claes, S. Claes, M. M. Erthal, M. Özkul, and R. Swennen, n.d., Geostatistical analysis of porosity-permeability and continental carbonate lithofacies distribution in the Ballik area, Denizli (Turkey), a case study of a reservoir analogue for Pre-Salt continental carbonate reservoirs: Marine and Petroleum Geology.

Soete, J., L. M. Kleipool, H. Claes, S. Claes, H. Hamaekers, S. Kele, M. Özkul, A. Foubert, J. J. G. Reijmer, and R. Swennen, 2015, Acoustic properties in travertines and their relation to porosity and pore types: Marine and Petroleum Geology, v. 59, p. 320–335, doi:10.1016/j.marpetgeo.2014.09.004.

Terra, G. J. S. et al., 2010, Carbonate rock classification applied to Brazilian sedimentary basins: Boletin Geociencias Petrobras, v. 18, no. 1, p. 9–29.

Thompson, L., and C. Oftebro, 2011, Salt gets in your eyes: the geological challenges and solutions to sub-salt exploration: First Break, v. 29, no. March, p. 93–98.

Török, Á., A. Mindszenty, H. (KU L. Claes, S. Kele, L. Fodor, and R. Swennen, 2016, Geobody architecture of continental carbonates: "Gazda" travertine quarry (Süttö, Gerecse Hills, Hungary): Quaternary International.

Tucker, M. E., and V. P. Wright, 1990, Carbonate Sedimentology: Oxford, UK, Blackwell Publishing Ltd., doi:10.1002/9781444314175.

Wright, V. P., 2012, Lacustrine carbonates in rift settings: the interaction of volcanic and microbial processes on carbonate deposition: Geological Society, London, Special Publications, v. 370, no. 1, p. 39–47, doi:10.1144/SP370.2.

Wright, V. P., and A. J. Barnett, 2015, An abiotic model for the development of textures in some South Atlantic early Cretaceous lacustrine carbonates Cretaceous (part): Microbial Carbonates in Space and Time: Implications for Global Exploration and Production, p. 418.

APPENDIX 2

Results of Geochemical Analysis

Sample	Ca	Al	As	Ba	Co	Cr	Cu	Fe	K	Li	Mg	Mn	Na	Ni	P	Rb	S	Sr	Ti	V	Zn
	%	µg/g	µg/g	µg/g	µg/g	µg/g	µg/g	µg/g	µg/g	µg/g	µg/g	µg/g	µg/g	µg/g	µg/g	µg/g	µg/g	µg/g	µg/g	µg/g	µg/g
QS11T	38.6	70	<5	7	<1	<5	<1	99	23	<1	1420	35	169	<1	72	<5	1100	388	1	<2	<2
QR15B	38.8	89	9	10	<1	<5	<1	42	41	<1	1765	20	211	<1	51	<5	1457	615	3	<2	<2
QR21	38.4	87	8	7	<1	<5	<1	73	43	<1	1756	26	216	<1	79	<5	1515	552	2	<2	<2
QR22	37.9	69	5	16	<1	<5	<1	43	33	<1	1408	17	195	<1	55	<5	1308	576	2	<2	<2
QR24V1	38.4	103	<5	6	<1	<5	<1	46	29	<1	1897	30	216	<1	85	<5	1555	502	2	<2	<2
QR24V2	38.6	125	7	9	<1	<5	<1	47	47	<1	1913	23	241	<1	75	<5	1724	690	3	<2	<2
QR28	38.3	152	7	10	<1	<5	<1	61	51	<1	1752	19	223	<1	63	<5	1428	612	5	<2	<2
QR29	38.9	124	9	7	<1	<5	<1	81	40	<1	1444	20	174	<1	61	<5	1066	552	3	<2	<2
QR31H	38.4	60	5	8	<1	<5	<1	29	44	<1	1867	18	237	<1	66	<5	1701	600	2	<2	<2
QR32V	16.0	<15	<5	5	36	<5	35	22	21	<1	757	9	144	<1	34	<5	757	272	1	<2	<2
QR33H	38.1	48	6	9	<1	<5	<1	31	39	<1	1937	21	223	<1	69	<5	1803	619	2	<2	<2
QR34V	38.2	70	<5	11	<1	<5	<1	36	42	<1	1878	23	219	<1	73	<5	1602	560	3	<2	<2
QR35H	38.4	128	7	12	<1	<5	<1	46	60	<1	1880	18	256	<1	60	<5	1684	717	5	<2	<2
QR36H	38.2	87	6	9	<1	<5	<1	42	44	<1	2032	24	233	<1	75	<5	1769	610	3	<2	<2
QR38H	35.9	73	7	9	<1	<5	<1	39	32	<1	1607	21	192	<1	53	<5	1286	553	2	<2	<2
QE40	38.0	59	6	15	<1	<5	<1	34	44	<1	1634	15	217	<1	46	<5	1602	713	2	<2	<2
QR47	38.5	105	5	9	<1	<5	<1	55	36	<1	1662	23	198	<1	63	<5	1331	505	3	<2	<2
QR52	38.4	84	7	11	<1	<5	<1	48	56	<1	1955	25	323	<1	71	<5	2760	801	2	<2	<2
QR55	38.2	113	<5	6	<1	<5	1	319	27	<1	1500	46	176	<1	77	<5	959	390	4	5	<2
QR63	38.3	55	<5	5	<1	<5	1	54	26	<1	1545	24	170	<1	72	<5	1052	363	3	<2	<2
QR65	38.9	73	7	9	<1	<5	<1	56	35	<1	1970	25	229	<1	73	<5	1655	558	3	<2	<2
QR68	38.3	243	<5	14	<1	<5	<1	89	61	<1	1871	38	302	<1	102	<5	2086	722	7	<2	<2
QR133H2	37.5	164	7	10	<1	<5	<1	83	43	<1	2336	36	294	<1	110	<5	2302	663	4	<2	<2
QR135H	39.8	66	6	7	<1	<5	<1	29	27	<1	1601	21	180	<1	60	<5	1246	433	2	<2	<2
QR136V1B	38.2	85	6	8	<1	<5	<1	27	33	<1	1588	22	184	<1	65	<5	1240	431	3	<2	<2
QR138H	38.1	80	4	9	<1	<5	<1	30	31	<1	1788	22	213	<1	86	<5	1586	523	2	<2	<2
QR139V	37.9	84	<5	10	<1	<5	<1	41	38	<1	1925	28	195	<1	83	<5	1894	558	2	<2	<2
QR140H1	37.9	88	11	17	<1	<5	<1	26	71	<1	2369	20	391	<1	64	<5	3207	962	2	<2	<2
QR103H1	37.6	110	10	8	<1	<5	1	75	47	<1	2029	22	249	<1	83	<5	1826	688	3	<2	<2
QR116H1	38.4	67	13	9	<1	<5	<1	131	34	<1	1812	22	148	<1	57	<5	1386	600	2	<2	<2
QR117H	38.6	52	6	7	<1	<5	<1	88	30	<1	1771	24	206	<1	63	<5	1344	504	1	<2	<2
QR118H	38.4	103	8	7	<1	<5	<1	185	31	<1	1985	32	229	2	91	<5	1698	476	2	<2	<2
CR002	37.3	263	<5	28	<1	<5	<1	213	86	<1	2884	31	437	<1	49	<5	3864	1270	5	<2	<2
CR03	37.8	194	<5	14	<1	<5	<1	73	76	<1	2422	22	301	<1	34	<5	2349	839	5	<2	<2
CR05	36.4	189	<5	23	<1	<5	<1	84	99	<1	2840	29	502	<1	34	<5	5720	1946	4	<2	<2
CR11H	38.1	288	<5	25	<1	<5	<1	143	99	<1	2565	35	366	<1	49	<5	2699	885	9	<2	<2
CR12	38.7	101	<5	10	<1	<5	<1	33	41	<1	2017	27	243	<1	88	<5	1780	621	3	<2	<2
QR71	36.9	138	16	16	<1	<5	<1	188	66	<1	1958	26	320	<1	93	<5	2330	781	5	<2	<2
QR95V	38.4	91	10	10	<1	<5	<1	53	47	<1	2449	19	242	<1	73	<5	1642	692	3	<2	<2
QR98H	38.3	204	10	8	<1	<5	<1	144	55	<1	2129	19	197	<1	86	<5	1534	573	4	<2	3
QR115H	38.6	41	<5	5	<1	<5	<1	78	24	<1	1793	25	160	<1	58	<5	1174	615	1	<2	<2
QR119V2	38.6	49	10	7	<1	<5	<1	65	32	<1	2147	15	205	<1	60	<5	1612	868	2	<2	<2
QR122H	38.1	162	8	10	<1	<5	<1	67	49	<1	2070	30	198	<1	71	<5	1486	790	6	<2	<2
QR67	37.7	826	14	29	<1	<5	<1	250	251	2	3229	25	583	<1	62	<5	3292	1349	35	<2	<2
QR69	37.8	1493	9	34	<1	<5	<1	360	378	2	2355	52	586	<1	117	<5	3064	1247	67	3	<2
QR74H	38.1	158	8	22	<1	<5	<1	78	57	<1	1777	19	244	<1	87	<5	1807	787	7	<2	<2
QR85H2	38.0	738	8	18	<1	<5	<1	198	191	<1	2181	26	347	<1	111	<5	2308	786	32	<2	<2
QR94H1	37.9	115	12	11	<1	<5	<1	107	52	<1	1867	15	215	<1	68	<5	1611	636	5	<2	<2
QR125H	35.8	7081	20	92	<1	7	2	1174	1713	9	3288	36	823	1	124	16	3593	1624	313	5	5
QR128V	36.1	4053	33	55	<1	5	1	1798	1011	5	2702	83	710	1	169	12	3394	1518	185	5	5
QR134V	38.0	37	6	8	<1	<5	<1	38	25	<1	1241	19	162	<1	62	<5	1075	408	1	<2	<2